

NATIONAL & INTERNATIONAL SCIENTIFIC EVENTS

46th Annual Conference of the IEEE Industrial Electronics Society-IECON 2020

Venue: Marina Bay Sands Expo and Convention Centre
Location: Malaysia

Begins: October 18, 2020
Ends: October 21, 2020

14th Mediterranean Congress of Chemical Engineering

Venue: Gran Via
Location: Barcelona, Spain

Begins: December 1, 2020
Ends: December 4, 2020

39th IEEE International Conference on Consumer Electronics (ICCE 2021)

Venue: Virtual
Location: Las Vegas, USA

Begins: January 10, 2021
Ends: January 12, 2021

33rd International Symposium on Power Semiconductor Devices and ICs (ISPSD)

Venue: Nagoya Congress Center
Location: Nagoya, Japan

Begins: May 30, 2021
Ends: June 3, 2021

39th IAHR World Congress

Venue: Palacio de Congresos de Granada
Location: Granada, Spain

Begins: July 4, 2021
Ends: July 9, 2021

25th International Congress of Theoretical and Applied Mechanics

Venue: MiCo Congress Centre
Location: Milano, Italy

Begins: August 22, 2021
Ends: August 27, 2021

23rd International Conference on Electrical Machines and Systems (ICEMS2020)

Venue: ACT CITY Hamamatsu
Location: Hamamatsu, Japan

Begins: November 24, 2020
Ends: November 27, 2020

73rd Annual Session of Indian Institute of Chemical Engineers (CHEMCON2020)

Venue: Institute of Minerals & Materials Technology
Location: Bhubaneswar, India

Begins: December 27, 2020
Ends: December 30, 2020

8th International Conference on Geological and Civil Engineering (ICGCE 2021)

Location: Tokyo, Japan

Begins: January 28, 2021
Ends: January 30, 2021

35th IAS Meeting of Sedimentology

Venue: Conference Centre of the Vienna House Diplomat Hotel
Location: Prague, Czech Republic

Begins: June 22, 2021
Ends: June 24, 2021

50th International Congress and Exposition on Noise Control Engineering

Venue: Marriott Wardman Park
Location: Washington, USA

Begins: August 1, 2021
Ends: August 4, 2021

20th International Conference on Soil Mechanics and Geotechnical Engineering 2021

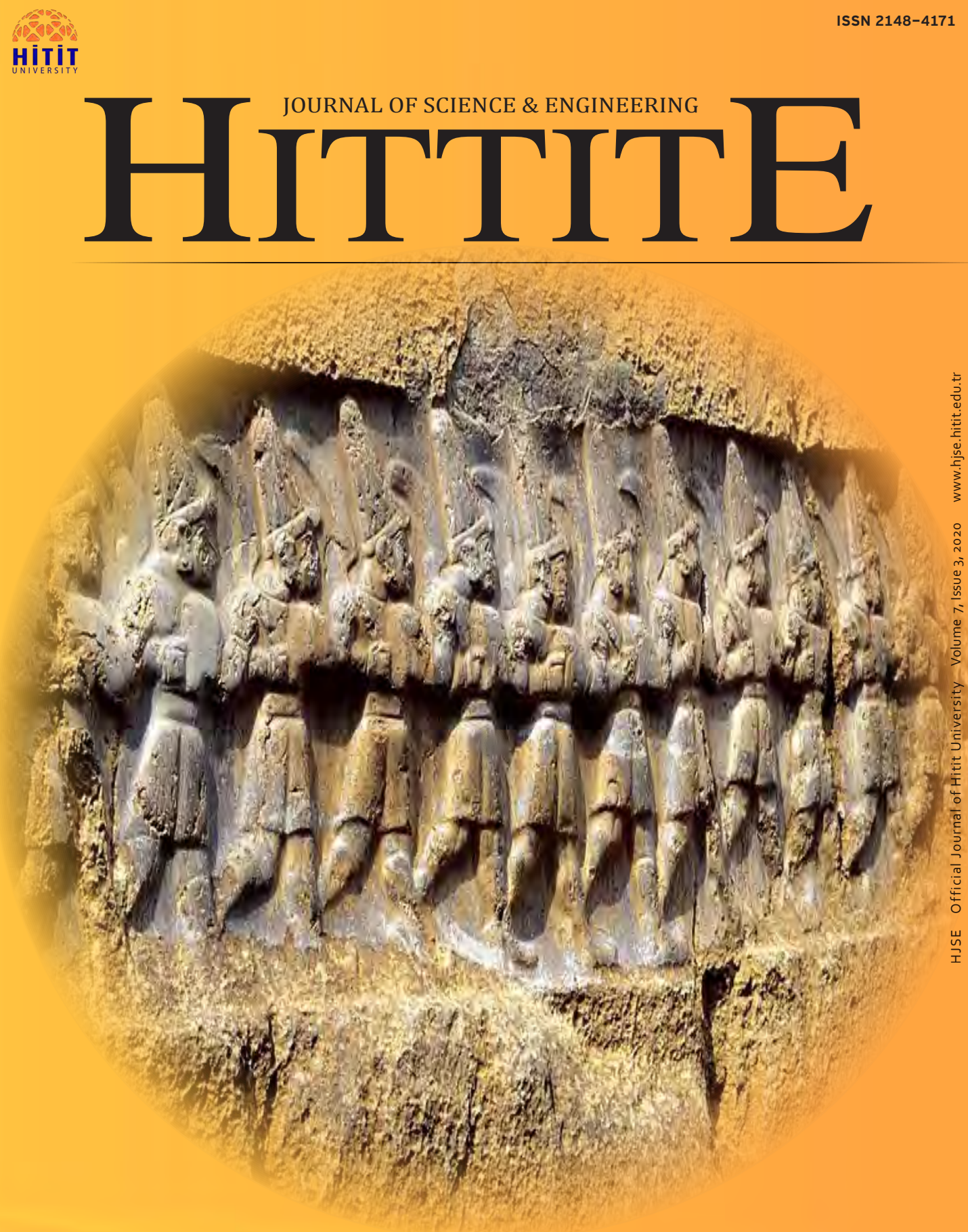
Venue: International Convention Centre
Location: Sydney, Australia

Begins: September 12, 2021
Ends: September 17, 2021

HITTITE

JOURNAL OF SCIENCE & ENGINEERING

HJSE Official Journal of Hitit University Volume 7, Issue 3, 2020 www.hjse.hitit.edu.tr



HJSE Official Journal of Hitit University Volume 7, Issue 3, 2020 www.hjse.hitit.edu.tr



Abstracted & Indexed in:

TR Dizin Mühendislik ve Temel Bilimler Veri Tabanı | CrossRef | Google Scholar | MIP Database | StuartxChange | ResearchBib | Scientific Indexing Services (SIS)

HITTITE

Volume 7, Issue 3, 2020

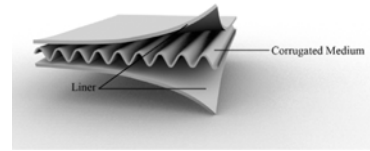
www.hjse.hitit.edu.tr

Investigation of Strength and Migration of Corrugated Cardboard Boxes

163-168

Betul Gok and Duygu Akpınar

In this study, E flute and BC flute corrugated cardboards were prepared by using different type of paper and their strengths were investigated.

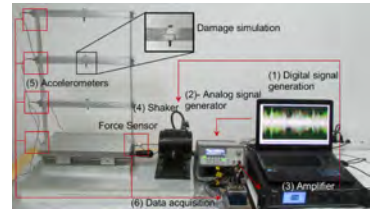


Damage Diagnosis of Bolt Loosening via Vector Autoregressive - Support Vector Machines

169-179

Mahmut Pekedis

The objective of this study is to detect the damage using the vector auto regression model (VAR) coupled with support vector machines (SVM).

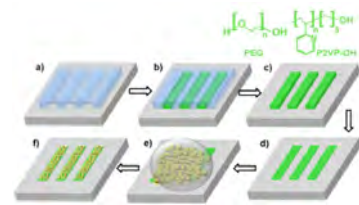


Arrays of Plasmonic Nanoparticles Assembled on Patterns of Polymer Brushes Fabricated by Soft Lithography

181-188

Hasan H. Ipekci, Afia Asif, Sema Karabel and M. Serdar Onses

This work employed end-grafted poly(ethylene glycol) (PEG) and hydroxyl-terminated poly(2-vinylpyridine) (P2VP) polymer chains for selective immobilization and pattern-ing of plasmonic nanoparticles (NPs).

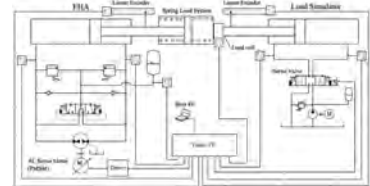


A Model - Based Jamming Detection Method for Electro-Hydrostatic Actuators

189-198

Emre Murat Poyraz, Hakan Caliskan and Ali Emre Turgut

In this paper, a novel threshold-based fault detection and diagnosis method is proposed.

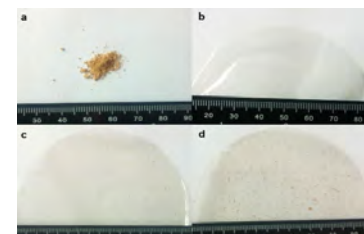


Reinforcement of Na-Alginate Based Films with Carrot Juice Processing Wastes

199-204

Hulya Cakmak and Fatma Unal

In this study, Na-alginate based films were produced with the addition of cellulosic fibres from carrot juice processing wastes for employment of agricultural wastes as reinforcing agent in biobased films for food packaging purposes.

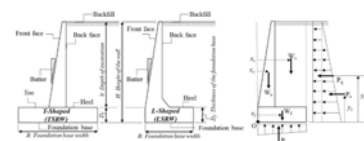


Effects of Soil Geotechnical Properties on the Prediction of Optimal Dimensions of Restricted Reinforced Concrete Retaining Walls

205-213

Aylin Ece Kayabekir, Zulal Akbay Arama, Gebrail Bekdas and Ilknur Dalyan

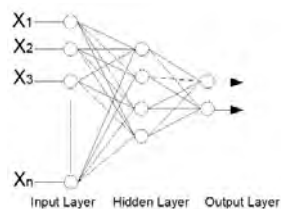
The aim of this paper is to investigate the effects of soil properties associated with the project requirements and environmental conditions, on the prediction of the design dimensions of L-Shaped restricted reinforced concrete retaining walls by the use of optimization algorithms.



Comparison of Neural Network Models for Nostalgic Sentiment Analysis of YouTube Comments 215-221

Seda Postalcioglu and Senem Aktas

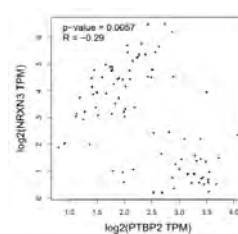
The aim of the study is to draw conclusions from the comments made under the songs whether they are nostalgic.



Analysis of miRNA-Mediated ceRNAs In The Pathogenesis of Renal Cell Carcinoma: An In Silico Approach 223-238

Orcun Avsar

The aim of this study was to define novel molecular biomarkers for RCC via in silico analysis.

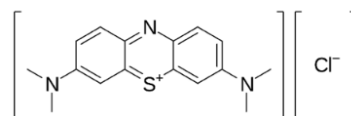


Adsorption Of Methylene Blue from Aqueous Solution with Sulfuric Acid Activated Corn Cobs: Equilibrium, Kinetics, and Thermodynamics Assessment

239-256

Pinar Bozbeyoglu, Celal Duran, Cemalettin Baltaci and Ali Gundogdu

This study aims to examine the effects of relatively dilute and concentrated acids on the activation process and to gain an economic value to waste materials through the production of a new adsorbent.



Owner

Prof. Dr. Ali Osman ÖZTÜRK on
behalf of Hitit University

Editor-in-chief

Prof. Dr. Ali KILIÇARSLAN

Associate Editors

Prof. Dr. D. Ali KÖSE

Assist. Prof. Dr. Öncü AKYILDIZ

Production

Assoc. Prof. Dr. Kazım KÖSE

Res. Asst. Dr. Erhan ÇETİN

Res. Asst. Mustafa Reşit HABOĞLU

Res. Asst. Harun Emre KIRAN

Res. Asst. Ömer Faruk TOZLU

Lect. Tugrul YILDIRIM

Editor's Office

Tel: +90 364 227 45 33 / 12 36

Fax: +90 364 227 45 35

Email: alikilicarslan@hitit.edu.tr

Subscription Service:

Tel: +90 364 227 45 33 / 12 82

Fax: +90 364 227 45 35

Email: hjse@hitit.edu.tr

EDITORIAL BOARD

Prof. Dr. İftikhar AHMAD

Prof. Dr. Mike BECKETT

Prof. Dr. İbrahim DİNÇER

Prof. Dr. Ali ELKAMEL

Prof. Dr. Mohamad S QATU

Prof. Dr. Saffa RIFFAT

Prof. Dr. Thanos SALIFOGLU

Assoc. Prof. Dr. Yuehong SU

Dr. Wojciech NOGALA

Prof. Dr. Yusuf AYVAZ

Prof. Dr. Adil DENİZLİ

Prof. Dr. Ali GENÇER

Prof. Dr. Metin GÜRÜ

Prof. Dr. Murat HOŞÖZ

Prof. Dr. Sadık KAKAÇ

Prof. Dr. Tarık Ömer OĞURTANI

Prof. Dr. Ender SUVACI

Assoc. Prof. Dr. Ali TOPÇU

Prof. Dr. Kazım Savaş BAHÇECİ

Assoc. Prof. Dr. Cengiz BAYKASOĞLU

Prof. Dr. Naki ÇOLAK

Prof. Dr. Vedat DENİZ

Prof. Dr. Hakan GÜNGÜNEŞ

Prof. Dr. Bülent KABAK

Prof. Dr. Ali KILIÇARSLAN

Prof. Dr. Dursun Ali KÖSE

Prof. Dr. İrfan KURTBAŞ

Prof. Dr. İbrahim SÖNMEZ

Assoc. Prof. Dr. Seyfi ŞEVİK

Prof. Dr. Dilber Esra YILDIZ

University of Malakand, Chakdara, Pakistan

Bangor University, Bangor, United Kingdom

Uoit Ontario University, Ontario, Canada

University of Waterloo, Ontario, Canada

Central Michigan University, Michigan, United States

The University of Nottingham, United Kingdom

Aristotle University of Thessaloniki, Thessaloniki, Greece

The University of Nottingham, United Kingdom

Polish Academy of Sciences, Poland

Suleyman Demirel University, Turkey

Hacettepe University, Turkey

Ankara University, Turkey

Gazi University, Turkey

Kocaeli University, Turkey

TOBB University, Turkey

Middle East Technical University, Turkey

Anadolu University, Turkey

Hacettepe University, Turkey

Hitit University, Turkey

Hitit University, Turkey

Hitit University, Turkey

Hitit University, Turkey

Hitit University, Turkey

Hitit University, Turkey

Hitit University, Turkey

Hitit University, Turkey

Hitit University, Turkey

Hitit University, Turkey

Hitit University, Turkey

Hitit University, Turkey

Journal Name : HITTITE JOURNAL OF SCIENCE AND ENGINEERING
Year : 2020
Managing Editor : Prof. Dr. Ali KILIÇARSLAN
Managing Office : Hitit University Faculty of Engineering
Managing Office Tel : +90 364 227 45 33 / 12 36
Publication Language : English
Publication Type : Peer Reviewed, Open Access, International Journal
Delivery Format : 4 times a year (quarterly)
Print ISSN : 2149-2123
Online ISSN : 2148-4171
Publisher Address : Hitit Üniversitesi Kuzey Kampüsü Çevre Yolu Bulvarı
19030 Çorum / TÜRKİYE
Publisher Tel : +90 364 227 45 33/1236



This new issue of Hittite Journal of Science and Engineering contains twelve manuscripts from the disciplines of chemistry, molecular biology and genetics, food engineering, materials science and engineering, mechanical engineering, civil engineering and computer engineering. These manuscripts was first screened by Section Editors using plagiarism prevention software and then reviewed and corrected according to the reviewer's comments. I would like to express my gratitude to all our authors and contributing reviewers of this issue.

I would like to thank to the new President of Hitit University, Prof. Dr.

Ali Osman Öztürk, for his support and interest in HJSE and also to the Associate Editors of HJSE, namely Prof. Dr. Dursun Ali Kose and Asst. Prof. Dr. Oncu Akyildiz, as well as our Production Editors Assoc. Prof. Dr. Kazim Kose, Mustafa Reşit Haboğlu, Dr. Erhan Çetin, Tugrul Yildirim, Harun Emre Kiran and Ömer Faruk Tozlu for their invaluable efforts in making of the journal.

It's my pleasure to invite the researchers and scientists from all branches of science and engineering to join us by sending their best papers for publication in Hittite Journal of Science and Engineering.

Prof. Dr. Ali Kiliçarslan

Editor-in-Chief

Investigation of Strength and Migration of Corrugated Cardboard Boxes

Betul Gok¹  Duygu Akpınar² 

¹Akdeniz University, Department of Chemistry, Antalya, Turkey

²Ankutsan Inc. R&D Center, Antalya, Turkey

ABSTRACT

Corrugated cardboard is a high-performance packaging material designed to protect and present a variety of products from agricultural products to industrial products. Because of this strength of corrugated cardboards are of great importance. In this study, E flute and BC flute corrugated cardboards were prepared by using different type of paper and their strengths were investigated. For this purpose, weight, thickness measured and edge crush test (ECT) were performed. Results shows that as the paper weight increase, the strength of corrugated cardboard increase. And also, migration tests were done whether corrugated cardboard is appropriate for food contact.

Keywords:

Corrugated cardboard strength; ECT; PCB; Migration; Cobb test; Secondary packaging.

INTRODUCTION

Paper and paperboard sheet materials obtained from an interwoven lattice of cellulose fibers made of cellulosic material like wood, linen or cotton [1]. The most important application of paper and paperboard is in corrugated paperboard packages.

A corrugated cardboard consisting of a single corrugated layer sandwiched between two liner layers (Fig. 1). This product consists of a combination of the three layers stronger than each layer is individually owned. In addition to single wall, double wall and triple wall corrugated cardboards are also in current use. Double wall corrugated cardboards consist of gluing five layers of paper; one inner, one outer, one intermediate liner paper and two fluted papers and forming a double wall corrugated cardboard.

Corrugated medium part of the cardboard is called as flute (Fig.2). Variations in flute height and number of flutes per unit of length defined as flute type (A, B, C, E)

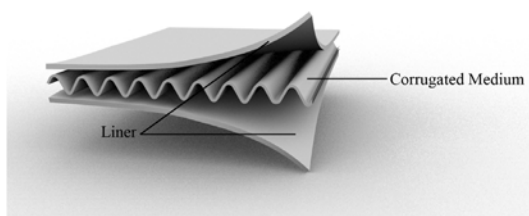


Figure 1. Schematic representation of corrugated cardboard

Article History:

Received: 2017/11/28

Accepted: 2020/09/28

Online: 2020/09/30

Correspondence to: Betul Gok,
Akdeniz University, Chemistry, Antalya,
Turkey

E-Mail: betulyitmez@akdeniz.edu.tr

Phone: +90 242 249 77 00

Fax: +90 242 249 77 07

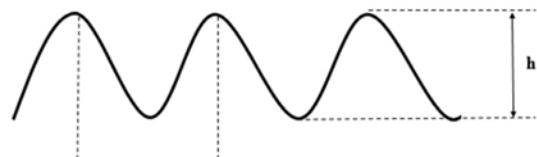


Figure 2. Schematic representation of corrugated medium part of the cardboard (λ :wavelength, h : height)

[2]. The take-up factor is a measure of the linear length of the medium per unit length of corrugated cardboard. Table 1 summarize the flute type classification.

Corrugated cardboard is the most widely used type of package for the packaging and distribution of a wide variety of commodities ranging from fruits and vegetables, consumer products, to industrial items. Corrugated cardboards have a high stiffness/weight ratio. Compared to other packaging materials, it delivers relatively high stiffness at a relatively low price [3] [4]. As a packaging material, corrugated cardboards have a lot of advantages over plastic packaging materials. Because it is a kind of environment- friendly packaging material made of reusable paper and water /starch-based glue, which are 100% recyclable, reusable and biodegradable [5].

It is equally suitable for all the different modes of storage and transport such as shipping by sea or by air. The most important feature of containers made from corrugated boards is to protect the packaged commo-

Table 1. Corrugated board flute type standards.

Flute Designation	Height (h) (mm)	Wavelength(f)(mm)	Flutes number per Linear Meter	Take-up factor
A	4.0-4.8	8.0-9.5	105-125	1.48-1.53
B	2.2-3.0	5.5-8.5	153-181	1.28-1.43
C	3.2-4.0	6.8-8.0	125-147	1.42-1.50
E	1.0-1.8	3.0-3.5	285-334	1.22-1.29

dities against all kind of damages during storage and transport. Therefore, the maintenance of strength of cardboard during storing, marketing and distribution of horticultural commodities is needed to take into consideration [6]. The weight, type and properties of the outer, inner and intermediate papers forming the corrugated cardboard are of great importance as they are directly related to the box performance. In addition to the papers used, the type of glue and additives should be chosen appropriately [7]. Paper and board materials that come into contact with foodstuffs must comply with the requirements of the European Framework Regulation (EC) No 1935/2004, which states that materials and products designed to enter foodstuffs do not pose health risks to consumers, affect organoleptic characteristics or alter food composition [8].

In this study we prepared ten different corrugated cardboard for making fresh fruit-vegetable box and pizza box. Then we analyzed the boxes' strength, water absorptivity and conformity with food contact.

MATERIALS AND METHODS

Starch and NaOH were purchased from Tate & Lyle Inc., Koruma Klor Alkali San. ve Tic. Inc., respectively. Borax ($\text{Na}_2\text{B}_4\text{O}_7 \cdot 10\text{H}_2\text{O}$) purchased from MTA. Starch Glue prepared according to Stein Hall Method [9]. Different type of papers, Kraft (KR), Neutral Sulfite Semi-Chemical (NC), White Kraft (WKR), White Test Liner (WTL) and Fluting (FL) used for corrugated cardboard production. Kraft papers purchased from 'International Paper Company. VinciLiner (WKR) and NSSC papers purchased from Reno De Medici Group, in Italy.

Preparation of Starch Glue

For preparation of starch glue, corn starch was used. Starch Glue is prepared according to Stein Hall Method [10] [9]. Stein Hall Method consists of two-phase concept. Primer phase is necessary to give a certain viscosity to glue and keep the viscosity constant.

For this reason, the primer phase is also called as the carrier. This means that the primer phase carries the glue. The secondary phase is the phase of the real glue formation which provides the adhesion of papers. Different resins were added the prescription to improve strengthens the starch stickiness, accelerates the drying and gives firmness. Starch glue viscosity should be stable from preparation to application.

Production of Corrugated Cardboard

Corrugated cardboards which used for the experiment were produced at Ankutsan A.Ş. production facilities. Corrugated cardboard is formed by gluing the flute layer between two flat liners with starch glue. Double-layer corrugated cardboard consist of three flat liner and two flute liner is also produced for more strength products. Corrugated cardboard manufacturing process begins with the selection of the appropriate type and amount of paper. Production side mainly consist of two parts as wet part and dry part. In the wet production side, paper softened by heat and steam preconditioners takes wave shape by passing through corrugating rolls. After this shaping, the starch-based glue is usually applied to the wave tops and adherence of the flute to pre-heated liner

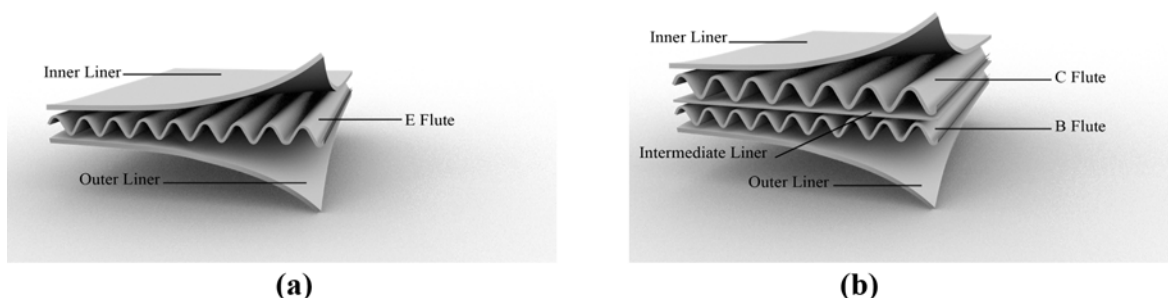


Figure 3. Illustration of board styles and layers (a) E flute Single Wall (b) BC Flute Double Wall

paper by pressing is ensured. In the dry production side, after the laminated cardboard sheet is removed from the wet part, the edges are trimmed and sized for the planned box production. Blunt blades pressed on the corrugated cardboard for facilitate box folding. Then the products are stacked on top. In this study, 10 corrugated cardboard samples were prepared with different paper combinations. Two of them are E wave single wall corrugated cardboards used in the production of pizza boxes and are named EF@WTL120 and EF@WTL125. The other eight are BC wave double wall corrugated cardboards used in the production of fresh fruit and vegetable (FFV) boxes. The paper types and properties used in the preparation of these 10 samples and the names given to the samples are given in Table-2. The nomenclature of the samples was made as “flute type@ changing paper”.

Chemical Analysis

Polychlorobiphenyls (PCBs) analysis of samples were done in Intertek Laboratories according to TS EN ISO 15318 [11] by using ISQ-GC/MS technique. Trace Element analysis of samples was done in Intertek Laboratories and according to NMKL 186 [12] by using ICAP Q ICP-MS technique.

Formaldehyde, chlorine and Pentachloro Phenol (PCP) analysis also was made in Intertek Laboratories according to EN 1541: 2001 [13], TS ISO 5647, Mohr Method and 35 LMBG B 82.02-8 standards, respectively.

Strength Test

ECT Test

Edge crush test (ECT) gives information about the strength of corrugated board on vertically positioned corrugations. During these tests it is important that the

force applied to the sample is exactly perpendicular. Edge Crush Test (ECT) is carried out according to DIN EN ISO 3037:2013 [14].

Edge Crush Test (ECT) is a true performance test and is directly related to the stacking strength of a carton. ECT is a measure of the edgewise compressive strength of corrugated board. ECT values are of great importance in estimating the quality of corrugated cardboard.

Cobb Tests

The Cobb test is used to determine the water absorptivity of paper, cardboard and corrugated cardboard. Cobb Test is carried out according to the TAPPIT441 standard [16]. The sample is weighed dry and placed under a cylinder with an inner diameter of about 100 cm². The cylinder is filled with approximately 100 ml of water. The water is drained after a certain waiting period. The excess water on the sample is wiped with a blotter. The sample is weighed and the amount of water sucked by 1 m² of the material is calculated (1).

$$\text{Weight of water } \left(\frac{g}{m^2} \right) = [m_2 - m_1] \times F \quad (1)$$

$$F = \frac{10000}{\text{Surface Area of Sample}} \quad (2)$$

where m₂ is final weight and m₁ is dry weight of samples.

RESULTS AND DISCUSSION

Strength Tests

ECT test was performed for investigation of paper type and weight effect on corrugated cardboards' strength. In Table 1, when the weight has increased 5 gram of outer

Table 2. Corrugated board flute type standards.

Sample Name	Flute Type	Paper Type and Weight (g/m ²)				
EF@WTL120	E	WTL 120	FL 80	WTL 120		
EF@WTL125	E	WTL 125	FL 80	WTL 120		
BC@NC150	BC	KR 175	NC 150	KR 170	NC 160	KR 170
BC@NC160	BC	KR175	NC 160	KR170	NC 160	KR 170
BC@FL80-FL75	BC	KR 100	FL 80	FL 75	FL 100	KR 100
BC@FL100-FL80	BC	KR100	FL100	FL 80	FL 100	KR 100
BC@NC164-KR185	BC	WKR 225	NC 164	KR 140	NC 170	KR 185
BC@NC127-KR189	BC	WKR 225	NC 127	KR 140	NC 150	KR 189
BC@KR135	BC	WKR 180	NC 160	KR 135	NC 160	KR 170
BC@KR170	BC	WKR 180	NC 160	KR 170	NC 160	KR 170

liner paper of E flute corrugated cardboard, strength enhanced % 15,6. Increasing weight of liner or flute paper led to the enhancement of the CCs strength, which was clear from Table 3, ascending between 7, 77% to 18,50%. As seen in Fig. 4, when the enhancement in ECT values of the CCs is examined the most significant increase in strength was observed in BC@NC160 and BC@NC127-KR189. When the weight of B flute paper of BC@NC150 was increased by 10 g, the strength enhancement was 18.50% with the highest increase. On the other hand, when the weight of the B flute paper (NC) of BC@NC164-KR185 was decreased from 164 to 127 and the weight of inner liner paper (KR) was increased from 185 to 189, there was an enhancement of 18.11%. When the weight of the intermediate liner paper (KR) of BC@KR135 was increased from 135 to 170 (BC@KR170), there was a 7.77% increase in strength. On the other hand, when the weight of both the intermediate liner paper and the B flute paper of BC@FL80-FL75 was increased (BC@FL100-FL80), there was an enhancement of 14.35%. Obviously, when the weight of the inner and outer liner papers of corrugated board is increased, there is a significant enhancement in strength. However, increasing the weight of the liner and flute papers has little effect on increasing the strength.

Cobb Tests

Cobb test were performed for determination of water absorptivity of corrugated cardboard samples. Due to their hygroscopic nature, paper and cardboard tend to hold moisture and water from the surrounding environment. The Cobb test is important because it determines the resistance of paper to water penetration and the amount of water absorbed. A high Cobb value indicates that the material is prone to absorb moisture, while a low value indicates that it is resistant to water penetration and humidity.

Table 3. Effect of the paper type and weight on strength of E flute and BC corrugated cardboard.

Sample name	ECT (kN/m)	Increase of Strength %
EF@WTL120	3,2	-
EF@WTL125	3,7	15,6
BC@NC150	11,61	-
BC@NC160	13,76	18,50
BC@FL80-FL75	4,11	-
BC@FL100-FL80	4,70	14,35
BC@NC164-KR185	12,20	-
BC@NC127-KR189	14,41	18,11
BC@KR135	12,60	-
BC@KR170	13,58	7,77

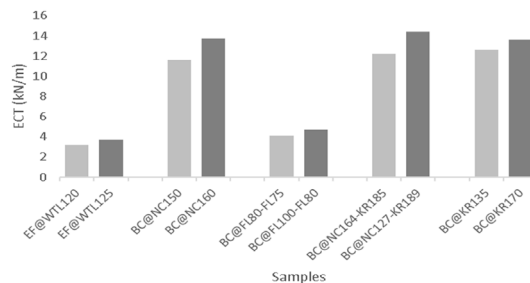


Figure 4. Edgewise compressive strength of corrugated board samples

The Cobb test was performed three times for BC@NC127-KR189 to obtain the exact value. Table 4 shows the water absorption and Cobb value of BC@NC127-KR189. There is no standard value for corrugated cardboard's Cobb value. We used Kraft paper (Kr) inner surface of the BC@NC127-KR189 that is the surface in contact with water. So, it is expected that the Cobb value of the corrugated cardboard is the same as the Kraft papers used on the inner surface. When the Cobb value of the Kraft paper used is 40g/m², the Cobb value of the corrugated cardboard is 66,35 g/m² on average. It can be said that the Cobb value of the corrugated cardboard is higher than the Cobb value of the paper due to the hydrophilic nature of the starch glue used as an adhesive.

ISQ-GC/MS Analysis

Polychlorinated biphenyls are organic chemicals that are one of the most hazardous environmental pollutants due to their persistence in the environment and their bioaccumulation [17]. PCBs are toxic to all living organisms, including humans, because they tend to accumulate in the lipid tissue. They alter immune functions and cause neurological, developmental, respiratory, and reproductive problems as well as cancer due to estrogenic activity [17].

The chemical formula of PCBs is C₁₂H_{10-n}Cl_n, where n ranges from 1 to 10. There are 209 different PCB congeners, but only 130 of them have been detected in commercial products. Ballschmiter and Zell [18] proposed a numbering system for the PCB congeners which has been adopted by the International Union of Pure and Applied Chemistry (IUPAC) [19].

Table 4. Effect of the paper type and weight on strength of E flute and BC corrugated cardboard.

Cobb test number	m ₂ (g)	m ₁ (g)	Absorbed Water(g)	Cobb (g/m ²)
1	12,17	11,135	1,035	66,02
2	12,195	11,080	1,115	71,02
3	12,055	11,085	0,970	62,02
Average				66,35

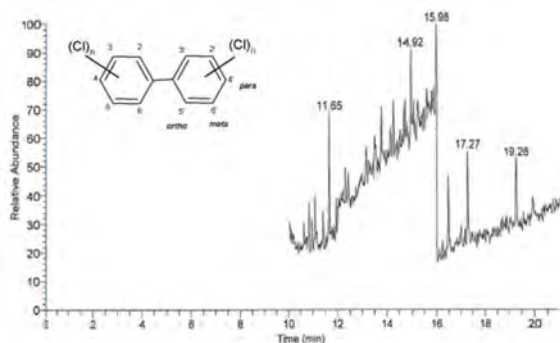


Figure 5. ISQ-GC/MS chromatogram of BC@NC127-KR189 (Inset shows the structure of Polychlorinated Biphenyl (PCB) molecule).

Table 5. PCBs ingredient of corrugated cardboard BC@NC127-KR189

RT (min)	Component Name	Amount mg/kg
10.84	PCB_18	0,00
11.65	PCB_28	0,00
12.30	PCB_52	0,00
14.25	PCB_101	0,00
16.48	PCB_138	0,00
17.27	PCB_153	0,01
19.26	PCB_180	0,01

Table 6. Interpretation of migration test results according to relevant standards

Analyses name	Method	LOQ	Results mg/kg	Requirement	Interpretation
Determination of Overall Migration*	TS EN 1186 13	1 mg/dm ²	1,9 mg/dm ²	≤10 mg/dm ²	Pass
Polichlorbiphenyl (PCB)	TS EN ISO 15318	0,5 mg/kg	Not Detected	≤ 2 mg/kg	Pass
Formaldehyde	EN 1541: 2001	5 mg/kg	<5 mg/kg	≤ 15 mg/kg	Pass
Pentachloro Phenol (PCP)	35 LMBG B 82.02-8	0,1 g/kg	Not Detected	≤ 0,15 mg/kg	Pass

* (Dry Food, Food Simulant E, Poly (2, 6-diphenyleneoxide)

Table 7. Trace element concentration of BC@NC127-KR189

Analyses name	⁴⁸ Ti	⁷⁵ As	¹¹¹ Cd	²⁰² Hg	²⁰⁸ Pb
	16,1670	0,0280	0.019	0,018	0,7510
Concentration (ppm)	15,6960	0,0270	0,019	0,018	0,7420
	15,6590	0,0270	0,019	0,018	0,7360
Concentration average (ppm)	15,8403	0,0273	0,019	0,018	0,7429

PCB content of corrugated cardboard-analyzed according to TS EN ISO 15318 by ISQ-GC/MS analysis technique in order to determine whether the corrugated cardboard BC@NC127-KR189 appropriate for food contact. As shown in Table 4 corrugated cardboard BC@NC127-KR189 has no PCB_18, PCB_28, PCB_52, PCB_101, PCB_138 and 0, 01 mg/kg PCB_153, PCB_180.

Pentachloro Phenol is not detected in sample BC@NC127-KR189 (Table 5). Overall migration from food packaging materials is one of the fundamental requirements according to TS EN 1186 13. Overall migration covers all kind of substances which are transferred from food packaging to food irrespective of the nature and the toxicological profile of the substance. Migration test results given in the Table 6. Overall migration from paper based food packaging materials is limited to 10 mg/dm² and sample BC@NC127-KR189's overall migration test result is 1,9 mg/dm², below 10 mg/dm².

Trace Metal Analysis

Heavy metal analysis was done in three replicates according to NMKL 186 [20] in Intertek laboratories by using

ICAP Q ICP-MS technique. This method describes the detection of trace elements such as arsenic (As), cadmium (Cd), mercury (Hg) and lead (Pb) at low concentrations in each food. As shown in Table 7 BC@NC127-KR189 contain 15,8403 ppm ⁴⁸Ti, 0,0273 ppm ⁷⁵As, 0,019 ppm ¹¹¹Cd, 0,018 ppm ²⁰²Hg and 0,7429 ppm ²⁰⁸Pb.

Restrictions on the trace element content of paper based materials that come into contact with food are determined by the Turkish Food Codex [21]. Lead, chloride and titanium dioxide content of BC@NC127-KR189 below the limitation according to relevant standards (Table 7 and Table 8).

Table 8. Interpretation of trace metal migration results according to relevant standards.

Analyses	LOQ mg/kg	Results mg/kg	Requirement	Method
Hg content	0.01 %	0.02	-	NMKL 186
Cl content	0,02 %	N/A	≤ 0.2 %	TS ISO 5647, Mohr Method
Cd content	0.01 %	0,02	-	NMKL 186
Pb content	0.05 %	0,74	≤ 20 mg/kg	NMKL 186

CONCLUSION

Corrugated cardboard boxes are often used as secondary packaging (carrying box), so the strength of boxes is highly important. In this study, the effect of the paper types and weight used in making corrugated cardboard on the box strength was examined. It can be said that generally increasing the paper quality and weight increases the strength of the box. While inner and outer liner papers of CCs have a significant effect on strength, the intermediate liner and flute papers have a minimal effect

In addition to high strength, it is extremely important that there is no migration from boxes to foods boxes that are in direct contact with food, such as a pizza boxes and fresh fruit and vegetable boxes. We also applied the migration test to the boxes. The results of the analysis show that the corrugated cardboard boxes are suitable for food contact.

ACKNOWLEDGMENTS

The authors gratefully acknowledge Research and Development Center Unit of Ankutsan Inc (AKS-P-115) for financial support.

References

1. T. Fadji, T. Berry, C. J. Coetzee and L. Opara, "Investigating the Mechanical Properties of Paperboard Packaging Material for Handling Fresh Produce Under Different Environmental Conditions: Experimental Analysis and Finite Element Modelling," *Journal of Applied Packaging Research*, vol. 9, no. 2, pp. 20-34, 2017.
2. L. L. Zhao, Evaluation of the Performance of Corrugated Shipping Containers: Virgin Versus Recycled Boards, 1993.
3. B. Steenberg, J. Kubat and L. Rudstrom, *Competition In Rigid Packaging Materials*, STOCKHOLM: ARBOR PUBLISHING AB, 1970.
4. N. Chibani, H. Djidjelli and A. Dufresne, "Study of effect of old corrugated cardboard in properties of polypropylene composites: Study of mechanical properties, thermal behavior, and morphological properties," *JOURNAL OF VINYL & ADDITIVE TECHNOLOGY*, pp. 231-238, 2016.
5. R. Coles, D. McDowell and M. J. Kirwan, *Food Packaging Technology*, CRC Press, 2003.
6. D. V. Hung, Y. Nakano, F. Tanaka, D. Hamanaka and T. Uchino, "Preserving the strength of corrugated cardboard under high humidity," *Composites Science and Technology*, vol. 70, p. 2123-2127, 2010.
7. M. Vishnuvarthanan and N. Rajeswari, "Additives for enhancing the drying properties of," *Alexandria Engineering Journal*, vol. 52, p. 137-140., 2013.
8. R. P. A. T. C. O. T. EUROPEAN, on materials and articles intended to come into contact with food and repealing Directives 80/590/EEC, 2004.
9. D. Vandevelde, "High dry substance stein hall adhesives and method for preparing high dry substance stein hall adhesives". Patent CA2470618 C, 29 09. 2009.
10. F. O. Ware and W. S. McDonald, "Process for the production of corrugated paperboard adhesive". Patent US4343654 A, 10 8 1982.
11. International Organization for Standardization, Pulp, paper and board -- Determination of 7 specified polychlorinated biphenyls (PCB), TS EN ISO 15318, 1999.
12. Trace elements - As, Cd, Hg, Pb and other elements. Determination by ICP-MS after pressure digestion. (NMKL 186), 2007.
13. Paper and board intended to come into contact with foodstuffs. Determination of formaldehyde in an aqueous extract, EN 1541, BSI, 2001.
14. EUROPEAN COMMITTEE FOR STANDARDIZATION, Corrugated fibreboard - Determination of edgewise crush resistance (unwaxed edge method) (ISO 3037:2013), 2013.
15. M. E. Biancolini and C. Brutti, "Numerical and Experimental Investigation of the Strength of Corrugated Board Packages," *PACKAGING TECHNOLOGY AND SCIENCE*, vol. 16, pp. 47-60, 2003.
16. Technical Association of the Pulp and Paper Industry, Water Absorptiveness of Sized (Non-bibulous) Paper, Paperboard, and Corrugated Fiberboard (Cobb Test), 2013.
17. J. J. Parnell, J. Park, V. Denef, T. Tsoi, S. Hashsham and J. Quensen, "Coping with Polychlorinated Biphenyl (PCB) Toxicity: Physiological and Genome-Wide Responses of Burkholderia xenovorans LB400 to PCB-Mediated Stress," *Applied and Environmental Microbiology*, vol. 72, no. 10, p. 6607-6614, 2006.
18. K. Ballschmiter and M. Zell, "Analysis of Polychlorinated Biphenyls (PCB) by Glass Capillary Gas Chromatography," *Fresenius' Zeitschrift für Analytische Chemie*, no. 302, pp. 20-31, 1980.
19. World Health Organization, "Polychlorinated biphenyls(PCBs)," in *Air Quality Guidelines For Europe-Second Edition*, Denmark, WHO Regional Publications, 2000, pp. 97-101.
20. "www.nmkl.org," [Online]. Available: <http://www.nmkl.org/index.php/en/webshop/item/tungmetaller-as-cd-hg-og-pb-bestemmelse-med-icp-ms-etter-syreoppslutning-under-trykk-nmkl-186-2007>. [Accessed 22 8 2017].
21. "resmigazete.gov.tr," 19 12 2011. [Online]. Available: <http://www.resmigazete.gov.tr/eskiler/2011/12/20111229M3-9.htm>. [Accessed 22 8 2017].
22. EUROPEAN COMMITTEE FOR STANDARDIZATION, Paper and board - Determination of water absorptiveness – Cobb Method, Turkish Standards Institute, 2014.

Damage Diagnosis of Bolt Loosening via Vector Autoregressive - Support Vector Machines

Mahmut Pekedis 

Ege University, Department of Mechanical Engineering, Izmir, Turkey

ABSTRACT

Developments in engineering techniques have concentrated on how to build better solutions for engineering structures in order to main the integrity and to reduce the costs in operations. Since the last two decades, advances in computational power have allowed machine learning algorithms to be applied as a powerful tool in anomaly detection problems, classification as well as in regression analysis. The objective of this study is to detect the damage using the vector auto regression model (VAR) coupled with support vector machines (SVM). A base excited three storey manufactured from an aluminium is investigated in a lab medium for various structural states. Accelerometers are fastened to the each corner of structure's floor to collect time series data. Damage simulation scenarios in structure are performed by releasing the bolt load which cause the nonlinear effects. Once the sensors' measurements are collected for each state and organized to represent the appropriate scenario's label, they are processed in VAR model to obtain feature vectors such as residuals and VAR parameters. Then, SVM with optimal kernels are implemented on those features to classify and locate the damage. The results demonstrate that the VAR residuals shows a significant performance over VAR parameters once they are used as features in SVM technique. Moreover, it is also found that detection performance rises as the number of damage increases.

Keywords:

Structural health monitoring, Pattern recognition, Machine learning, Damage diagnosis, Vector autoregressive - Support vector machines

INTRODUCTION

The engineering systems are the potential damage accumulated structures at environmental and operational conditions. The most research conducted in structural health monitoring (SHM) has focused on ways of detecting the damages in these structures at the earlier possible time. The ability of monitoring accurately the all parts of the structure is crucial to improve both the reliability and safety. During the last two decades, the structural monitoring techniques have been focused to diagnose the damage by equipping the structure with various types of sensor. One such a monitoring procedure is vibration based damage identification which is based upon the changes in dynamic response such as crack, stiffness reduction or loosed connection that alter the response of that structure [1-4]. There has been a much research on this field such as Doebling et al. presented a review for the vibration based damage detection techniques [5]. The model based SHM approach is generally implemented by building a physics based model for the system. Once the model of the system is established based on a physical description, it is updated

on measurements obtained from sensors that attached to structure. Although the much of vibration based SHM studies were concentrated on model based SHM, Farrar et al., have presented statistical pattern recognition paradigm for diagnosing the damage using direct data of vibrations [6]. This paradigm includes of four parts: (a) operational evaluation, (b) data acquisition, (c) feature extraction and reduction, (d) statistical model development. Recent advancements regarding of this technique is demonstrated in detail by Farrar and his coworker [7].

The algorithms mostly used in statistical model development can be categorized as, (1) classification [7-8], (2) regression [9] and (3) outlier detection [10]. The suitable technique to be selected is based on the capability of performing unsupervised or supervised learning. Supervised learning depicts that, the data of undamaged and damaged conditions are available. It is mostly used in group classification. However, unsupervised learning refers the structural state where the data are available

Article History:

Received: 2019/12/10

Accepted: 2020/09/08

Online: 2020/09/30

Correspondence to: Mahmut Pekedis,

Department of Mechanical Engineering,

Ege University, Izmir, Turkey

Tel: +90 2323114970

Fax: +90 2323888562

E-Mail:mahmut.pekedis@ege.edu.tr

only for the healthy state of the system. This procedure is performed in SHM techniques to fit a time series predictive model. Once the model is set, the anomalies can be checked by using the observations. In other words, the residuals are used as a sensitive features for the damages. Then, the changes in residuals are considered to be caused due to damage in structure. Typically, linear based autoregressive (AR) model [11-12] and non-linear based autoregressive SVM [9] are employed on time series to compute the damage sensitive feature. After the model has been established, the residual parameter which reflects the damage indicator has been interpreted with procedures such as sequential probability test [13] and sliding window [14]. The majority of the studies reported above have used auto regressive model (AR) model as damage sensitivity vector [9-12]. However, AR model does not include the relation between multiple time series. On the other hand, vector auto regression (VAR) which is a generalized form of univariate AR Model captures the interdependencies between multivariate time series. Here, we propose a VAR (Vector Autoregressive) model coupled with SVM (Support Vector Machines) technique to diagnose and classify the damage using an array of sensors' measurements. The study is investigated on a base excited three storey in a lab condition. The damage is performed by releasing the bolt load which causes a nonlinear effect on the system response. The measuring data of the sources that caused from variability such as temperature, humidity or external noises are not essential herein this technique.

The layout of this study is as follow. First, the basic theory of VAR - SVM framework is briefly described. Next, experimental setup of the test structure is demonstrated. Then, the results obtained from the approach is presented in detail. Finally, the diagnosing performance is summarized and discussed.

VECTOR AUTO REGRESSIVE - SUPPORT VECTOR MACHINE MODEL

Consider $\{x_1, x_2, \dots, x_T\}$ are zero mean time multivariate time series collected from SHM networks. Each x_i sensor $\{x_{i1}, x_{i2}, \dots, x_{im}\}$ is the vector observations, m is the total number of sensor, T is time points and x_{it} is the observation of i th sensor at time t . A VAR model is described as

$$x_t = \sum_{i=1}^p \phi_i x_{t-i} + \varepsilon_t \tag{1}$$

where p is the order of the model and $\varepsilon_i = \{\varepsilon_{i1}, \varepsilon_{i2}, \dots, \varepsilon_{im}\}$, $\varepsilon_i \in R$ are the residuals having normal distribution. The $\Phi_1, \Phi_2, \dots, \Phi_p$ parameters can be estimated by maximum likelihood method [15-16]. The optimum

order of the model is predicted by Akaike [17] and Bayesian [18] information criterions as following equations.

$$AIC(p) = -2\ln L(p) + 2k \tag{2}$$

$$BIC(p) = -2\ln L(p) + k \ln T \tag{3}$$

where k is the total parameter number of the model, T is the total observation points and $L(p)$ is likelihood of the model. These criterions provide details about how the predicted parameters fit into the model. The model parameters and residuals are sensitive to varieties for structures in environmental and operational conditions. Each of these feature computed for various case is labeled with a structural case, then processed in support vector machines (SVM) to diagnose the damage. Briefly, SVM is a statistical technique which seeks the separate of classes [19]. Initially, the theory of SVM has been discussed for separation of two class data, then extended to separate of multi classes data [20].

Consider the training dataset contains N input vectors such that $x_1, x_2 \dots x_N$, and target values t_1, \dots, t_N , where $t_N \in \{-1, 1\}$, the new data are classified in $D(\underline{x}_k)$.

The linear separation situation is

$$\begin{aligned} \underline{x}_k \in C_1 &\Rightarrow D(\underline{x}_k) = w\underline{x}_k + b \geq 1 \\ \underline{x}_k \in C_2 &\Rightarrow D(\underline{x}_k) = w\underline{x}_k + b \leq -1 \end{aligned} \tag{4}$$

where C_1, C_2 refer the class label, w is the weight vector and b is bias parameter [21].

Equation (4) could be written in Euclidean space as following

$$D(\underline{x}_k) = y_k \langle \underline{w}, \underline{x}_k \rangle \geq 1 \tag{5}$$

where y_k is a class label.

The distance of each data to the separated hyperplane is defined as

$$y_k \frac{D(\underline{x}_k)}{\|\underline{w}\|} \geq \tau \tag{6}$$

where τ is the distance between two hyper planes. The parameterization of the hyper plane is unreasonable. It could be adjusted as

$$\|\underline{w}\| \tau = 1 \quad (7)$$

The maximizing the margin can be conducted by minimizing the $\|\underline{w}\|$. Then, the optimization problem simply requires that, $\min\left[\frac{1}{2}\|\underline{w}\|^2\right]$ is to be maximized. By minimizing the $\|\underline{w}\|$ and subjected to constraints defined in equation (5), the objective function is defined as

$$Q(\underline{w}) = \frac{1}{2}\|\underline{w}\|^2 - \sum_{i=1}^N \alpha_i y_i (\langle \underline{w}, \underline{x}_i \rangle - 1) \quad (8)$$

where α_i are the Lagrange multipliers. It is noted that, the minus sign of the Lagrange multiplier term is due to minimization with respect to w . The parameters of w could be written in terms of α_i by performing Kuhn Tucker conditions. Then, the dual formulation will be as

$$\frac{\partial Q}{\partial \underline{w}} = 0 \Rightarrow \underline{w} = \sum_{i=1}^N \alpha_i y_i \underline{x}_i \quad (9)$$

The Lagrange multipliers α_i only can be nonzero if the constraints hold with

$$\alpha_i y_i (\langle \underline{w}, \underline{x}_i \rangle - 1) = 0 \quad (10)$$

The data points x_i observed at margin limits are named support vectors. The formulation of dual could be maximized with respect to α_i by substituting equation (10) into (8) such that

$$Q(\underline{w}) = \sum_{i=1}^N \alpha_i - \frac{1}{2} \sum_{i=1}^N \sum_{j=1}^N \alpha_i \alpha_j y_i y_j \langle \underline{x}_i, \underline{x}_j \rangle \quad (11)$$

subjected to the following constraints

$$\sum_{i=1}^N y_i \alpha_i = 0 \quad \alpha_i \geq 0, \quad i = 1, 2, 3, \dots, N \quad (12)$$

After the optimal parameter is determined by gradient descent or quadratic programming, the optimal separating hyperplane given in equation (9) could be written as the following equation

$$D(\underline{x}) = \sum_{i=1}^N \alpha_i y_i \langle \underline{x}_i, \underline{x} \rangle \quad (13)$$

This statement provides that the data are separable linearly. If they are not separable linearly, ξ_i slack variables are added to the non separable data as

$$D(\underline{x}_i) = y_i \langle \underline{w}, \underline{x}_i \rangle \geq 1 - \xi_i \quad (14)$$

where ξ_i assess the non-separability. This can be solved by adding the penalty form $\sum_{i=1}^N \xi_i^p$ to the objective function.

The essential objective function is defined as

$$Q(\underline{w}) = \frac{1}{2}\|\underline{w}\|^2 + C \sum_{i=1}^N \xi_i - \sum_{i=1}^N \alpha_i y_i (\langle \underline{w}, \underline{x}_i \rangle - 1 + \xi_i) - \sum_{i=1}^N \mu_i \xi_i \quad (15)$$

and subject to the following constraints

$$\sum_{i=1}^N y_i \alpha_i = 0 \quad C \geq \alpha_i \geq 0, \quad i = 1, 2, 3, \dots, N \quad (16)$$

where the C value arranges the complexity for the model. The procedure is applied on nonlinearly separable datasets by asserting them in high dimensions [20,22].

The optimization includes the following objective function in high dimensional space

$$Q(\underline{w}) = \sum_{i=1}^N \alpha_i - \frac{1}{2} \sum_{i=1}^N \sum_{j=1}^N \alpha_i \alpha_j y_i y_j \langle \langle \varphi(\underline{x}_i), \varphi(\underline{x}_j) \rangle \rangle \quad (17)$$

where $\langle \langle \cdot \rangle \rangle$ depicts the inner product on the feature space. The solution of CPU time increases as the feature space increases.

The resulting nonlinear discriminant function for two label classes is given by

$$D(\underline{x}_i) = \sum_{i=1}^N \alpha_i y_i H(\underline{x}_i, \underline{x}) \quad (18)$$

where $H(\underline{x}_i, \underline{x}_j)$ is assessed for input space

$\langle\langle\varphi(\underline{x}_i), \varphi(\underline{x}_j)\rangle\rangle$. if $D(\underline{x}_i) \geq 0$; x is designated on the class label 1; else, x is designated on the class label 2. Most commonly used kernel functions $\varphi(\underline{x}_i, \underline{x}_j)$ in SVM are polynomial, normalized, polynomial, radial based and sigmoid. These functions are described by Bishop in detail [20]. It is noted that, if the parameters of the kernels are not optimized, low classifications performance could be occurred due the separation problems of hyperplanes. The VAR-SVM model is constructed using MATLAB econometrics, Statistics and Machine Learning Toolbox. The regularization C in SVM is implemented via the box-constraint parameter with a value of 1. It is noted that as this value increases more points are allowed in the margin. Hence, this regularization relaxes this constraint. The parameters processed in VAR are also standardized by centering and dividing them by their standard deviations.

The methodology used in VAR-SVM model is as follows:

- a. Initially, the VAR model is established for the raw sensor measurements. The optimum model order p is determined at minimized values of AIC(p) or BIC(p) function.
- b. The VAR model is re-established with an optimized p order. Then, the VAR parameters and residual vectors are used as features in SVM.
- c. Once the features data are obtained from VAR model for various cases, they are partitioned into two groups. The 1st group is the training dataset. This training group is then separated into more two groups. One training group is used to develop the SVM model and the other is determine the optimal kernel parameters.
- d. The 2nd group is testing dataset. This group is used to determine the performance of the model that is created in the first group. Once the kernel parameters are optimized in first group, the diagnosing performance of SVM is assessed on testing dataset.

EXPERIMENTAL SETUP

Three storey structure made of aluminum frames is manufactured as a test platform (Fig. 1). The structure can slides on rails that allow movement in lateral direction only and its ground storey has been excited with an electromagnetic shaker vibrating at band limited random frequencies (15 - 150 Hz). In order to prevent the system to move away during excitation, a tensional spring is placed between the lower surface of structure and the base plate. It is noted that the stretch magnitude of this spring can be controlled with a bakelite screw. The connections of columns, frames and lower base are carried out by bolts. The loosen bolt during excitation yields in a non-linear behavior that represents a damages. In other words, exciting the system while no joints loosened presents a linear

response of structure, while loosed joints result in a non-linear dynamic response.

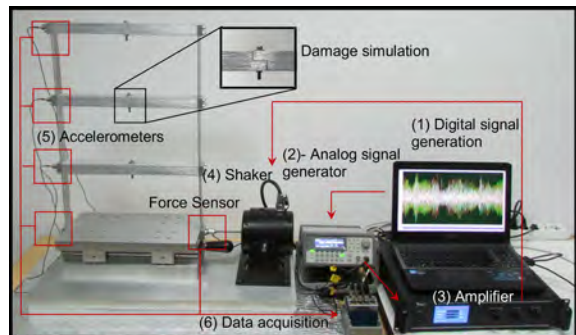


Figure 1. Experimental setup

The structure which located on base plate is excited by a YMC, MS-50 type electrodynamic shaker. This shaker is amplified with a YMC, LA-100 instrument. This amplifier is embedded with a signal generator that can only produce sine signals. However, the real world engineering systems are exposed to environmental and operational uncertainties. In order to simulate this variability, the system is excited with band limited signals generated by Agilent 33210A. The procedure steps that we deployed are numbered in Fig 1, and these are briefly as follows. Initially, band limited digital random signals (1) are transferred to Agilent 33210A on TCP/IP connection to generate analog signals (2). Then, these analog signals are amplified in YMC, LA-100 (3). Finally, the amplified band limited analog signals are transferred to the shaker to excite the structure (4). The base plate slides on rails and the entire system (three storey, shaker) is placed at a foam to minimize external sources of unmeasured excitation. Four YMC piezo accelerometers have a sensitivity of 9.39 mV/g are attached on the corner of each storey (5).

The shaker is centered at the edge of base plate. Moreover, the structure and accelerometers are placed on the same axes line of base plate's axis to reduce the torsional effects during excitation. The measurements are collected with NI 9234 (6). The force sensor at base floor and accelerometers located at 1st, 2nd and 3rd floor are connected to channel 1, 2, 3, 4 and 5 of the device, respectively. Then, these measurements are processes with Labview software. Totally, 8298 data points are acquired with a sampling rate of 1765.53 Hz for each case. The structure is excited at band limited random frequencies at 15 -150 Hz. Note that, these levels are chosen to avoid rigid motion caused by 1st mode, and these values are slightly above the first mode. The excitation level of amplifier is set to be as 3.4 V RMS (root mean square error). The datasets collected for these cases are categorized in accordance for bolt loose variation as given in Table 1. Here, while the case 1 represents the healthy condition, the rest 7 cases shows the damaged states. Note that, each datasets given in Table 1 consist of 6 dimensions where

the 1st is the time (s), 2nd is force (N), and the rests are accelerations (g). Since the system consist of 3 horizontal frames including loosing bolts, eight different damage cases combinations $2^3=8$ could be investigated. We note that, there is not a general rule about how many repeated datasets should be collected for each test. However we know that as the number of case is increased higher datasets are needed to be collected. Initially, in order to determine to each algorithm' classification sensitivity the investigations have been performed for the 4 cases listed in Group I (Table 1). Then, the algorithm which reflect the highest accuracy has been implemented for all cases given in Group I and II.

Table 1. Structural state cases

Case no	Bolt loose option		
	1st floor	2nd floor	3rd floor
1	-	-	-
2	-	-	•
3	-	•	•
4	•	•	•
5	•	-	-
6	-	•	-
7	•	•	-
8	•	-	•

• " represents the bolted joint is loosened, while "-" shows the bolt is not loosened

RESULTS

In this study, machine learning based active structural health monitoring techniques have been implemented on a base excited three storey structure to diagnose the bolt loosening damage. In order to include the effects of environmental and operational varieties, this system is excited by a band limited random vibrations. The raw measurements includes time (s), force (N) and accelerations (g) for a typical dataset are represented in Fig 2. The

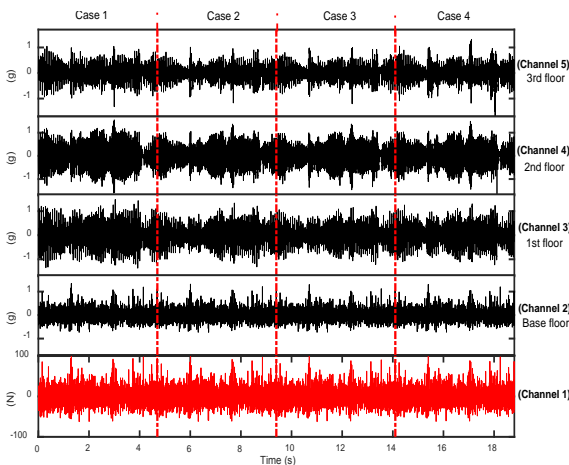


Figure 2. Typical raw data measurements of the 1st dataset

sensor measurements located at base floor (Channel 1 and 2) show more random distributions due to excitation.

For the duplicated measurements, uncertainties may arise at different stages of a measurement process. In order to evaluate these uncertainties, the measurements have been evaluated using robust statistical techniques such as cumulative density function, Z-score and analysis of variance (ANOVA). For instance, the cumulative density function distribution of the discrete data obtained for the 4 repeated tests at Channel 1 and 5 are represented in Fig 3 and Fig 4,

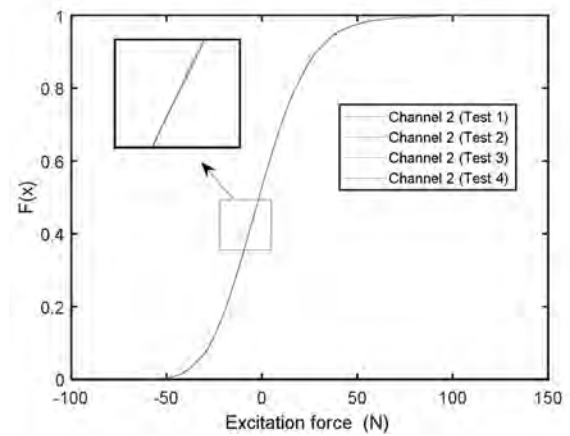


Figure 3. Cumulative density functions for the repeated raw force measurements [case 1].

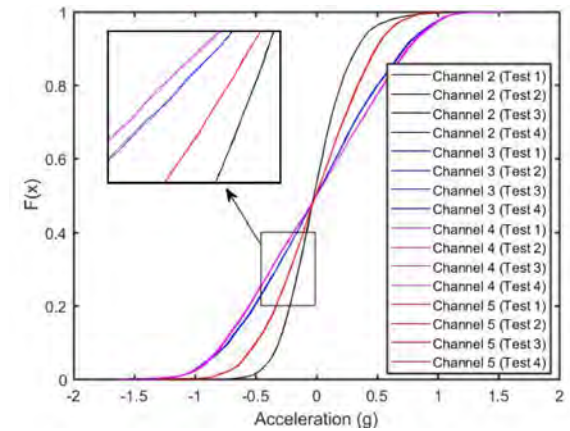


Figure 4. Cumulative density functions for the repeated raw acceleration measurements [case 1].

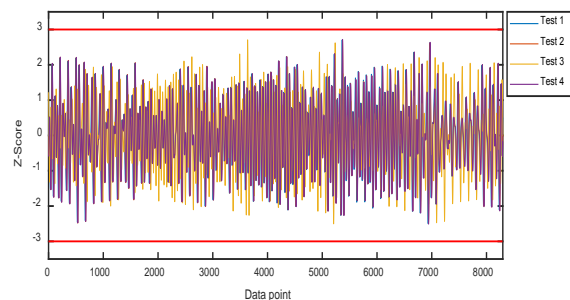


Figure 5. Z-scores of the raw measurements obtained for repeated raw acceleration measurements [case 1, Channel 4].

respectively. The duplicated measurements converge each other which may show the uncertainty due to the DAQ device is low.

Next, uncertainty is also evaluated using Z-scores based on robust statistics. It is widely implemented for the processing of experimental data obtained from inter laboratory comparisons [23-24]. Here, Z-score gives a measurement of how far a result is from the assigned value, and also gives a score to each result relative to the other results in the group. The measurement uncertainty can be estimated from Z-score and a value less than 3 is accepted an appropriate from the data group. In other words, $|Z| \leq 3.0$ indicates a satisfactory performance [23]. For instance, Z-scores of the duplicated measurements are in the range of -3 and 3 (Fig 5). Moreover, these signals do not include outliers.

We finally have evaluated the raw measurement uncertainty using box plots. Typically, the box plot is a standardized method of representing the distribution of samples corresponding to features using boxes and whiskers. The boxes show the inter quartile range of the data and the whiskers refer a multiple of the first and third quartiles of the variable. Any data that laid at the outside of this limit is considered as outliers. Box plots based on Z-scores for the raw repeated measurements for various channels are given in Fig 6. Note that each test data in each channel consist of 8298 data points. It can be seen that while the channel 2 and 5 include outliers, channel 3 and 4 do not. For instance, test data 1, 2, 3 and 4 from the channel 1 include 162, 154, 149 and 159 outliers. Additionally, data from channel 4 covers 10, 11, 11, 11 outliers for test 1, 2, 3 and 4 respectively. We expect that the reason of higher outliers encountered in Channel 2 may occurred due the this sensor is laid at the excitation floor which include random distribution.

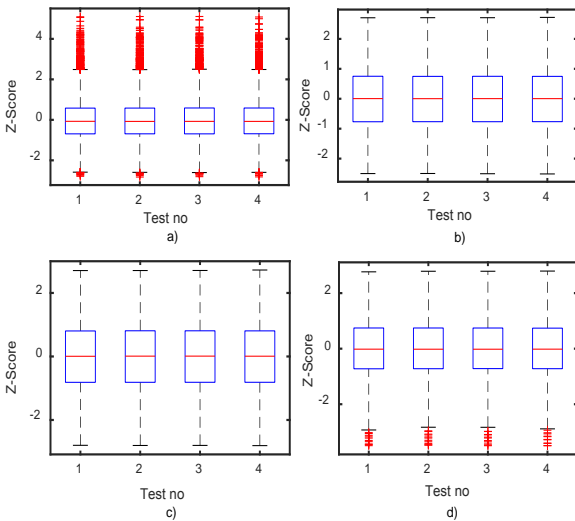


Figure 6. Box plots of the Z-scores for the raw repeated measurements[case 1]. a) Channel 2, b) Channel 3, c) Channel 4, d) Channel 5

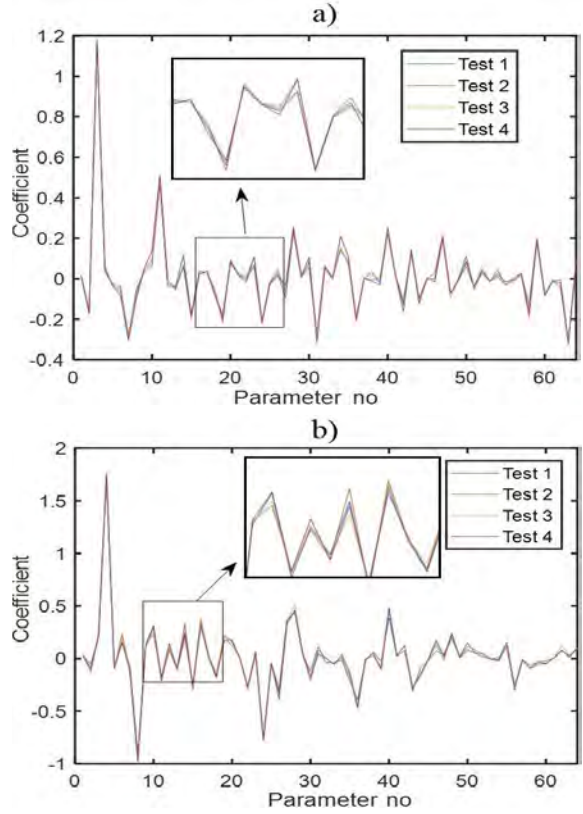


Figure 7. VAR(16) parameters distribution for various repeated tests [case 1]. a) Channel 4, b) Channel 5

Once the datasets are collected and the raw measurement uncertainty is investigated, the next step is to establish the VAR model. The optimum VAR order p has been determined to be as 16. This value is obtained by asserting the minimum values of $AIC(p)$ and $BIC(p)$ function. Hence, VAR (16) model for 8298x4 acceleration data points is resulted in 64x4 VAR parameters and 8282x4 residuals for each damage scenario case. VAR(16) parameters distributions for various duplicated tests at case 1 for channel 4 and 5 are given in Fig 7.a and Fig 7.b, respectively. In order to assess whether there is significant difference between these VAR parameters, they are processed using ANOVA statistical analysis. The F ratios and p values for the duplicated test from the channel 1, 2, 3 and 4 have been found as ($F = 3.7487e-09$, $p = 1.0$), ($F = 1.2992e-08$, $p = 1.0$), ($F = 2.0614e-09$, $p = 1.0$) and ($F = 9.2864e-10$, $p = 1.0$), respectively. There is not a statistical difference between each repeated measurement ($p > 0.05$) which may show that any test data that will process in learning algorithms may not effects the classification performance.

The computational results of the VAR parameters and residuals obtained by VAR(16) model for all cases are shown in Fig 8 and 9, respectively. It can be seen that the residuals of the 2nd channel sensor exhibits more random distributions due to it is aligned with the axis of random excitation

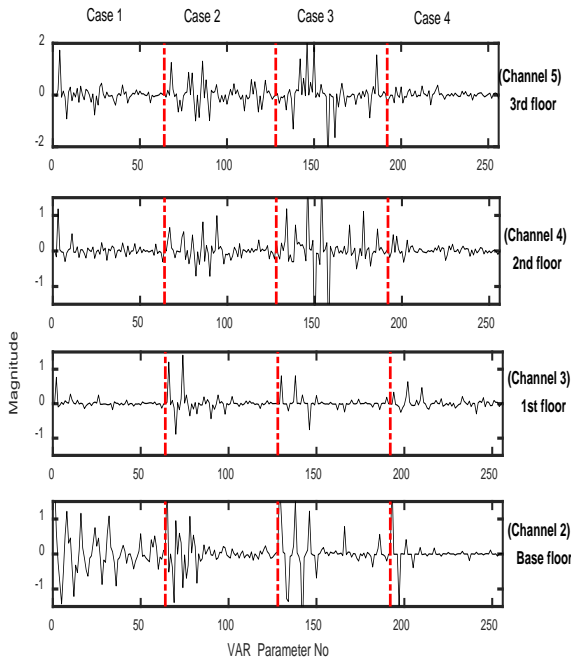


Figure 8. Typical VAR(16) parameters of the 1st dataset

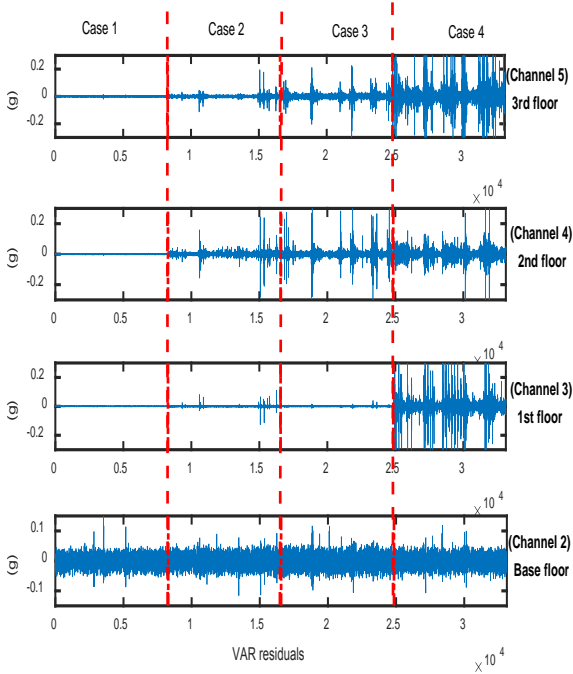


Figure 9. Typical VAR(16) residuals for the 1st dataset

(Fig 9).

Fig 10 represents a typical SVM diagram with the decision boundary for a healthy (Case 1) and damaged case (Case 4). This diagram can be used to improve the shape of decision by modifying the kernel type and its parameters. For instance, the decision boundaries for polynomial ($p=2$) and radial type kernel are given in Fig 10.a and 10.b, respectively.

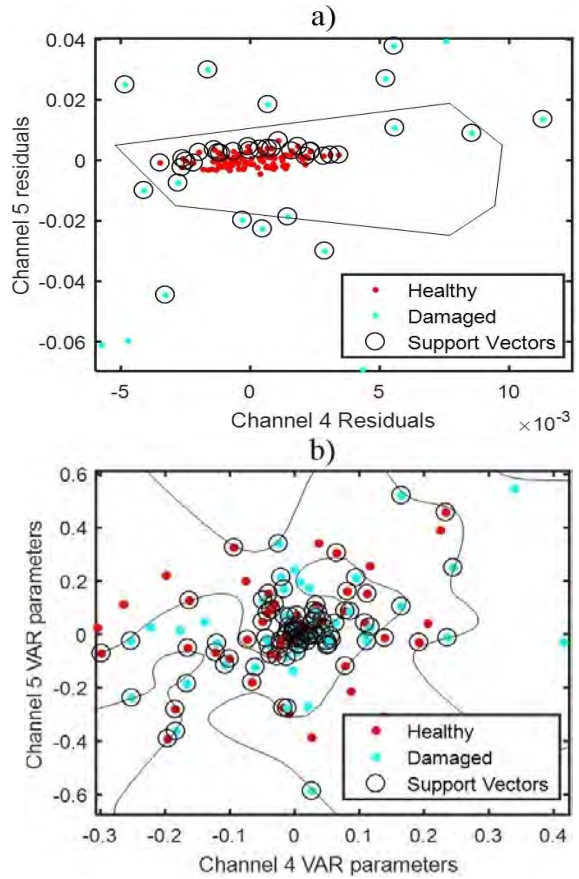


Figure 10. A typical scatter diagram with the decision boundary for VAR(16) model. a) VAR residuals, b) VAR parameters

The damage diagnosis scores are assessed by receiver operating characteristic (ROC) curves. These curves summarize the performance of the classifiers. They are typically built by plotting the false positive rate (FPR) and true positive rate (TPR) in decision threshold. Once the curve closes the correct positive ratio (TPR) axis the success increases, while it closes false positive ratio (FPR) axis the score decreases. Therefore, a curve with high performance passes through a point at top left side (0, 1) of the graph. Each point on the curve complies with a certain threshold and the overall performance of the curve is evaluated in terms of area under curve (AUC). The highest score is obtained when the area under curve (AUC) is equal to 1, while the worst is 0.5 [25]. As mentioned before, each structural case investigated in this study includes 4 repeated measurements. These datasets are categorized as 50 % for training, 25 % for verifications and the rest of them for testing datasets. The optimal parameters of the kernels are obtained with cross validation.

In first algorithm raw data measurements have used as feature vectors for the SVM classifier. Here, 500x4 feature vectors from each case have been used to establish the SVM model with an optimum radial bases type kernel. One vs. one type approach is used for binary multi classifications.

Fig 11 represents the ROC curves of SVM technique for raw data observations. It can be seen that AUC values of around 0.5 are obtained, which indicate that the SVM with raw measurements could not discriminate structural states from each other.

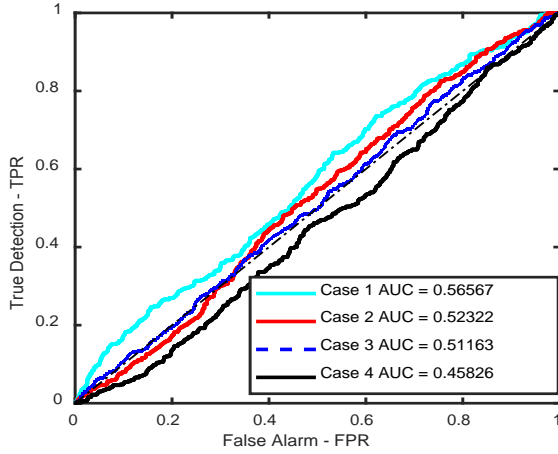


Figure 11. ROC curves of the raw signals processed in SVM model for each case

The performance of each damage diagnosis techniques can further be assessed by confusion matrix plot. The diagonal elements of this matrix show the percentage score for which the estimated case is equal to true case, while off diagonal elements are those that false diagnosed by the technique. The higher values in diagonal elements allows to determine the performance of the diagnosing classifier particularly at individual scenario. Confusion matrix plot obtained with the raw signals processed in SVM model for each case is shown in Fig 12. Overall, SVM scheme gives a low value of 27.8 % correct classifications for the testing datasets.

In the second algorithm, the VAR parameters with a size of 64x4 observations from each case have been used as feature vectors in SVM. The best results have been obtained

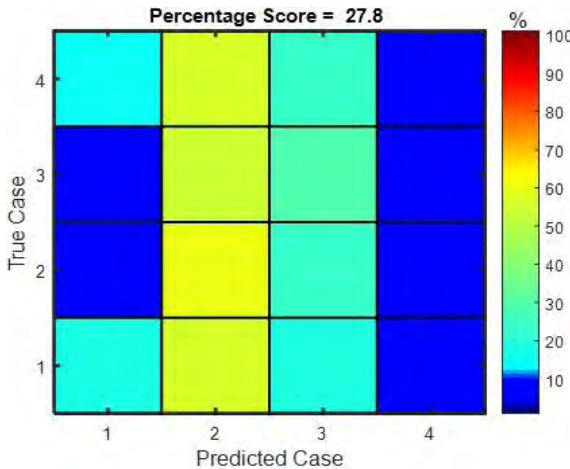


Figure 12. Confusion matrix plot obtained with the raw signals processed in SVM model for each case

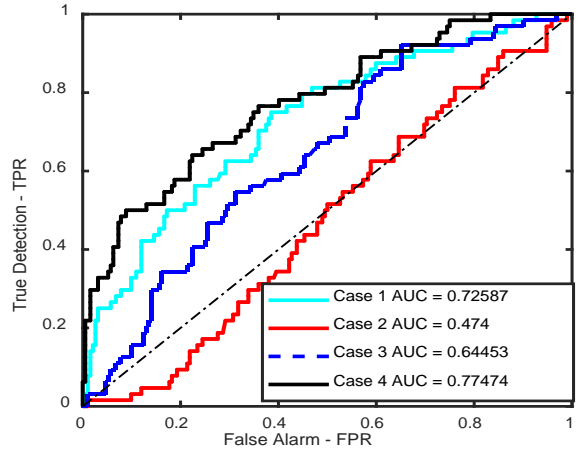


Figure 13. ROC curves of the VAR parameters - SVM model

for RBF type kernel at validation step. ROC curves obtained by VAR SVM technique for each case are represented in Fig 13. AUC values of these curves are 0.7258, 0.474, 0.6445 and 0.7747 for case 1, 2, 3 and 4, respectively. It is clear from these results that the classification performance has been improved when the raw observations are processed in VAR model. The maximum correct classification performance is obtained for the case 1 and 4 while the minimum is in case 2 and 3. As the number of the bolt loosening damage increases, higher classifications performance are obtained. This result probably shows that, the more the nonlinear variations in structures, the better the discrimination being reached (Fig 13).

Confusion matrix plot obtained with the VAR parameters features processed in SVM model for each testing case is shown in Fig 14. It is noted that here, the optimal kernel which obtained in validation stage is used during testing. The correct percentage of case 1, 2, 3 and 4 are 81.25, 53.13, 59.38 and 64.06, respectively. As illustrated in Fig 14, the overall performance "VAR Parameters-SVM" model shows

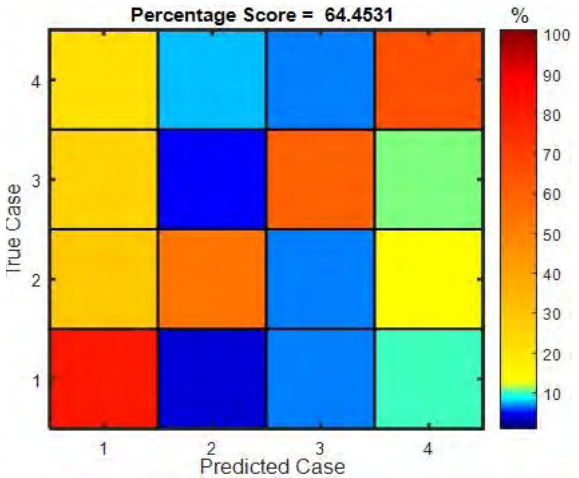


Figure 14. Confusion matrix plot obtained with the VAR parameters - SVM damage identification model

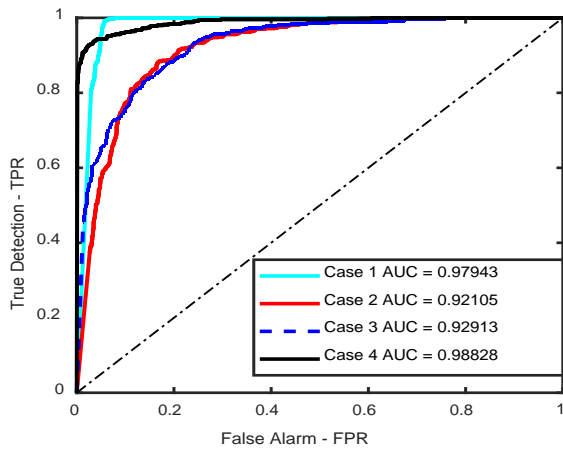


Figure 15. ROC curves of the VAR residuals - SVM diagnosis model

that the algorithm could identify structural damage with a moderate accurate value of 64 %. It is also noted that prediction with multi cases is intrinsically more complicated than multiple predictions because of that the algorithm has to learn to construct the separation boundaries or relations of the observation data.

The main objective of the third algorithm is to detect the structural case by evaluating the VAR residuals in SVM model. The residuals with a size of 500x4 observations (1st dataset) from each case have been used as feature vectors for establishing the SVM model. It is observed that a polynomial kernel with an order of 2 gives the best results. The ROC curves obtained from the this approach are given in Fig 15. The highest AUC values of classifying the structural states are found in case 1 and case 4, while the lowest values are in case 2 and 3.

Finally, the confusion matrix plot obtained in third approach (VAR residuals - SVM) is represented in Fig 16. It is observed that the algorithm diagnoses the correct struc-

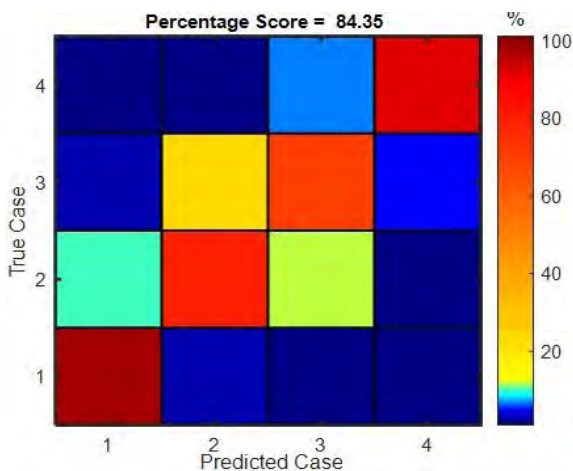


Figure 16. Confusion matrix plot obtained with VAR residuals - SVM damage identification model

tural case with a percentage score of 97.4, 78.6, 69.8 and 91.6 for the testing datasets. The false-positive (Type I Error) and false-negative (type 2 error) is a common technique that used to determine classification performance. The results of "VAR residuals -SVM" shows a significant performance over both "VAR parameters -SVM" and "raw measurements -SVM" in terms of Type I and Type 2 errors.

Once the algorithm which give the highest accuracy has been determined, the final step is determine its performance for all cases. The ROC curves of the VAR residuals - SVM diagnosis model for all cases are represented in Fig 17. The highest AUC values of classifying the structural case is found in case 1, while the lowest value is in case 7. It is observed that the algorithm diagnoses the overall correct structural case with a percentage score of 70.25 (Fig 18). Once the performance of the this algorithm for 8 cases compared to 4 cases, the accuracy decreased by 16.15 %. This result shows that as the number of case increase, the prediction performance decreases due to separation boundaries as expected.

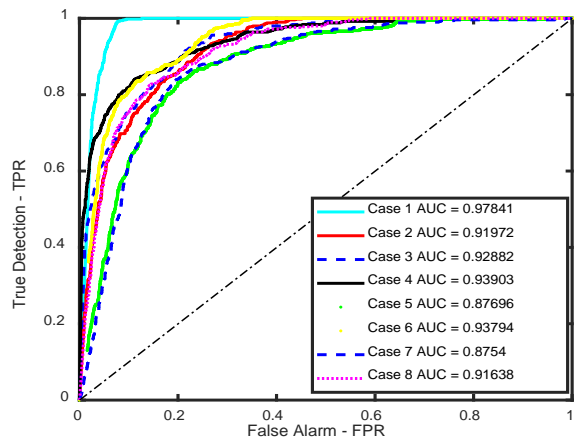


Figure 17. ROC curves of the VAR residuals - SVM diagnosis model for all cases

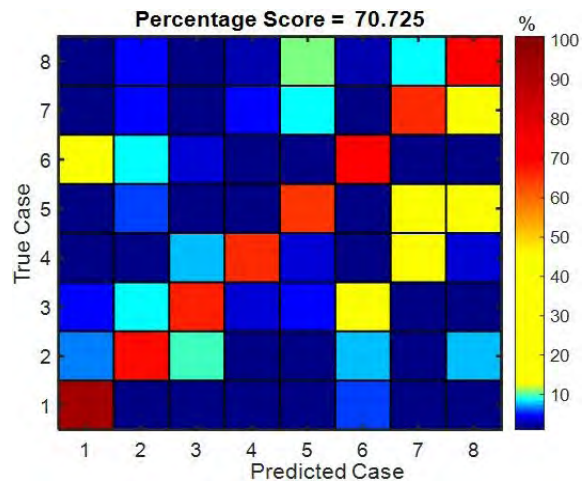


Figure 18. Confusion matrix plot obtained with VAR residuals - SVM damage identification model for all cases

CONCLUSION

This study investigates of using time series to diagnose the damages by vector autoregressive - support vector machines . Initially, three floor structure has been manufactured as a test bed. The damage in this structure is simulated by releasing the bolt load which causes a nonlinear effect on the system response. The structure placed on rails is excited by a electrodynamics shaker. The measurements of the four sensors located at different regions have been acquired for various cases. Then, these measurements have been processed in VAR model to generate features of SVM for damage identification. Although improvements have been carried in unsupervised learning structural health monitoring techniques, they are still limited to identify damage sensitive features derived from models of individual sensor. In other words, they are particularly limited to identifying which sensor/sensors is/are associated with the damage [7,9,10]. Therefore, we processed the raw measurements in VAR model to improve of damage identification performance. This model captures the interdependencies between multivariate sensor measurements. Once the features such as residuals and parameters are obtained from VAR model, they are divided into learning and testing group for SVM. In order to further summarize the performance of each damage diagnosis methods, the ROC curves for binary classification (healthy, damaged) are given in Fig 19. Note that, while the case 1 is health, the rest cases are the damaged conditions as given in Table 1. The optimum points of ROC curves are determined as (0.9700, 0.9920), (0.1146, 0.5156), and (0.05870, 0.9580) for "Raw measurements-SVM", "VAR parameters-SVM" and "VAR parameters-SVM" algorithms, respectively. The first magnitude given in parentheses herein is the "false positive rate" (FPR) or false diagnosis, and the second is the "true positive rate" (TPR) or the correct diagnosis. The most successful diagnosis of damage is achieved when the VAR model residuals are used with SVM. Moreover, it is seen that the binary two case classification scores obtained from each algorithm are higher than multi cases in terms of AUC. This result shows that separating the damaged case from the healthy is easier than separating from another damaged condition. In order to overcome this issue, the stochastic residual errors needs to pre-processed by Markov regime switching Copula model to investigate whether there is a relationship between these errors.

It is expected that the advancements in machine learning procedures will reflect as of increasing their potential uses in SHM applications. One such a machine learning algorithm SVM rises with a number of possible applications. For example considering damage identification problems, an increase in classifier performance may reduce the main-

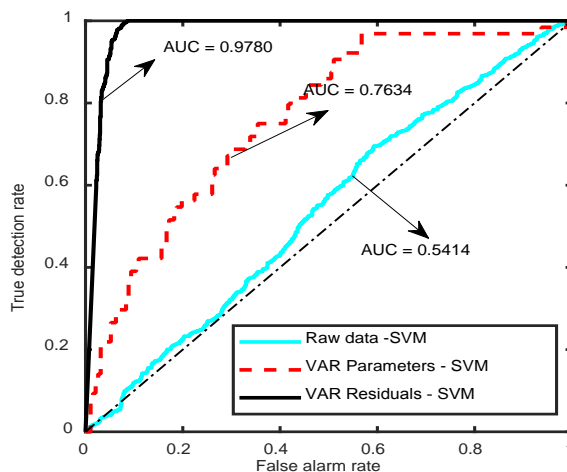


Figure 19. ROC curves of each damage diagnosis model

tenance period requirements for valuable engineering structures. It is noted that the VAR model coupled with Artificial Neural Network (ANN) could also be performed algorithm to detect the damage in engineering structures at environmental and operational conditions. However, the solution CPU time may lengthen which may not be a practical way particularly for real time SHM applications [20, 26].

The limitations of this study is that the VAR-SVM model has been investigated for a structure in a well controlled laboratory settings. Moreover, this structure is not a scale model of any engineering system and the uncertainties due to humidity and temperature should also be investigated by acquiring large datasets. It is also should be considered whether the created synthetic random excitations reflect the environmental uncertainties. The system this has been designed to validate the algorithms that develop for SHM research. Future struggles should be leaded to deploying of this approach in real physical engineering applications. Additionally, further investigations may focus on the developing a graphical user interface (GUI) for real time damage diagnosing applications. In overall conclusion is that the VAR - SVM has been deployed to diagnose the damages in a well controlled structure. The results indicated that this approach appears to be a promising tool for autonomous SHM implementations.

ACKNOWLEDGEMENT

The authors would like to thanks Prof. Dr. Hasan Yildiz at Ege University for his valuable suggestions and comments regarding the concepts investigated in this study. This study is partly supported by Ege University, Office of Scientific Research Projects with a designated project ID of 17-ÜYDAUM-001.

REFERENCES

1. Gopalakrishnan S, Ruzzene M. and Hanagad S. Computational Techniques for Structural Health Monitoring, Springer, London,

- UK, 2011.
2. Pekedis M, Mascarenas D, Turan G, Ercan E., Farrar CR and Yildiz H. Structural health monitoring for bolt loosening via a non-invasive vibro-haptics human-machine cooperative interface. *Smart Materials and Structures*, 24, 085018, 2015.
 3. Pekedis M, Yildiz H. Damage diagnosis of a laminated composite beam and plate via model based structural health monitoring techniques. *Journal of the Faculty of Engineering and Architecture of Gazi University*, 31(4), 813-831, 2016.
 4. Avendaño Valencia L.D, Fassois SD. Damage/fault diagnosis in an operating wind turbine under uncertainty via a vibration response Gaussian mixture random coefficient model based framework. *Mechanical Systems and Signal Processing*, 91, 326–353, 2017.
 5. Doebbling S, Farrar C., Prime M. and Shevitz D. A review of damage identification methods that examine changes in dynamic properties. *Shock Vib. Dig.*, 30, 91-105, 1998.
 6. Farrar C, Doebbling S. and Nix D. Vibration based structural damage identification. *Philos Trans R Soc A.*, 356(1778), 131-149, 2001.
 7. Farrar CR and Worden K. *Structural Health Monitoring a Machine Learning Perspective*, Chichester: John Wiley & Sons Ltd., 2013.
 8. Worden K. and Lane AJ. Damage identification using support vector machines. *Smart Materials and Structures*, 10, 540–547, 2001.
 9. Bornn L, Farrar CR, Park G, Farinholt K., Structural health monitoring with autoregressive support vector machines. *Journal of Vibration and Acoustics*, 131(2), 021004, 2009.
 10. Figueiredo E, Park G, Farrar CR, Worden K., Figueiras J. Machine learning algorithms for damage detection under operational and environmental variability. *Structural Health Monitoring*, 10(6), 559-72, 2011.
 11. Sohn H, Farrar CR. Damage diagnosis using time series analysis of vibration signals. *Smart Materials and Structures*, 10, 446-451, 2001.
 12. Sohn H, Robertson AN. and Farrar CR. Holder exponent analysis for discontinuity detection. *Structural Engineering and Mechanics An Int'l Journal*, 17(3), 409-428, 2004.
 13. Allen D, Sohn H, Worden K. and Farrar C. Utilizing the sequential probability ratio test for building joint monitoring. *Proc SPIE*, 4704, 2002.
 14. Ma J, Perkins S. Online novelty detection on temporal sequences. *Proceedings of the 9th ACM SIGKDD International Conference on Knowledge Discovery and Data Mining*, Washington DC, 613-618, 2003.
 15. Johansen S. *Likelihood -based inference in co integration vector auto-regressive models*, Oxford University Press Inc, Newyork, USA, 1995.
 16. Krolzig H.M. *Markov-Switching vector auto regressions, Modelling, Statistical Inference, and Application to Business Cycle Analysis*, Springer-Verlag, Berlin, Heidelberg, Newyork, USA, 1997.
 17. Ljung L, *System identification -theory for the use*, Prentice Hall, Englewood Cliffs, NJ, USA, 1987.
 18. Schwarz G. Estimating the dimension of a model. *Annals of a statistics*, 6(2), 461-464, 1978.
 19. Vapnik VN. *The Nature of Statistical Learning Theory*, Springer-Verlag, New York, USA, 1998.
 20. Bishop CM. *Pattern recognition and machine learning*, Springer-Verlag, New York NY, USA, 2006,
 21. Osuna EE, Freund R. and Girosi F. *Support vector machines: training and applications*, A.I. Memo No: 1602, C.B, C.L., 144, Massachusetts, 1997.
 22. Haykin S. *Neural Networks, A comprehensive Foundation*, Macmillan, London, UK, 1995.
 23. Osabe K and Kato T. Estimation of standards compliance uncertainty for radiated emission measurement in the PT program, in *Proc. IEEE Int.Symp. Electromagn. Compat.*, Long Beach, CA, USA, Aug. 14–19, pp. 994–998, 2011.
 24. Carobbi C.F.M, Lalléchère S. and Arnaut L.R. Review of Uncertainty Quantification of Measurement and Computational Modeling in EMC Part I: Measurement Uncertainty," in *IEEE Transactions on Electromagnetic Compatibility*, 61(6), 1690-1698, 2019.
 25. Fawcett T. An introduction to ROC analysis, *Pattern Recogn. Lett.* 27, 861–874, 2006.
 26. Raczko E and Zagajewski B. Comparison of support vectormachine, random forest and neural network classifiers for tree species classification on airbornehyperspectral APEX images, *European Journal of Remote Sensing*, 50(1), 144-154, 2017.

Arrays of Plasmonic Nanoparticles Assembled on Patterns of Polymer Brushes Fabricated by Soft Lithography

Hasan H. Ipekci^{1,4}  Afia Asif^{2,5}  Sema Karabel^{3,4}  M. Serdar Onses^{3,4} 

¹Necmettin Erbakan University, Department of Metallurgical and Materials Engineering, Konya, Turkey

²Ozyegin University, Department of Electrical and Electronics Engineering, Istanbul, Turkey

³Erciyes University, Department of Materials Science and Engineering, Kayseri, Turkey

⁴Erciyes University, Nanotechnology Research Center (ERNAM), Kayseri, Turkey

⁵Technical University of Denmark, Department of Biotechnology and Biomedicine, Kongens Lyngb, Denmark

ABSTRACT

This work employed end-grafted poly(ethylene glycol) (PEG) and hydroxyl-terminated poly(2-vinylpyridine) (P2VP) polymer chains for selective immobilization and patterning of plasmonic nanoparticles (NPs). A soft lithographic method which called micromolding in capillaries (MIMIC) used in this study. The polymers are deposited the capillary flow by the channels which formed by an elastomeric mold and substrate. The localized coatings are referred as polymer brushes and show great promise in the assembly of NPs due to the tunable interaction between the polymer chains and particles. The results show that the width of patterns defined by the channels is smaller than 1.5 μm with a length of around 0.5 cm. Also, the heights of the patterns are ~ 3.5 nm for P2VP and ~ 10 nm for PEG. The fabricated structures exhibited high levels of plasmonic activity and surface enhanced Raman scattering due to the immobilized Au NPs. The patterning polymer brushes and plasmonic NPs over large areas by a low-cost process show great promise for a variety of applications that range from molecular sensors to biotechnology.

Keywords:

Soft-lithography, Polymer brushes, Nanoparticles, Plasmonics.

Article History:

Received: 2020/03/07

Accepted: 2020/09/01

Online: 2020/09/30

Correspondence to: Hasan H. Ipekci,

E-mail: hhipekci@erbakan.edu.tr;

Phone: +90 332 325 20 24 (4000)

INTRODUCTION

Functionalization of surfaces with polymer brushes shows important promise for a range of applications in materials engineering [1, 2], nanotechnology [3, 4] and biotechnology [5, 6]. A particular area where these end-grafted polymer chains are receiving increasing attention is immobilization and assembly of colloidal NPs [7-9]. The ultra-smooth surfaces, mechanical robustness, long-term durability and ability to tune the chemistry, thickness and grafting density of the brushes present a highly useful platform for benefiting from the interesting properties of NPs that are available in precisely defined size, shape and material composition in massive quantities through wet chemistry approaches [10]. Tailoring the interaction of polymer brushes with NPs through the intrinsic properties such as the length of polymer chains [11] and external stimuli such as pH [12] allows for assembly of particles into specific architectures that can be dynamically tuned. Assembly of NPs into or-

dered structures is particularly critical for plasmonic NPs, since collective properties of these materials arise when they are separated by small gaps [13]. The use of NPs in applications such as sensors [14], structural coloration [15], antennas [16], optoelectronics devices [17] and directing cellular behavior for bioengineering [18], on the other hand, requires methods to control the position of assemblies of particles on the surface of technologically relevant substrates. For these applications, it requires the development of low cost, high efficiency and versatile patterning of polymer brushes for the selective placement and assembly of colloidal NPs.

A variety of different methods exists for fabrication of patterned polymer brushes using methods including electron beam lithography [19], photolithography [20], dip-pen nanolithography [21], and jet printing [22, 23]. These methods have all addressed different aspects such

as high resolution and additive patterning of multiple materials; however, these methods typically suffer from costly and specific setups that are not widely accessible and inability to pattern large areas at short processing times. Self-assembled templates can be used to fabricate polymer brush patterns with periodic features of the certain geometries and dimensions [24, 25]. Soft lithography [26, 27] approaches allow for low-cost, large area patterning of materials using elastomeric stamps usually made from poly(dimethylsiloxane) (PDMS). A commonly adapted approach in patterning polymer brushes is microcontact printing of self-assembled monolayers which serve as initiator molecules for surface-initiated polymerization from sites defined by the stamp [28-32]. Referred as “grafting from”, end-tethered polymer chains grown on the surface have the advantage of achieving high grafting densities and thicknesses. The challenges associated with surface-initiated polymerization include synthesis and characterization of polymers with well-defined molecular weights and polydispersities, lengthy polymerization reactions requiring experienced personnel and specialized tools (e.g. schlenk line) that are not commonly available. A versatile strategy overcoming these challenges is direct attachment of preformed end-functional polymers synthesized and characterized with bulk polymerization techniques. The use of commercially available polymers greatly simplifies the surface functionalization with this approach called as grafting to. The thickness and grafting density of polymer brushes are typically not as high as those that can be achieved with grafting from; however, sufficient for many applications such as nanolithography, engineering of surface wetting, and NP assembly [33-35]. A soft-lithographic approach to patterning preformed end-functional polymers was recently [36] demonstrated using micromolding in capillaries [37] (MIMIC) which is based on capillary flow of fluids through microchannels formed by placing a PDMS mold onto a substrate. Different hydrophilic polymers were synthesized via the reversible addition-fragmentation chain process to include a functional group that can react with a substrate functionalized with self-assembled monolayers presenting diene groups. The resulting patterns were used for surface passivation against biofouling. It remains a challenge to pattern polymer brushes on technologically relevant substrates for organization of plasmonic NPs by one-step grafting of end-functional macromolecules deposited via soft-lithography.

Here we demonstrate fabrication of micropatterns of polymer brushes for selective immobilization and assembly of metallic NPs by MIMIC. The strength of the presented work is that silicon oxide terminated substrates that are widely used in most applications can be patterned with polymer brushes by one-step direct grafting of end-functional polymers. Poly(ethylene glycol) (PEG) and hydroxyl-terminated poly(2-vinylpyridine) (P2VP) were deposited on regions de-

fined by the elastomeric stamp through the capillary flow of the polymer solutions followed by evaporation and removal of the stamp. The polymers were then end-grafted through a fast thermal annealing step to silicon oxide terminated substrates. The localized grafting of P2VP and PEG brushes was studied via optical and atomic force microscopy (AFM). The fabricated patterns served as binding sites for colloidal gold NPs. The functionality and uniformity of the plasmonic NP arrays were demonstrated by mapping their activity in surface-enhanced Raman scattering (SERS).

MATERIALS AND EXPERIMENTAL PROCEDURES

Materials

PDMS and curing agent (Sylgard 184) were purchased from Dow Corning. SU-8 2050 was purchased from Microchem Inc. AFM calibration grid (629-30AFM) and Au NPs (20 nm in diameter) were purchased from Ted Pella Inc. Silicon wafers < 100 > were purchased from Wafer World Inc. P2VP-OH (20.5 kg/mol) was purchased from Polymer Source Inc. Methanol, chloroform and *N, N*-dimethylformamide, chlorobenzene were purchased from Merck. PEG (35.0 kg/mol, BioUltra), propylene glycol monomethyl ether acetate (PGMEA), rhodamine 6G and cyclopentanone were purchased from Sigma-Aldrich.

Fabrication of Master Substrates

SU-8 was diluted with cyclopentanone to achieve films of 10 μm in thickness by spin-coating at 3800 rpm. Patterns of SU-8 were then fabricated by photolithography: pre-bake (95 $^{\circ}\text{C}$ for 4 min.), UV exposure (~ 280 mJ/cm²), post-bake (95 $^{\circ}\text{C}$ for 4 min.), development in PGMEA (5 min). AFM calibration grids were used directly without any processing. The surface of the master substrates was modified with 3-Aminopropyl triethoxysilane before casting PDMS for easy separation of the mold from the substrate following curing.

Preparation of Elastomeric Molds

The elastomeric molds were prepared by casting the mixture (10:1) of the PDMS and curing agent on top of the master substrates followed by desiccation for 10 min and heating at 65 $^{\circ}\text{C}$ for 2 h. The cured PDMS molds were then separated from the master substrate.

Patterning of P2VP and PEG brushes Using MIMIC

The elastomeric molds were washed in DMF under sonication for 10 min and then dried at 90 $^{\circ}\text{C}$ for 2 h, prior to the MIMIC process. PDMS molds were then placed on top of the silicon substrates that were freshly cleaned in a UV-ozone chamber (Bioforce, procleaner) for 20 min.

Solutions (~5 μL) of (1% for AFM grids, 3% for 20 μm wide channels) P2VP-OH in DMF and (1% for AFM grids, 6% for 20 μm wide channels) PEG in methanol were placed near the open-end of the micro-channels. The molds were then removed from the silicon substrate following the filling of the channels and evaporation of the solvents which were monitored under an optical microscope. This process typically took ~2 h. The silicon substrates with the patterns of end-functional polymers were then annealed in a glove-box filled with argon at 180 $^{\circ}\text{C}$ for 5 min for the grafting of chains. The excess and ungrafted polymers were then removed by 3 cycles of sonication in solvents (DMF for P2VP and chloroform for PEG) for 3 min per cycle. The substrates were then dried with nitrogen.

Selective Immobilization of Plasmonic Nanoparticles on the Patterned Surfaces

Substrates containing patterned substrates were treated with citrate-stabilized Au NPs by spotting a droplet (~100 μL) of particle solution for 1 h in a humid atmosphere (a petri dish sealed with a parafilm, containing a little water near the substrate). The substrate was then washed in water under sonication for 2 min and dried with nitrogen. A solution of 100 μM rhodamine 6G in ethanol was dropped on the immobilized NPs for investigating the SERS response of the particles.

Characterization of Patterned Brushes and Nanoparticle Arrays

The process of grafting brushes were investigated by analyzing the topography of patterns following MIMIC, annealing and washing with an AFM (Veeco, Multimode 8). The surface morphology of the master substrates and arrays of NPs were imaged with a SEM (Zeiss EVO LS10) at 20 kV. The activity of the immobilized NPs were investigated via SERS mappings obtained by Witec alpha M+ Raman Microscopy system equipped with a 532 nm laser source, 50x objective (N.A.=0.85), motorized stage at x, y dimensions with 0.1 μm resolution. All Raman spectroscopy measurements were performed with 0.05s acquisition time, 0.1mW laser power, 2 μm spot size diameter. Raman mappings were obtained with 0.5 μm resolution. Each Raman spectra performed baseline correction and Si substrate subtraction.

RESULTS AND DISCUSSION

The schematic description of the process for fabricating arrays of NPs immobilized on patterns of polymer brushes prepared by MIMIC is presented in Fig. 1. The elastomeric molds were prepared by casting PDMS on top of the master substrates containing linear patterns of trenches using standard soft-lithography procedures. Placing the mold on top of a freshly cleaned silicon sub-

strate resulted in open-ended channels sealed by the conformal contact enabled by the compliant nature of the PDMS. Organic solutions of polymers were spotted near the open end of the channels. We investigated polymers with two different backbone chemistries with identical end-functionality. Hydroxyl-terminated P2VP and PEG were dissolved in DMF and methanol, respectively. The latter polymer has hydroxyl groups at both ends of the polymer. The solutions filled the channels by capillary action and the mold was removed from the substrate following evaporation of the solvent. The resulting patterns of end-functional polymers were then subjected to a brief thermal annealing for grafting of the polymer chains to the substrate. Since the amount of deposited polymer is in excess of grafted chains, ungrafted polymer chains were removed by sonication in DMF and chloroform for P2VP and PEG, respectively. Patterns of polymer brushes then served as templates for guided attachment of colloidal gold nanoparticles which were immobilized by spotting a solution of Au NPs on the entire region followed by washing in water under sonication. After sonication the physically bound NPs removed from the surface. The particles only attached to the patterned polymer brushes, thanks to the well-defined chemical patterning via MIMIC.

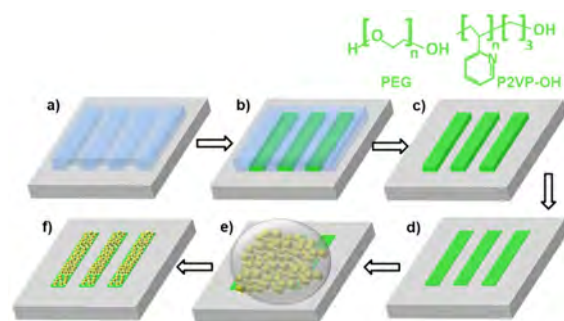


Figure 1. Schematic description of the process for fabricating arrays of plasmonic NPs on top of patterns of polymer brushes prepared by a soft-lithography approach. a) An elastomeric mold consisting of PDMS is placed on a silicon substrate forming open-ended channels. b) A drop of end-functional polymers dissolved in an organic solvent is placed at the end of the channels. The polymer solution fills the channel by capillary action. Two polymers are used: hydroxyl-terminated P2VP dissolved in DMF and PEG dissolved in methanol. c) Separation of the mold leads to patterns of end-functional polymers. d) A thermal annealing followed by washing of the excess material leads to grafted polymer chains on the areas defined by the channels. e) A drop of colloidal Au NPs is placed on the entire substrate. f) Au NPs specifically bind to the patterns of polymer brushes.

We employed two different types of master substrates to fabricate the PDMS molds. The master with the large features was fabricated by photolithography using a negative tone photoresist, whereas the other master consisted of a commercially available AFM grid (Fig. 2). The master with the large features consisted of steps with the width of 20 μm , height of 10 μm and period of 100 μm . The grating patterns

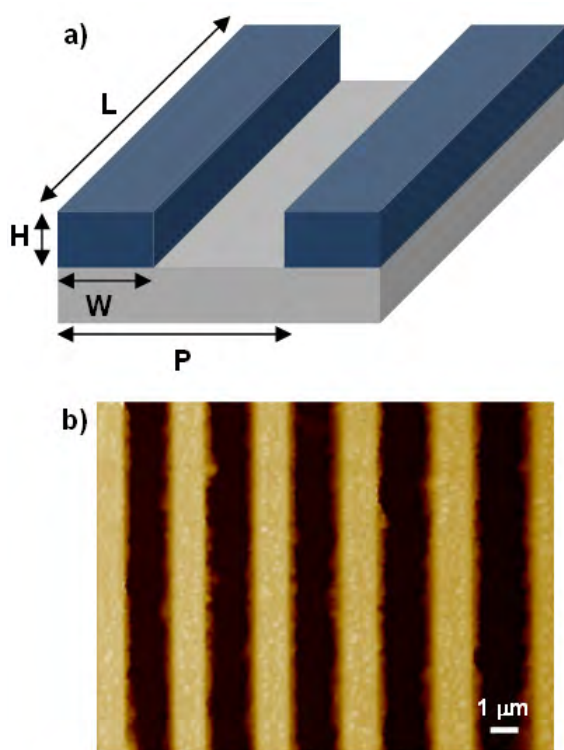


Figure 2. Master substrates. a) Schematic description of the dimensions of the master substrates. For the master with the large features: $L = 5$ mm, $H = 10$ μm , $W = 20$ μm , $P = 100$ μm . For the AFM grid: $L = 2$ mm, $H = 500$ nm, $W = 1.5$ μm , $P = 3$ μm . b) AFM image of the master substrate consisting of the 1:1 grating patterns.

of the AFM grid had 1:1 ratio of the width to spacing with the width of 1.5 μm and height of ~ 500 nm. The patterns were fabricated with the specified dimension over large areas with the minimum number of defects. Note that the patterns in the mold are complementary to those on the master substrate; however, the patterns on the master are replicated on the surface of the target substrate following MIMIC.

The complete filling of the channels formed by the mold and target substrate by the polymer solutions without loss of the conformal contact is the most critical aspect of patterning polymer brushes with the MIMIC process. Several factors including the surface energy of the channels, surface tension and viscosity of the solutions affect the filling the process [37]. Another important factor for organic solvents, is the swelling of the PDMS molds. Swelling not only can change the dimensions of the patterns, but also can destroy the conformal contact between the PDMS and target substrate. We chose DMF and methanol which swell PDMS at low levels [38], for dissolving P2VP and PEG, respectively. Chlorobenzene used in spin-coating films of PEG, for example, led to immediate loss of the conformal contact of the mold with the substrate. Both polymer solutions completely filled the channels (Fig. 3a,c). The complete filling of the channels with the polymer solutions can be exp-

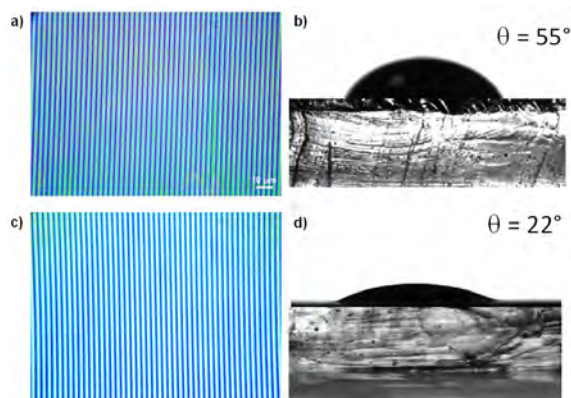


Figure 3. Filling of the channels. a, c) Optical microscope images of the target substrates following the MIMIC process and removal of the PDMS mold for a) 1% P2VP-OH in DMF and c) 1% PEG in methanol. b, d) Images of droplets of b) 1% P2VP-OH in DMF and d) 1% PEG in methanol. The contact angle of the droplets are given at the top-right of the image.

lained by their wetting behavior of the silicon substrate and channels (Fig. 3b,d). A solution of (1%) P2VP in DMF had a contact angle of 55° on PDMS and $<10^\circ$ on silicon wafer. A solution of (1%) PEG in methanol had a contact angle of 22° on PDMS and $<10^\circ$ on silicon wafer. Since the contact angles of the solutions on both the target and mold substrate is much less than 90° , the filling of the channels are thermodynamically favorable [37]. Note that oxidizing PDMS molds by a plasma treatment can further decrease these contact angles; however, such process leads to the permanent bonding of the PDMS to the bare silicon wafer. The polymer solutions typically filled the channels at a rate of ~ 1.1 mm/s based on the relatively low molecular weight and therefore low viscosity of the solutions.

The height profile of the patterns after MIMIC, annealing and washing steps inform about the localized grafting of brushes. We systematically characterized the height profile of the patterned samples after each step by AFM imaging. The images after each step were taken from the same region of the same substrates for consistency. Fig. 4 presents the results for grafting P2VP and PEG brushes. The average height of the deposited patterns of end-functional polymers was above 200 nm after the MIMIC process. The edges of the patterns were slightly higher for the both polymers. Such edge effects are likely due to transport of materials to the edge regions during the evaporation of the solvent with a phenomena known as the coffee-ring effect [39]. The width of the patterns was ~ 1.4 μm which was defined by the channels (Table 1). The slightly lower width of the patterns in comparison to the width of the channels is probably a result of swelling and distortion of the PDMS molds during the MIMIC process. Thermal annealing of the patterns resulted in a certain level of spreading of the patterns with an increase in the width and decrease in the height of the patterns. Thermal annealing induced flow also led to a parabolic

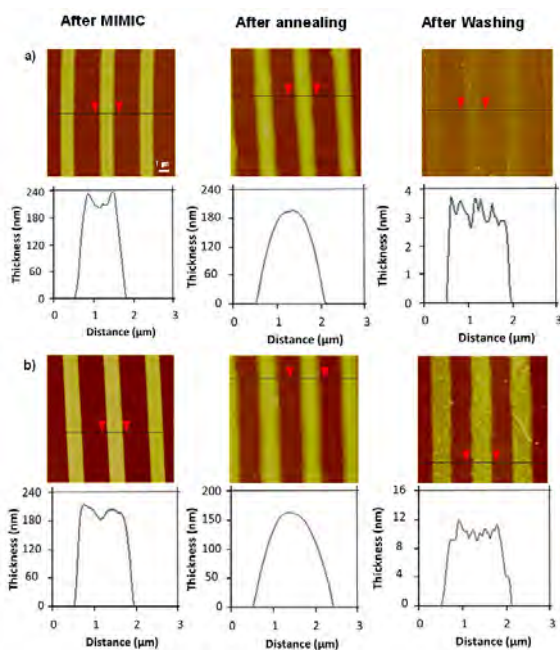


Figure 4. Characterization of the height profiles of the patterns following the MIMIC process, grafting and washing steps. a) Grafting of P2VP brushes from 1% P2VP-OH in DMF and b) Grafting of PEG brushes from 1% PEG in methanol.

height profile with the maxima at the center of the pattern. PEG showed a slightly higher extent of spreading than P2VP, which could be related to the lower glass transition of the molecules. The removal of the excess and ungrafted material through washing resulted in grafted polymer chains with heights defined by the molecular weight of the polymers and grafting densities. The height of the patterned polymer brushes was ~ 3.5 nm and ~ 10.0 nm for P2VP and PEG, respectively. These values are slightly lower than the thicknesses (~ 5.3 nm for P2VP, ~ 12.0 nm for PEG) obtained for brushes grafted in identical conditions from films deposited by spin-coating and correspond to grafting densities of 0.10 and 0.19 for P2VP and PEG brushes, respectively. The final patterns of grafted brushes has a roughness smaller than 1 nm. Irregularities in the center and edges of the patterns following the MIMIC process are not reflected to the patterns of brushes, since only chemically bound polymers remain attached to the substrate following the washing step. The width of the grafted brushes was typically lower than the width of the patterns following the thermal annealing. This interesting observation could be related to the presence of residual PDMS on the silicon in the regions where there was a contact between the mold and substrate. Another factor could be the low heights of the patterns in the edge regions following the thermal annealing step.

Arrays of plasmonic NPs over large areas can be readily achieved on patterns of P2VP and PEG brushes prepared by the MIMIC process. Patterned P2VP and PEG brushes surrounded by silicon oxide serve as binding sites for the

Table 1. The width and height of the patterns after different steps.

Brush	Step	Width (μ m)	Height (nm)
P2VP	After Mimic	1.33 ± 0.03	237.92 ± 11.48
	After Annealing	1.68 ± 0.03	215.31 ± 9.15
	After Washing	1.42 ± 0.04	3.50 ± 0.27
PEG	After Mimic	1.43 ± 0.03	218.67 ± 9.50
	After Annealing	1.94 ± 0.03	189.67 ± 6.80
	After Washing	1.70 ± 0.13	10.0 ± 0.65

selective immobilization of citrate-stabilized Au NPs. SEM images presented in Fig. 5 show that colloidal Au NPs attached to the patterns with a high level of specificity, i.e. the particles bound at high densities on the patterns with none or negligible binding to the background regions. The high level of specificity is a consequence of several factors: i) The MIMIC process enables additive patterning of materials without deposition of the materials to the background regions, thanks to the compliant nature of PDMS. ii) Citrate-stabilized Au NPs have a strong binding affinity towards P2VP and PEG brushes, allowing strong washing of the substrates under sonication following the immobilization of the particles. iii) The absence of interaction between the citrate-stabilized Au NPs and silicon oxide terminated background regions results in low levels of immobilized particles which are removed in the washing step. SEM images show that uniform arrays of particles could be obtained in widths defined by the mold. The use of molds with widths as small as several hundred nanometers could be possible based on the previously reported soft-lithography studies; however, several factors[40] such as incomplete filling and distortion in the patterns prevent from scaling down this process below 100 nm. We found that the number of immobilized Au NPs was significantly higher on the patterned PEG brushes in comparison to homogenous PEG brushes deposited by spin-coating. The number of immobilized Au NPs (20 nm in diameter) per square micrometer was 778 ± 11 and this number reduced to 246 ± 8 particles on homogenous PEG brushes. This result is consistent with the previous study [11] where the density of bound particles on lithographically patterned PEG brushes was higher in comparison to homogenous substrates. It is likely that the kinetics of particle adsorption is enhanced by generating PEG brush grafted patterns surrounded by regions where there is no interaction with the Au NPs. The density of immobilized particles on patterned P2VP brushes, on the other hand, was 287 ± 7 NPs/ μm^2 which is consistent with the values observed on homogenous PEG brushes deposited by spin-coating [41]. The contrast in the variance of the density of immobilized NPs between the patterned and homogeneous substrates for PEG and P2VP brushes probably relates to the different types of polymer-particle interaction.

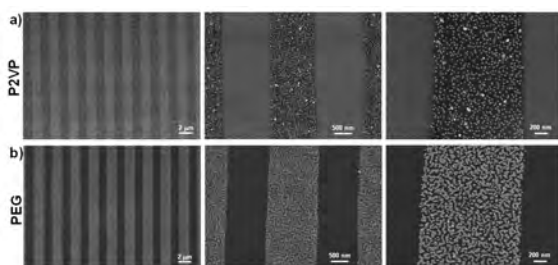


Figure 5. SEM images of the NP arrays. a) P2VP and b) PEG brushes. The diameter of the particles is 20 nm.

We finally investigated the functionality, uniformity and reproducibility of the patterned gold nanoparticles by mapping the SERS response of the fabricated substrates. Localized surface plasmon resonances of metallic nanostructures result in electromagnetic enhancement of signals observed in Raman spectroscopy [42]. Therefore, mapping the characteristic peak of a reporter molecule in Raman spectroscopy directly informs about the functionality and uniformity of the fabricated NP arrays. Fig. 6 and Fig. 7 summarizes SERS results on the arrays of NPs generated on patterns of P2VP and PEG brushes using rhodamine 6G as the reporter molecule. The peaks positioned at 611, 774, 1184, 1311, 1361, 1507, 1573 and 1648 cm^{-1} were detected on the immobilized NPs. The mapping of the peak at a position of 1361 cm^{-1} shows specific and strong signals are received from the patterns where Au NPs are located. An interesting result is that the intensity of signals was higher for NPs immobilized on the patterned brushes in comparison to homogenous brushes prepared by spin-coating (Fig. 6.c). Two factors contribute to such enhancement of the signals. First, the density of particles per unit area is larger in the case of patterned brushes, resulting in higher density of scattering centers. Second, the placement of NPs in close-proximity results in areas where electromagnetic fields are focused in small gaps called as hot-spots. The mapping of the SERS response also inform about the uniformity of the density of the bound particles over areas that are much larger than that can be observed by SEM imaging. The intensity of the signals from the patterns was mostly uniform; however, some of the lines had regions of weak SERS response. We found out that the density of particles in these defective regions are lower than the rest of the patterns. These defective regions were typically less than 10% of the total area and probably formed as a result of issues during the MIMIC process such as contaminations from the PDMS molds. To show the reproducibility of the patterned gold nanoparticles, SERS spectrum was measured at 50 randomly selected regions. (Fig. 7a,b). The SERS spectrum was measured at 15 randomly selected regions and showed that a relatively uniform and RSD value of the RG6 at 1361 cm^{-1} was 6.7% and 5.9% for the PEG and P2VP, respectively (Fig. 7c,d).

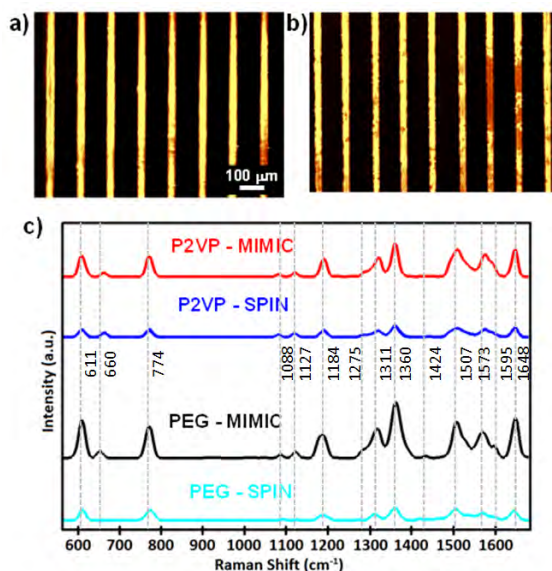


Figure 6. SERS results on the patterned P2VP and PEG brushes. Raman mapping of rhodamine 6G on patterns of a) P2VP and b) PEG brushes. c) Raman scattering spectra of rhodamine 6G on immobilized particles. The diameter of the particles is 60 nm.

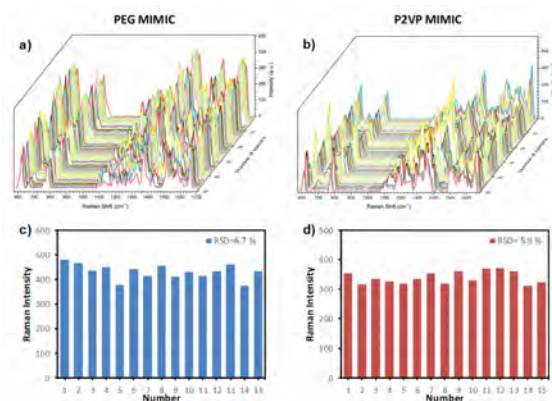


Figure 7. SERS spectra of rhodamine were collected from 50 random points on patterns of a) PEG and b) P2VP brushes. Relative standard deviation (RSD) of specific Raman modes at 1361 cm^{-1} of the 15 random points c) PEG and d) P2VP brushes.

CONCLUSION

A soft lithographic approach relying on capillary flow of solutions containing end-functional P2VP and PEG molecules into channels is used to fabricate patterns of polymer brushes. This approach enables low-cost, large area patterning of end-grafted polymer chains via one-step grafting reaction. The lateral dimensions of the patterns are defined by the mold, whereas the height of the resulting brushes are determined by the grafting process as a function of the chain length and grafting length. The ability to pattern end-grafted polymer chains with a high level of specificity allowed for fabrication of pat-

terned assemblies of plasmonic NPs which show strong SERS effects. This platform can serve as foundation for advanced sensor systems through integration of multiple analyte molecules on the plasmonic NPs using microfluidic channels. The backbone chemistry of the patterned polymers as well as colloidal NPs can be varied according to the needs of specific applications.

ACKNOWLEDGEMENT

This work was supported by Scientific and Technological Research Council of Turkey (TUBITAK) Grant No. 115M220.

References

- Sugnaux C, Mallorqui AD, Herriman J, Klok HA, Morral, AFI. Polymer Brush Guided Formation of Conformal, Plasmonic Nanoparticle-Based Electrodes for Microwire Solar Cells. *Adv Funct Mater* 25 (2015) 3958–3965.
- Ipekci HH, Arkaz HH, Onses MS, Hancer, M. Superhydrophobic coatings with improved mechanical robustness based on polymer brushes. *Surf Coat Tech* 299 (2016) 162–168.
- Mansky P, Liu Y, Huang E, Russell TP, Hawker, CJ. Controlling polymer–surface interactions with random copolymer brushes. *Science* 275 (1997) 1458–1460.
- Thode CJ, Cook PL, Jiang YM, Onses MS, Ji SX, Himpfel FJ, Nealey, PF. In situ metallization of patterned polymer brushes created by molecular transfer print and fill. *Nanotechnology* 24 (2013).
- Kroning A, Furchner A, Aulich D, Bittrich E, Rauch S, Uhlmann P, Eichhorn KJ, Seeber M, Luzinov I, Kilbey SM, Lokitz BS, Minko S, Hinrichs, K. In Situ Infrared Ellipsometry for Protein Adsorption Studies on Ultrathin Smart Polymer Brushes in Aqueous Environment. *ACS Appl Mater Inter* 7 (2015) 12430–12439.
- Yu K, Lo JCY, Mei Y, Haney EF, Siren E, Kalathottukaren MT, Hancock REW, Lange D, Kizhakkedathu, JN. Toward Infection-Resistant Surfaces: Achieving High Antimicrobial Peptide Potency by Modulating the Functionality of Polymer Brush and Peptide. *ACS Appl Mater Inter* 7 (2015) 28591–28605.
- Onses MS, Liu CC, Thode CJ, Nealey, PF. Highly Selective Immobilization of Au Nanoparticles onto Isolated and Dense Nanopatterns of Poly(2-vinyl pyridine) Brushes down to Single-Particle Resolution. *Langmuir* 28 (2012) 7299–7307.
- Nguyen M, Kanaev A, Sun XN, Lacaze E, Lau-Truong S, Lamouri A, Aubard J, Felidj N, Mangeney, C. Tunable Electromagnetic Coupling in Plasmonic Nanostructures Mediated by Thermoresponsive Polymer Brushes. *Langmuir* 31 (2015) 12830–12837.
- Christau S, Genzer J, Klitzing, RV. Polymer Brush/Metal Nanoparticle Hybrids for Optical Sensor Applications: from Self-Assembly to Tailored Functions and Nanoengineering. *Zeitschrift Fur Physikalische Chemie-International Journal of Research in Physical Chemistry & Chemical Physics* 229 (2015) 1089–1117.
- Lu XM, Rycenga M, Skrabalak SE, Wiley B, Xia, YN. Chemical Synthesis of Novel Plasmonic Nanoparticles. *Annu Rev Phys Chem* 60 (2009) 167–192.
- Onses MS, Nealey, PF. Tunable Assembly of Gold Nanoparticles on Nanopatterned Poly(ethylene glycol) Brushes. *Small* 9 (2013) 4168–4174.
- Tokareva I, Minko S, Fendler JH, Hutter, E. Nanosensors based on responsive polymer brushes and gold nanoparticle enhanced transmission surface plasmon resonance spectroscopy. *J Am Chem Soc* 126 (2004) 15950–15951.
- Romo-Herrera JM, Alvarez-Puebla RA, Liz-Marzan, LM. Controlled assembly of plasmonic colloidal nanoparticle clusters. *Nanoscale* 3 (2011) 1304–1315.
- Liu Y, Xie SW, Xiao X, Li SH, Gao FH, Zhang ZY, Du, JL. Fabricating metal nanoparticle arrays at specified and localized regions of microfluidic chip for LSPR sensing. *Microelectron Eng* 151 (2016) 7–11.
- Wang GP, Chen XC, Liu S, Wong CP, Chu, S. Mechanical Chameleon through Dynamic Real Time-Plasmonic Tuning. *ACS Nano* 10 (2016) 1788–1794.
- Liu N, Tang ML, Hentschel M, Giessen H, Alivisatos, AP. Nanoantenna-enhanced gas sensing in a single tailored nanofocus. *Nat Mater* 10 (2011) 631–636.
- Kim BH, Onses MS, Lim JB, Nam S, Oh N, Kim H, Yu KJ, Lee JW, Kim JH, Kang SK, Lee CH, Lee J, Shin JH, Kim NH, Leal C, Shim M, Rogers, JA. High-Resolution Patterns of Quantum Dots Formed by Electrohydrodynamic Jet Printing for Light-Emitting Diodes. *Nano Lett* 15 (2015) 969–973.
- Zhu M, Baffou G, Meyerbroeker N, Polleux, J. Micropatterning Thermoplasmonic Gold Nanoarrays To Manipulate Cell Adhesion. *ACS Nano* 6 (2012) 7227–7233.
- Kim SO, Solak HH, Stoykovich MP, Ferrier NJ, Pablo JJ, Nealey, PF. Epitaxial self-assembly of block copolymers on lithographically defined nanopatterned substrates. *Nature* 424 (2003) 411–414.
- Poelma JE, Fors BP, Meyers GF, Kramer JW, Hawker, CJ. Fabrication of Complex Three-Dimensional Polymer Brush Nanostructures through Light-Mediated Living Radical Polymerization. *Angew Chem Int Edit* 52 (2013) 6844–6848.
- Chen CJ, Zhou XC, Xie Z, Gao TT, Zheng, ZJ. Construction of 3D Polymer Brushes by Dip-Pen Nanodisplacement Lithography: Understanding the Molecular Displacement for Ultrafine and High-Speed Patterning. *Small* 11 (2015) 613–621.
- Onses MS, Ramirez-Hernandez A, Hur SM, Sutanto E, Williamson L, Alleyne AG, Nealey PF, Pablo JJ, Rogers, JA. Block Copolymer Assembly on Nanoscale Patterns of Polymer Brushes Formed by Electrohydrodynamic Jet Printing. *ACS Nano* 8 (2014) 6606–6613.
- Parry AV, Straub AJ, Villar-Alvarez EM, Phuengphol T, Nicoli JE, Lim X, WK, Jordan LM, Moore KL, Taboada P, Yeates, SG. Sub-Micron Patterning of Polymer Brushes: An Unexpected Discovery from Inkjet Printing of Polyelectrolyte Macroinitiators. *J Am Chem Soc* (2016).
- Onses MS. Fabrication of Nanopatterned Poly(ethylene glycol) Brushes by Molecular Transfer Printing from Poly(styrene-block-methyl methacrylate) Films to Generate Arrays of Au Nanoparticles. *Langmuir*. 31 (2015) 1225–1230.
- Li YF, Zhang JH, Fang LP, Jiang LM, Liu WD, Wang TQ, Cui LY, Sun HC, Yang, B. Polymer brush nanopatterns with

- controllable features for protein pattern applications. *J Mater Chem* 22 (2012) 25116–25122.
26. Weibel DB, DiLuzio WR, Whitesides, GM. Microfabrication meets microbiology. *Nat Rev Microbiol* 5 (2007) 209–218.
 27. Singh A, Kulkarni SK, Khan–Malek, C. Patterning of SiO₂ nanoparticle–PMMA polymer composite microstructures based on soft lithographic techniques. *Microelectron Eng* 88 (2011) 939–944.
 28. Zhou F, Zheng ZJ, Yu B, Liu WM, Huck, WTS. Multicomponent polymer brushes. *J Am Chem Soc* 128 (2006) 16253–16258.
 29. Chen T, Jordan R, Zauscher, S. Dynamic Microcontact Printing for Patterning Polymer–Brush Microstructures. *Small* 7 (2011) 2148–2152.
 30. Rolling O, De Bruycker K, Vonhoren B, Stricker L, Korsgen M, Arlinghaus HF, Ravoo BJ, Du Prez, FE. Rewritable Polymer Brush Micropatterns Grafted by Triazolinedione Click Chemistry. *Angew Chem Int Edit* 54 (2015) 13126–13129.
 31. Diamanti S, Arifuzzaman S, Elsen A, Genzer J, Vaia, RA. Reactive patterning via post–functionalization of polymer brushes utilizing disuccinimidyl carbonate activation to couple primary amines. *Polymer* 49 (2008) 3770–3779.
 32. Chen T, Jordan R, Zauscher, S. Extending micro–contact printing for patterning complex polymer brush microstructures. *Polymer* 52 (2011) 2461–2467.
 33. Felts JR, Onses MS, Rogers JA, King, WP. Nanometer Scale Alignment of Block–Copolymer Domains by Means of a Scanning Probe Tip. *Adv Mater* 26 (2014) 2999–3002.
 34. Liu XY, Biswas S, Jarrett JW, Poutrina E, Urbas A, Knappenberger KL, Vaia RA, Nealey, PF. Deterministic Construction of Plasmonic Heterostructures in Well–Organized Arrays for Nanophotonic Materials. *Adv Mater* 27 (2015) 7314–+.
 35. Onses MS, Wan L, Liu XY, Kiremitler NB, Yilmaz H, Nealey, PF. Self–Assembled Nanoparticle Arrays on Chemical Nanopatterns Prepared Using Block Copolymer Lithography. *ACS Macro Lett* 4 (2015) 1356–1361.
 36. Vonhoren B, Langer M, Abt D, Barner–Kowollik C, Ravoo, BJ. Fast and Simple Preparation of Patterned Surfaces with Hydrophilic Polymer Brushes by Micromolding in Capillaries. *Langmuir* 31 (2015) 13625–13631.
 37. Kim E, Xia YN, Whitesides, GM. Micromolding in capillaries: Applications in materials science. *J Am Chem Soc* 118 (1996) 5722–5731.
 38. Lee JN, Park C, Whitesides, GM. Solvent compatibility of poly(dimethylsiloxane)–based microfluidic devices. *Anal Chem* 75 (2003) 6544–6554.
 39. Yunker PJ, Still T, Lohr MA, Yodh, AG. Suppression of the coffee–ring effect by shape–dependent capillary interactions. *Nature* 476 (2011) 308–311.
 40. Xia YN, Whitesides, GM. Soft lithography. *Angew Chem Int Edit* 37 (1998) 550–575.
 41. Yilmaz H, Pekdemir S, Ipekci HH, Kiremitler NB, Hancer M, Onses, MS. Ambient, rapid and facile deposition of polymer brushes for immobilization of plasmonic nanoparticles. *Appl Surf Sci* 385 (2016) 299–307.
 42. Shalabaeva V, La Rocca R, Miele E, Dipalo M, Messina GC, Perrone M, Maidecchi G, Gentile F, De Angelis, F. Plasmonic microholes for SERS study of biomolecules in liquid. *Microelectron Eng* 158 (2016) 59–63.

A Model - Based Jamming Detection Method for Electro-Hydrostatic Actuators

Emre Murat Poyraz¹ Hakan Caliskan¹ Ali Emre Turgut¹

Middle East Technical University, Department of Mechanical Engineering, Ankara, Turkey

ABSTRACT

An anomaly or a fault, which may be treated as insignificant in a complicated engineering system, like an electro-hydraulic flight control actuator, can cause considerable performance degradation and deteriorating effects or even worse it may end up with a catastrophic system failure. One of the problems commonly observed in air vehicles is called jamming. Jamming is the type of failure where an actuator connected to a flight control surface permanently gets stuck at a certain position and does not move anymore. This might cause a loss of control of the air vehicle causing severe consequences. Although, there are several methods to detect jamming in the literature, still there is not a universally accepted solution. In this paper, a novel threshold-based fault detection and diagnosis method is proposed. The method is based on the variance of time rate of change of disturbance load and the average tracking error. When these two quantities are above a certain corresponding threshold, jamming is detected. The method is tested on an experimental setup. The experiments show that the detection performance of the method is satisfactory and the detection is performed under one second for all the test cases.

Keywords:

Fault detection and diagnosis; Disturbance observer; EHA; Jamming; Flight control actuation.

INTRODUCTION

Due to increasing demand towards higher system reliability and safety, a great amount of research about fault detection and diagnosis are being carried out. For safety critical systems, like an aircraft, consequences of faults in a flight control system can be extremely hazardous for human life. Flight control systems mostly rely on electro hydraulic actuation technology for providing necessary power to control surfaces of aircrafts. Design and integration of a flight control systems often includes fault detection algorithms in order to make the system more robust against failures. There are many studies on fault detection and diagnosis of different faulty cases in flight control systems such as; oscillatory failure case [1], stall load [2], jamming [3], runaway [4], and incipient sensor failures [5]. One of the most important of them all is jamming. Jamming is a system failure where an actuator connected to a control surface is permanently stuck at a random position. This has several consequences such as undesirable aircraft motion, increase in drag force and fuel consumption.

Several model-based approaches for jamming detection exist in the literature. Among them, Kalman filtering and observer-based approaches are the most well-

known and preferred ones. Ossmann et al. [2] proposed a model-based fault detection and diagnosis method for the actuator jamming at small surface deflections. For the detection of jamming, a discrete version of the linear parameter varying (LPV) modelling approach is proposed in [6] and; it also has the fault identification functionality as in [2]. The error residual $r(t)$ is generated based on the position output of LPV model of the hydraulic actuator. Then, the residual evaluation signal $\theta_r(t)$ is obtained by using a Narendra type fault evaluator [7]. The detection performances have been assessed by simulating the jamming failure scenario, during level flight and special maneuver cases. The results show a high degree of robustness in fault detection and diagnosis (FDD) for the whole range of tests and a satisfactory detection performance. Kalman filter has also been extensively used in fault detection and diagnosis applications. Goupil et al. [3] proposed a Kalman filter-based approach for jamming detection. Proposed method has received certification on the new generation Airbus A350 aircraft.

In this paper, a threshold-based FDD method is designed for an electro-hydrostatic actuator (EHA). The method is based on two indicators; variance of the time

Article History:

Received: 2020/03/16

Accepted: 2020/09/14

Online: 2020/09/30

Correspondence to: Emre Murat Poyraz,
Middle East Technical University,
Mechanical Engineering, 06800, Ankara,
TURKEY

E-Mail: emremuratmetu@gmail.com

Phone: +90 533 332 96 76

rate of change of disturbance load and average tracking error. One threshold for each indicator is defined and when two indicators exceed their corresponding threshold, jamming is detected by the method. In the design of the FDD method, first the linear mathematical model of the EHA is obtained. Then, the state and disturbance observers are designed. The information from the mathematical model (including the state observer) and the disturbance observer are then used in the threshold-based model. The model is also verified extensively in an experimental setup.

The main contributions of this study are: firstly, to the best of our knowledge, none of the studies about jamming focuses on the actuator dynamic. In this paper, the dynamics of the actuator is considered to extract information related to the failure. Secondly, unlike the other studies, in this paper, only the available actuator states are used to identify the jamming not the aircraft states or feedbacks as in [6]. This approach might make the integration of the developed algorithm a lot easier as the only states used for detection of jamming failures are already available as actuator feedback that is continuously processed for the position control loop. Whereas integration of aircraft state feedbacks like calibrated air speed, center of gravity position, aircraft mass and the altitude used in [6] would significantly complicate the overall integration process, requiring various sensor (air data sensor, inertial measurement unit, etc.) outputs, and need a lot more complex interface management for both hardware and software.

The paper is organized as follows: In Section 2, the method, including the mathematical modelling of the EHA, observer design and the fault identification steps, for the detection of jamming are introduced. Then in Section 3, verification of the proposed method is performed. Finally, in Section 4, the results are discussed and the conclusion is made.

METHODOLOGY

The overall methodology for the detection and identification of jamming starts with the mathematical modelling

of the actuator. Later, a state and a disturbance observer are designed based on the mathematical model of the actuator. At the last step, the output of the disturbance observer is analyzed for fault detection purposes.

Mathematical Modelling

The EHA system consists of a hydraulic piston, a pump, an AC electric servo motor driving the pump, a shuttle valve and a hydraulic accumulator for differential flow compensation [8]. Details of physical relations within the EHA system are illustrated in [9].

There are basically two working regions for the EHA. Depending on the load pressure value, the shuttle valve adjusts its opening and lets the flow go into the accumulator and/or the actuator chambers. When the load pressure is low, about 7-8 bar, the shuttle valve opens partially to both chambers or only one of the chambers. The pilot-operated spool of the shuttle valve positions itself naturally. For the other case where the load pressure exceeds these 7-8 bar of the differential pressure, then the shuttle valve fully opens. In this configuration, one of the two chambers is connected to the accumulator and thus the accumulator and the connected chamber can be assumed to have the same pressure. Within the scope of this paper, the EHA is operated in the fully-opened shuttle valve configuration by adjusting the counter loading.

In order to develop a simplified mathematical model of the system in Fig. 1, several assumptions are made. The accumulator pressure and temperature responses are assumed to be considerably slow so that the accumulator dynamics are neglected. The electric motor current dynamics is assumed to be very fast and it is also neglected. Shuttle valve is assumed to be fully open. Therefore, spool dynamics of the shuttle valve is not considered. In a fully-opened shuttle valve condition, only one hydraulic chamber determines the pressure dynamics since the hydraulic accumulator capacitance together with the hydraulic conductance of the shuttle valve are assumed to be considerably high. In other words,

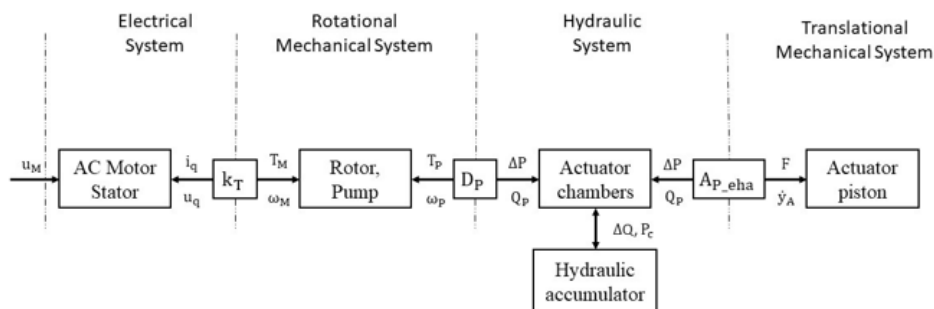


Figure 1. Components and their relations within the EHA system.

change in the load pressure is equal to one of the chamber pressures as $\delta P_L = \delta P_a$ or $\delta P_L = \delta P_b$ depending on the open side of the shuttle valve [9].

In Fig. 1, T_M is the torque generated by the servo motor, P_C is the accumulator pressure, Q_p is the hydraulic flowrate between the pump and the actuator. ΔP represents the pressure difference and the ΔQ shows the hydraulic flow.

Electrical and Rotational Mechanical System

The electric motor and the hydraulic pump are assumed to be coupled through a rigid coupling. Therefore, the pump inertia together with the frictional losses is lumped into electric motor dynamics. The resulting equation of motion of the motor shaft is:

$$k_T i_q = (J'_M) \dot{\omega}_M + (b'_M) \omega_M + D_p (P_a - P_b) \cdot 10^{-3} \quad (1)$$

where, $J'_M = J_M + J_P$ and $b'_M = b_M + b_P$ are the total effective inertia and friction coefficients, respectively. Note that for consistency of units, the right-hand side of the equation, $D_p(P_a - P_b)$ term, is multiplied by 10^{-3} . k_T is the electric motor torque constant. ω_M is the angular speed of the pump in, J_M is the inertia of the rotor of the electric motor, J_P is the inertia of the hydraulic pump rotor, D_p is the pump displacement, P_a and P_b are piston and rod side chamber pressures, respectively, b_p is the viscous friction coefficient of the pump and b_M is the viscous friction coefficient of the motor.

Hydraulic and Translational Mechanical System

The equation of motion for the hydraulic actuator is:

$$A_p (P_a - aP_b) = m \ddot{y}_A + F_D + F_f \quad (2)$$

where, y_A is the actuator piston position, A_p is the piston cross sectional area, m is the mass of the piston and the rod of the actuator, a is the pressure area ratio of the hydraulic cylinder, F_D is the disturbance force acting on the actuator and b is the viscous friction coefficient of the actuator.

The friction force here is modelled as:

$$F_f = b \dot{y}_A \quad (3)$$

where \dot{y}_A is the velocity of the piston. The continuity equation for the piston and the rod side chambers can be written considering the leakage flow to be proportional to the load pressure (P_L) as follows:

$$C_a \dot{P}_L = D_p \omega_M - A_p \dot{y}_A - H P_L \quad (4)$$

$$C_b \dot{P}_L = -D_p \omega_M + a A_p \dot{y}_A - H P_L \quad (5)$$

where H is the leakage flow coefficient of the pump, C_a

and C_b are the piston side hydraulic chamber capacitance, the rod side hydraulic chamber capacitance, respectively. \dot{P}_L is the time rate of change of load pressure.

State Space Representation of the Overall System

The state variables are defined as:

$$x_1 = y_A \quad (6)$$

$$x_2 = \dot{y}_A \quad (7)$$

$$x_3 = P_L = (P_a - aP_b), \quad (8)$$

$$x_4 = \omega_M \quad (9)$$

In matrix form the system is:

$$\dot{x} = A[x] + B[u] \quad (10)$$

The input vector u includes u_M the motor torque and F_d disturbance load as:

$$[u] = \begin{bmatrix} u_M \\ F_d \end{bmatrix} \quad (11)$$

$$A = \begin{bmatrix} 0 & 1 & 0 & 0 \\ 0 & -\frac{b_p}{m} & \frac{A_p}{m} & 0 \\ 0 & -\frac{A_p}{C} & -\frac{H}{C} & \frac{D_p}{C} \\ 0 & 0 & -\frac{D_p}{J'_M} & -\frac{b'_M}{J'_M} \end{bmatrix} \quad (12)$$

$$B = \begin{bmatrix} 0 & -\frac{1}{m} & 0 & 0 \\ 0 & 0 & 0 & \frac{1}{J'_M} \end{bmatrix}^T \quad (13)$$

The parameters used for the mathematical modelling of the electrical and rotational mechanical subsystems are shown in Table 1.

Table 1. Parameters of the electrical and rotational mechanical subsystems [9].

Parameter	Description	Value	Unit
k_T	torque constant	1.52	Nm/A
J_M	rotor inertia of the electric motor	$27.3 \cdot 10^{-4}$	kg · m ²
J_P	hydraulic pump rotor inertia	$1.93 \cdot 10^{-4}$	kg · m ²
D_p	pump displacement	8	cm ³ /rad
b_M	motor viscous friction coefficient	$7 \cdot 10^{-3}$	Nms/rad
$b_{p,vis}$	pump viscous friction coefficient	0.035	Nms/rad

The parameters used for the mathematical modelling of the hydraulic and translational mechanical subsystems are shown in Table 2.

Table 2. Parameters of the hydraulic and translational mechanical subsystems [9].

Parameter	Description	Value	Unit
A_{p_eha}	piston side cross sectional area	2827.4	mm ²
a_{eha}	area ratio	0.75	-
m_{eha}	mass of the piston and the rod	9.6	kg
b_{eha}	viscous friction coefficient of the actuator	6.3	Ns/mm
C_a	piston side hydraulic chamber capacitance	302.5	mm ³ /s · MPa
C_b	rod side hydraulic chamber capacitance	302.5	mm ³ /s · MPa

Capacitance values of C_a and C_b are assumed to be constant to a value of C that is calculated at the position where the two chamber volumes are equal.

State and Disturbance Observer Design

State Observer

A Luenberger observer is designed for the EHA. Using the state-space form in (12) and (13) together with the system parameters, the following matrix equations are obtained:

$$\begin{aligned} \dot{x} &= \begin{bmatrix} 0 & 1 & 0 & 0 \\ 0 & -673.07 & 302072.465 & 0 \\ 0 & -9.35 & 0 & 0.4408 \\ 0 & 0 & -5369.86 & -2.39 \end{bmatrix} x \\ &+ \begin{bmatrix} 0 & 0 \\ -0.107 & 0 \\ 0 & 0 \\ 0 & 342.465 \end{bmatrix} \begin{bmatrix} F_d \\ u \end{bmatrix} \end{aligned} \quad (14)$$

$$y = \begin{bmatrix} 1 & 0 & 0 & 0 \\ 0 & 0 & 0 & 1 \end{bmatrix} x + \begin{bmatrix} 0 & 0 \end{bmatrix} \begin{bmatrix} F_d \\ u \end{bmatrix} \quad (15)$$

Open loop poles of the EHA system is calculated as:

$$p_0 = 0 + 0i, -336.26 + 1646.9i, -336.26 - 1646.9i, -2.9594 \quad (16)$$

The desired poles for the observer are chosen as:

$$p_c = -5 + 0i, -400 + 1646.9i, -400 - 1646.9i, -3.0 + 0i \quad (17)$$

Finally, the gain matrix of the observer is found using pole placement technique:

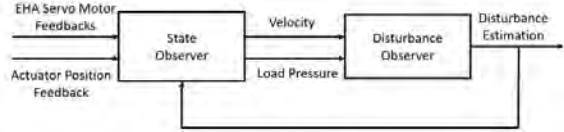


Figure 2. Observer Structure of State and Disturbance Estimations.

$$L = \begin{bmatrix} 30 & 0.5 \\ 2.25 \cdot 10^5 & 125 \\ 1.2 \cdot 10^3 & 0.1 \\ 3.2 \cdot 10^2 & 20 \end{bmatrix} \quad (18)$$

Eventual aim of the designed state observer is to supply unknown state information to the disturbance observer. However, the disturbance load acting on the actuator is an unknown too. Therefore, a structure including two observers working simultaneously is developed for both the state and disturbance estimations. Two observers work together with one estimating the state variables while the other estimating the disturbance as shown in Fig. 2.

Disturbance Observer

The force equilibrium on the piston can be re-written as:

$$F_d = -m_p \ddot{x}_p + p_L A_p - b_p \dot{x}_p \quad (19)$$

which may also be expressed in terms of state variables as:

$$F_d = -m_p \dot{x}_2 + A_p x_3 - b_p x_2 \quad (20)$$

Estimation of the disturbance load is defined as \hat{d} and the dynamics of this estimation with an observer gain L_0 is designed as follows: [10]

$$\dot{\hat{d}} = -L_1(m_p \dot{x}_2 - A_p x_3 + b_p x_2 + \hat{d}) \quad (21)$$

In Eq. 23, the derivative of the state x_2 which amplifies the noise in x_2 decreasing the estimation performance. In order to avoid this problem, an auxiliary variable ζ , as represented in [11], is defined as:

$$\zeta = -\hat{d} - L_1 m_p x_2 \quad (22)$$

and the dynamics of the auxiliary variable is

$$\dot{\zeta} = -L_1(\zeta + L_1 m_p x_2) + L_1(b_p x_2 - A_p x_3) \quad (23)$$

The load pressure and the velocity estimations together with the piston position are used in the disturbance observer model. At this point, it's worth noting that the direct usage of the chamber pressure information would significantly increase the fidelity of the disturbance observer model. It is not used in this study because the pressure feedback may not always be available for a fly-by-wire actuator in an aircraft [12].

Fault Identification

As the first step, time rate of change of the estimated disturbance load is calculated as the residual signal. A detection signal $i(t)$, in Eq. 24, is generated that triggers the fault identification process, when the variance, σ , of the disturbance rate \dot{F}_{d_obs} exceeds a predefined threshold. The threshold value τ for jamming is chosen based on the not-jammed test cases. Jamming results in an increase in the time rate of change of the disturbance load and it also changes its variance. Using these facts, fault information could be extracted from output test data.

$$i(t) = \begin{cases} 1 & \text{if } \sigma(\dot{F}_{d_obs}) \geq \tau \\ 0 & \text{if } \sigma(\dot{F}_{d_obs}) < \tau \end{cases} \quad (24)$$

One possible drawback of variance computation is that it requires the storage of n many samples, which may not be desirable for real time operations. An alternative way is to use recursive methods for mean and variance calculation [13].

Another parameter is needed to enhance the reliability of the proposed FDD method. Since the actuator rod stays approximately constant at the jammed position, moving average \bar{x} of the position tracking error may be analyzed to create a jamming indicator. A fault confirmation signal $\mu(t)$ is generated that decides the presence or absence of a fault if the moving average \bar{x} of the position tracking error $|e|$ exceeds a predefined threshold. The threshold value τ_j for jamming cases is based on not-jammed test cases. Two threshold-based steps consolidate the fault detection function and increase the reliability of the developed FDD system.

$$\mu(t) = \begin{cases} 1 & \text{if } \bar{x}|e| \geq \tau_j \\ 0 & \text{if } \bar{x}|e| < \tau_j \end{cases} \quad (25)$$

where $|e| = y_{reference} - y_{measured}$ is the tracking error.

EXPERIMENTAL ANALYSIS

Test Setup

A schematic drawing of the hydraulic test bench, which was designed and constructed by Çalışkan [9] and Akova [14] is shown in Fig. 3. It consists of two hydraulic actuation systems. The one on the left is an electro hydrostatic actuation system controlled by a hydraulic pump whereas the one on the right is a conventional hydraulic system that acts as the load simulator and it is controlled by a servo proportional valve. Two systems are connected to each other via a flexible coupling mechanism with a force sensor. Closed-loop force control of the load simulator is accomplished using the force sensor. The piston position is also measured which is used in the disturbance feedforward controller as the feedback signal.

The EHA is a closed-loop position system where position tracking is achieved through a closed-loop feedback and feedforward control. An AC servo motor is placed to drive the hydraulic pump in the system. The hydraulic actuator used in the study is a single rod type hydraulic piston which creates unequal flowrates for the retraction and extension sides. Çalışkan developed a novel method to compensate this unequal flowrate difference using a hydraulic accumulator and a 3-position 3-way shuttle valve [8]. Together with the position of the piston of the EHA, speed of the motor is

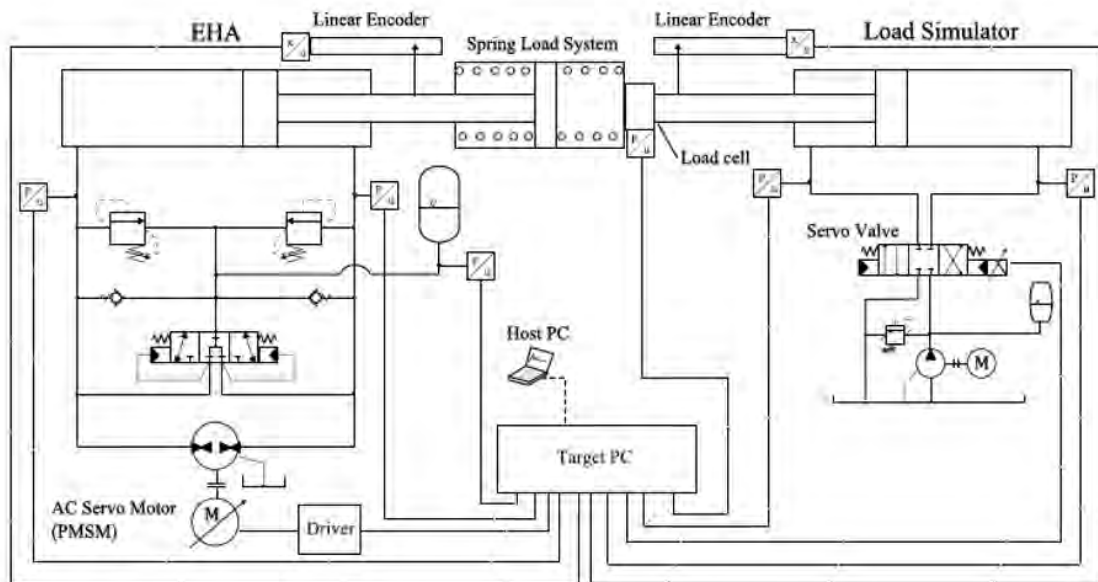


Figure 3. Schematic drawing of the hydraulic test bench [9].

controlled in closed-loop manner. Speed and torque of the servo motor, pressures in the two piston chambers and in the accumulator is measured simultaneously together with the actuator position.

The SpeedGoat real time target PC is equipped by IO105 analog input and IO111 analog output modules. The servo motor speed and torque, pressures of the two chambers of the EHA and accumulator, and the actuator position are measured simultaneously, with a 1 kHz sampling frequency. The pressure transducers are made by Trafag and rated up to 250 bar with 0-10 V output. They are mounted on the hydraulic manifold. The EHA position is measured by a linear encoder made by ATEK. The encoder is connected to the rod of the EHA, it has 20 μ m grid spacing and enables 5 μ m resolution at 4X decoding. [9]. The accuracy of the pressure transducer (Trafag, 8472) is $\pm 0.5\%$ and the load Cell (Burster Model 8524) is $\pm 0.25\%$.

Verification of the Observer Models

A set of test data is used where the reference position of the EHA and the magnitude of the force of the load simulator are controlled as shown in Figs 4 and 5.

In the closed-loop tests, position of the EHA is kept constant at 100mm after $t=6$ secs (Fig. 4). A force signal with varying amplitude is generated as the reference input for the load simulator. Both positive and negative disturbance loads of 12kN are applied and its amplitude is changed between 1-2 kN while the frequency of the square waves is varied bet-

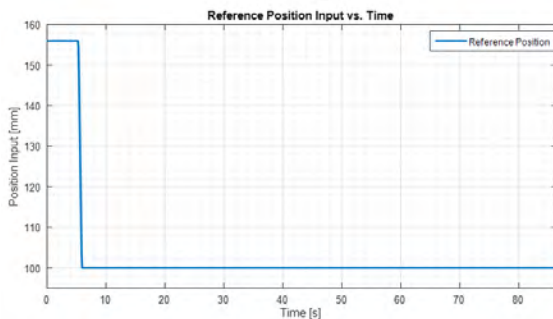


Figure 4. Reference Position Input to the EHA.

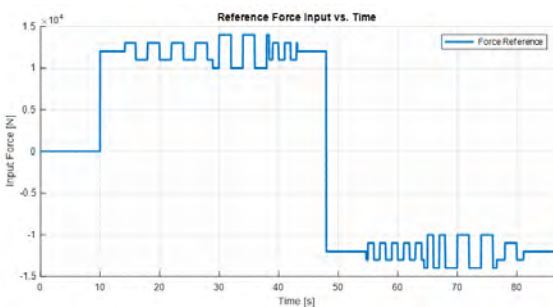


Figure 5. Reference Force Input to the Load Simulator.

ween 0.5-2 Hz (Fig. 5). Velocity estimation via a dedicated Kalman Filter [9] is also used together with the velocity estimation output of the state observer. Some operating regions in the following test results are zoomed in to show the estimation performance of the observers. Especially, the region where the disturbance load is varied is tried to be focused on. Comparison of the estimated states and disturbances with measured feedbacks, via the transducers in the setup, is given in the following figures.

The state observer gives accurate results, being less than 0.1%, for the estimation of position (Fig. 6). This is in fact an expected result since feedback is available for this state variable.

Velocity estimation (Fig. 7) shows some differences between the estimation by state observer and the estimation by a Kalman Filter [9]. This can be explained by the fact that the Kalman Filter, uses a kinematic filtering method whereas in the velocity estimation by the state observer relies more on the system dynamics. There is also a very small error in the estimation of observer for the zero-velocity region which might be overcome by increasing the related gain term in the observer gain matrix.

For the estimation of the load pressure, some undesirable peak points are observed like the ones in 32th and 34th seconds of the simulation as in Fig. 8. The main reason

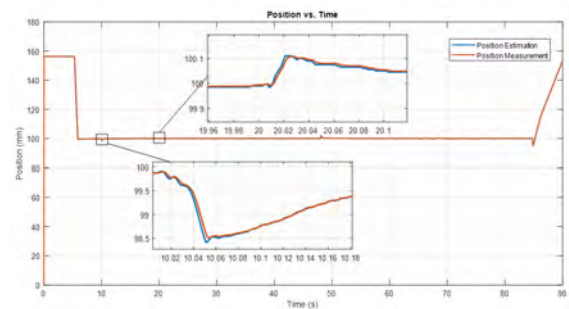


Figure 6. Measured Position Response and the Position Estimation of the EHA.

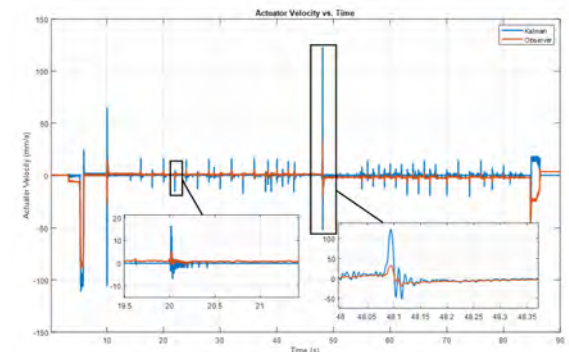


Figure 7. Kalman Filtered Velocity Estimation [9] vs. Observer based Velocity Estimation of the EHA.

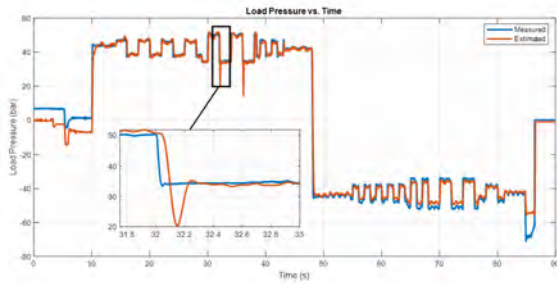


Figure 8. Measured Load Pressure and the Load Pressure Estimation of the EHA.

why such peak points are observed is due to the fact that the EHA system automatically switches its working regions. As the load pressure difference between two hydraulic chambers decrease below a point the shuttle valve starts to open and actuator dynamics gets much more complex, where in this study these complexities are not focused, including flows from accumulator to the chambers depending on the shuttle valve opening. Apart from these points, load pressure estimation includes slight deviations in the transient regions and gives better results for the steady state regions.

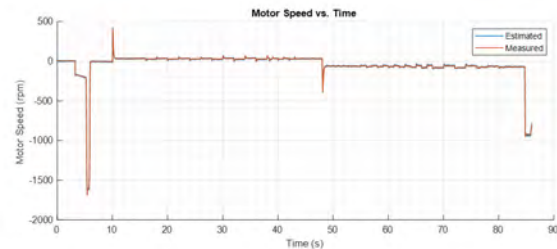


Figure 9. Measured Motor Speed and the Motor Speed Estimation for the EHA.

The state observer gives accurate results for the estimation of the servo motor speed as can be seen in Fig. 9. This is also an expected result since feedback is available for this state variable. In addition to the state estimations, the comparison for the disturbance force estimation is also given with the following figures.

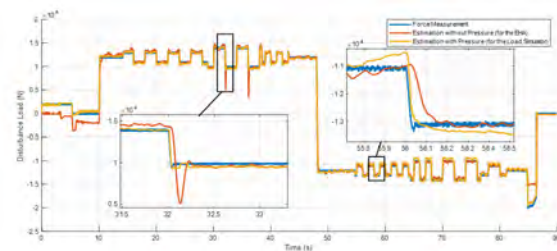


Figure 10. Disturbance Force Estimation (with & without Pressure Feedback) and the Measured Disturbance.

Considering the results for the disturbance estimation, it could be concluded that the designed disturbance observer gives good estimation results for the steady state cases

as can be seen in Fig. 10. Though, there are some deviations from the measured force between the disturbance estimation without using pressure feedback especially in transient regions (for example around 0.2-0.3 second difference in rise time), the estimation still reflects the disturbance dynamics with an adequate level of accuracy.

After about 7-8 bar load pressure, the disturbance and the state observer start to give much better results. This is an expected situation since the shuttle valve inside the EHA system fully opens after about 7-8 bar differential pressure and in the observer dynamics the shuttle valve is assumed to be fully opened to one side.

Test Scenario and Results for Jamming

Several faulty jamming cases are simulated in the experimental setup and the detection performance of the proposed method is analyzed in this subsection. The most critical and difficult cases in terms of detection and identification of jamming are at low deflection signals where the reference position input to the actuator is quite low especially in cruise (steady state flight) condition. Therefore, low amplitude input signals around the jammed position are inserted to the control system. To simulate several different cases, both sinusoidal and sawtooth signals are used in jamming conditions. In order not to cause an excessive sudden increase in the load and in order not to damage the setup, step signals are not preferred for jamming simulations. It should be noted here that this study basically focuses on the detection of jamming cases for a test setup on ground before any implementation on a real flight test with more realistic pilot (or flight control computer) input behavior. Therefore, generic input signals, whose amplitude and frequency can be varied easily, like sawtooth and sinusoidal waves are used. In this way, amplitude and frequency ranges of actuator input signals under which the jamming cases are observed can be realized. The test scenario is applied under both jammed and not-jammed cases to compare the performance of the developed FDD system under faulty and non-faulty cases. The test cases investigated are listed in Table 3. Amplitude and frequency values of the selected reference position signals are presented in the 5th column of the table. Since the actuator input demand is relatively low in cruise condition with the control surface being quite close to its neutral position, amplitudes of 0.25mm, 0.5mm and 1mm are chosen. To reflect different demand behaviors of the actuator position, sinusoidal and sawtooth signals with two different frequency values are used. All of the faulty jamming conditions are also simulated for the not-jammed nominal case. For all of the jamming conditions in the following table, a disturbance load of 14000N is applied as this value is very close to the maximum force

Table 3. Test Cases for Jamming.

Test Case	Condition	Initial Condition	Input Signal	Signal Amplitude and Frequency	Disturbance Load
1	Jammed	50 mm	Sine Wave	0.25 mm, 2 Hz	14000 N
2	Notn-Jammed	50 mm	Sine Wave	0.25 mm, 2 Hz	4000 N
3	Jammed	50 mm	Sine Wave	0.5 mm, 1 Hz	14000 N
4	Notn-Jammed	50 mm	Sine Wave	0.5 mm, 1 Hz	4000 N
5	Jammed	50 mm	Sine Wave	1 mm, 0.5 Hz	14000 N
6	Notn-Jammed	50 mm	Sine Wave	1 mm, 0.5 Hz	4000 N
7	Jammed	50 mm	Sawtooth	0.25 mm, 2 Hz	14000 N
8	Notn-Jammed	50 mm	Sawtooth	0.25 mm, 2 Hz	4000 N
9	Jammed	50 mm	Sawtooth	0.5 mm, 0.5 Hz	14000 N
10	Notn-Jammed	50 mm	Sawtooth	0.5 mm, 0.5 Hz	4000 N
11	Jammed	50 mm	Sawtooth	1 mm, 0.5 Hz	14000 N
12	Notn-Jammed	50 mm	Sawtooth	1 mm, 0.5 Hz	4000 N

that can be measured by the load cell in the test setup. Not-jammed cases are simulated under a load of 4000N.

Experiments are performed based on the test scenario in Table 3. Jamming cases are tried to be simulated under the counter load by the load simulator using a mechanical locking assembly. By this way, EHA piston is kept at the desired position. Reference and measured position, rate of the estimated disturbance, recursive variance calculation of disturbance rate, moving average of the tracking error and the eventual output of the developed FDD method, which is the fault signal, are plotted in the results of the test cases. Moving average of the position tracking error, disturbance rate and its variance are given including both jammed and not-jammed cases in the same figures. Note that both jamming and unjamming conditions are simulated by cancelling integral gain of the controller. Therefore, developed FDD method is analyzed under proportional controller for all jammed and not-jammed conditions. Disturbance loads of 14kN and 4kN are applied (at t=19s) for the jammed and not-jammed cases, respectively. After the counter load (dis-

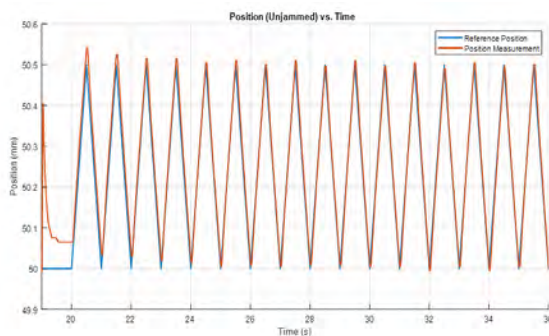


Figure 11. EHA Position Response under the Not-jammed Case for test cases 9.

turbance), the reference position is inserted to the EHA at t=20s. Results are given for just one set of test case (Test Cases 9&10) in the following figures.

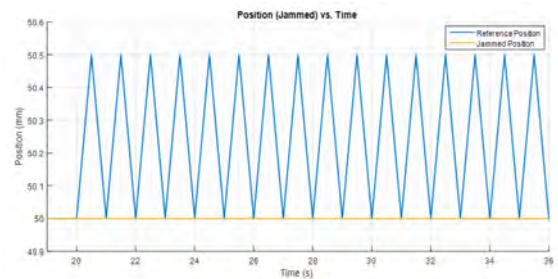


Figure 12. EHA Position Response under the Jammed Cases for test cases 10.

Several remark regarding the given plots for the fault detection and diagnosis of jamming failures are highlighted as follows:

Position responses of the EHA under jammed and not-jammed cases are as expected. Because of the high disturbance load (14kN) the actuator cannot track the given position input as can be seen in Fig. 12. Whereas small tracking error occurs (Fig. 11) for the not-jammed case due to the considerably lower disturbance load (4kN). Note that control system is the same for all jammed and not-jammed cases, so the only difference is created by changing the external disturbance load by means of counter loading and the mechanical locking which have been mentioned before. Rate of the estimated disturbance load seems quite noisy and it is difficult to extract valuable information about the faults from Fig. 13. Therefore, the variance of this disturbance rate is calculated in Fig. 14. There is a quite bit of difference between the jammed cases and the not-jammed ones. High

position tracking errors are inevitable for jamming cases because of the low disturbance rejection characteristics under mechanical locking or counter loading. The deviation between the tracking error for the not-jammed case and the jammed cases is quite large as expected. The fault is identified (Fig. 16) in a considerably small-time interval for this test case because of the high deviations in the indicators (disturbance rate and the tracking error) between jammed and not-jammed conditions. For all of the simulated test cases, developed FDD system gives very similar results for the fault indicators, detection time and deviations between jamming and unjamming conditions. Using the developed FDD method, all of the failure cases could be identified under 1s. It should be noted that detection time of the faults strictly depends on the chosen threshold values in the fault identification step. The higher the threshold value is, the longer it takes the system to identify the jamming cases. In order to be more robust against false alarms, higher threshold might be chosen but this would considerably increase the lag between the occurrence of the error and the detection time. Overall results are summarized in the following table.

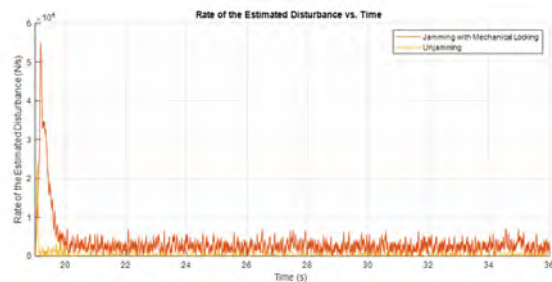


Figure 13. Rate of the Estimated Disturbance for test cases 9 and 10.

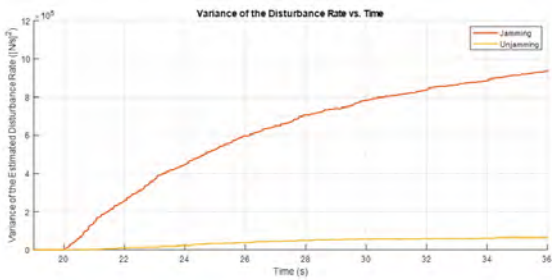


Figure 14. Variance of the Estimated Disturbance Rate for test cases 9 and 10.

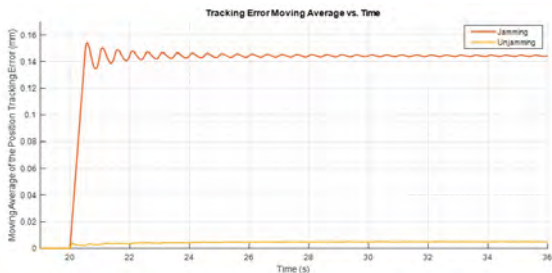


Figure 15. Moving Average of the Position Tracking Error for test cases 9 and 10.

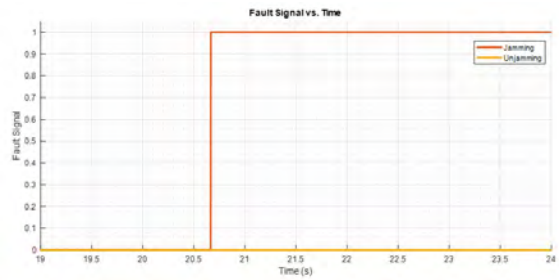


Figure 16. Generated Fault Signal for test cases 9 and 10.

Considering the results provided in Table 4 and 5, a number of comments can be made regarding failure dynamics, fault detection performance and the overall effectiveness of the developed methodology. A single threshold value is selected in the developed FDD algorithm for both the moving average of the tracking error and the variance of the estimated disturbance rate. Yet, a single threshold set could give comparably good detection times. Maximum fault detection time, 0.68s, occurs at the amplitude of 0.25mm. We assumed that an actuator stroke of 0.25mm nearly corresponded to a minimum surface deflection of a typical flight control surface. Since the detection time would decrease as the given input is increased at the time of jamming, this 1.26s of detection time might be considered as the maximum detection time for a jamming failure of a typical flight control surface.

DISCUSSION AND CONCLUSION

In this paper, a threshold-based fault detection and diagnosis (FDD) method is developed for jamming. The method is tested on an experimental setup. In order to estimate the state variables correctly, firstly system dynamics of the EHA is modelled. Then, the state and disturbance observers are designed to estimate both unknown system states and the disturbance load.

The whole FDD method is based on two indicators. One indicator is selected as the variance of the time rate of change of the disturbance. When this variance exceeds a predefined threshold value then the second indicator regarding the fault is checked. This indicator is the moving average of the tracking error. In order to test the performance of the proposed FDD method, a fault scenario is created. Low amplitude sine and sawtooth waves with different frequency values around a specific actuator position are taken as the reference inputs. After considering the results, it is realized that the disturbance rejection characteristics of the actuator has a great influence on the fault detection performance of the designed method. Depending on the disturbance rejection of the actuator, its estimated disturbance rate under the jamming case could diverge rapidly from the not-jammed nominal condition.

Table 4. Summary of the Results for the Sine Wave Inputs.

Test Case	Input Signal	Variance of the Estimated Disturbance ($(N/s)^2$)	Moving Average of the Tracking Error (mm)	Detection Time (s)
1-2	0.25mm Sine	7.2×10^5 – Jammed 6×10^4 – Not jammed	0.09 – Jammed 0.025 – Not-jammed	0.62
3-4	0.50mm Sine	9.1×10^5 – Jammed 5×10^4 – Not jammed	0.17 – Jammed 0.022 – Not jammed	0.51
5-6	1.00mm Sine	10×10^5 – Jammed 5×10^4 – Not jammed	0.28 – Jammed 0.02 – Not jammed	0.47

Table 5. Summary of the Results for the Sawtooth Wave Inputs.

Test Case	Input Signal	Variance of the Estimated Disturbance ($(N/s)^2$)	Moving Average of the Tracking Error (mm)	Detection Time (s)
7-8	0.25mm Sawtooth	6.6×10^5 – Jammed 6.5×10^4 – Not jammed	0.06 – Jammed 0.023 – Not-jammed	0.68
9-10	0.50mm Sawtooth	9×10^5 – Jammed 6×10^4 – Not jammed	0.14 – Jammed 0.02 – Not jammed	0.66
11-12	1.00mm Sawtooth	9.6×10^5 – Jammed 6×10^4 – Not jammed	0.23 – Jammed 0.025 – Not jammed	0.62

At the end, the results are given for one of the test cases with jamming and without jamming Figs 11-16. Faults are successfully detected (Tables 4-5) for all of the jammed cases and no false positives for not-jammed cases. The detection times are quite low, less than one second for each case which is considerably lower than the values achieved by different methods like LPV model-based detection method where the mean detection and identification time of jamming is 3.57s and maximum detection time of 10.65s [6]. Last but not the least, several aspects of this study should be addressed before considering any real time flight control system implementation. First point is that every control surface actuator has its own dynamics with its parameters. Therefore, a high-fidelity actuator model needs to be constructed according to the specific architecture selected for the concerning flight control application. Then, realistic actuator inputs shall be generated through either real pilot inputs or processed inputs via a dedicated flight control computer. Taking these points into consideration, the developed method in this paper might be implemented to a flight control application with minimal modifications.

References

- Zolghadri, A., Cieslak, J., Efimov, D., Henry, D., Goupil, P., Dayre, R., Leberre, H.. Signal and model-based fault detection for aircraft systems. IFAC-PapersOnLine (2015), 48(21), 1096-1101.
- Ossmann, D., & Varga, A. Detection and identification of loss of efficiency faults of flight actuators. Paper presented at the Conference on Control and Fault-Tolerant Systems (SysTol), October, 2013.
- Cieslak, J., Efimov, D., Zolghadri, A., Gheorghe, A., Goupil, P., & Dayre, R. A Method for Actuator Lock-in-place Failure Detection in Aircraft Control Surface Servo-loops. IFAC Proceedings Volumes, 47(3), 10549-10554, 2014.
- Model-Based Approaches for Fast and Robust Fault Detection in an Aircraft Control Surface Servo Loop: From Theory to Flight Tests [Applications of Control]. IEEE Control Systems, 33(3), 20-84, 2013.
- Jayakumar, M., & Das, B. Diagnosis of Incipient Sensor Faults in a Flight Control Actuation System. 2006 SICE-ICASE International Joint Conference, 2006.
- Varga, A., Ossmann, D., Goupil, P., & Sabot, G. Verification and validation of a FDD system for identification of aircraft control surface jamming*. IFAC Proceedings Volumes, 46(19), 84-89, 2013.
- Narendra, K., Balakrishnan, J., Adaptive control using multiple models. IEEE Trans. Automat. Control 42, 171-187, 1997.
- Çalışkan, H., Balkan, T., and Platin, B. E. "A Complete Analysis and a Novel Solution for Instability in Pump Controlled Asymmetric Actuators." ASME. J. Dyn. Sys., Meas., Control. September, 137(9): 091008, 2015.
- H. Çalışkan. "Development and Control of a Single Rod Electro Hydrostatic Actuator" Ph.D. Thesis, Middle East Technical University, Mechanical Engineering Department, 2015.
- Won, D., & Kim, W. Disturbance Observer based backstepping for position control of electro-hydraulic systems. International Journal of Control, Automation and Systems, 13(2), 488-493, 2015.
- W. Chen, D. Balance, P. Gawthrop, and J.O'Reilly. "A nonlinear disturbance observer for robotic manipulators," IEEE Trans. Ind. Electron., vol. 47, no. 4, pp. 932-938, 2000.
- Maré Jean-Charles. Aerospace Actuators 1 Needs, Reliability and Hydraulic Power Solutions. UK, 2016.
- Welford, B.P. Note on a method for calculating corrected sums of squares and products. Technometrics, 4, 419-420, 1962.
- H. U. Akova. "Design, Construction and Control of an Electro-Hydraulic Load Simulator for Testing Hydraulic Drives," M.Sc. Thesis, Middle East Technical University, Mechanical Engineering Department, 2014.

Reinforcement of Na-Alginate Based Films with Carrot Juice Processing Wastes

Hulya Cakmak¹  Fatma Unal² 

¹Hitit University, Department of Food Engineering, Corum, Turkey

²Hitit University, Department of Metallurgical and Materials Engineering, Corum, Turkey

ABSTRACT

In this study, Na-alginate based films were produced with the addition of cellulosic fibres from carrot juice processing wastes for employment of agricultural wastes as reinforcing agent in biobased films for food packaging purposes. These films were characterized by water vapour permeability (WVP), colour, XRD, transmittance and the SEM analysis. The WVP of the Na-alginate based films were significantly decreased upon the addition of carrot fibre at each level of incorporation (1% and 5%, w/w on alginate basis). Depending on the colour values, the obtained films were highly transparent, but the yellowness of the 5% carrot fibre film (CFF) was significantly higher than control (0% CFF) and 1% CFF samples ($p < 0.05$). The transmittance of control film was higher than the carrot fibre added films, since the lower light impermeability of 5% CFF was notable in the visual observations and the SEM images. The results revealed that the obtained carrot fibre cellulosic material may be used as reinforcing agent in biobased films for food packaging applications.

Keywords:

Carrot pulp; Alginate; Edible film; Food packaging; Waste.

INTRODUCTION

Alginate is naturally found in the structure of brown microalgae and composed of D-mannuronate and L-guluronate monomers [1, 2, 3]. It is water-soluble and biodegradable polysaccharide that has film-forming ability thus can be utilized in bio-based film formulations for food packing applications [1, 4, 5]. By having a hydrophilic matrix, alginate has a poor resistance to water vapour, therefore either cross linking with the polyvalent ions or reinforcement with cellulosic fibres for improving the water barrier and mechanical properties is recommended in the literature [1, 2, 6, 7, 8].

Nanocellulose addition to the Na-alginate based films at 5% rate improved the WVP and the tensile strength was also increased at the same nanocellulose enrichment level [9]. However, the cellulose fibres and cellulose nanowhiskers that were extracted from mulberry pulp addition to Na-alginate based films had different impact on mechanical and water barrier properties [8]. The cellulose nanowhiskers at each reinforcement level had higher tensile strength and elastic modulus compared to the control film, while the cellulose fibre addition had a negative effects on these mechanical parameters. Both of these cellulosic sources did not improve

the water vapour permeability (WVP), however cellulose nanowhiskers reinforced films had significantly lower WVP than the cellulose fibre added films. Similar to this study, Sirviö et al. [10] had studied the effects of nanofibrillated cellulose extracted from birch pulp on the mechanical and water barrier properties of alginate based films. The tensile strength and elastic modulus of the films were improved when compared with the pristine alginate films up to 10% reinforcement level, but WVP of nanofibrillated cellulose reinforced films were similar with the control film.

Agro-industrial wastes especially from fruit and vegetable processing by-products mainly composed of cellulosic fibres, and recently these wastes are taking part in the biodegradable packaging film formulations as novel and "green" alternatives for mechanical reinforcement and improvement of barrier properties of films [7, 11, 12, 13]. For example, seaweed based films that were reinforced with microcrystalline cellulose extracted from bamboo had better mechanical and water barrier properties compared to neat seaweed films [14]. Also, nanofibrillated cellulose extracted from sugar palm wastes were incorporated into the sugar palm starch films, and the tensile strength and modulus values were

Article History:

Received: 2020/03/20

Accepted: 2020/06/30

Online: 2020/09/30

Correspondence to: Hulya Cakmak,
Hitit University, Food Engineering, 39030,
Corum, TURKEY

E-Mail: hulyacakmak@hitit.edu.tr

Phone: +90 364 227 43 33

Fax: +90 364 227 45 35

improved with respect to sugar palm fibre addition [13]. In recent studies, carrot pulp was also employed in the biobased pectin or HPMC films in order to improve the mechanical properties of the films as well as functional properties like hydration and antioxidant capacity [7, 12].

The aim of this article was to investigate the effect of carrot pulp cellulose addition into the Na-alginate based films on water vapour permeability and characterization of the obtained films was carried out by using spectroscopic (colour), optical (transmittance), morphological (SEM) and crystalline structure (XRD) analysis.

MATERIAL AND METHODS

Materials

Na-alginate with 99% purity (Protanal PH 6160, FMC International, Ireland) was kindly supplied from FMC International. Depending on the specifications given by the supplier, the sample had 12.4% moisture, 24.7% d.b. ash, while 99.92% of alginate powder diameter was smaller than 180 μm . HCl (37-38%, Merck KGaA, Germany), NaOH (99%, Tekkim Kimya San. Tic., Bursa), K_2CO_3 (99.6%, JT Baker Chemical Co., Phillipsburg) and glycerin (99.5%, Smart Kimya Ltd. Sti., Izmir) was supplied from local distributors.

Extraction of Carrot Fibre

The fresh carrots were washed with tap water and hand-peeled. Following the slicing into 3 cm thickness, the juice and the pulp of carrots were separated by the juice extractor (Arzum Multivit AR 1060, Turkey). The excessive juice remained on the separated pulp was drained with a sieve and it was heat treated at 95°C for 5 min for enzyme inactivation, then air dried at 70°C for 8.5h in an oven (Memmert, UN 55, Germany). Dried carrot pulp was crushed with a hammer mill (Brabender, SM3, Germany), and the fibres passing through 355 μm sieve was used in further extraction step. The cellulosic material extraction from carrot was carried out according to the study of Manzato et al. [15], Sogut and Cakmak [16] with minor modifications.

8 g of dried carrot pulp with 1:30 (w/v) of 20% (w/v) NaOH was autoclaved at 135°C for 30 min (Alp, CL 40M, Japan). Prior to the centrifugation, the mixture was neutralized using 0.1 M HCl. 30 ml of this neutralized extract was centrifuged at 20°C 4000 rpm for 2 min (Sigma 3-30K, Germany). Approximately 20 ml of supernatant was discarded and replaced with tridistilled water, and this step was repeated for 10 times until a clear supernatant was obtained. The

insoluble cellulosic precipitate from carrot was dried at 60°C for 24 h in a universal oven (Memmert, UN 55, Germany).

Preparation of Films

Na-alginate based films were prepared by solvent casting method. 1% (w/w) Na-alginate powder was mixed with distilled water for 3h at 65°C with a magnetic stirrer (Wisd, MSH20A, Korea). After the mixture was completely homogenized, 25% (w/w, on alginate basis) glycerol was mixed with the alginate solution for 1h at the same conditions. 20 ml of prepared mixture was poured into the PET petri dishes ($\varnothing=90$ mm), and then allowed to dry at 40°C for 48 h in an oven (Memmert, UN 55, Germany). The dried films were peeled from the petri dishes and further used in the analysis.

Carrot fibre added films were produced similarly to the control film, 1% or 5% (w/w, on alginate basis) carrot fibre was weighed into the beaker that contained distilled water with Na-alginate powder and they were mixed for 3h at 65°C with a magnetic stirrer (Wisd, MSH20A, Korea). Then the rest of the procedure was repeated.

Water Vapour Permeability (WVP) Measurement

The WVP of films were measured according to the method of Huang et al. [17] with some modifications. One third of the plastic test cups were filled with distilled water and the specimen was tightly attached to the lid which was open to the testing chamber. The test cups then placed in a desiccator conditioned to 43% RH and 25°C with saturated K_2CO_3 solution. The test cups were weighed with an analytical balance (Precisa Gravimetrics, XB220A, Switzerland) every 1 h for total of 24 h in order to determine the mass change depending on the relative humidity difference. The slope of the mass change versus time graph (g/h) was obtained and WVTR was calculated by dividing the slope to the film area open to the testing environment. WVP (g/kPa.h.m) was calculated according to the following formulae;

$$WVP = \frac{WVTR \times d}{P(R_c - R_e)} \quad (1)$$

here d is the thickness of film (m), P is the saturated water vapour pressure (kPa) at 25°C, R_c is relative humidity inside the test cup and R_e is relative humidity inside the conditioned environment of desiccator.

The thickness of the films was measured with a calliper from randomly selected five different points of the films and the averages of them were reported.

Table 1. Thickness, WVP and colour values of films.

Sample*	Film thickness (μm)	WVP (g/kPa.h.m)	L*	a*	b*
CF	44.30 \pm 5.30 ^a	3.777 \times 10 ⁻⁶ \pm 8.955 \times 10 ^{-8c}	96.82 ^b	-0.24 ^b	2.86 ^a
1% CFF	46.30 \pm 5.20 ^a	1.961 \times 10 ⁻⁶ \pm 9.498 \times 10 ^{-8a}	96.68 ^b	-0.28 ^a	2.93 ^a
5% CFF	53.30 \pm 5.00 ^b	2.235 \times 10 ⁻⁶ \pm 1.175 \times 10 ^{-8b}	96.00 ^a	-0.22 ^b	3.64 ^b

*-c Different letters in the same column are significantly different (p<0.05).

*CF: control film (pure alginate), 1% CFF: 1% carrot fibre film, 5% CFF: 5% carrot fibre film.

Colour Measurement

The colour of the films were measured with a spectrophotometer (Konica Minolta, CM3600D, Japan) using CIE L* a* b* colour scale. In this scale, the lightness is represented by L* (0: black, 100: white), while +a*/-a* is redness/greenness, and +b*/-b* is yellowness/blueness. The standard white calibration plate was used as a background for the films [8].

XRD Analysis

X-ray diffraction (XRD) patterns with monochromatic Cu K $_{\alpha}$ radiation ($\lambda=0.15406$ nm) at 40 kV and 40 mA were recorded in the 2 θ angle range from 10 $^{\circ}$ to 90 $^{\circ}$ with a scan step of 0.05 $^{\circ}$ using an X-ray diffractometer (Philips, PW3710 XPert Pro, The Netherlands). From using XRD patterns, the average crystallite size calculations were made by using the following Debye-Scherrer formula [15];

$$D = \frac{k\lambda}{\beta_D \cos\theta} \quad (2)$$

where k is a constant (0.91), λ is wavelength of the X-ray source (0.15406 nm), D is average crystallite size, β_D is the peak width at half-maximum intensity and θ is the peak position.

Crystallinity index (CI) values of the samples were calculated using the following formula after the peak areas were measured from the peak fitting [18];

$$CI\% = (A_{crystalline} / A_{total}) \times 100 \quad (3)$$

where $A_{crystalline}$ is the area of crystalline diffractogram and A_{total} is the total area of the original diffractogram.

Transmittance of The Films

Transmittance spectra of the films between 300-800 nm with 1 nm step size were recorded by using UV-Vis-NIR spectrophotometer (Shimadzu, UV-3600 with an integrated ISR 3100 sphere attachment, Japan).

Film Morphology

The surface of the films and the carrot fibre were evaluated with a scanning electron microscope (Quanta 450

FEG, Oregon, USA) under low vacuum conditions at 2 kV accelerating voltage. The samples were sputter coated with gold for 60 sec. at 5 mA sputter current, and the film sample was mounted on the sample holder with double-sided tape. The images were recorded between the magnification levels of 1500 \times to 10000 \times .

Statistical Analysis

The statistical differences between the obtained results were compared with SPSS vers. 16.0 (SPSS Inc., USA) with one-way ANOVA Duncan multiple comparison test at 95% significance level.

RESULTS AND DISCUSSION

Water Vapour Permeability

The WVP of control and carrot fibre added films were given in Table 1. The neat alginate film (CF) had the highest WVP, while the incorporation of 1% and 5% carrot fibre improved the WVP significantly (p<0.05). The polysaccharide based films, especially alginate has a hydrophilic nature, and therefore the WVP of the alginate films were not comparable to the petroleum based plastic film counterparts [10]. However, the addition of carrot fibre into Na-alginate matrix enhanced the neat film structure against the water vapour diffusion by creating a barrier to the water molecules that were trapped in the matrix [19]. Similar results were observed in the literature, the micro cellulose or nanocellulose fibre addition to the neat alginate films decreased the WVP by creating a tortuous pathway to the water molecule transport [8, 9, 10, 14, 16]. Both of the filler contents acted as a barrier against water vapour transport; however the WVP of 1% CFF were significantly lower compared to the 5% CFF independent of the average film thickness (Table 1). The reduction of WVP with added fillers is associated with well dispersion of filler inside the matrix, although there is a limit for addition of cellulosic filler [6]. Over this limit, the filler may be agglomerated inside the matrix which leads to the stagnation of WVP reduction or even cause an increase the water vapour transmission [6, 9, 16]. Therefore, higher WVP of 5% CFF might be associated with the agglomeration of carrot fibre inside the matrix.

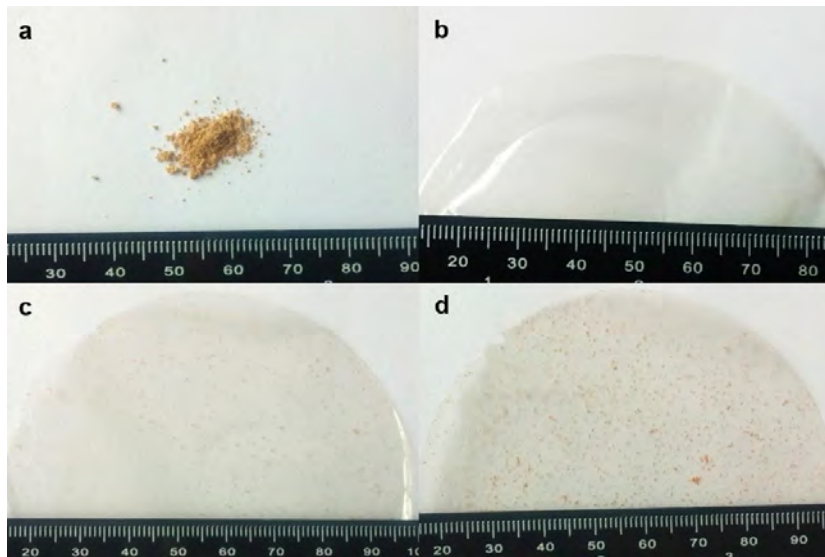


Figure 1. The images of a: carrot fibre, b: CF, c. 1% CFF, d. 5% CFF samples.

Colour of The Films

The surface colour values of the films are given in Table 1. The L^* values that are close to 100 represents the highest transparency, therefore the lightness observation is crucial for film transparency observation. Besides, the incorporation of cellulosic fibre at micro or nano scale may increase the haze and decrease the transparency regardless of source of cellulosic fibre or the type of matrix [10, 19, 20]. L^* of the films were quite closer to the 100, and highly transparent with respect to their visual appearance (Fig. 1), while the 5% CFF had the lowest lightness compared to neat alginate and 1% CF films. This could be due to the light hindrance effect of carrot fibres

in the alginate, especially at the 5% level by possible inhomogeneous distribution of the filler within the matrix [8]. Besides, the highest yellowness was obtained from 5% CFF ($p < 0.05$). This observation was also in agreement with the study of Wang et al. [8] upon the mulberry pulp cellulose addition into alginate-based films. However, the yellowness of corn starch-based films with carrot fibre fillers did not increase significantly by increasing the fibre amount from 20% to 40% [19]. Therefore, the change in colour values might be related to the colour of the matrix, the source of cellulose, particle diameter and shape of the cellulosic fibre and film production method [7, 8, 19].

XRD and Transmittance of The Films

The diffraction peaks at $2\theta \approx 13^\circ$ and 16° were observed in XRD patterns (Fig. 2). The peaks at 13.94° and 16.73° were characteristic diffraction peaks of Na-alginate and cellulose, respectively [9, 21, 22]. It was observed that the intensity of the peak around 16° increased with the increasing the amount of carrot fibre and the peak intensity around 13° decreased with the increasing amount of carrot fibre. This behaviour indicates that the Na-alginate matrix had a good interaction with the carrot fibre filler.

Crystallinity index values of control, 1% CFF and 5% CFF films were 32%, 41% and 45% respectively. Crystallite size values obtained by Debye-Scherrer formula were calculated as 9, 10 and 12 nm for control film, 1% CFF and 5% CFF samples, respectively. The addition of carrot fibre and the increment of the fibre amount in the film resulted in an improvement of crystallinity. Increased crystallinity is important for the packaging films, since it provides more permeability to water vapour and other gases [10, 11]. It was observed that the water vapour permeability values were in

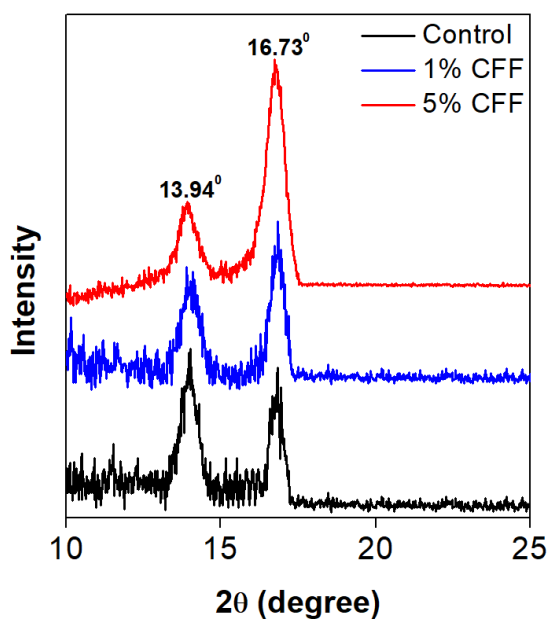


Figure 2. XRD patterns of control film, 1% CFF and 5% CFF samples.

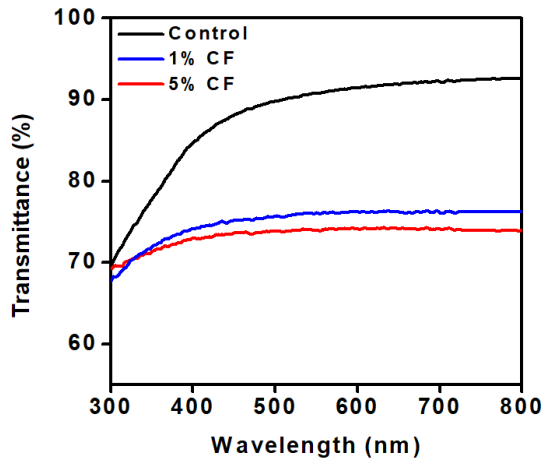


Figure 3. Transmittance curves of control film, 1% CFF and 5% CFF samples.

accordance with the crystallinity results. The water vapour permeability values decreased with the increasing crystallinity due to the increment of fibre content in the film.

Transmittance versus wavelength values was given in Fig. 3. The optical transmittance value at 800 nm of the films decreased from 92.7% to 74.1% by increasing the carrot fibre content from 0% to 5% wt. The loss in optical transmittance value may be due to the reflection and/or scattering of light at the interface of the fibres. As the amount of fibre in the structure increases, the optical transmittance value

decreases as expected; this indicates that the incoming light is reflected and/or scattered more because the interface was increased. Transmittance values were compatible with previous studies, transmittance values of composite films reinforced with the modified ramie fibres and composite films with microcrystalline cellulose particles decreased with increasing fibre/particle content because of the light reflected and/or scattered at the interface [17, 21].

Surface Morphology of The Films

SEM images of carrot fibre and the films were given in Fig. 4. There are no cracks or voids found on the surface of the film samples. In accordance with the visual observations of the films (Fig. 1), the surface of 5% CFF sample (Fig. 4d) had some irregularities and roughness. The inhomogeneous particle diameter distribution was also present in the images of both the fibre and the fibre added samples. There are also some micron level bubbles visible on the surface of each film; however the surface of control film had more homogeneous structure without any observable porosity. Depending on the addition of carrot fibre especially at the highest level, homogeneous dispersion of fibre might be hindered [6, 9, 19]. The more homogeneous structure of 1% CFF sample was also confirmed by the results of WVP, that the well dispersed particles inside the alginate matrix had limited the water vapour permeability [19].

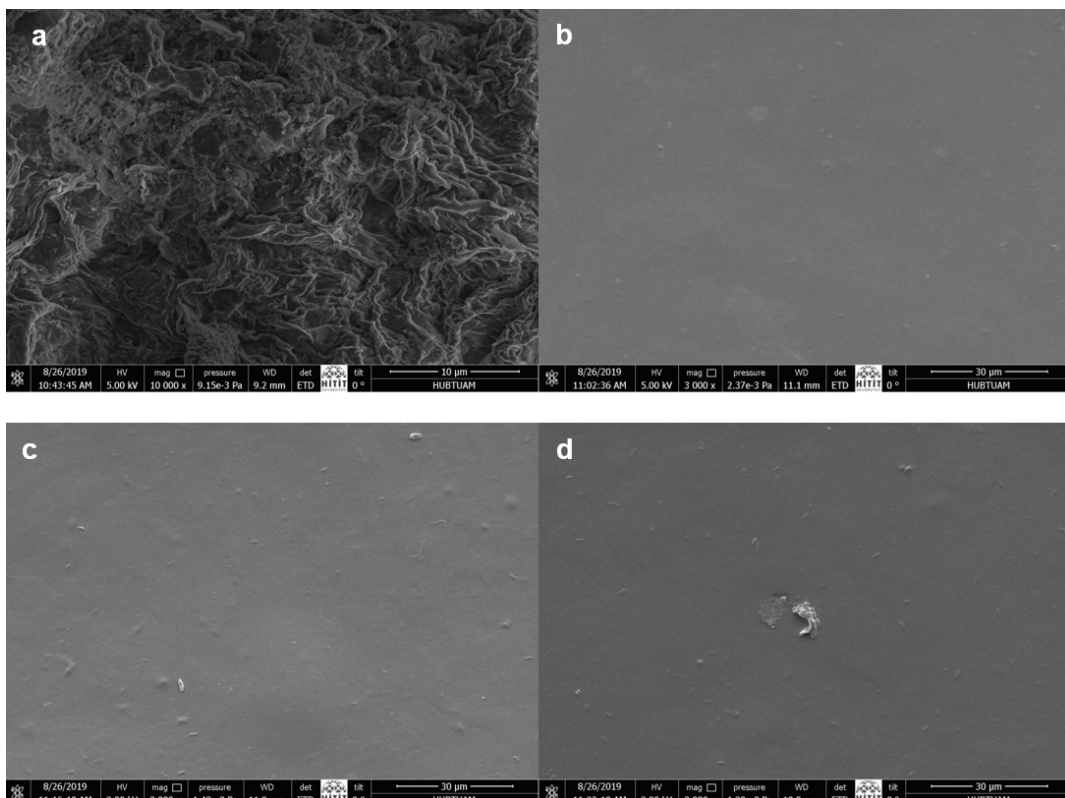


Figure 4. SEM micrographs of (a) carrot fibre at 10000x scale, (b) CF, (c) 1% CFF and (d) 5% CFF at 3000x scale.

CONCLUSION

The current efforts in food packaging application are based on decreasing the environmental burden of plastic films. Completely bio-based films are characterized and further developed as sustainable and environmental friendly alternatives of petroleum based food packaging materials. Therefore, this study is mainly focused on utilizing the carrot juice processing residues as cellulosic filler in the alginate-based films.

The addition of the carrot fibre into the Na-alginate based films improved the film structure against the water vapour permeability; however 5% (w/w, on alginate basis) CF films had higher WVP compared to 1% (w/w) carrot fibre films. The colour and the transmittance values of the 5% CFF were significantly different from the control and 1% CFF ($p < 0.05$). Depending on the SEM images, each film had no cracks or pores on the surface, besides there were some irregularities visible on the 5% CFF sample depending on the variability of particle diameter distribution of carrot fibre and possible agglomeration behaviour of fibre at 5% level.

These findings show us that the carrot juice processing wastes as cellulosic fibre resource had a potential to be used in biobased films by enhancing the film properties. However, further studies may focus on mechanical fractionation of the obtained carrot fibres for obtaining much lower particle diameter with homogeneous diameter distribution.

ACKNOWLEDGEMENT

The authors would like to thank Prof. Dr. Kursat Kazmanli for his help in characterization studies.

References

- Maizura M, Fazilah A, Norziah MH, Karim AA. Antibacterial activity and mechanical properties of partially hydrolyzed sago starch-alginate edible film containing lemongrass oil. *Journal of Food Science* 72(6) (2007) C324-C330.
- Benavides S, Villalobos-Carvajal R, Reyes JE. Physical, mechanical and antibacterial properties of alginate film: Effect of the crosslinking degree and oregano essential oil concentration. *Journal of Food Engineering* 110(2) (2012) 232-239.
- Bierhalz ACK, da Silva MA, Kieckbusch TG. Natamycin release from alginate/pectin films for food packaging applications. *Journal of Food Engineering* 110(1) (2012) 18-25.
- Rhim JW. Physical and mechanical properties of water resistant sodium alginate films. *LWT-Food Science and Technology* 37(3) (2004) 323-330.
- Tavassoli-Kafrani E, Shekarchizadeh H, Masoudpour-Behabadi M. Development of edible films and coatings from alginates and carrageenans. *Carbohydrate Polymers* 137 (2016) 360-374.
- Abdollahi M, Alboofetileh M, Behrooz R, Rezaei M, Miraki R. Reducing water sensitivity of alginate bio-nanocomposite film using cellulose nanoparticles. *International Journal of Biological Macromolecules* 54 (2013) 166-173.
- Encalada AMI, Basanta MF, Fissore EN, De'Nobili MD, Rojas AM. Carrot fiber (CF) composite films for antioxidant preservation: Particle size effect. *Carbohydrate Polymers* 136 (2016) 1041-1051.
- Wang LF, Shankar S, Rhim, JW. Properties of alginate-based films reinforced with cellulose fibers and cellulose nanowhiskers isolated from mulberry pulp. *Food Hydrocolloids* 63 (2017) 201-208.
- Huq T, Salmieri S, Khan A, Khan RA, Le Tien C, Riedl B, Fraschini C, Bouchard J, Uribe-Calderson J, Kamal MR, Lacroix M. Nanocrystalline cellulose (NCC) reinforced alginate based biodegradable nanocomposite film. *Carbohydrate Polymers* 90(4) (2012) 1757-1763.
- Sirviö JA, Kolehmainen A, Liimatainen H, Niinimäki J, Hormi OE. Biocomposite cellulose-alginate films: Promising packaging materials. *Food Chemistry* 151 (2014) 343-351.
- Zain NM, Yusop SM, Ahmad I. Preparation and characterization of cellulose and nanocellulose from pomelo (*Citrus grandis*) albedo. *Journal of Nutrition & Food Sciences* 5(1) (2014) 334.
- Otoni CG, Lodi BD, Lorevice MV, Leitão RC, Ferreira MD, de Moura MR, Mattoso LH. Optimized and scaled-up production of cellulose-reinforced biodegradable composite films made up of carrot processing waste. *Industrial Crops and Products* 121 (2018) 66-72.
- Ilyas RA, Sapuan SM, Ibrahim R, Abrial H, Ishak MR, Zainudin ES, Atikah MSN, Nurazzi NM, Atiqah A, Ansari MNM, Syafri, E, Asrofi M, Sari HS, Jumaidin R. Effect of sugar palm nanofibrillated cellulose concentrations on morphological, mechanical and physical properties of biodegradable films based on agro-waste sugar palm (*Arenga pinnata* (Wurmb.) Merr) starch. *Journal of Materials Research and Technology* 8(5) (2019) 4819-4830.
- Hasan M, Lai TK, Gopakumar DA, Jawaid M, Owolabi FAT, Mistar EM, Alfatah T, Noriman NZ, Haafiz MKM, Khalil HA. Micro crystalline bamboo cellulose based seaweed biodegradable composite films for sustainable packaging material. *Journal of Polymers and the Environment* 27(7) (2019) 1602-1612.
- Manzato L, Rabelo LCA, de Souza SM, da Silva CG, Sanches EA, Rabelo D, Mariuba LAM, Simonsen J. New approach for extraction of cellulose from tucumã's endocarp and its structural characterization. *Journal of Molecular Structure* 1143 (2017) 229-234.
- Sogut E, Cakmak H. Utilization of carrot (*daucus carota* L.) fiber as a filler for chitosan based films. *Food Hydrocolloids* 106 (2020) 105861 <https://doi.org/10.1016/j.foodhyd.2020.105861>.
- Huang X, Xie F, Xiong X. Surface-modified microcrystalline cellulose for reinforcement of chitosan film. *Carbohydrate Polymers* 201 (2018) 367-373.
- Park S, Baker JO, Himmel ME, Parilla PA, Johnson DK. Cellulose crystallinity index: measurement techniques and their impact on interpreting cellulase performance. *Biotechnology for Biofuels* 3(1) (2010) 10.
- Guimarães IC, dos Reis KC, Menezes EGT, Rodrigues AC, da Silva TF, de Oliveira IRN, Boas EVDBV. Cellulose microfibrillated suspension of carrots obtained by mechanical defibrillation and their application in edible starch films. *Industrial Crops and Products* 89 (2016) 285-294.
- Ramesh S, Radhakrishnan P. Cellulose nanoparticles from agro-industrial waste for the development of active packaging. *Applied Surface Science* 484 (2019) 1274-1281.
- Yang Q, Lue A, Zhang L. Reinforcement of ramie fibers on regenerated cellulose films. *Composites Science and Technology* 70(16) (2010) 2319-2324.
- Alshhab A, Yilmaz E. Sodium alginate/poly (4-vinylpyridine) polyelectrolyte multilayer films: Preparation, characterization and ciprofloxacin HCl release. *International Journal of Biological Macromolecules* 147 (2020) 809-820.

Effects of Soil Geotechnical Properties on the Prediction of Optimal Dimensions of Restricted Reinforced Concrete Retaining Walls

Aylin Ece Kayabekir¹  Zülal Akbay Arama¹  Gebrail Bekdas¹  İlknur Dalyan² 

¹Istanbul University-Cerrahpasa, Department of Civil Engineering, Istanbul, Turkey

²Ministry of Interior Disaster and Emergency Management Presidency, Presidential of Earthquake Department, Ankara, Turkey

ABSTRACT

The aim of this paper is to investigate the effects of soil properties associated with the project requirements and environmental conditions, on the prediction of the design dimensions of L-Shaped restricted reinforced concrete retaining walls by the use of optimization algorithms. Numerous parametric analysis was conducted with Flower Pollination Algorithm to examine the influence of soil geotechnical properties such as internal friction angle and unit weight. The backfill soil, surrounding earth and foundation soil was modelled same and assumed to be comprised of granular soils for modelling. Additionally, dual effects of external surcharge load application and excavation depth change was also analyzed against the change of soil properties. As a result, the change of the retaining wall height and the foundation base width has been discussed and the achievement of the cost-effective optimized sizing of the system has been obtained. Finally, the design differences caused by the changes in soil properties have been revealed and the practicalness of the use of the optimization algorithms for the design of restricted type of retaining walls are shown.

Keywords:

Soil properties, Granular soils, L-Shaped retaining walls, Flower Pollination Algorithm, Optimization

Article History:

Received: 2020/03/24

Accepted: 2020/08/04

Online: 2020/09/30

Correspondence to:

Zülal Akbay Arama,

Department of Civil Engineering, Istanbul

University-Cerrahpaşa, Istanbul

Tel: +90 553 266 4880

E-Mail: zakbay@istanbul.edu.tr

INTRODUCTION

Reinforced concrete retaining walls are the most preferred type of supporting structures that are constructed in order to resist lateral soil forces, especially activated due to the excavation works which the soil properties of the construction field cannot permit to hold the unbalanced soil mass with slopes. The shape and dimensions of the retaining wall system can be changed due to the project requirements, soil conditions, land ownership situation, infrastructure locations or environmental restrictions and it can be essential to build the sections of the wall with restrictions. The most known type of restricted reinforced concrete retaining walls is L-shaped type. L-shaped retaining walls (LSRW) are generally used for simple loading applications where the foundation length is extended only on the heel side of the wall. In this study, the mentioned L-Shaped type of reinforced concrete retaining walls was considered due to the preferability rather than other restricted type of supporting structures, according to the easiness of their construction works, the attainability of used materials and easiness of the mobilization of necessitated equipment for construction. The design process of

the L-shaped retaining walls is being divided into two main steps as geotechnical and structural, similar with other non-restricted types. The control of stability requirements like sliding, overturning and bearing capacity adequateness, forms geotechnical part of the design process. But in order to perform stability calculations, pre-design has to be done generally according to the suggested sizing by well-accepted literature sources [1]. These pre-design methods envisage some restrictions to the structural sections of the wall and require to control if the stability necessities are supplemented. Trial and error method is used to check all proposed walls sizing at pre-design step and this recalculation loop leads loss of time [2].

Because not only the dimensions of the system will be the variants of the stability analysis of the first design stage, but also the geotechnical properties of soil conditions will change the necessitated sizing. The achievement of soil geotechnical properties is associated with the existence and interpretation of site investigations [3]. But only for the construction of such simple structures like retaining walls, it is a common application all over

the world not to do a soil survey to reduce expenses for the constructions or it will not be possible to obtain the essential parameters of the design directly with the performed tests. This condition directs designers to predict soil properties with the use of existing site investigations or to use envisaged upper and lower limits of defined values of soil properties by well-known sources of literature or to use empirical relationships [1, 4]. In this context, the recalculation loop that is performed at the first step of the pre-design will be grown up and unexpected additional analysis will have to be done to find optimum sizing and cost balance. On behalf of to reduce these undesired additional analysis, it has been a significant factor to acquire proper geotechnical conditions representing the general characteristics of encompassing earth of the wall. At the second step of the design, it is being necessary for the wall sections to ensure enough shear and moment capacities and besides this the steel reinforcement must satisfy the proper code requirements to obtain structural design adequateness [5]. According to the pre-design procedure of the retaining walls, it will be hard to achieve the proper stability conditions against conceivable sizing for restricted type. Because the lack of one of the structural part of the wall leads to decrease the resisting forces [6]. In addition to this condition, necessitation to the extension of the wall heel is being arose. In such a case, the construction of L-Shaped walls caused to be chargeable. Therefore, new techniques are developed based on the advancing information and computer technologies to design retaining walls, considering the optimization of sizing and cost. Optimization methods are one of the technique that is used to design retaining walls effectively and nowadays there performed lots of studies to possess the most useful and cost-effective method to design wall systems [7, 8, 9, 10, 11, 12]. In this study, an optimization algorithm is used to predict optimum dimensions of L-Shaped retaining walls via minimum cost achievement against the change of soil geotechnical properties. The main theme of the study is to investigate the effects of the soil geotechnical properties individually and calculate the rate of influence on the de-

sign with dual comparisons. For that purpose, the effects of the loading conditions and excavation depth is also taken into consideration as secondary influence parameters and 105000 different analysis cases are conducted with Flower Pollination Algorithm (FPA). In the analysis, the surrounding soil was assumed to be sandy and its shear strength is represented by the existence of only internal friction angle. The unit weight of soil was evaluated as other definer parameters of soil conditions to reach the minimum value of the safety of static limit equilibrium analysis. The results of the optimization analyses are estimated according to the change of foundation base width and thickness respectively. Consequently, it is shown that the internal friction angle is the most significant geotechnical parameter in the design of retaining walls for the fictionalized structures that are embedded in sandy soils. The width and thickness of the wall base are both affected by the change of internal friction and also the dual effect of the increase of the external load and excavation depth raises the wall sizing significantly. The unit weight of the soil affects the width of the base but has little influence on the thickness. The results of the optimization analyses show that L-Shaped restricted walls are not proper to resist lateral earth pressures which are caused because of bigger than 9 meters deep excavations.

MATERIAL AND METHODS

In the context of this study, reinforced concrete retaining walls are taken into consideration to designate the restrictions of construction that are caused by the variety of soil geotechnical properties against the achievement of quick and cost effective design. The retaining wall system was assumed to be L-Shaped and restricted by the absence of a foundation toe. The structural elements of a standard type of retaining wall and an L-Shaped retaining wall is shown in Fig. 1 for comparison. It can be clearly seen from Fig. 1 that the absence of wall toe causes to reduce resisting wall forces that is acting according to the weight of the wall base. H , represents the height of the wall stem; h , is the excavation depth and D_f , is the thickness

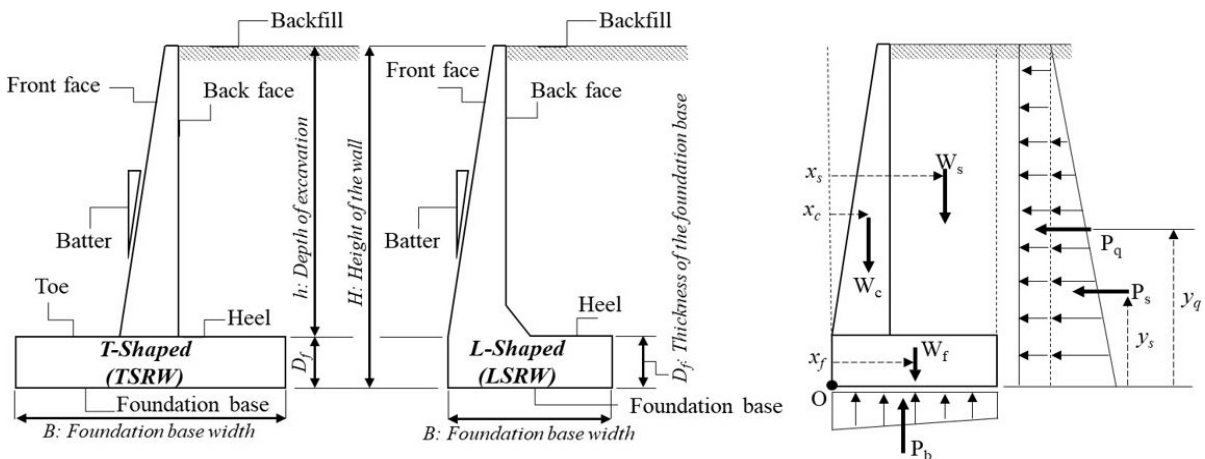


Figure 1. The structural parts of T-Shaped (TSRW) and L-Shaped (LSRW) reinforced concrete retaining walls

of foundation base in Fig. 1. The generated pressures and related forces that are acting on the wall system and the distances to "O" turning point are given in Fig.1. W_c and W_f is the weight of the wall stem and the foundation base and x_c and x_f is the horizontal distances of the mentioned weights to the O point respectively. W_c and W_f can be calculated by the multiplication of unit weight of concrete with the dimensions of the related sections according to plain strain condition. W_s is the weight of the backfill soil retained on the heel of the foundation and x_s is the lateral distance of this weight to O point. W_s can be calculated by the multiplication of the unit weight of the backfill soil (γ_s is the unit weight of the surrounding soil for this study) with the cross-section of backfill material that is retained on the heel of the wall. P_b is the average value of foundation base pressures acting at the center of the gravity of foundation. P_s is the lateral active soil force and P_q is the lateral reflection of applied vertical surcharge loading. y_s and y_q represents the vertical distance of active soil force and lateral surcharge loading to the moment point O. The achievement of lateral reflection of vertical loadings like surcharge or the calculation of lateral soil forces can be determined by the use of earth pressure theories that are proposed by several researchers [13, 14, 15]. The Rankine earth pressure theory has been preferred to be used to calculate the lateral earth coefficients in this study because of its simple form containing only the effect of internal friction angle [14]. K_a is the active lateral earth pressure coefficient that can be determined by a function of internal friction angle ($K_a = \tan^2[45-\Phi/2]$). K_a is used for the calculation of lateral value of affected active forces like $P_s=0.5H^2\gamma_s K_a$. The term γ_s is used for representing the unit weight of the soil and it is evaluated as a variant of this study. P_q is the lateral effect of the applied vertical infinite surcharge load like q and it can be calculated by the use of K_a ($P_q = K_a q$). According to the calculated forces and moments, the wall structure has to be controlled against sliding, overturning stability safety and bearing capacity adequateness.

Lateral active forces can lead the wall to slide lengthwise of the base but on the contrary situation, the self-weight of the wall tries to resist to ensure stability. The division of the whole lateral resisting forces to the active forces has to be procured enough safety for sliding ($SF_{sliding}$). Besides sliding safety research, the existence of unbalanced active and passive forces in a structure causes to enforce the system to turn about its toe point (point "O" in Fig. 1) so another component of safety has born and it is called overturning ($SF_{overturning}$). The division of moments induced by resisting forces to the moments induced by sliding forces gives the degree of overturning safety. The third ingredient of safety is bearing capacity research. The bearing capacity failure has to be checked with the division of ultimate bearing pres-

sure to the maximum mobilized soil pressure through the base foundation of the wall. The limits of ultimate bearing pressure of the base of the wall can be determined by the use of traditional equations of shallow foundation ultimate bearing capacity calculations [16, 17, 1, 3]. The obtainment of the stability against the mentioned three stages allows to continue designing with regard to structural necessities. In the context of this research, all the design steps of the wall are controlled by the use of Flower Pollination Algorithm (FPA) with the analysis performed by Matlab Software. The algorithm is a population-based metaheuristic algorithm confirmed for its simple formulation and the effectiveness in terms of computational performance [18, 19]. The logic of the Flower Pollination Algorithm is based on the evolutionary mechanism of biological flowering plant systems via pollination either biotic or biotic and developed by Yang (2012). Abiotic pollination happens at short distances so a local pollination mechanism is noted. Biotic pollination is eased by the pollinators like bees and butterflies that can travel long distances during their routine circulation. Here-with the method is utilized as a global pollination procedure. Flower constancy can be evaluated as the other significant property of the algorithm. Actually the pollinators have a direct tendency to choose certain flower species and ignore the other types [20]. By this way, the risks are decreased by pollinators and the intake of nectar is ensured. In addition to all these, four standard rules are described to determine the calculation of FPA.

1. The movement of the pollinators satisfies Levy flights.
2. Abiotic pollination is evaluated as a local pollination.
3. Flower constancy is equivalent to a reproduction probability and this situation is proportional to the similarity of the involved flowers.
4. The switch probability; p is a pre-fixed situation that is constant in $[0, 1]$ and used to control the type of pollination either local or global.

Flower Pollination Algorithm consists a candidate solution vector x_i that is characterized by a flower i in a population of n flowers. The flowers can present global or local pollination for the text population modelling. The global pollination algorithm regarding to flower constancy rule can be determined by Equation 1.

$$x_i^{t+1} = x_i^t + L(g^* - x_i^t) \quad (1)$$

x_i^t is the flower i at iteration t , g^* is the best flower of all the populations at iteration t , and L is a Levy distribution. Besides Equation 1, the local pollination in relation to flower

Table 1. The design variables of the wall system

	Symbol	Description of parameter
Variables interrelated with	X_1	Width of the heel
Cross-section dimension	X_2	Thickness of the wall stem at the top
	X_3	Thickness of the wall stem at the bottom
	X_4	Thickness of base foundation
Variables interrelated with reinforced concrete design	X_5	Area of the reinforcing bars of the stem
	X_6	Area of the reinforcing bars of foundation heel

constancy rule can be modelled by Equation 2.

$$x_i^{t+1} = x_i^t + \varepsilon(x_j^t - x_k^t) \quad (2)$$

In Equation 2, x_j^t and x_k^t represents the different flowers of a same population and ε is drawn from a uniform distribution in $[0, 1]$. This rule calculates the type of flower pollination is either local or global. If the random number drawn in $[0, 1]$ is evaluated lower than p , the global pollination is carried out. In the contrary case, local pollination is conducted. In order to perform cost-effective analysis of L-Shaped retaining walls with FPA it is necessary to specify the parameters of design and additionally it is essential to note the ranges of these parameters for obtaining the initial solutions. Six design variables ($X_1, X_2, X_3, X_4, X_5, X_6$) selected to perform the analysis of L-Shaped walls (Table 1).

The design of the wall is started with the achievement of safety against the failure modes then if the satisfaction is ensured it becomes essential to identify the application of the requirements of reinforced concrete design. ACI 318-05 code is used due to its prevalent usage. The ACI 318-05 code suggests to identify equivalent rectangular compressive stress distribution. By the equivalent compressive stress distribution, the moment capacity of the wall can be calculated and only the critical sections of the stem and base is checked. The constraints of design about strength of safety and dimensions are given in Table 2.

Table 2. The design constraints of solution

Description	Description of parameter
Safety for overturning	$g_1(X)$: $FoS_{\text{overturning,design}} \geq FoS_{\text{overturning}}$
Safety for sliding	$g_2(X)$: $FoS_{\text{sliding,design}} \geq FoS_{\text{sliding}}$
Safety for bearing capacity	$g_3(X)$: $FoS_{\text{bearingcapacity,design}} \geq FoS_{\text{bearingcapacity}}$
Minimum bearing pressure (q_{min})	$g_4(X)$: $q_{\text{min}} \geq 0$
Flexural strength capacities of critical sections (M_d)	$g_{5-7}(X)$: $M_d \geq M_u$
Shear strength capacities of critical sections (V_d)	$g_{8-10}(X)$: $V_d \geq V_u$
Minimum reinforcement areas of critical sections (A_{smir})	$g_{11-13}(X)$: $A_s \geq A_{\text{smir}}$
Maximum reinforcement areas of critical sections (A_{smax})	$g_{14-16}(X)$: $A_s \leq A_{\text{smax}}$

The objective function is only consisted with the evaluation of material costs. Material costs are defined by the use of the costs per unit volume/weight. The mathematical formulation of the used objective function can be shown with Equation 3. In Eq. 3, unit cost of the concrete is C_{con} and its volume is V_{con} and the unit cost of the reinforcement is C_{st} and its weight is W_{st} .

$$\text{min } f_x = C_{\text{con}} \cdot V_{\text{con}} + C_{\text{st}} \cdot W_{\text{st}} \quad (3)$$

The proposed algorithm is used with the mentioned restrictions and equations to acquire the optimal dimensions of the wall against the change of soil geotechnical properties.

RESULTS AND DISCUSSION

In the light of this mentioned study method, parametric analyses were conducted to control the effects of soil geotechnical properties on the optimal design of L-Shaped retaining walls. Arbitrarily selected cases have been used to model the cost and dimension optimization processes. The excavation depth was selected 3, 5, 7 and 9 meters and the surcharge load application were assumed to be 0, 10, 20 kPa respectively for all the fictionalized cases. The variants of the soil geotechnical properties were assumed to be the internal friction angle and the unit we-

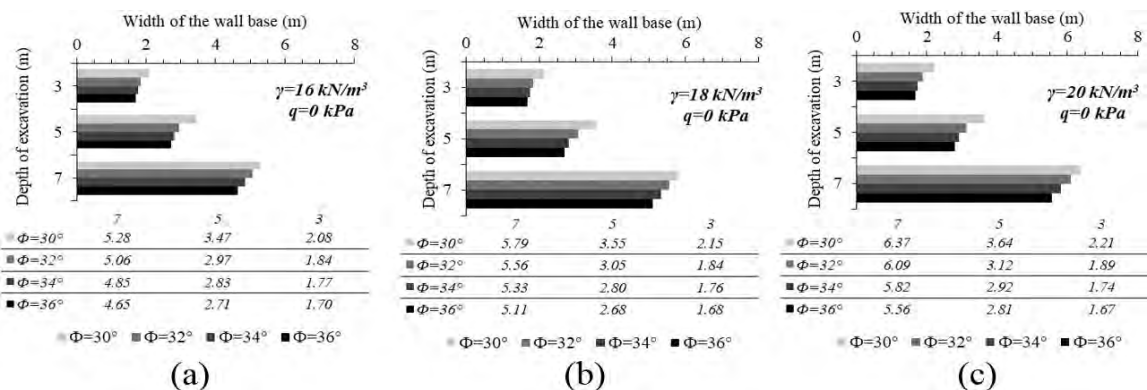


Figure 2. Change of wall base width against the unit weight of soil

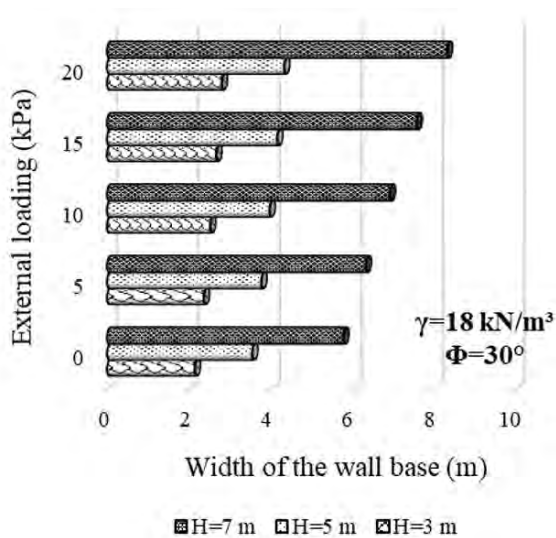


Figure 3. Change of wall base width against external loading

ight of the soil. The internal friction angle was selected 30 and 32° to represent medium dense sandy soils and 34 and 36° to represent dense sandy soils according to the given limits by Bowles (1988). Numerical analyses were performed to obtain the cost-effective sizing in relation with both geotechnical safety and structural necessities. Consequently, the optimization based design of LSRW is taken into consideration with the evaluations done by individual and dual interaction of parameters to designate the influence on optimum sizing. The optimization based design of LSRW is investigated with the performed 105000 analyses by Matlab software. The design has been controlled by evaluating the changes happened for the width and thickness of the foundation base. The wall height is also taken into consideration with the sum of excavation depth and foundation base thickness. In Fig. 2, the change of wall base width is identified for different soil unit weights in relation with the change of internal friction angle. All graphs were illustrated for three different excavation depths (3, 5, 7 meters). The absence of external surcharge load is assumed to be applied in whole selected cases. It has to be noted that the vertical and ho-

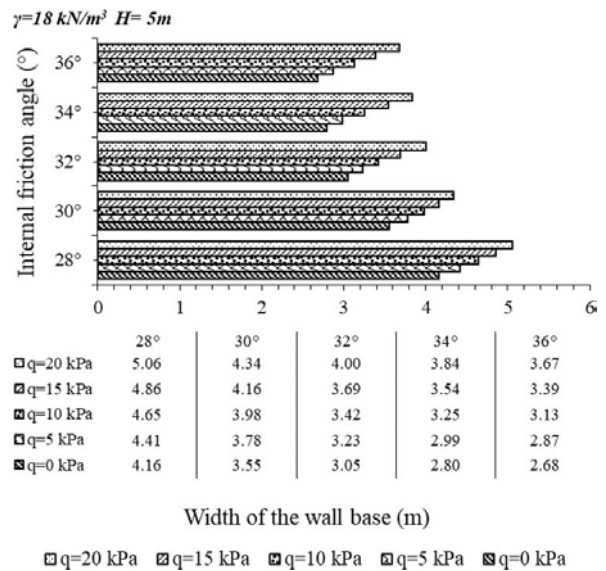


Figure 5. Change of wall base width against external loading and friction angle

orizontal axes of the illustration are selected as the same to ease comparison.

The unit weight of soil has been selected 16 kN/m³, 18 kN/m³ and 20 kN/m³ in Fig. 2 a, b and c respectively. As a general evaluation, the comparison of Fig. 2 a, b and c shows that the increase of unit weight of soil leads to enlarge the width of soil base. This condition is especially significant for the cases that are identified for deeper excavation depths. The increase of soil unit weight from 16 to 20 kN/m³, for 3 meters excavation depth, leads the design to enlarge the foundation base width %6. Besides this if the excavation depth is increased to 7 meters, the increment of soil unit weight leads the design to enlarge the foundation base width %20 for all the internal friction angle assumptions. The evaluation of the increase of excavation depth from 3 meters to 7 meters, by the consideration of same soil conditions, leads the foundation base to be bigger than %150 for 16 kN/m³ soil unit weight, bigger than %170 for 18 kN/m³ soil unit weight and bigger than %190 for 20 kN/m³ soil unit weight approxi-

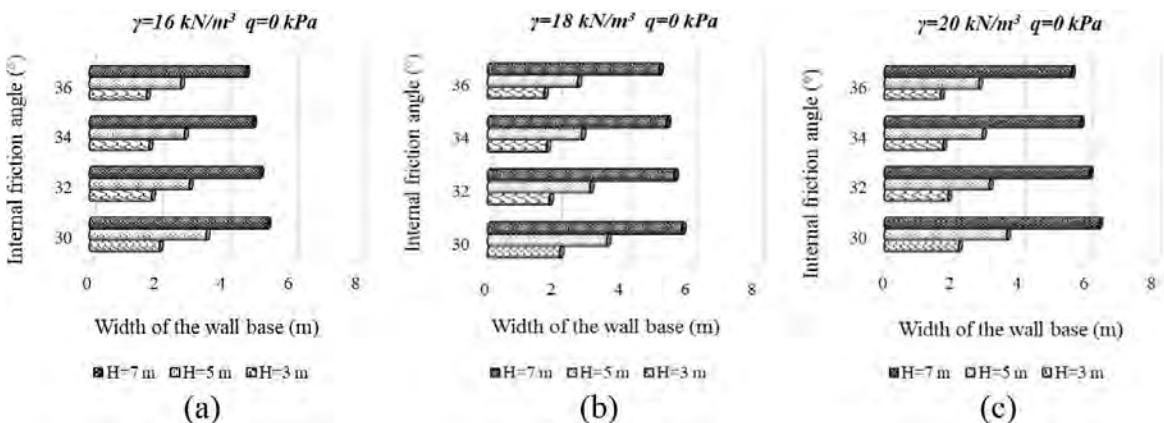


Figure 4. Change of wall base width against the internal friction angle

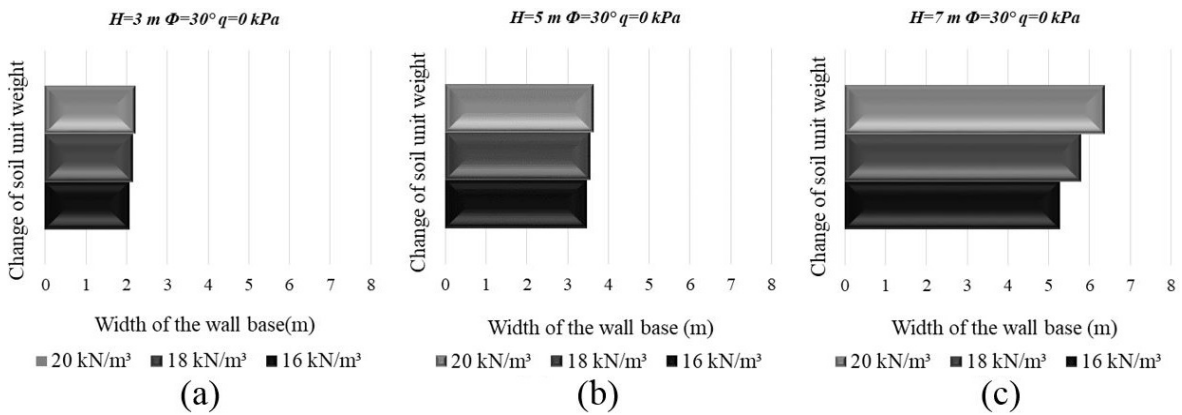


Figure 6. Change of wall base width against the change of soil unit weight and excavation depth

mately. In addition to these, it can be said that the increase of internal friction angle tends to decrease the width of foundation base related to the increment degree. Fig. 3 shows the change of wall foundation base width against different external surcharge loading conditions. The absence of surcharge loading and 5, 10, 15, 20 kPa loading situations has been investigated as a case within the concern of this paper. The internal friction angle was 30° and the unit weight of soil was 18 kN/m³ for the selected reference case. The differentiation of wall base width was also investigated in relation with the change of excavation depth. It can be seen from Fig. 3 that the wider base width causes the bigger external loading. The reference case was selected the absence of an external loading situation for comparisons. In a situation which the excavation depth is assumed to be 3 meters, the increase of the external load from zero to 5, 10, 15, 20 kPa leads the base width to enlarge 10%, 17%, 24%, 30% respectively. If the excavation depth was assumed to be 7 meters, the increase of external load causes to widen the base width %9, %19, %31, and % 43 as regard to the reference case. As a result, it is clear to say that the degree of the surcharge effect is raised in accordance with the depth of excavation.

Fig. 4 is illustrated to define a clear relationship of the effects of internal friction change on the design of the retaining wall system. The absence of the surcharge was assumed and the difference of soil unit weight was also shown. The increase of soil internal friction angle decreases the width of the wall base for the cases evaluated. But the maximum dimension change between the maximum and minimum values of envisaged internal friction angles were not bigger than %25. Fig. 4 a, b and c is drawn for different soil unit weights to make dual interacted evaluations between variants of the analyses. Depending on, it will be proper to say that, excavation depth is the most influencer parameter of design process. The change of internal friction angle is almost more effective than the change of unit weight of soil for L-Shaped walls especially in the cases assumed in this study. In addition, it is necessary to say that the envisaged numerical difference between the selected parameters are

also important to interpret the interaction behavior through the obtained variants.

Fig. 5 shows a detailed relationship between the effects of external load change related to different internal friction angles. The unit weight of the soil is assumed to be same with Fig. 4 (18 kN/m³) and the excavation depth is selected 5 meters as a constant value. It can probably seen from the Fig. 5 that the increase of external loading is perceived bigger by dense sands in terms of the dimension change. In such a case that, if the relative base width increase difference between upper and lower bounds of the surcharge is evaluated, the dimension change of the wall happens approximately % 10 bigger than the loose sand condition for dense sand.

In Fig. 6, the effect of the unit weight change of the soil on the wall base width is investigated based on different excavation depths. The relative width differentiation between the upper and lower limits of soil unit weight for 3 meters excavation depth seems not to be important vis-a-vis the changes happened for 7 meters excavation depth. Correspondingly, it can be said that the influence ratio of the soil unit weight increases depending on the increase of the excavation depth.

Fig. 7 considers the subject from a different angle by assuming the foundation base thickness as an affected dimension by the variants of the analyses. Fig. 7 is an integrated illustration of the dual interaction of variants. The change of soil unit weight is drawn with the use of subdivisions of the figure and also the change of internal friction change and the deepening of the excavation depth is taken into consideration. The absence of the surcharge load is assumed for all the cases. The thickness of the foundation base was unaffected till 5 meter excavation depth and 36° internal friction angle. At 5 meters excavation depth, the increase of internal friction angle to 36° was caused to increase the thickness of the base at a rate of %33. The increment of the excavation depth has been increased the thickness of the base approximately %100 for dense sandy soils.

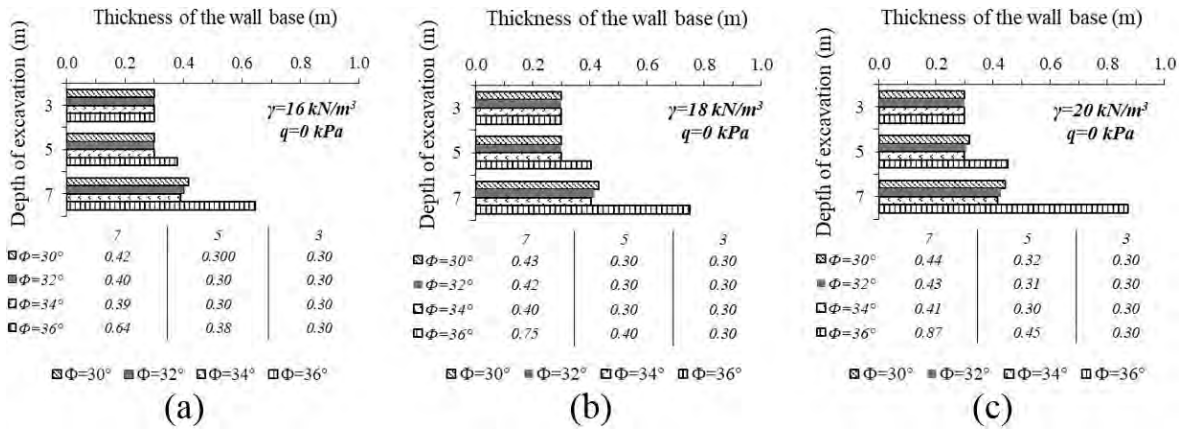


Figure 7. Change of wall base thickness against the change of soil unit weight ($q=0 \text{ kPa}$)

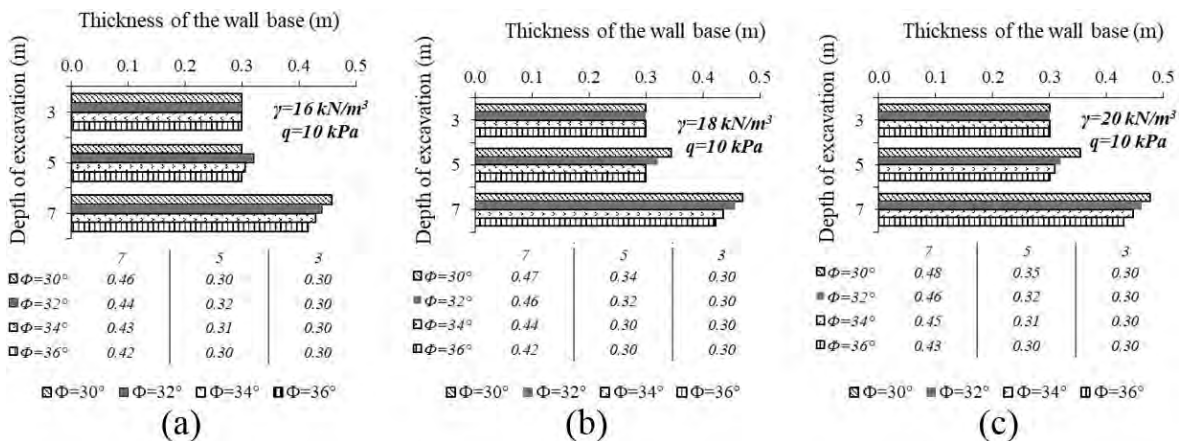


Figure 8. Change of wall base thickness against the change of soil unit weight ($q=10 \text{ kPa}$)

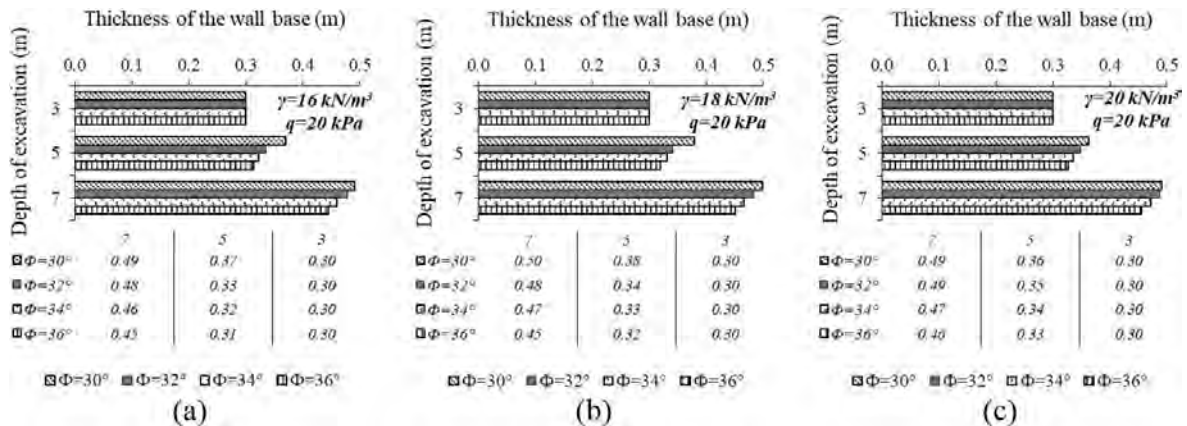


Figure 9. Change of wall base thickness against the change of soil unit weight ($q=20 \text{ kPa}$)

In Fig. 8, the change of foundation base thickness is given based on the increase of external load to 10 kPa. The subdivisions of the figure are drawn to show the change of soil unit weight and internal friction angle and excavation depth is also taken into account. Comparison of Fig. 7 and Fig. 8 shows that the increase of external load directly raises the thickness of the wall base nearly at a rate of %33. On the other hand, the change of soil unit weight under the condition that the increase of surcharge is actual, had not

got an influence on the thickness of the base. A similar behavior trend is seen in Fig. 8 with Fig. 7 and the increasing of the excavation depth causes to increase the thickness of the foundation base. But differentiated from Fig. 7 that the effect of the increase of internal friction angle had affected the thickness of the base for all selected cases.

Fig. 9 represents the change of base thickness with the increase of external load to 20 kPa value. Same subdivisions

are prepared with the same parameters in Fig. 7 and Fig. 8 for to ease comparison. The change of soil unit weight has no effect on the base thickness dimension of the wall. Besides this, if the application of external load to an envisaged maximum value was occurred (10 kPa for this study), the thickness of the wall base was not changed. Therefore, it can be said that the dominant effect of the change of the design parameters on the sizing of the wall is reflected to the width of the foundation base.

CONCLUSION

In this study, huge number of comparative parametrical analyses were conducted to achieve the effects of soil geotechnical properties on the cost effective sizing of L-shaped reinforced concrete retaining walls. The studies about the design of L-shaped retaining walls are very limited in the literature so this study is special for the achievement of design limits of restricted type of walls. The width and thickness of the retaining wall were assumed to be the affected dimensions of the wall structure. The parametrical analyses were performed by the use of Matlab software Flower Pollination Algorithm. The results of the analyses show that:

- The change of excavation depth is the major influencer factor of sizing. The increase of the excavation depth raises the wall dimensions directly proportional.
- Internal friction angle is the most important soil geotechnical parameter for the design of retaining walls that are embedded in sandy soils. The increase of internal friction angle leads to narrow the width of the base. In addition to these, the increase of the friction angle of sandy soils leads to decrease the thickness of the base after a boundary excavation depth (this depth is 7 meters for the cases analyzed in this study).
- The increase of surcharge is also an effective external factor in sizing because the increase of surcharge causes enlarging the base. This increase ratio increases proportional to the excavation depth. The increase of external loading is perceived bigger by dense sand in terms of the dimension change. In addition to these, the raise of surcharge increases the thickness of the base nearly one third of the dimension that is acquired in the case which the absence of the external load is assumed.
- The increase of the unit weight of the soil enlarges the foundation base width, but has no effect on the thickness.
- The thickness of the wall base is not influenced by the change of variants until a reference excavation depth is reached.
- The results of the optimization analyses show that L-Shaped restricted walls are not proper to resist lateral earth pressures which are caused because of bigger than 9 meters deep excavations. Because there could not be obtained a proper design due to the lack of technical ade-

quateness (either geotechnical or static design safety requirements) within the limits of defined design variables.

- It has to be noted that these mentioned results are acquired based on the fictionalized cases within this study. According to this situation, the change of the assumptions of the cases will affect the influence ratios of the design variables.

REFERENCES

1. Bowles JE. Foundation analysis and design, fifth ed. McGraw-Hill, New York, 1988.
2. Das BM, Sobhan K. Principles of geotechnical engineering, eighth ed. Cengage Learning, Stamford, 2010.
3. Yıldırım S. Zemin inceleme ve temel tasarımı, Third ed. Birsen Yayınevi, İstanbul, 2002.
4. Azizi F. Applied Analyses in geotechnics, first ed. E & FN Spon, London, 2000.
5. Sasidhar T, Neeraja D, Sudhindra VSM. Application of genetic algorithm technique for optimizing design of reinforced concrete retaining wall. International Journal of Civil Engineering and Technology 8(5) (2017) 999-1007.
6. Rouili A. Design of Rigid L- Shaped Retaining Walls. World Academy of Science, Engineering and Technology, International Journal of Civil Science and Engineering 7(12) (2013) 908-911.
7. Ceranic B, Fryer C, Baines RW. An application of simulated annealing to the optimum design of reinforced concrete retaining structures. Computers & Structures 79(17) (2001) 1569-1581.
8. Ahmadi-Nedushan B, Varaee H. Optimal Design of Reinforced Concrete Retaining Walls using a Swarm Intelligence Technique. in Topping BHV, Tsompanakis Y (Eds). Paper presented at the first International Conference on Soft Computing Technology in Civil, Structural and Environmental Engineering, Stirlingshire, January 2009.
9. Camp CV, Akin A. Design of Retaining Walls Using Big Bang-Big Crunch Optimization. Journal of Structural Engineering 138(3) (2012) 438-448.
10. Kaveh A, Kalateh-Ahani M, Fahimi-Farzam M. Constructability optimal design of reinforced concrete retaining walls using a multi-objective genetic algorithm, Structural Engineering and Mechanics 47(2) (2013) 227-245.
11. Bekdas G, Temur R. Grey Wolf Optimizer for Optimum Design of Reinforced Concrete Cantilever Retaining Walls. Paper presented at International Conference of Numerical Analysis and Applied Mathematics (ICNAAM), Thessaloniki, 25-30 September 2017.
12. Uray E, Çarbaş S, Erkan İH, Tan Ö. Parametric investigation for discrete optimum design of a cantilever retaining wall. Challenge Journal of Structural Mechanics 5(3) (2019) 108-120.
13. Coulomb CA. Essai sur une application des regles des maximis et minimis a quelques problemes de statique relatifs a l'artitecture. De l'Imprimerie Royale, Paris, 1776.
14. Rankine WJM. On the stability of loose earth, The Royal Society, London, 1857.
15. Terzaghi K. General wedge theory of earth pressure, Transactions, ASCE. 106 (1941) 68-97.
16. Dembicki E, Chi T, System analysis in calculation of cantilever retaining walls. International Journal for Numerical and Analytical Methods in Geomechanics 13(6) (1989) 599-610.
17. Powrie W. Limit equilibrium analysis of embedded retaining walls. Geotechnique 46(4) (1996) 709-723.

18. Alyasseri ZAA, Khader AT, Al-Betar MA, Awadallah MA, Yang XS. Variants of the flower pollination algorithm: a review. *Studies in Computational Intelligence* 744 (2018) 91–118.
19. Mergos PE, Mantoglou F. Optimum design of reinforced concrete retaining walls with the flower pollination algorithm. *Structural and Multidisciplinary Optimization* 61 (2020) 575–585.
20. Yang XS. Flower Pollination Algorithm for Global Optimization. In: Durand-Lose J., Jonoska N. (eds) *Unconventional Computation and Natural Computation (UCNC 2012)*, Lecture Notes in Computer Science 7445 (2012) 240-249.
21. ACI 318. *Building Code Requirements for Structural Concrete and Commentary*. ACI Committee, 2014

Comparison of Neural Network Models for Nostalgic Sentiment Analysis of YouTube Comments

Seda Postalcioglu  Senem Aktas 

Bolu Abant İzzet Baysal University, Department of Computer Engineering, Bolu, Turkey

ABSTRACT

For this study Sentiment Analysis (SA) is applied for the music comments using different Neural Network (NN) Models. SA is commonly used for Natural Language Processing (NLP). With the help of NLP, the evaluations / tips about the future can be obtained by analyzing the correspondences and comments. The aim of the study is to draw conclusions from the comments made under the songs whether they are nostalgic. Data is captured using the YouTube Data API. Data extraction is done by entering the link of the song whose comments will be taken. CSV files are obtained and then labeled as nostalgic and non-nostalgic. Different neural network models as MLPNN (Multi-Layer Perceptron Neural Network), CNN (Convolutional Neural Network), RNN-LSTM (Recurrent Neural Network-Long Short-Term Memory) are applied for sentiment analysis. Their performances are analyzed. MLPNN, CNN, RNN-LSTM performance results are 78%,88%,88%, respectively.

Keywords:

CNN, MLPNN, NLP, RNN, YouTube comments.

Article History:

Received: 2020/05/15

Accepted: 2020/09/01

Online: 2020/09/30

Correspondence to: Seda Postalcioglu,

E-mail: postalcioglu_s@ibu.edu.tr;

Phone: +90 3742541000

INTRODUCTION

With the rapid development of social networking sites, people need to explain their opinions and thoughts. People share not only information with websites but also they begin to express their thoughts and feelings more easily [1]. They expressed these posts by tweeting them on Twitter, posting on Instagram or commenting on social media. Based on this case, the feelings and thoughts of the interpreters can be analyzed [1]. Reference 11 can be shown as an example.

It is possible to analyze such comments or posts according to some criteria such as what team hits, political opinion, positive/negative/neutral content of comments. This kind of analyzes may affect future production progress by enabling the public to learn the opinions, parties, and thoughts before the political election or to make a customer analysis for the products produced. It has a wide usage area. These analyses are carried out for many different purposes. With these studies, it is tried to predict the future. These analyses are referred to as "Sentiment Analysis" in terminology [1]. Sentiment analysis is one of the techniques commonly used in Natural Language Processing (NLP). NLP helps us to understand the content of a text [2]. There are different

approaches based on natural language processing and machine learning techniques to get the features for the sentiment analysis [3].

In this study sentiment analysis is studied for the music comments. Music is universal, it has no language, and it has always been the best way to express emotions, at least that is how many people think. When you listen to a song, you can remember your memories of your childhood/youth or find something from yourself.

One of the most used music video platforms today is YouTube. It has a very large archive and is free. We can listen to any song from the 1960s or a song from today. YouTube also provides a section that allows you to post comments under these music videos. Here, feelings and opinions about the music listened to are shared.

The aim of the study is to draw conclusions from the comments made under the songs whether they are nostalgic. Comments captured using the YouTube Data API are tagged according to whether they are nostalgic in the CSV file. Choices are made from comments were taken before tagging, comments that will not be useful for analysis are deleted from the CSV file. "Natural lan-

guage processing" (NLP) operations are applied to the data. These data are divided into two as education data and test data. After training the models with training data, performance evaluation is made with test data. The difference of this study from the other articles is compared with the performance of NN using deep learning technique.

In this study, nostalgic sentiment analysis is done using different neural network models as MLPNN, CNN, RNN-LSTM. These models are performed on the database which is constructed by us. Performance results are compared.

MATERIAL AND METHODS

It is very important to create a suitable database for the study. Nostalgia literally means longing for the past. In the labeling of the comments, it is labeled as nostalgic in the comments that contain information about the real meaning of the word nostalgia as well as "remembering the past, childhood-youth years, memories of those years".

To find nostalgic comments, it is necessary to look at the comments under the old songs. The relevant website is given in reference 4 has been used to easily access such songs. CSV files are obtained and then labeled as nostalgic and non-nostalgic. The data is partially ready.

These prepared data are exposed to some pre-processing stages before modeling such as removing punctuation, numbers, stopwords, extra spaces. After a pre-processing dataset is used in neural network models. 80% of the dataset obtained is used as training data to train the model, and the remaining 20% is used as test data to test the model. Fig. 1 shows the dataset for the study. Dataset size is 1500.

Sentiment Analysis needs a pre-processor to transform a word into a vector [2]. This process is called "Word Embedding"[2]. Extracting features from words for NLP, there are two popular methods; word2vec and GloVe (The Glo-

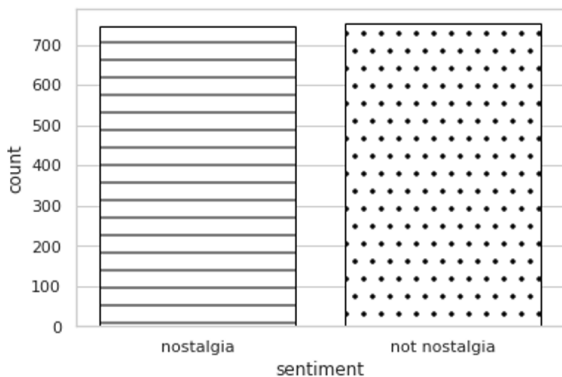


Figure 1. Dataset for the study

bal Vectors for Word Representation) [3]. Word embedding maps the words in vocabulary into real-valued vectors [5].

The word vectors shows semantics and their dimension is usually low, this transformation obtains to calculate the connection among words and dimensionality reduction for efficient representation [6,5]. The NN takes words from a vocabulary as input and then embeds them as vectors into a lower-dimensional space, which is denoted to as Embedding Layer [5]. Fig. 2 shows the word embedding model using a NN [5].

The word embedding model used in this study. The GloVe is utilized. GloVe stands for global vectors for word representation. Fig. 3 shows the system architecture. Pre-processing and feature extraction are important for the study.

Word Embedding is applied as the Glove technique. For pre-processing stages, tokenization, stop word, noise removal is used. Tokenization breaks a stream of text into words, phrases, symbols, or other meaningful elements named tokens. This process provides the analysis of the words in a sentence [7]. The most common technique to deal with "a", "about", "above", "across", "after", "afterward", "again" which is not contain important impact for the sentence is Stop Words. This method removes them from the text [7]. For this reason, stop words are applied for the study. Text datasets cover redundant characters such as punctuation and special fonts. Critical punctuation and special fonts are significant for people understanding of text [7]. It can be causes a problem for classification algorithms. So for this study noise removal is applied. An example of the dataset before pre-processing is given in Fig. 4. An example of the dataset after pre-processing is given in Fig. 5.

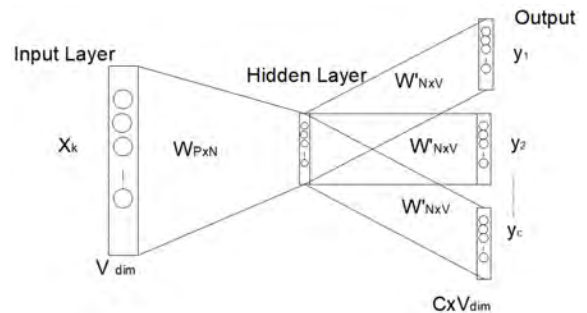


Figure 2. Word Embedding Model [5]

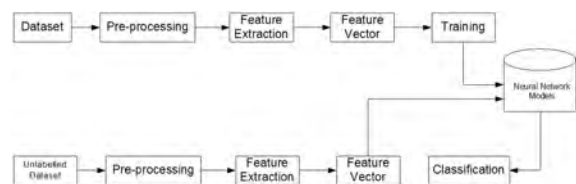


Figure 3. System Architecture

Index	sentiment	comment
0	not nostalg...	I have listened to and enjoyed this song for many ...
1	nostalgia	My Dad and Mom used to play this all the time and ...
2	not nostalg...	He was a singer with a golden voice that I love to...
3	nostalgia	The most beautiful voice ever I listened to him wh...
4	nostalgia	I have most of Mr. Reeves songs. Always love his ...
5	not nostalg...	30 day leave from 1st tour in Viet Nam to convince...
6	nostalgia	listening to his songs reminds me of my mum who pl...
7	nostalgia	Every time I heard this song as a child, I used to...
8	nostalgia	My dad loved listening to Jim Reeves, when I was a...
9	nostalgia	I HAVE ALSO LISTENED TO Jim Reeves since childhood...
10	not nostalg...	Wherever you are you always in my heart
11	not nostalg...	Elvis will always be number one no one can come cl...
12	not nostalg...	ill bet if they begin to play this song on the rad...

Figure 4. Dataset before pre-processing

Index	Type	Size	Value
0	str	1	listened enjoyed song many years years old widower driving distant cit...
1	str	1	dad non used play time great reeves fans grew music love lost nana num...
2	str	1	singer golden voice love hear time great fan age years days still alth...
3	str	1	most beautiful voice ever listened kid still love singing never forgot...
4	str	1	mr reeves songs always love smooth voice comforting sounds like peopl...
5	str	1	day leave st tour viet convince mary lou narry came back nd tour years...
6	str	1	listening songs reminds mum played everyday
7	str	1	every time heard song child used cry reminded funerals got fear death ...
8	str	1	dad loved listening reeves teenager back time changes things
9	str	1	listened reeves since childhood nostalgic feeling comes tunes love fee...
10	str	1	wherever always heart
11	str	1	elvis always number close taking place king always king
12	str	1	bet begin play song radio new generation could still hit goes anytime ...
13	err	1	know came center wear high school texas netherlands found forbidden kn...

Figure 5. Dataset after pre-processing

The system has two stages as training and testing. For training stage, to cope with over fitting problem, L2 regularization is preferred. The aim of L1 and L2 regularizations are avoiding over-fitting problem. L2 is the most common regularization in deep learning [12]. After training, the test dataset is applied to the system. The performance results of the networks are calculated using Equation (1). TP is the true positive, TN is the true negative, FP is false positive and FN is the false-negative predictions.

$$\text{Accuracy} = (\text{TP} + \text{TN}) / (\text{TP} + \text{TN} + \text{FP} + \text{FN}) \quad (1)$$

RESULTS AND DISCUSSION

Nowadays, there are different neural networks structures. Each of them has different architectural and working mechanisms. Specially used neural networks have been developed for various machine learning processes such as image processing, natural language processing etc. In this study, three different neural networks are used. These are MLPNN, CNN, RNN-LSTM.

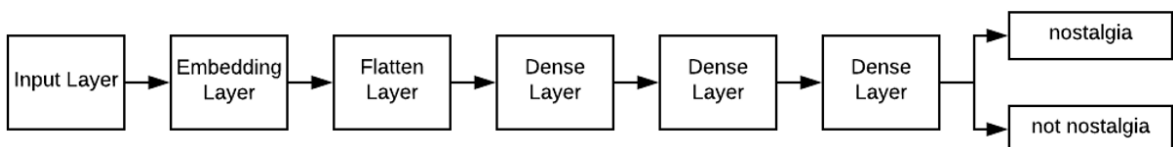


Figure 7. Architecture of the MLPNN Model

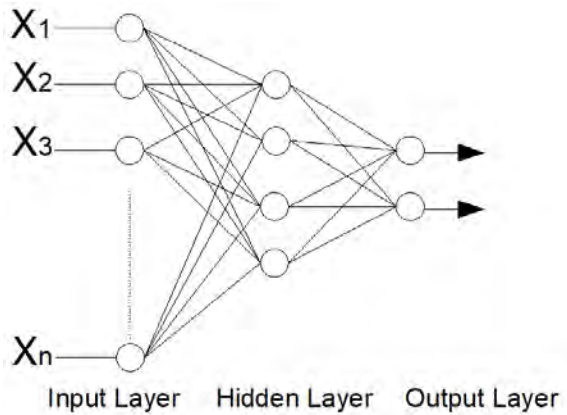


Figure 6. MLPNN Model

MLPNN is a feed-forward neural network. The structure has units which has one-way connections to other units. The units can be arranged in layers so that connections go from one layer to a later layer [13]. It has one or more layers called a hidden layer. MLPNN works especially effectively in classification, regression prediction problems. It can be used for image, text and many other different datasets. Linearly not separable problems are solved by MLPNN [8]. MLPNN Model is shown in Fig. 6.

The Embedding layer was used as the first layer in all our neural networks. This layer turns positive integers (indexes) into fixed-sized dense vectors to reduce the costs of one-hot encoded vectors, which are high-dimensional and sparse. The flatten layer was used to flatten the input, converting the layer to the 1D array so it could feed the layer. Then three dense layers were used to connect each node of the current layer to the next node of the next layer. The single-unit last dense layer gives the classification result. MLPNN model architecture is given in Fig. 7.

Table 1 shows the MLPNN properties and performance results. ReLu is used as an activation function. Adam is used as an optimizer. Mean Squared Error is used. The batch size technique is used for modeling. The batch size is a hyper parameter of gradient descent and it controls the number of training samples [9]. Fig. 8 shows the MLPNN results for Sentiment Analysis (SA) as to accuracy and loss, respectively. Accuracy is calculated as 78%.

CNN, which is widely used especially in computer vision tasks, gives very successful results. Although they have been specially developed and used for image data, they are

also used for sentiment analysis and classification processes obtained using text data. CNNs are constructed with convolutional layers [14]. Reference 15 states that convolutional networks are suitable for recognizing or rejecting shapes [15].

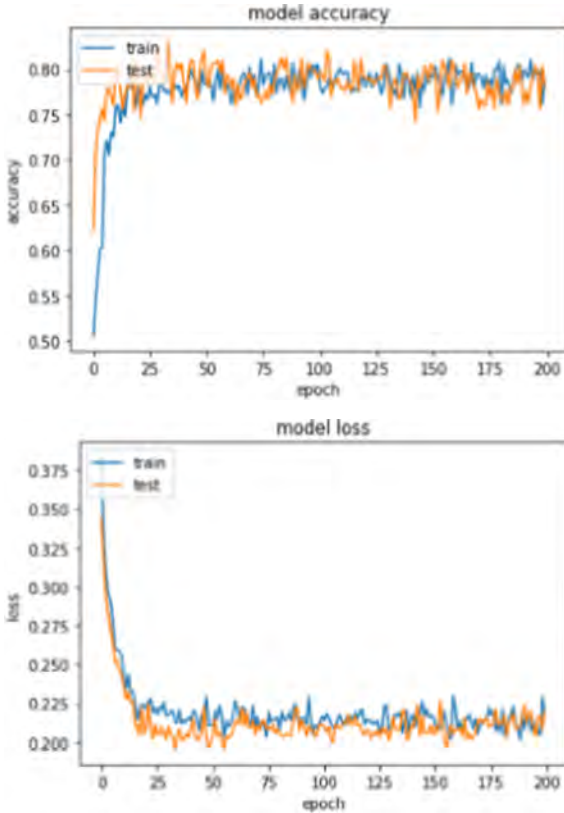


Figure 8. MLPNN results for Sentiment Analysis

As can be seen in Fig. 9, CNN architecture has Conv1D layers and Global Max Pooling layer different from MLPNN architecture. Conv1D was applied because the texts are one-dimensional data strings. This layer creates a convolution kernel.

CNN (Convolutional Neural Network) contains three layers as the Convolutional, Pooling and Full-Connected Layers [6]. Convolution layer extracts the features of the input by using a slide filter and applies the scalar product [6]. Feature map is the output of convolution [6]. Matrices obtained by convolution operators are transformed with an activation function. ReLu (Rectified Linear Unit) is used as an activation function. ReLu is given in Equation (2) and its effect is given in Fig. 10 [6]. For the output layer, the sigmo-

id function is used as an activation function. The sigmoid function is given in Equation (3).

$$ReLU(x) = \begin{cases} x & \text{if } x > 0 \\ 0 & \text{if } x \leq 0 \end{cases} \quad (2)$$

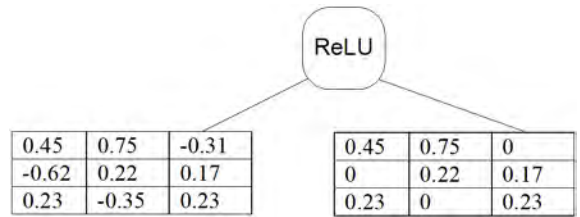


Figure 10. ReLU

$$f(x) = 1/(1 + e^{-x}) \quad (3)$$

The second one is the Pooling layer. It reduces the size of the feature map. Pooling works by sliding a window over the input. Finally, the Fully Connected layer filters high-level representation of the input and converts them into votes. Fully connected is a way to connect layers in two layers together [6].

Fig. 11 shows the CNN results for SA as accuracy and loss, respectively. Table 1 gives the CNN model properties. Accuracy is calculated as 88%.

LSTM algorithm is very popular for NLP [2]. It is one of the RNN models that can learn sequential data [2]. For training stage, RNN is hard to report the vanishing gradient problem. By using its internal memory, RNN sends the output it produces back to the network to obtain the next new output. Therefore, all the inputs in RNN are dependent. LSTM-RNN is advanced to solve the vanishing gradient problem and capture long-term dependency. So, LSTM-RNN is applied to language modeling [10]. The simple design of RNN is shown in Fig. 12 [10]. We consider $X=(x_1,x_2,\dots,x_T)$ as the input word sequence and $Y=(y_1,y_2,\dots,y_T)$ as the hidden sequence. RNN's hidden layer is the recurrent layer. Recurrent Layer is used to capture the contextual information of sentence [10].

LSTM-RNN adds output gate, forget gate, input gate and memory cell and an important information can be store over long time duration [10]. For this model, the tanh activation function is used. The activation function is given in Equation (4).

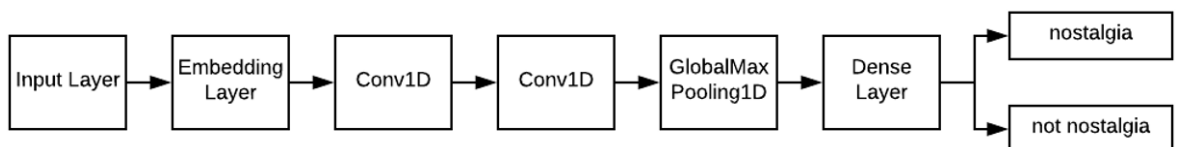


Figure 9. Architecture of the CNN Model

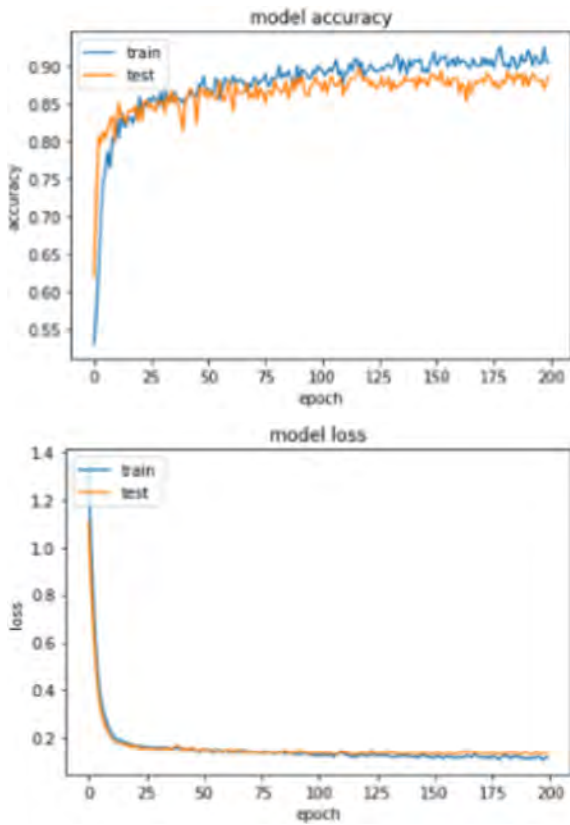


Figure 11. CNN results for Sentiment Analysis

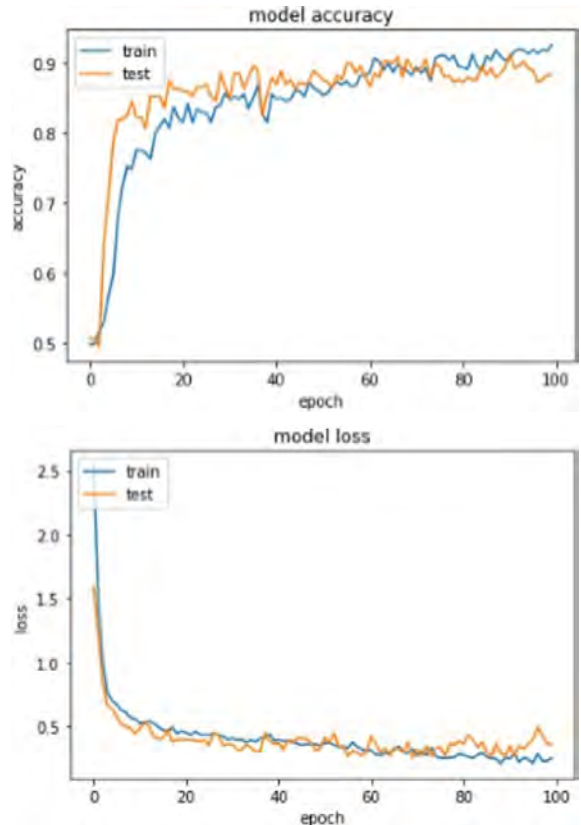


Figure 13. RNN-LSTM results for Sentiment Analysis

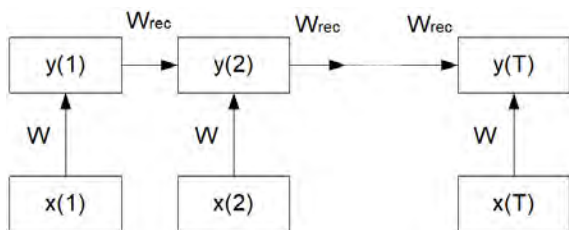


Figure 12. The basic architecture of RNN

$$\tanh(x) = 2 / (1 + e^{-2x}) - 1 \quad (4)$$

Fig. 13 shows the RNN-LSTM results for SA as accuracy and loss, respectively. Table 1 gives the RNN-LSTM model properties. Accuracy is calculated as 88%.

The architecture of RNN-LSTM model is shown in Fig. 14. It consists of three layers. Embedding layer is used as the input layer and dense layer is used as the output layer. The power of the RNN-LSTM neural network has been demonstrated using a not so deep architecture.

Table 1 gives the models properties. Adam is an efficient stochastic optimization method that only requires first-order gradients with little memory requirement [16]. As stated in reference 16, Adam gives good results in our practice compared to other stochastic optimization methods. Adam can be used to update network weights. Update expressions are shown in Equation (5) [17].

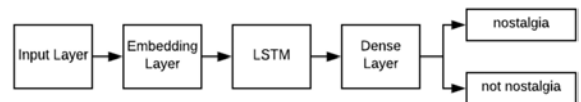


Figure 14. Architecture of the RNN-LSTM Model

$$\begin{aligned} v_t &= \beta_1 * v_{t-1} - (1 - \beta_1) * g_t \\ s_t &= \beta_2 * s_{t-1} - (1 - \beta_2) * g_t^2 \\ \Delta w_t &= -\eta \frac{v_t}{\sqrt{s_t + \epsilon}} * g_t \\ w_{t+1} &= w_t + \Delta w_t \end{aligned} \quad (5)$$

η is the initial learning rate, g_t is the gradient at time t along w^j , v_t is the exponential average of gradient along w_j , s_t is the exponential average of squares of gradients along w_j , β_1 and β_2 are hyperparameters [17].

As Loss function, MSE was used for MLPNN and CNN. MSE has been described as an excellent metric in the context of optimization, it is widely preferred as it saves time and effort [18]. The best result was obtained by using binary cross-entropy loss function in RNN-LSTM. Other features of the models are defined on the table.

Fig. 15 shows the confusion matrices of MLPNN, CNN, RNN-LSTM networks are given respectively. According to these matrices, Precision, Recall and F1 score values can be

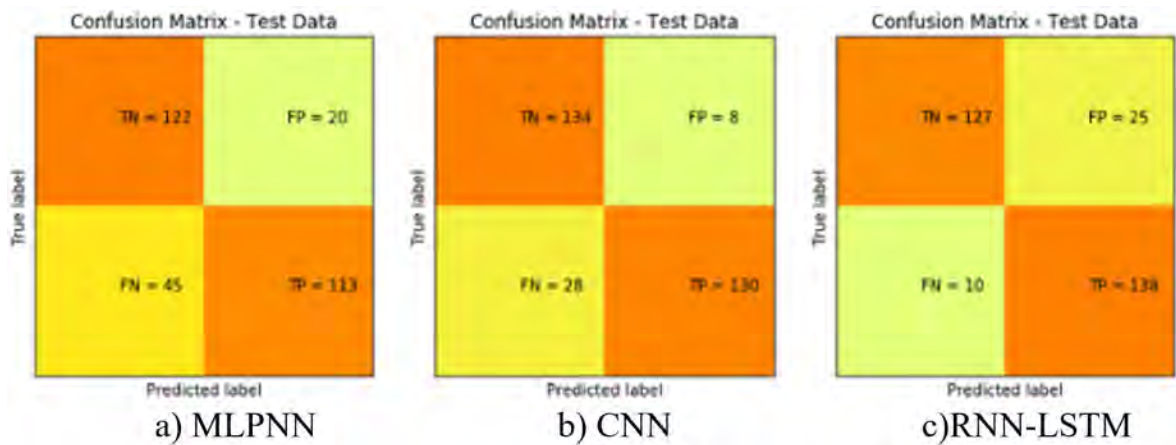


Figure 15. Confusion Matrices

obtained to better measure and evaluate the performance of the models. The Equation 6 is given below [19]. The F1 scores of the models are calculated as 0.78, 0.88, and 0.89 for MLPNN, CNN, RNN-LSTM, respectively.

$$F_1 = \left(\frac{2}{recall^{-1} + precision^{-1}} \right) = 2 \cdot \frac{precision \cdot recall}{precision + recall} \quad (6)$$

Table 1. Model properties.

Model	Optimizer	Loss function	Batch size	Epoch	Accuracy (%)
MLPNN	Adam	MSE	64	200	78
CNN	Adam	MSE	32	200	88
RNN-LSTM	Adam	Binary Crossentropy	128	100	88

Fig. 16 shows the comparison of MLPNN, CNN, and RNN performance results. CNN and RNN-LSTM give better results. RNN-LSTM model completed the training for 100 epochs. It means RNN-LSTM is faster than CNN for this study.

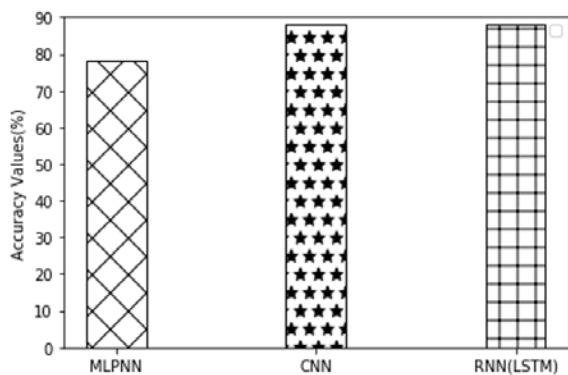


Figure 16. Comparison of MLPNN, CNN and RNN performance results

CONCLUSIONS

SA is one of the techniques used in NLP. It analyzes the text or comment and tries to find the main point. By using such techniques, planning for the future can be made by predicting the feelings and thoughts of people in all areas such as product development and marketing. In this study, comment analysis is performed with SA. Classification is done after the analysis using different NN models as deep learning which is popular today. A performance comparison is made. As a result of the performance, CNN and RNN-LSTM gives good results for the study. In future studies, analysis can be expanded by creating deeper networks and using various word embeddings. The created networks can be used easily in the analysis of application data such as Twitter, not just YouTube data.

References

1. Kumar A, Rani R. Sentiment analysis using neural network, 2nd International Conference on Next Generation Computing Technologies (NGCT), Dehradun, pp. 262-267, 2016.
2. Ayuthaya T S N, Pasupa K. Thai Sentiment Analysis via Bidirectional LSTM-CNN Model with Embedding Vectors and Sentic Features. International Joint Symposium on Artificial Intelligence and Natural Language Processing (ISAI-NLP), Pattaya, Thailand, pp. 1-6, 2018.
3. Goularas D, Kamis S. Evaluation of Deep Learning Techniques in Sentiment Analysis from Twitter Data. International Conference on Deep Learning and Machine Learning in Emerging Applications (Deep-ML), Istanbul, Turkey, pp. 12-17, 2019.
4. <http://www.officialcharts.com/charts/singles-chart/>, Acces date:02/01/2020

5. Bhoir S, Ghorpade T, Mane V. Comparative analysis of different word embedding models. International Conference on Advances in Computing, Communication and Control (ICAC3), Mumbai, pp. 1-4, 2017.
6. Huynh T, Le A. Integrating Grammatical Features into CNN Model for Emotion Classification. 5th NAFOSTED Conference on Information and Computer Science (NICS), Ho Chi Minh City, pp. 243-249, 2018.
7. Kamran K, Meimandi J, Heidarysafa K, Mendu M, Barnes S, Brown L, Id D, Barnes L. Text Classification Algorithms: A Survey. Information (Switzerland), 10 (2019) 1-68.
8. Wan F. Sentiment Analysis of Weibo Comments Based on Deep Neural Network. International Conference on Communications, Information System and Computer Engineering (CISCE), Haikou, China, pp. 626-630, 2019.
9. Brownlee J. <https://machinelearningmastery.com/difference-between-a-batch-and-an-epoch/> Accessed on: 20.11.2019
10. Lu Y, Shi Y, Jia G, and Yang J. A new method for semantic consistency verification of aviation radiotelephony communication based on LSTM-RNN. IEEE International Conference on Digital Signal Processing (DSP), Beijing, pp. 422-426, 2016.
11. Timoney J, Raj A, Davis B. Nostalgic Sentiment Analysis of YouTube Comments for Chart Hits of the 20th Century. 26th AIAI Irish Conference on Artificial Intelligence and Cognitive Science, AICS, pp:1-10, 2018.
12. Xiong H, Liu Q, Song S, Cai Y. Region-based convolutional neural network using group sparse regularization for image sentiment classification. Journal on Image and Video Proc. 30 (2019), pp. 2-9.
13. Ripley B. Feed-forward Neural Networks. Pattern Recognition and Neural Networks Cambridge: Cambridge University Press, pp. 143-180, 1996. doi:10.1017/CBO9780511812651.006
14. Huang X. Convolutional Neural Networks In Convolution, https://www.researchgate.net/publication/328189519_Convolutional_Neural_Networks_In_Convolution. Accessed date:18.06.2020.
15. Lecun Y, Bottou L, Bengio Y, Haffner P. Gradient-based learning applied to document recognition. Proceedings of the IEEE, 86(11), pp.2278-2324, 1998. doi:10.1109/5.726791
16. Kingma D, Ba J. Adam: A method for stochastic optimization. ICLR Conference, pp:1-15,2015.
17. Kathuria A, Intro to optimization in deep learning: Momentum, RMSProp and Adam, <https://blog.paperspace.com/intro-to-optimization-momentum-rmsprop-adam/> (Visited:01.09.2020)
18. Wang Z, Bovik A. Mean squared error: love it or leave it? – A new look at signal fidelity measures. Signal Processing Magazine, IEEE. 26 (2009) 98 – 117. 10.1109/MSP.2008.930649.
19. Powers D, Ailab. Evaluation: From precision, recall and F-measure to ROC, informedness, markedness & correlation. J. Mach. Learn. Technol. 2 (2011),pp. 2229-3981. 10.9735/2229-3981.

Analysis of miRNA-Mediated ceRNAs In The Pathogenesis of Renal Cell Carcinoma: An *In Silico* Approach

Orcun Avsar 

Hitit University, Department of Molecular Biology and Genetics, Corum, Turkey

ABSTRACT

Renal cell carcinoma (RCC) is the most common form of kidney cancers and derived from kidney epithelium. The prognosis of RCC is still poor despite recent developments in surgical and other novel treatment strategies. Competing endogenous RNAs (ceRNAs) are considered as significant post-transcriptional regulators that modulate gene expression via miRNA-mediated regulatory networks. Furthermore, it has been demonstrated that ceRNAs have remarkable functions in the pathogenesis of cancers by modulating the expression of oncogenes or tumor-suppressive genes. The aim of this study was to define novel molecular biomarkers for RCC via *in silico* analysis. Seven miRNAs which have clinical significance for renal cell carcinomas were exported through miRTarBase database. 1001 genes which are targeted by these 7 miRNAs simultaneously were determined by ComiR database. The genes with T-UCR in their exonic regions and which have the potential ceRNA activities were extracted. Gene expression differences between RCC and normal kidney tissues according to the renal cell carcinoma-associated ceRNAs involving T-UCR were identified by GEPIA. The statistical analysis of the relationship between NRXN3 and PTBP2 genes with RCC was determined by Spearman correlation test. NRXN3 and PTBP2 were found to be significantly associated with RCC ($p=0.0057$; $R=-0.29$). The current study demonstrates for the first time that PTBP2 gene is associated with renal cell carcinoma. The results of *in silico* analysis suppose that PTBP2 gene may have potential tumor suppressor role in RCC and NRXN3 gene may have potential oncogenic activity in RCC. Further *in vitro* and *in vivo* studies are required in order to clarify tumor suppressor role of PTBP2 and oncogenic activity of NRXN3 in RCC.

Keywords:

miRNA; ceRNA; T-UCR; Renal cell carcinoma; PTBP2; NRXN3

INTRODUCTION

Renal cell tumors represent approximately 3% of all cancers in males and lower incidence in females. Several factors such as genetics, obesity, tobacco smoking, hypertension, diuretics, medications such as acetaminophen and non-aspirin non-steroidal anti-inflammatory drugs, viral hepatitis, and chemical carcinogens (asbestos, arsenic, etc.) are implicated in the pathogenesis of renal cell tumors [1, 2, 3]. Renal cell carcinomas are divided into three subtypes: chromophobe, renal clear cell carcinoma and renal papillary cell carcinoma and this classification is verified by genetic and cytogenetic analysis [4, 5]. The most common form of renal cell tumors (approximately 70% of renal tumors) is renal clear cell carcinoma in adults. Papillary renal cell carcinoma is the second most frequent kidney tumors in adults [6].

MicroRNAs (miRNAs) are small non-coding RNA molecules (composed of 18-22 nucleotides) and conserved among different organisms. miRNAs are also defined as post-transcriptional regulators. miRNAs can bind to the complementary sequence of target mRNAs (target specificity is determined by miRNA sequence that is 6-8 nucleotide in length) and then cause to the degradation of mRNA. Furthermore, miRNAs are able to suppress translation and hence modulate gene and protein expression. miRNA biogenesis and functions are associated with various cancer types and they take significant roles in initiation, progression and metastasis of these cancers. Dysregulated miRNA expression profiles might be used as biomarkers of diagnosis and treatment of cancer [7, 8].

Article History:

Received: 2020/06/01

Accepted: 2020/09/17

Online: 2020/09/30

Correspondence to: Orcun Avsar,
Hitit University, Molecular Biology and
Genetics, 19030, Corum, Turkey
E-Mail: orcunavsar.gen@gmail.com
Phone: +90 364 227 1658

In recent years, competing endogenous RNAs (ceRNAs) are considered as significant post-transcriptional regulators that modulate gene expression via miRNA-mediated regulatory networks. Recent studies have showed that ceRNAs have significant functions in the pathogenesis of cancers by modulating the expression of oncogenes or tumor-suppressive genes. In the human genome, it is supposed that >50% of human mRNA might involve microRNA recognition elements (MREs) and ceRNAs share these sequences. miRNA can modulate several targets which include the typical MRE for miRNA. Similarly, the mRNA which have multiple MREs can be regulated by several miRNAs. Hence, the miRNA-mediated ceRNA network may be a common form of post-transcriptional regulation. ceRNA activity is affected by several factors such as RNA secondary structures, binding affinity of miRNAs, RNA editing, localization of ceRNA components. Disruptions in these factors may cause to the dysregulation of ceRNA network and then some diseases such as cancer [9, 10].

Ultraconserved regions (UCRs) which are 481 DNA elements longer than 200 base pair were discovered in 2004 by bioinformatics analysis. UCRs are completely conserved (no insertions or deletions) among rat, human, and mouse genomes and involved in diverse biological functions. According to the localization, UCRs are divided into five subtypes: intergenic, intronic, exon-containing, partly exonic, and exonic. Most of UCRs are transcribed in human tissues and these transcripts are named as transcribed UCRs (T-UCRs). It has been demonstrated that T-UCRs share tissue-specific expression pattern and have differential expression profiles between tumors. Moreover, it has been suggested that T-UCRs might have a significant role in the pathogenesis of diverse cancers [11, 12].

Studies in recent years have showed that miRNAs are promising for the understanding of the molecular mechanisms of cancer pathogenesis. Novel biomarkers are required to identify in order to elucidate the basis of miRNA-mediated cancer pathogenesis and novel RNA-mediated cancer treatment strategies. In this regard, the aim of the study is to identify novel promising biomarkers for renal cell carcinomas by bioinformatics analysis.

MATERIAL AND METHODS

miRNA Selection for The Pathogenesis of Renal Cell Carcinoma

Seven miRNAs which have clinical significance for renal cell carcinomas and have been proved experimentally were exported through miRTarBase database. The miRTarBase has been developed in order to present experimentally validated and predicted data on miRNA-target

interactions due to the biological significance of miRNA. That database enables scientists to verify novel targets of miRNAs. Chou et al. (2018) has described the 'Verified Target Module' [13].

Analysis of Renal Cell Carcinoma-Specific miRNA-Mediated ceRNAs

1001 genes which are targeted by these 7 miRNAs simultaneously were determined by the use of online ComiR database. ComiR, combinatorial miRNA targeting, is an online tool and estimates if a specific mRNA is targeted by a cluster of miRNAs. ComiR defines the potency for being targeted by a cluster of miRNAs. The ComiR database computes the potency of the regulation of each individual mRNA by a group of miRNAs according to the expression levels of miRNA in a combinational way. It is estimated that RNA transcripts of the genes might have the potential of ceRNA activity of the defined miRNAs [14].

Matching of Renal Cell Carcinoma-Associated ceRNA with Genes Consisting T-UCR

Ultraconserved regions (UCRs) with evolutionary conservation among organisms were determined in the human genome. Genes which contain these ultraconserved regions are divided into two as upstream (in the exonic region) and downstream [15]. In this study, the genes with T-UCR in their exonic regions and also genes which have the potential ceRNA activities among them were described.

Analysis of Renal Cell Carcinoma-associated ceRNAs Involving T-UCR for the Gene Expression Comparison Between Renal Cell Carcinoma and Normal Kidney Tissues

Gene expression differences between renal cell carcinomas and normal kidney tissues according to the renal cell carcinoma-associated ceRNAs involving T-UCR were determined by using Gene Expression Profiling Interactive Analysis (GEPIA) database. GEPIA which is a web-based and interactive bioinformatics tool is used for the analysis of gene expression [16].

Correlation Analysis of NRXN3 and PTBP2 Genes in Renal Cell Carcinoma

The statistical analysis of the relationship between NRXN3 and PTBP2 genes with renal cell carcinoma was determined by the use of Spearman correlation test in the GEPIA database.

RESULTS AND DISCUSSION

The list of seven miRNAs which are experimentally associated with RCC by the use of miRTarBase database is given in Table 1.

Table 1. List of miRNAs which are involved in the pathogenesis of renal cell carcinomas.

hsa-miR-141
hsa-miR-15a
hsa-miR-192
hsa-miR-200c
hsa-miR-21
hsa-miR-215
hsa-miR-23b

The list of 1001 genes which are targeted by the 7 miRNAs simultaneously is seen in Table A.1. According to the study that was conducted by Bejerano et al. [15] the genes which contain T-UCR in their exonic regions were given in Table A.2. The genes which have potential ceRNA activities were extracted and shown in Table 2. The genes which have expression profile differences between RCC and normal kidney tissue among renal cell carcinoma-associated ceRNAs with T-UCR have been designated. This analysis enabled to show that PTBP2 gene expression was significantly higher in normal kidney tissue than in kidney chromophobe. On the other hand, NRXN3 gene expression was significantly higher in kidney chromophobe and in renal clear cell carcinoma than in normal kidney tissue (Table 3, Table 4, Table 5).

Table 2. The list of renal cell carcinoma-associated ceRNAs cross-matching with genes involving T-UCR in the exonic regions.

UCR number	Length (bp)	Gene Name
uc.33	312	PTBP2
uc.378	251	NRXN3
uc.393	275	CLK3
uc.406	211	NFAT5

The association between NRXN3 and PTBP2 genes and renal cell carcinomas were carried out by the use of GEPIA database. Spearman correlation analysis has determined that NRXN3 and PTBP2 gene pair are significantly associated with renal cell carcinoma (figure 1) ($p=0.0057$; $R=-0.29$).

Renal cell carcinoma is the most common form of kidney cancers and derived from kidney epithelium. Renal cell carcinoma is the third frequent urogenital malignancy and

Table 3. Expression values of renal cell carcinoma-associated ceRNAs involving T-UCR between kidney chromophobe and normal kidney tissue.

Gene ID	Kidney chromophobe	Normal kidney
PTBP2*	2.94	8.36
NRXN3*	19.24	0.88
CLK3	30.35	35
NFAT5	7.54	6.82

*significant differential expression pattern between kidney chromophobe and normal kidney tissues

Table 4. Expression values of renal cell carcinoma-associated ceRNAs involving T-UCR between renal clear cell carcinoma and normal kidney tissue.

Gene ID	Renal clear cell carcinoma	Normal kidney
PTBP2	8.33	7.15
NRXN3*	2.25	1.09
CLK3	37.42	27.7
NFAT5	5.91	8.74

*significant differential expression pattern between renal clear cell carcinoma and normal kidney tissues

Table 5. Expression values of renal cell carcinoma-associated ceRNAs involving T-UCR between renal papillary cell carcinoma and normal kidney tissue.

Gene ID	Renal clear cell carcinoma	Normal kidney
PTBP2	8.33	7.15
NRXN3*	2.25	1.09
CLK3	37.42	27.7
NFAT5	5.91	8.74

the twelfth most frequent cancer type in the world [17, 18]. The prognosis of RCC is still poor despite recent developments in surgical and other novel treatment strategies. Molecular characterization of renal cell carcinomas has led to the definition of particular molecular pathways, genes and miRNAs. Moreover, the increasing knowledge about the functions of miRNAs in the pathogenesis of cancers may give remarkable clue for the determination of potential diagnostic biomarkers and therapeutic targets for RCC. It appears that identification of disease-specific miRNAs may help to better clarify prognostic and therapeutic aspects of renal cell carcinomas [19, 20]. For these reasons, identification of molecular biomarkers for early diagnosis, the surveillance of RCC treatments and classification becomes more of an issue. The aim of this study was to define novel molecular biomarkers for RCC via *in silico* analysis. In this regard, RCC-specific miRNAs, their combinatorial target genes (potential ceRNAs) were determined and those with T-UCR were selected. Subsequently, the relationship between miRNA-mediated ceRNAs and RCC was analyzed by the use of statistical correlation methods.

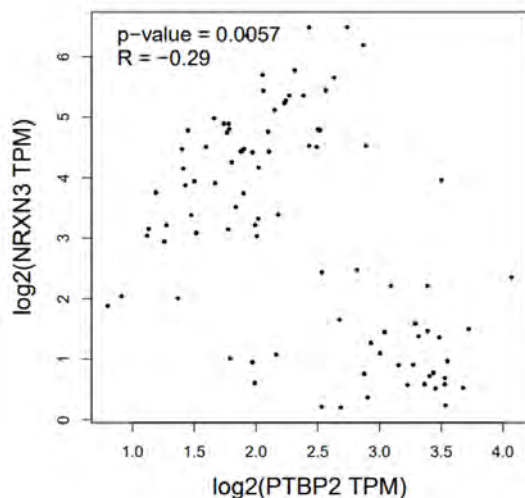


Figure 1. Spearman correlation analysis of NRXN3 and PTBP2 genes with renal cell carcinomas.

In this study, seven miRNAs experimentally associated with RCC were designated through miRTarbase database (Table 1). The genes with ComiR equal abundance score were listed among 1001 genes targeted by these seven miRNAs simultaneously. Then, the genes with T-UCR in exonic regions were determined according to the genes that contain T-UCR [15]. Furthermore, the ones with potential ceRNA activities were identified (Table 2). Afterwards, the genes with remarkable expression differences between RCC and normal kidney tissues from RCC-associated ceRNAs that contain T-UCR were selected. According to this study, PTBP2 gene expression was significantly lower in kidney chromophobe than in normal kidney tissue and NRXN3 gene expression was significantly higher in kidney chromophobe and in renal clear cell carcinoma than in normal kidney tissue. On the other hand, the other genes did not demonstrate any remarkable differential expression patterns. According to the Spearman correlation analysis, NRXN3 and PTBP2 gene pair were shown to be remarkably associated with RCC. PTBP2 gene has not been experimentally associated with renal cell carcinoma in the literature. This study is the first one to associate these two genes (NRXN3 and PTBP2) with RCC.

Neurexins are a class of protein family and encoded by the three mammalian neurexin genes NRXN1, NRXN2, NRXN3. Neurexin-3 protein which is encoded by NRXN3 gene takes a role in cell adhesion and cell recognition and modulates intracellular signaling. It has been reported that polymorphism of NRXN3 gene (rs10146997) and mutations of NRXN3 gene are related with higher breast cancer risk [21, 22]. Forkhead box protein Q1 (FOXQ1) is a transcription factor and takes a role in cancer, aging and development. It has been demonstrated that overexpression of FOXQ1 is associated with various cancer types such as lung cancer and breast cancer and the upregulation of this gene promo-

tes tumor proliferation, invasion and metastasis. It is supposed that FOXQ1 may stimulate tumor growth and invasion via targeting NRXN3 gene in a direct way [23].

Polypyrimidine tract-binding protein 2 (RNA-binding protein) which is encoded by PTBP2 gene binds to clusters of polypyrimidine in pre-mRNAs and involved in the regulation of assembly of the other splicing-regulatory proteins. PTBP2 is implicated in neural differentiation, brain development and function and essential for postnatal survival. Moreover, in neuroblastoma and HeLa cells, PTBP2 modulates alternative splicing of several RNA molecules. Expression of PTBP2 is affected by tissue-specific miRNAs [24]. It has been reported that PTBP2 as a splicing factor induces proliferation and migration in glioma cell lines [25]. It has been known that PTBP2 is highly expressed in cancer cells and acts as a proto-oncogene and promotes the growth of tumor cells [26]. On the other hand, it has been reported that PTBP2 as a target of the oncomir miR-132 acts as a tumor suppressor in glioblastoma cells [27]. Similarly, in a study conducted with *in vitro* experiments, it was shown that PTBP1 (paralog of PTBP2) stimulated proliferation, migration, and invasion in clear-cell renal cell carcinoma [28].

The current study demonstrates for the first time that PTBP2 gene is associated with renal cell carcinoma. The results of *in silico* analysis suppose that PTBP2 gene may have potential tumor suppressor role in RCC and NRXN3 gene may have potential oncogenic activity in RCC.

CONCLUSION

Studies in recent years have showed that miRNAs are promising for the understanding of the molecular mechanisms of cancer pathogenesis. On the other hand, results of various studies for miRNAs in RCC have been contradictory. It has been supposed that variable roles of miRNAs at different stages of RCC or their potencies to interact with numerous targets may affect these discrepancies [29, 30]. Novel biomarkers and studies are required to identify in order to elucidate the basis of miRNA-mediated RCC pathogenesis and novel RNA-mediated cancer treatment strategies. NRXN3 and PTBP2 genes are significantly correlated with RCC for the first time. Further *in vitro* and *in vivo* studies are required in order to illuminate tumor suppressor role of PTBP2 and oncogenic activity of NRXN3 in RCC.

References

1. Okoń K. Pathology of renal tumors in adults. Molecular biology, histopathological diagnosis and prognosis. Polish Journal of Pathology 59 (2008) 129-76.
2. Choueiri TK, Je Y, Cho E. Analgesic use and the risk of kidney cancer: a meta-analysis of epidemiologic studies. International Journal of Cancer 134 (2014) 384-96.

3. Macleod LC, Hotaling JM, Wright JL, Davenport MT, Gore JL, Harper J, White E. Risk factors for renal cell carcinoma in the VITAL study. *The Journal of Urology* 190 (2013) 1657-61.
4. Moch H, Cubilla AL, Humphrey PA, Reuter VE, Ulbright TM. The 2016 WHO classification of tumours of the urinary system and male genital organs- part A: Renal, penile, and testicular tumours. *European Urology* 70 (2016) 93-105.
5. Moch H, Humphrey PA, Ulbright TM, Reuter VE. WHO classification of tumours of the urinary system and male genital organs. Fourth Edition. 2016.
6. Goyal R, Gersbach E, Yang XJ, Rohan SM. Differential diagnosis of renal tumors with clear cytoplasm. *Archives of Pathology and Laboratory Medicine* 137 (2013) 467-480.
7. Huang Y, Shen XJ, Zou Q, Wang SP, Tang SM, Zhang GZ. Biological functions of microRNAs: a review. *Journal of Physiology and Biochemistry* 67 (2011) 129-139.
8. Rama K, Srinivasa Rao PVLN, Bitla AR. MicroRNAs in health and disease. *Journal of Clinical and Scientific Research*. 6 (2017) 25-34.
9. Qi X, Zhang DH, Wu N, Xiao JH, Wang X, Ma W. ceRNA in cancer: possible functions and clinical implications. *Journal of Medical Genetics* 0 (2015) 1-9.
10. Kartha RV, Subramanian S. Competing endogenous RNAs (ceRNAs): new entrants to the intricacies of gene regulation. *Frontiers in Genetics*. 5 (2014) 8.
11. Zambalde EP, Mathias C, Rodrigues AC, de Souza Fonseca Ribeiro EM, Gradia DF, Calin GA, de Oliveira JC. Highlighting transcribed ultraconserved regions in human diseases. *WIREs RNA* 11 (2020) e1567.
12. Mudgapalli N, Shaw BP, Chava S, Challagundla KB. The transcribed-ultra conserved regions: Novel non-coding RNA players in neuroblastoma progression. *Non-coding RNA* 5 (2019) 39.
13. Chou CH, Shrestha S, Yang CD, Chang NW, Lin YL, Liao KW, Huang WC, Sun TH, Tu SJ, Lee WH, Chiew MY, Tai CS, Wei TY, Tsai TR, Huang HT, Wang CY, Wu HY, Ho SY, Chen PR, Chuang CH, Hsieh PJ, Wu YS, Chen WL, Li MJ, Wu YC, Huang XY, Ng FL, Buddhakosai W, Huang PC, Lan KC, Huang CY, Weng SL, Cheng YN, Liang C, Hsu WL, Huang HD. miTarBase update 2018: a resource for experimentally validated microRNA-target interactions. *Nucleic Acids Research* 46 (2018) D296-D302.
14. Davis JA, Saunders SJ, Mann M, Backofen R. Combinatorial ensemble miRNA target prediction of co-regulation networks with non-prediction data. *Nucleic Acids Research* 45 (2017) 8745-8757.
15. Bejerano G, Pheasant M, Makunin I, Stephen S, Kent WJ, Mattick JS, Haussler D. Ultraconserved elements in the human genome. *Science* 304 (2004) 1321-5.
16. Thang Z, Li C, Kang B, Gao G, Li C, Zhang Z. GEPIA: a web server for cancer and normal gene expression profiling and interactive analysis. *Nucleic Acid Research* 45 (2017) W98-W102.
17. Grange C, Brossa A, Bussolati B. Extracellular vesicles and carried miRNAs in the progression of renal cell carcinoma. *International Journal of Molecular Sciences* 20 (2019) 1832.
18. Sanchez-Gastaldo A, Kempf E, del Alba AG, Duran I. Systemic treatment of renal cell cancer: A comprehensive review. *Cancer Treatments Review* 60 (2017) 77-89.
19. Alaghebandan R, Montiel DP, Luis AS, Hes O. Molecular genetics of renal cell tumors: A practical diagnostic approach. *Cancers* 12 (85) 1-24.
20. Li M, Wang Y, Song Y, Bu R, Yin B, Fei X, Guo Q, Wu B. MicroRNAs in renal cell carcinoma: A systemic review of clinical implications (Review). *Oncology Reports* 33 (2015) 1571-1578.
21. Sun HT, Cheng SX, Tu Y, Li XH, Zhang S. FoxQ1 promotes glioma cells proliferation and migration by regulating NRXN3 expression. *PLoS ONE* 8 (2013) e55693.
22. Hirohata H, Yanagawa T, Takaoka S, Uchida F, Shibuya Y, Miyabe S, Tabuchi K, Akagi Y, Hasegawa S, Sakai S, Takeuchi Y, Ishibashi-Kanno N, Yamagata K, Bukawa H. Synaptic-adhesion molecules neurexin 1 and neuroligin 1 as novel prognostic factors in oral squamous cell carcinoma. *Journal of Dentistry and Dental Medicine* 1 (2018) 111.
23. Xiang XJ, Deng J, Liu YW, Wan LY, Feng M, Chen J, Xiong JP. MiR-1271 inhibits cell proliferation, invasion and EMT in gastric cancer by targeting FOXQ1. *Cellular Physiology and Biochemistry* 36 (2015) 1382-1394.
24. Licatalosi DD, Yano M, Fak JJ, Mele A, Grabinski SE, Zhang C, Darnell RB. Ptpb2 represses adult-specific splicing to regulate the generation of neuronal precursors in the embryonic brain. *Genes and Development* 26 (2012) 1626-1642.
25. Cheung HC, Hai T, Zhu W, Baggerly KA, Tsavachidis S, Krahe R, Cote GJ. Splicing factors PTBP1 and PTBP2 promote proliferation and migration of glioma cell lines. *Brain* (2009) 2277-88.
26. Ji Q, Zhang L, Liu X, Zhou L, Wang W, Han Z, et al. Long non-coding RNA MALAT1 promotes tumour growth and metastasis in colorectal cancer through binding to SFPQ and releasing oncogene PTBP2 from SFPQ/PTBP2 complex. *British Journal of Cancer* 111 (2014) 736-748.
27. Lou S, Ji J, Cheng X, Ruan J, Li R, Guo Z. Oncogenic miR 132 sustains proliferation and self renewal potential by inhibition of polypyrimidine tract binding protein 2 in glioblastoma cells. *Molecular Medicine Reports* 16 (2017) 7221-8.
28. Jiang J, Chen X, Liu H, Shao J, Xie R, Gu P, et al. Polypyrimidine Tract-Binding Protein 1 promotes proliferation, migration and invasion in clear-cell renal cell carcinoma by regulating alternative splicing of PKM. *American Journal of Cancer Research* 7 (2017) 245-259.
29. Di Meo A, Saleeb R, Wala SJ, Khella HW, Ding Q, Zhai H, et al. A miRNA-based classification of renal cell carcinoma subtypes by PCR and in situ hybridization. *Oncotarget* 9 (2018) 2092-2104.
30. Ying G, Wu R, Xia M, Fei X, He QE, Zha C, et al. Identification of eight key miRNAs associated with renal cell carcinoma: A meta-analysis. *Oncology Letters* 16 (2018) 5847-5855.

APPENDIX

Table A.1. List of genes that are targeted by seven renal cell carcinoma-associated miRNAs simultaneously.

Gene ID	ComiR equal Abundance score
HS3ST1	0.9066
HECW1	0.9112
CFLAR	0.9157
SLC7A2	0.915
SARM1	0.9153
THSD7A	0.9116
LIG3	0.9065
KDM7A	0.907
CDKL5	0.9181
REV3L	0.9229
IYD	0.912
VTA1	0.9154

ZNF207	0.9232	RRP15	0.9154
IDS	0.9118	POLR1A	0.9117
BTBD7	0.907	NUCKS1	0.9117
MBTD1	0.9138	HS3ST1	0.9066
DCN	0.9195	HECW1	0.9112
NRXN3	0.9196	CFLAR	0.9157
NDUFS1	0.9121	SLC7A2	0.915
SEC63	0.9112	SARM1	0.9153
SNX1	0.912	THSD7A	0.9116
SLC39A9	0.9143	LIG3	0.9065
IKZF2	0.9208	KDM7A	0.907
UBA6	0.912	CDKL5	0.9181
VCL	0.9108	REV3L	0.9229
CUL3	0.9204	IYD	0.912
TLL1	0.9147	VTA1	0.9154
INPP4A	0.9223	ZNF207	0.9232
RAB27B	0.9196	IDS	0.9118
ADAM28	0.9067	BTBD7	0.907
DCUN1D1	0.9155	MBTD1	0.9138
PREX2	0.9068	DCN	0.9195
HDAC9	0.9196	NRXN3	0.9196
RSF1	0.9217	NDUFS1	0.9121
CELF2	0.9072	SEC63	0.9112
ADAMTS6	0.9069	SNX1	0.912
SLC4A8	0.918	SLC39A9	0.9143
PTGER3	0.9068	IKZF2	0.9208
HEBP2	0.9232	UBA6	0.912
SIKE1	0.9112	VCL	0.9108
FNIP2	0.9108	CUL3	0.9204
AP5M1	0.9232	TLL1	0.9147
KIF1B	0.9151	INPP4A	0.9223
EIF2AK2	0.9155	RAB27B	0.9196
KMT2C	0.9238	ADAM28	0.9067
SOAT1	0.9175	DCUN1D1	0.9155
BCAT1	0.918	PREX2	0.9068
PRDM6	0.912	HDAC9	0.9196
NCKAP1	0.924	RSF1	0.9217
MON2	0.9217	CELF2	0.9072
EPN1	0.9219	ADAMTS6	0.9069
CDON	0.9067	SLC4A8	0.918
HIPK2	0.9225	PTGER3	0.9068
GNAI3	0.924	HEBP2	0.9232
WDR3	0.9206	SIKE1	0.9112
MYLK	0.9202	FNIP2	0.9108
SNAP91	0.915	AP5M1	0.9232
CYB5R4	0.9071	KIF1B	0.9151
ASB1	0.9118	EIF2AK2	0.9155
SLC9A7	0.9198	KMT2C	0.9238
CD84	0.9071	SOAT1	0.9175
ATXN3	0.9237	BCAT1	0.918

PRDM6	0.912	TMED8	0.907
NCKAP1	0.924	PPM1A	0.9197
MON2	0.9217	SIX4	0.9147
EPN1	0.9219	DICER1	0.9219
CDON	0.9067	ZC3H14	0.9238
HIPK2	0.9225	PCNX	0.9116
GNAI3	0.924	RPS6KA5	0.9241
WDR3	0.9206	YY1	0.9196
MYLK	0.9202	RNF24	0.9207
SNAP91	0.915	NDUFAF5	0.9108
CYB5R4	0.9071	CDS2	0.9198
ASB1	0.9118	VAPA	0.9177
SLC9A7	0.9198	ST8SIA5	0.9155
CD84	0.9071	CEP192	0.9121
ATXN3	0.9237	MIB1	0.9208
RRP15	0.9154	XIAP	0.9206
POLR1A	0.9117	ZC3H12B	0.911
NUCKS1	0.9117	FGF14	0.9225
SH3BP2	0.9118	NDFIP2	0.9111
C14orf166	0.9153	FGF9	0.9105
KLHL42	0.9149	DGKH	0.9234
PTPN4	0.9228	KATNAL1	0.9119
MAVS	0.9198	INTS6	0.9234
ZBTB25	0.9224	NFAT5	0.9181
GPATCH2L	0.9238	SLC7A6	0.9151
IRAK3	0.9119	CMC2	0.9155
ZNF268	0.9181	MLYCD	0.9198
TNRC6A	0.9198	KNOP1	0.9205
OSBPL8	0.9115	ATP8B4	0.9068
WDR7	0.9218	DTWD1	0.9234
TXNL1	0.9154	SLC30A4	0.9118
NA	0.9154	MYEF2	0.9121
RGS17	0.9176	ZDHHC2	0.9174
AGO1	0.918	FZD3	0.92
RFFL	0.915	UBE2W	0.9154
NUP50	0.9107	ERI1	0.911
SEC22C	0.9149	MTMR9	0.9175
CBX5	0.9199	FCGRT	0.9077
FKBP5	0.9154	DMPK	0.9216
MTAP	0.912	ELL	0.9103
CECR2	0.9067	AVL9	0.917
MAPK1	0.9217	GTPBP10	0.9207
ADRBK2	0.9179	CDK6	0.9122
MIEF1	0.9146	ITGB8	0.9148
TNRC6B	0.9236	MPP6	0.9154
KIAA0930	0.9066	TFEC	0.9196
DESI1	0.9141	LMBR1	0.9118
KCNK10	0.9153	PLEKHA8	0.9207
NIN	0.9171	RBM28	0.9229
DDHD1	0.9181	TMEM106B	0.9074

FSD1L	0.9227	QKI	0.9218
NCS1	0.9107	CLIC5	0.915
ATRNL1	0.9149	TBX18	0.9191
RAB11FIP2	0.921	SEMA5A	0.918
PLEKHA1	0.9236	RNF130	0.9072
BMPR1A	0.9156	CDH6	0.9178
CPEB3	0.9153	NPR3	0.9113
MTPAP	0.911	PRLR	0.9155
CCNY	0.9106	SKP1	0.9209
TSPAN14	0.921	PPP2CA	0.9108
NUFIP2	0.9199	LIFR	0.9071
FBXL20	0.9073	RARS	0.912
CPD	0.9152	WWC1	0.9163
LUC7L3	0.9152	SMAD5	0.9152
SMURF2	0.9154	ARMC8	0.9099
TMEM33	0.912	XRN1	0.9068
DCUN1D4	0.9066	FXR1	0.9217
GAB1	0.9153	HEMK1	0.9074
TRIM2	0.9173	ACVR2B	0.9236
CLNK	0.9065	INO80D	0.9218
WHSC1	0.9154	PIKFYVE	0.9145
CTSC	0.9068	LANCL1	0.9099
CBL	0.9155	GGCX	0.9115
PVRL1	0.9107	KDM3A	0.9153
HIPK3	0.917	STRN	0.9117
FBXO3	0.9197	PRKD3	0.9101
SLC1A2	0.9156	KYNU	0.9239
SOX6	0.9069	ORC4	0.9176
LIN7A	0.922	AAK1	0.923
PPM1H	0.9116	PLEKHA3	0.92
KCNA1	0.9194	PARD3B	0.9067
C12orf49	0.9119	RALGPS2	0.9215
CAND1	0.912	KCNC4	0.9219
CPSF6	0.9116	RAP1A	0.9066
KRR1	0.9229	C1orf21	0.9181
NT5DC3	0.9177	SLC35D1	0.915
ST8SIA1	0.9179	TROVE2	0.9153
FRK	0.9229	TTF2	0.9154
RWDD1	0.9065	TMED5	0.9149
CEP85L	0.9212	DR1	0.9209
SASH1	0.9167	PTBP2	0.921
SOD2	0.9181	DIEXF	0.9203
MDGA1	0.9119	RCAN3	0.9068
GPR63	0.917	PROX1	0.9069
FBXL4	0.9152	RCN2	0.9066
E2F3	0.9138	STAG1	0.9174
SIM1	0.9069	CAMSAP2	0.9138
KIAA1244	0.918	ATF6	0.9115
SLC16A10	0.9228	CREB1	0.9069
PHACTR2	0.9217	FILIP1	0.9146

FBXO30	0.9179	AGO3	0.9237
MED28	0.9218	PCNXL4	0.9237
SLC16A7	0.9199	TRMT5	0.9142
KLF12	0.9229	BCL11B	0.9114
PCDH17	0.9173	MASP1	0.9102
CCND2	0.9068	HELB	0.9218
ELL2	0.917	RAP1B	0.9225
FKBP15	0.9114	RAB3IP	0.9121
ONECUT2	0.921	PTPRB	0.9067
YLPM1	0.9111	DYRK2	0.9198
AREL1	0.9104	FOXP2	0.9069
RBM25	0.9111	MKLN1	0.9199
NRDE2	0.9155	NDUFA5	0.9195
YIPF4	0.9218	MYO5C	0.9146
OGFRL1	0.9198	TTBK2	0.9197
PRLHR	0.9145	ICE2	0.912
WDR11	0.9109	FAM63B	0.9179
PANK3	0.9156	SPCS3	0.9167
TEK	0.9108	KIF1C	0.9139
TARDBP	0.911	CCNT1	0.9215
PAPD5	0.9179	TULP4	0.9065
NAA50	0.9152	PRRG1	0.9144
CD80	0.9139	GFAP	0.9177
ZMYM2	0.9177	RLIM	0.9118
GTDC1	0.9155	GRSF1	0.9068
ACVR2A	0.9201	XPO4	0.9208
SERAC1	0.9069	CHRM3	0.9118
ODF2L	0.9173	SCO1	0.9121
FAM126A	0.9181	MPRIP	0.9155
MED13L	0.9073	DCLK1	0.9071
RASSF8	0.9202	FAM83F	0.9219
NLN	0.907	TRPM1	0.9109
USP45	0.9117	SYT6	0.9147
FAM199X	0.907	WNT2B	0.9121
METTL8	0.9155	KIDINS220	0.9208
ACVR1C	0.9208	RSAD2	0.9158
LPGAT1	0.9154	IL6ST	0.9071
TTPAL	0.9067	NAV1	0.9153
NCOA3	0.9109	CRB1	0.9068
VAPB	0.912	EMP1	0.9151
ZNF831	0.9173	SOX5	0.9174
RAB22A	0.9071	KLRD1	0.9234
BCAS4	0.9068	DSC2	0.9228
ATP8A1	0.9222	ELP2	0.9153
SSR1	0.9199	CLOCK	0.9217
ATXN1	0.9155	DZIP1	0.9171
EFNB2	0.9108	ARHGAP32	0.9117
ATP5S	0.9154	KLB	0.9101
GTF3C4	0.912	APC	0.9228
CEP250	0.9222	HRK	0.9114

GDF11	0.912	KCNH5	0.9209
ESPL1	0.9149	SLC24A4	0.9178
REPS1	0.9067	FGF7	0.9203
USP15	0.9229	BNIP2	0.9175
CPM	0.9065	TSPAN3	0.9065
MDM2	0.9181	NCOA2	0.9147
NTPCR	0.9116	IGF1R	0.907
FAM129A	0.9105	ABHD2	0.9177
REV1	0.9112	NTRK3	0.9234
GCC2	0.9154	FTO	0.918
ITM2B	0.9198	NKD1	0.9178
TMOD1	0.9095	CDH11	0.9167
TFAP2A	0.9124	KSR1	0.9115
KIAA0319	0.9133	VPS53	0.9157
RAB30	0.9198	ASXL3	0.9068
PPP2R1B	0.9147	GAREM	0.9111
ITGA11	0.9116	RNF165	0.9066
ADAM10	0.9072	ZFP14	0.9116
SEMA6D	0.9142	IFNAR1	0.9109
TLL7	0.9066	SIK1	0.9192
DBT	0.9199	WTIP	0.9121
EPT1	0.912	PRKACB	0.914
PREPL	0.9109	ZNF697	0.9108
ENTPD1	0.9218	POU2F1	0.9226
HECW2	0.9071	ILDR2	0.9219
SSFA2	0.9067	SDHC	0.9157
ABI2	0.924	ABL2	0.918
ITGAV	0.911	TOR1AIP1	0.9197
USP8	0.9219	SNX27	0.9069
SECISBP2L	0.9107	GABPB2	0.9207
TMOD3	0.9223	SYT14	0.9157
PCDH10	0.9149	VASH2	0.914
FGF2	0.9227	GATAD2B	0.9116
BMP2K	0.9171	LYST	0.918
CNOT6L	0.9227	ASXL2	0.912
METTTL20	0.9113	SPOPL	0.9111
ETNK1	0.9151	GULP1	0.9072
NDUFA9	0.9154	UNC80	0.9146
LLPH	0.9179	RBMS3	0.9117
GLIPR1	0.9116	OSBPL10	0.9117
PHLDA1	0.9107	PTPRG	0.9149
TMTC3	0.9065	LIMD1	0.9224
GAS2L3	0.9139	ZNF660	0.9065
NUPL1	0.9114	NXPE3	0.9118
WDFY2	0.9121	LPP	0.9234
SRRM4	0.9149	TIFA	0.9112
NOVA1	0.907	GLRA3	0.9072
C14orf37	0.92	RPL37	0.9179
SYT16	0.9219	SSBP2	0.9071
ESR2	0.9115	PPIP5K2	0.921

BDP1	0.9141	AKRIC2	0.9098
TNFAIP8	0.9117	KIN	0.915
GFOD1	0.9154	WWC2	0.915
IRAK1BP1	0.9174	BICD1	0.9151
MMS22L	0.9112	GABRA2	0.9153
FAXC	0.9209	CACUL1	0.9218
TBC1D32	0.9151	RABGAP1L	0.9114
CLVS2	0.9236	FAM168B	0.9067
RNF217	0.9234	PTPN14	0.9229
SHPRH	0.9156	MGAT5	0.9144
CREB5	0.9217	PDK1	0.9225
EGFR	0.9178	UHMK1	0.912
ATXN7L1	0.91	GUCY1A2	0.9157
TMEM168	0.9117	CCDC50	0.9217
NLGN4X	0.9101	CAMK4	0.9219
LANCL3	0.9122	GPR180	0.9155
CASK	0.9237	WDR78	0.9198
FBXO25	0.9073	FARP1	0.9069
ERLIN2	0.9144	ZNF117	0.9232
TACC1	0.9194	RAB3C	0.918
WHSC1L1	0.9176	SREK1IP1	0.9217
PMP2	0.9141	SCOC	0.9204
VLDLR	0.9222	HNRNPU	0.9107
NFIB	0.912	ASAP1	0.9069
CEP78	0.9071	PLEKHG4B	0.9067
NTRK2	0.9152	CNKSR3	0.9238
SNX30	0.9197	DGKE	0.9155
NR6A1	0.9115	HS2ST1	0.9206
WDR31	0.9102	CACNA2D1	0.9109
USP6NL	0.921	PPP2R5E	0.9175
ZEB1	0.9236	CHST9	0.9181
EIF4EBP2	0.9155	OTULIN	0.907
CNNM2	0.9225	UBASH3B	0.9068
ADAM12	0.9194	TBRG1	0.9107
SLC5A12	0.9065	PITPNC1	0.9149
CELF1	0.9152	PRKCA	0.9153
SESN3	0.9179	ABCA5	0.9107
TENM4	0.9066	ENAH	0.92
ZC3H12C	0.9154	CCSAP	0.9066
HMGA2	0.9209	PDE1C	0.912
CDH8	0.9224	ADAMTS5	0.912
LPHN3	0.9207	TTC39B	0.9199
CD226	0.9073	C16orf87	0.9119
FREM2	0.9155	MIER3	0.9116
THRB	0.9151	FAM126B	0.9228
GXYLT1	0.9177	SLC26A2	0.9119
AKAP6	0.9071	AFF2	0.9218
ADAMTS12	0.9171	GNAQ	0.9152
FER	0.918	MMP16	0.9237
FAM160B1	0.9166	KCNMA1	0.9155

N6AMT1	0.9147	CCDC127	0.9121
PPP2R2B	0.918	CREBRF	0.9152
SAMD8	0.9178	KIF6	0.9153
MYO1E	0.9174	USP49	0.9154
KCNJ6	0.9237	ZNF704	0.9219
KCNJ15	0.9153	FOKK1	0.9207
TAB3	0.9178	DIRAS2	0.9112
DGKI	0.9073	KIAA1958	0.912
UBN2	0.9236	PTCHD1	0.921
AGAP1	0.9118	PCDH19	0.9175
CLSTN2	0.9181	BRWD3	0.9066
SHROOM4	0.9177	SLITRK5	0.9233
ELK4	0.9198	FAT3	0.9221
RUNX1	0.9203	CFL2	0.9216
ZNF230	0.9149	SUGT1	0.9219
ZNF233	0.9163	AMER2	0.9072
ZNF761	0.92	PDZD8	0.9177
TAOK1	0.921	TSC1	0.9194
IL6R	0.9144	RET	0.9102
ACOX1	0.9118	KIAA1462	0.9145
ZYG11B	0.9213	TTC7B	0.9226
PRKAA2	0.9121	TC2N	0.9107
GMEB1	0.911	CPSF2	0.9073
AK4	0.9117	HIF1AN	0.92
NFIA	0.9217	AVPR1A	0.9066
ZNF326	0.9072	FRS2	0.9117
ARPC5	0.9154	ARIH1	0.924
DDR2	0.9178	STXBP4	0.923
ARL5A	0.9116	TRIM44	0.9199
PDLIM5	0.9065	TRIM66	0.9176
CCNYL1	0.9101	PRTG	0.9231
GABRG1	0.9195	PRKCB	0.9115
NIPAL1	0.9196	NA	0.9209
EIF4E3	0.9199	TMED3	0.9234
LRRC58	0.9196	GALR1	0.9122
AZI2	0.9103	SLFN5	0.9071
NFASC	0.9178	TMEM170A	0.911
PPM1L	0.9238	ZBTB39	0.911
RYBP	0.9216	GREM1	0.9209
PPM1K	0.9115	FBXO22	0.918
GMPS	0.9231	TBC1D16	0.9197
SMIM14	0.9153	MYO5B	0.917
RPP14	0.907	ZNF226	0.9195
GRIK3	0.9152	ZNF641	0.9117
INTU	0.9199	TRANK1	0.9112
HSPA4L	0.9223	HOOK3	0.9225
OTUD4	0.9111	MAPK11P1L	0.9153
LMBRD2	0.9196	RFWD3	0.909
C5orf63	0.9151	FNTA	0.9194
CFAP97	0.9101	LDLRAD4	0.9228

SNTB2	0.9228	PEAK1	0.9233
SPRY3	0.9155	NABP1	0.9199
IRS1	0.9177	CHD2	0.9188
MECP2	0.9121	CEP83	0.916
RAB3B	0.9122	SULT1B1	0.9069
B3GALNT1	0.9096	NUDT4	0.9122
SHE	0.9118	SCAI	0.9199
SLC33A1	0.9119	AGFG1	0.9178
PTK2	0.9111	PHC3	0.9218
PLEKHA2	0.9065	UBXN2A	0.9115
C15orf40	0.9072	CD34	0.9071
LUZP1	0.915	CYB561D1	0.9149
REPS2	0.9215	ATP2A2	0.9116
OTUD3	0.9152	TMEM167A	0.9174
MAP3K2	0.9217	C4orf32	0.9121
TMEM154	0.9209	FZD4	0.9193
SIK2	0.9071	PDE12	0.912
RNF150	0.9069	GK5	0.911
USP38	0.9066	VCPIP1	0.9069
LONRF2	0.92	ZNF654	0.9143
NUDCD2	0.9197	CADM2	0.9156
SGCD	0.9231	PPM1E	0.9173
ATF7	0.9148	SMAD2	0.9241
SOCS6	0.9191	ARL10	0.9181
TTLL6	0.9136	PPP2R2D	0.9072
FOXN2	0.9109	DPP10	0.9144
PYGO1	0.9217	ALG10B	0.918
INSR	0.9171	SLC35E3	0.921
KCNK3	0.9148	CREG2	0.9195
CLCN5	0.9119	ZDHHC21	0.9231
APLN	0.9076	UNC119B	0.9111
KSR2	0.9122	JAKMIP2	0.9177
MCC	0.9114	IP6K1	0.9121
ZNF562	0.9157	SPRYD4	0.9209
ATF7IP	0.9175	SYNE3	0.9224
PCDHB1	0.9146	KIAA2018	0.9069
PTEN	0.9198	RNF152	0.9155
MALT1	0.9094	POLE	0.9067
NEGR1	0.9199	ZBTB34	0.9232
CERS6	0.907	RIMKLA	0.918
ARNT2	0.9203	RPS6KA3	0.9151
FUT9	0.9239	CHD9	0.9113
ZNF24	0.912	MIEF2	0.9153
ZMAT3	0.9198	NR2C2	0.9179
CORO1B	0.9098	ZBTB33	0.9104
DCP2	0.9218	ST8SIA3	0.9121
BNC2	0.9232	TBL1XR1	0.915
VANGL1	0.9071	IL17RA	0.9112
STOX2	0.9071	FAM26E	0.9121
SFT2D3	0.9103	C2orf69	0.9092

PDE4DIP	0.9152	GPRIN3	0.921
LCORL	0.9112	SV2B	0.9179
GEN1	0.9179	LSAMP	0.9121
CD28	0.9109	BRWD1	0.9177
EPM2AIP1	0.9175	C16orf52	0.9147
ERBB4	0.9155	KCNQ5	0.9143
CSRNP3	0.9121	PIGP	0.912
KCTD12	0.9067	PTCH1	0.9228
CLK3	0.9179	LRCH3	0.9206
CIITA	0.9069	MARC1	0.9069
AKAP5	0.9067	MKL2	0.907
FAM73A	0.9112	KPNA4	0.9216
SSTR2	0.9194	PCLO	0.9146
PCGF5	0.9178	LYRM7	0.9068
YOD1	0.9213	PPARA	0.9198
CHRM2	0.911	NAP1L1	0.9218
ZNF678	0.9223	AKR1C1	0.9117
PLAG1	0.9222	TSPYL4	0.9107
RFX7	0.9178	SESTD1	0.9199
RNF41	0.9115	FAM9C	0.9116
MGAT4C	0.9241	DCC	0.9117
ZNF716	0.9106	TET3	0.9119
ZNF708	0.9213	LIN28B	0.9193
EXT1	0.9195	ZNF626	0.9149
FIGN	0.9179	ZC3H6	0.9198
CLN8	0.9068	NCR3LG1	0.9115
PAPPA	0.9178	DCUN1D3	0.9116
C16orf72	0.9181	ZNF793	0.9066
GJCI	0.9153	CENPP	0.9155
CADM1	0.9208	ZNF559	0.9096
SLC8A1	0.9226	PDCD1	0.9106
CALN1	0.907	CHM	0.9108
CHST6	0.9151	PTAR1	0.9217
CTNNA3	0.9224	VWC2	0.9122
GRIN2A	0.9156	RPL14	0.9106
FAM46C	0.9102	BEND4	0.912
LHFP	0.9077	LRRK2	0.9177
MACC1	0.9229	PTPLAD2	0.9072
KCTD16	0.9234	SF3B3	0.
B3GALT5	0.9181	TMEM194B	0.9113
ST6GALNAC3	0.9196	IL1RAP	0.9144
PCDH9	0.924	PTPRT	0.9121
AMER1	0.9171	ACADSB	0.9198
SDR42E1	0.9156	LCOR	0.9178
RBM33	0.9069	XPNPEP3	0.9207
FLRT2	0.9241	ZNF471	0.9068
PURA	0.9232	ZNF493	0.9166
ZBTB37	0.9237	FUT4	0.9114
HS6ST3	0.9227	ZNF774	0.9067
RAD51D	0.9176	ZNF765	0.9153

TSC22D2	0.9218	MBD5	0.9117
ESRRG	0.9112	FAM155A	0.9198
GDAP2	0.9227	C9orf170	0.9103
AJAP1	0.9209	ZNF468	0.9195
MYO6	0.9149	PCDHA4	0.9218
HDAC2	0.9218	SLC35B4	0.9214
WNK3	0.9206	TMEM170B	0.9209
SLC30A10	0.9133	CCDC85C	0.9181
ZNF431	0.9225	ITPRIPL2	0.9116
NF1	0.912	DOK6	0.9198
VKORC1L1	0.9067	TMEM200C	0.9197
CD47	0.9065	VGLL3	0.9181
NHLRC2	0.9156	TRIM71	0.9117
SCN8A	0.9173	XKR4	0.9234
FLNA	0.9222	STK38L	0.911
TMEM26	0.9108	C17orf51	0.9224
SRGAP1	0.924	ZNF611	0.9203
ZNF138	0.9217	DENND1B	0.9195
GMFB	0.9198	FGFR1OP	0.9181
ZNF257	0.9227	ARHGAP19	0.9172
DDI2	0.9156	PPP1CB	0.9191
TRIM33	0.9176	DNASE1	0.9176
ZNF655	0.9174	GANC	0.911
DCHS2	0.9104	ZNF891	0.9226
ZNF81	0.9152	LYRM4	0.915
ZNF780A	0.9118	HAUS3	0.9108
PLCG2	0.9108	EML6	0.9092
MBP	0.9072	PEX26	0.9123
DLGAP2	0.9154	SIAH3	0.9152
MRPL42	0.92	APOL6	0.9121
ZNF273	0.9202	ANKRD34C	0.9111
ZNF667	0.9145	SHISA9	0.9068
SVIP	0.9114	N4BP2L2	0.918
CACNA1E	0.918	NA	0.9212
HELZ	0.9209	FMN1	0.918
ASPH	0.9176	PCDHA10	0.9238
GFPT1	0.9178	ATXN7L3B	0.9231
ZNF26	0.9238	PCDHGA6	0.9105
ITSN2	0.9107	SOGA3	0.9156
NUDT16	0.9118	NOX5	0.9153
TLK1	0.9165	CLU1	0.9101
IPO9	0.9217	CUX1	0.9209
SLC5A3	0.9234	FRRS1L	0.912
LRIG2	0.918	TMEM178B	0.9199
MFAP3L	0.9067	GAN	0.9181
RORB	0.9155	DYNLL2	0.907
ZNF525	0.9199	RNF115	0.9179
INF2	0.9234	RASSF5	0.9174
CHIC1	0.9117	GTF2H5	0.9217
BMPR2	0.918	NUDT3	0.9181

GRIN2B	0.9241
ZBTB8B	0.9229
NA	154
SOCS7	0.9118
TRPM1	0.9109
NA	0.9191
PIP4K2B	0.9147
ZNF8	0.9152

Table A.2. The list of genes including T-UCR in their exonic regions according to the study [2].

UCR number	Length (bp)	Gene Name
uc.13	237	EIF2C1
uc.28	355	SFRS11
uc.33	312	PTBP2
uc.45	203	HNRPU
uc.46	217	HNRPU
uc.48	298	PUM2
uc.49	207	BC060860
uc.50	222	SFRS7
uc.61	326	BCL11A
uc.77	296	ZFHX1B
uc.97	442	HAT1
uc.102	338	PTD004
uc.129	212	MBNL1
uc.135	201	AK096400
uc.138	419	SFRS10
uc.143	218	AB014560
uc.144	205	HNRPDL
uc.151	214	ZFR
uc.174	260	MATR3
uc.183	236	FBXW1B
uc.184	230	CPEB4
uc.185	411	CLK4
uc.186	305	HNRPH1
uc.189	573	SFRS3
uc.193	319	SYNCRIP
uc.194	201	EPHA7
uc.203	203	AB067798
uc.208	218	TRA2A

uc.209	250	TRA2A
uc.233	266	CENTG3
uc.263	207	HNRPK
uc.264	267	HNRPK
uc.280	220	PBX3
uc.282	207	GRIN1
uc.285	232	CARP-1
uc.292	217	MLR2
uc.313	231	TIAL1
uc.324	225	C11orf8
uc.330	207	RBM14
uc.331	218	DLG2
uc.333	270	FLJ25530
uc.338	223	PCBP2
uc.339	252	ATP5G2
uc.356	251	MBNL2
uc.375	300	MIPOL1
uc.376	290	PRPF39
uc.377	217	PRPF39
uc.378	251	NRXN3
uc.393	275	CLK3
uc.395	249	RBBP6
uc.406	211	NFAT5
uc.409	244	L32833
uc.413	272	BC060758
uc.414	246	THRA
uc.419	289	SFRS1
uc.436	210	TCF4
uc.443	239	HNRPM
uc.454	208	SLC23A1
uc.455	245	RNPC2
uc.456	320	SFRS6
uc.471	239	DDX3X
uc.473	222	NLGN3
uc.474	210	ZNF261
uc.475	397	OGT
uc.477	209	RAB9B
uc.478	252	GRIA3
uc.479	302	GRIA3

Adsorption Of Methylene Blue from Aqueous Solution with Sulfuric Acid Activated Corn Cobs: Equilibrium, Kinetics, and Thermodynamics Assessment

Pinar Bozbeyoglu¹  Celal Duran²  Cemalettin Baltaci³  Ali Gundogdu⁴ 

¹Gumushane University, Department of Biotechnology, Gumushane, Turkey

²Karadeniz Technical University, Department of Chemistry, Trabzon, Turkey

³Gumushane University, Department of Food Engineering, Gumushane, Turkey

⁴Karadeniz Technical University, Department of Pharmacy Services, Trabzon, Turkey

ABSTRACT

Three adsorbents with different characteristics were produced in this study by activation of sulfuric acid with different concentrations, from corn (*Zea mays* L.) cobs, which is an agricultural waste by-product resulting from harvesting. After characterization by the parameters such as Boehm titration, determination of pH-pHpzc, and methylene blue – iodine number, and IR analysis, their methylene blue adsorption potentials from aqueous medium were investigated based on equilibrium, kinetics, and thermodynamics evaluations. This study aims to examine the effects of relatively dilute and concentrated acids on the activation process and to gain an economic value to waste materials through the production of a new adsorbent. It was observed that the initial solution pH did not have a significant effect on the adsorption efficiency. The adsorption process reached the equilibrium at the end of the first 120 minutes, and the kinetic data fit the pseudo-second-order kinetic model. Langmuir adsorption capacity (295.5 mg/g) of the adsorbent produced by activating with 50% sulfuric acid was found higher than those produced with 75% and 98% acids. An increase in ambient temperature effected the adsorption positively. As a result, in this study, very low-cost adsorbents were produced from the waste by-product corn cobs, and a new approach was proposed for cleaning wastewater containing dyestuffs.

Keywords:

Adsorption; Corn cobs; Methylene blue; Removal; Sulfuric acid activation

INTRODUCTION

Natural waters are getting more and more polluted due to the activities of many industry organizations such as juice, coffee, and cereal processing plants. The contamination of the water used for drinking and other purposes by partially treated or untreated discharges from chemical industries, petrochemical industries, oil refineries, oil spills, rolling steel mills, unrefined domestic sludge, and pesticide runoff threaten both human health and environmental health [1]. Dyestuffs, one of many different types of contaminants, are among the chemicals that pose this threat. Synthetic dyestuffs are widely used worldwide in textile staining processes. Synthetic dyestuff classes are the azo type, including reactive, disperse, and acid dyes. Azo dyes account for 65% of the total dye production in the world [2]. Today, biological treatment is the most widely used method to decompose dye waste. However, this process is not very successful in removing dyes effectively. For this reason, dyes

are often found chemically unchanged in the waters of wastewater treatment plants; and they can both contaminate drinking water and cause potential aquatic toxicity by condensation in sludge.

In the textile industry, about 1 m³ (1000 mL) of water is required for every 1 ton (1000 kg) of clothes to be stained. The discharge of wastes of these processes into rivers and lakes can have toxic effects on aquatic life. Color impedes the penetration of light into the water and thus impedes the growth of biota by retarding photosynthetic activity. It also chelates metal ions in the water, causing micro-toxicity for aquatic life [3]. It should be borne in mind that even 1.0 mg/L concentration of any dye in drinking water can impart a significant amount of color making it highly unsuitable for human consumption. Most of the dyes used in industrial applications are very stable against photo-degradation, biodegradation and oxidizing agents. Today, several physi-

Article History:

Received: 2020/09/02

Accepted: 2020/09/17

Online: 2020/09/30

Correspondence to: Ali Gundogdu,
Karadeniz Technical University, Macka
Vocational School, Pharmacy Services,
61750, Macka, Trabzon, TURKEY
E-Mail: a.ramazan.gundogdu@gmail.com
Phone: +90 462 512 35 35
Fax: +90 462 512 35 52

cal and chemical processes are used to treat wastewater. However, many of these processes are expensive and cannot be used effectively to treat a wide variety of dye effluents [4,5].

Activated carbon-based industrial processes are the most widely used methodologies as they have excellent removal efficiency for dyes and of course many other types of contaminants, but the use of these processes is often limited due to the high cost of commercial activated carbons and high energy-process [6]. Therefore, it is inevitable to develop new adsorption-based technologies that can be a powerful alternative to activated carbon-based ones. Number of alternative methods are increasing day by day to reduce costs and also increase efficiency, or at least to compete with other methodologies. For this purpose, studies on lignocellulosic agricultural wastes or by-products are available in the literature. These agricultural wastes can be used inexpensively as a direct adsorbent or by converting into activated carbons or by activating with various agents to improve their adsorption capabilities. This type of agricultural waste by-products can be easily obtained from many industrial establishments, or farming peasants at very low costs.

Hundreds of agricultural-based waste by-products such as corn cob, barley straw [7], carrot waste [8], alder sawdust [9], rice husks, olive pomace, orange waste [10], Kiwicumcumber-potato peel [11], sago waste [12], coffee husk [13], peanut shells [14], rice husk waste, coconut shell [15], hazelnut husk [16], and tea-industry waste [17] are used either directly or by converting into activated carbons to remove various pollutants from aqueous medium. In this way, very low cost and high-performance adsorbents can be obtained from these by-products with no economic value.

In this study, three different adsorbents were produced from corn cobs (CCs) by chemical activation using the different concentrations of sulfuric acid. CCs is a waste by-product after processing of the maize plant (*Zea Mays* L.) cultivated in almost every region of Turkey as well as all over the world. In the 2018/2019 period, approximately 5.7 million tons of corn were produced in Turkey [18]. Significant amounts of waste CCs are released from these products. There is no document that these wastes are used in any area.

The potential of these adsorbents to remove methylene blue (MB), a basic cationic dyestuff, from aqueous solution was investigated in this study. MB is one of the most used dyestuffs in the medical field, but also in dyeing wool, wood, paper, silk and leather, painting, and ink dyes. However, MB may cause some harmful effects on human health. A person exposed to MB may experience heart palpitations, vomiting, shock, cyanosis, known as blue disease, jaundice, arm, and leg paralysis, and tissue gangrene [19–21]. MB is very sensitive to heat. When left at 110 °C for 2 hours, it emits a bad odor

and loses about 14% mass. Anhydrous MB is 94.5% pure and creates foam in aqueous solution [22]. Besides, MB, which has a maximum absorption wavelength of 668 nm, is widely used as a model adsorbate to test the adsorption capacity of the relevant adsorbent or the degradation potential of any TiO₂ film [23,24]. Also, one of the characterization steps of a newly produced adsorbent is of course determination of MB number as well as I₂ number.

In a study in the literature, although it was reported that a new adsorbent was obtained from CCs by activating with concentrated sulfuric acid [25], three different adsorbents were obtained by using different concentrations of sulfuric acid in this study. Relatively dilute acids dissociate more than concentrated acids. Therefore, the adsorbent obtained by activating with relatively dilute acid is expected to have richer surface functional groups. The primary aim of this study is to prove that the adsorbents produced by changing the concentration of sulfuric acid used for activation of CCs have different adsorption capabilities and that dilute acids perform better than concentrated ones. In other words, this study aims to monitor the development and reorganization of adsorption sites on the adsorbent surface containing functional groups and to reveal the adsorption capabilities of the adsorbents produced by changing the concentration of the activation agent. Since we do not find such a study in the literature, we think that this work is original, and the novelty is high. New adsorbents have been produced from CCs, which are an agricultural waste by-product, at almost zero cost, thereby gaining an economic value for such a worthless material. Besides, we believe that this study is very valuable as it is expected that these adsorbents will contribute to the prevention of environmental water pollution.

MATERIAL AND METHOD

Chemicals, Solutions and Matter-Materials Used

All chemicals used in the experimental stages were of analytical purity and were purchased from Merck (Darmstadt, Germany). Ultra-pure water was used in all experiments. Methylene blue (MB) used as an adsorbate in adsorption tests is a basic cationic dye. Other known names of MB, whose empirical Eq. and molar mass are C₁₆H₁₈ClN₃S and 319.85 g/mol, respectively, are methylothioninium chloride, CI 52015, and basic blue 9 [26]. Its molecular structure is shown in Fig. 1.

The appropriate amount of MB was weighed and dissolved in water, and its stock solution of 2500 mg/L was prepared. The six consecutive solutions of 50, 100, 250, 500, 750 and 1000 mg/L were prepared from this stock solution by diluting. Capped PP Falcon tubes of 15- and 50-mL volumes were used in the adsorption tests.

A vacuum filtration system (Isolab, GmbH) was used to separate the adsorbate molecules (MB) and adsorbent particles (CCs-SA) from each other. In this setup, the nitrocellulose membrane (Sartorius Stedim Biotech, France) with a pore size of 0.45 μm was used as a filter paper.

Devices Used

In this study, MB concentrations were determined in a Unicam UV-2 model Spectrophotometer device. Adsorption tests were made with a mechanical shaker (Edmund Bühler GmbH), pH adjustments were made with a Hanna pH-211 model benchtop pH meter (Hanna Inst., USA) and substance weighing was done with a BP1106 model analytical balance (Sartorius Stedim Biotech, France). The IR spectra of the adsorbents were obtained from a Perkin Elmer 1600 FT-IR spectrophotometer (4000–400 cm^{-1}) device.

Preparation of the Adsorbents:

The corn cobs (CCs) were obtained from Akçaabat district of Trabzon province-Turkey. After separating the grains, the remaining CCs were dried in an oven at 105 $^{\circ}\text{C}$ for 24 hours and stored in a desiccator. The dried CCs wastes were used after being milled and sieved to a size of approximately 4 mm.

20 g of CCs were taken and 20 g of H_2SO_4 solutions of three different concentrations (98%, 75% and 50% by weight) were added separately (mixing ratio 1:1). After mixing the mixtures thoroughly, they were kept in the oven at 200 $^{\circ}\text{C}$ for 24 hours. The activated adsorbents were first washed thoroughly with boiling distilled water to remove acid residues and then neutralized by treatment with a 1% NaHCO_3 solution for 24 hours. After the adsorbents were filtered, they were washed again with ultrapure water and finally they were used after drying in the oven at 105 $^{\circ}\text{C}$ for 24 hours [27]. The three different adsorbents obtained were coded as CCs-SA₅₀, CCs-SA₇₅, and CCs-SA₉₈.

Characterization of the Adsorbents:

Analysis of The Surface Acidic Functional Groups (SAFG) of The Adsorbents

The surface acidic functional groups of the adsorbents are mainly examined in three groups as carboxylic, lactic and phenolic. The amounts of these groups in mmol can be determined by Boehm Titration. With 0.05 g adsorbent, 0.1 N 50 mL NaOH, NaHCO_3 and Na_2CO_3 solutions were treated separately for 24 hours. At the end of the process, after the samples were filtered through the cellulose nitrate membrane with pores 0.45 μm in size, the filtrates were titrated with 0.1 N HCl [28].

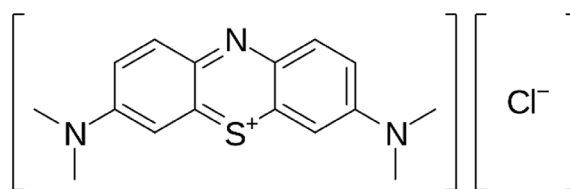


Figure 1. Molecular structure of methylene blue.

Total surface acidic groups (lactic, phenolic and carboxylic) are all determined by NaOH-neutralization. Lactic and carboxylic groups are determined by Na_2CO_3 -neutralization, and only carboxylic groups by NaHCO_3 -neutralization [29].

The amount of surface acidic functional groups in mmol is calculated by the following Eq. 1:

$$SAFG = \frac{[N \times (T_b - T) \times 2.5]}{m} \quad (1)$$

where SAFG means surface acidic functional groups (mmol/g). N is the normality of the titrant solution (HCl). T_b is the titrant consumption (mL) for blank experiments. T represents the titrant consumption (mL) for the different solutions, and m is the amount of adsorbent (g).

pH and pH_{pzc} Values of The Adsorbents

The pH values of the adsorbents were determined by measuring the filtrate with a pH meter after treating the 0.05 g adsorbent with 10 mL ultrapure water heated to boiling point for 24 hours [30].

The pH of an adsorbent at the neutral charge point (pH_{pzc} , pH of point of zero charge) or at the isoelectric point means the pH value at the point where the net charge on the surface of adsorbent is zero. If $\text{pH} > \text{pH}_{\text{pzc}}$, adsorption of cationic species on the adsorbent is more suitable. In the case of $\text{pH} < \text{pH}_{\text{pzc}}$, on the contrary, adsorption of anionic species is more suitable. Knowing the pH_{pzc} value, an appropriate value of the solution pH can be estimated for the adsorption of cationic or anionic species without the need for a wide pH scan. Below pH_{pzc} , the net charge on the surface of an adsorbent is positive and above it is negative.

For the determination of pH_{pzc} values of the adsorbents, a series of 0.1 M NaCl solutions in which their initial pH values were adjusted between 2.0 and 10.0 with 0.1 M NaOH or 0.1 M HNO_3 were treated with 0.1 g of the adsorbent for 24 hours. At the end of the process, after the adsorbent and solution were separated by filtration, the equilibrium pH values of the filtrates were measured with a pH meter. A graph was drawn by subtracting the equilibrium pH values from the initial pH values and placing them on the y-axis (ΔpH) and the initial pH values on the x-axis. The point where the graph cuts the x-axis from the value where y is zero was recorded as pH_{pzc} [31,32].

Methylene blue and Iodine Numbers of The Adsorbents

The methylene blue number (MBn) is a measure of the ability of an adsorbent to adsorb large molecules. This test is one of the most important tests that characterize activated carbons. To find MBn in this study, 10 mL of 1000 mg/L MB solution and 0.02 g of each adsorbent were treated for 12 hours. After the mixture was filtered through a 0.45 μm nitrocellulose membrane, the MB concentration remaining without adsorbed in the filtrate was determined by UV-Vis spectrophotometer. Then, the quantity of MB adsorbed per gram adsorbent (mg/g) was calculated with the help of Eq. 2 below [22].

$$MB_n = \frac{(C_o - C_e)}{m} x V \quad (2)$$

where MBn, it means methylene blue number. C_o and C_e are the initial and equilibrium methylene blue concentrations (mg/L), respectively. V is the solution volume (mL) and m is the adsorbent mass (g).

Iodine (I_2) is a much smaller molecule compared to MB. The high number of I_2 gives important information about the adsorbents' ability to adsorb small atoms or molecules such as metal ions [33]. The increase in surface area, porosity and active groups is a factor that increases I_2 adsorption. The following procedure was used to determine the I_2 number of the adsorbents:

0.2 g of the adsorbent was weighed into a 50 mL pp Falcon tube. 40 mL 0.1 N standard iodine solution (12.7 g I_2 and 19.1 g KI dissolved in 1 L water in total) was added and carefully shaken for 30 \pm 1 h. After the mixture was filtered, the amount of unadsorbed iodine in the solution was titrated with a 0.1 N standard sodium thiosulfate solution. A new 40 mL iodine solution was taken, and the consumption was recorded as a blank by titrating with 0.1 N standard sodium thiosulfate solution without adding the adsorbent and shaking [34]. The I_2 numbers of the adsorbents were calculated by the following equations (Eq.s 3, 4 and 5):

$$I_2 \text{ number (mg / g)} = FxC \quad (3)$$

$$F = \frac{126.93xN_{I_2}xV_f}{mxV_k} \quad (4)$$

$$C = V_k - V_t \quad (5)$$

where N_{I_2} refers to the normality of the standard iodine solution. V_f and V_k mean the filtrate volume (mL) and the standard thiosulfate consumption (mL) for the samples, respectively. m is the adsorbent mass (g).

IR analysis of the adsorbents

Infrared spectrometry (IR) is a frequently used method to illuminate the chemical structures and surface groups

of various adsorbents. In this study, IR spectra were taken by FT-IR (Fourier Transform–Infra-Red) spectrometry for CCs, CCs-SA₅₀, MB loaded CCs-SA₅₀ and MB, and the changes occurring before and after adsorption were examined.

Approximately 10 mg of the well-dried adsorbents were taken into the chamber of the device and IR spectra were taken directly.

Adsorption Tests

In this study, three different adsorbents were obtained by activating the corn cob with sulfuric acid at different concentrations. The adsorption performance of a total of four adsorbents from aqueous solution together with the original corn cob was tested. As the adsorbate, methylene blue (MB), a basic cationic dye, was used to represent the total dyes in the adsorption studies.

0.050 g of the adsorbents were weighed and mixed with 10 mL of 6 different MB solutions between 50-1000 mg/L and treated separately until equilibrium was reached. Then, adsorbent particles and adsorbate molecules were separated from each other with the help of a vacuum filtration device. The concentrations of MB remaining in the filtrate were determined at 668 nm in a UV-Vis spectrophotometer in the mg/L concentration unit. The results were then converted to mg/g by Eq. 6 and % by Eq. 7.

$$Q_e \text{ (mg / g)} = \frac{C_o - C_e}{m} x V \quad (6)$$

$$Q_e \text{ (%) } = \frac{C_o - C_e}{C_o} x 100 \quad (7)$$

where Q_e (mg/g) and Q_e (%) mean the amount of MB molecules adsorbed on the adsorbent at equilibrium. C_o and C_e represent the initial and equilibrium MB concentrations (mg/L), respectively. m is the adsorbent mass (g).

RESULTS AND DISCUSSION

Characterization Results

The results obtained by Boehm titration applied to determine the surface functional groups of the adsorbents are given in Table 1. The table contains quantitative values of the carboxylic, phenolic and lactonic groups of the adsorbents in mmol, and as can be seen, the adsorbents have very rich surface groups. When the surface acidic groups of all adsorbents are compared with each other, CCs-SA₅₀ is the richest adsorbent in total acidic groups. That is, as the concentration of H_2SO_4 used in production increases, the total amount of surface functional groups decreases (Table 1). Due to the greater dissociation of acids in dilu-

te solutions, an increase in the number of active groups bonded on the adsorbents may occur.

When acidic groups are evaluated separately, the richest adsorbent in terms of carboxylic groups is the original CCs. It can be said that some of the carboxyl groups may be degraded during the activation of MK with sulfuric acid at high temperature. On the other hand, CCs are the poorest adsorbent in terms of phenolic and lactonic groups. During the activation with sulfuric acid at high temperature, phenolic and lactonic based new structures are formed on the adsorbents. Besides, depending on the degree of dissociation, large amounts of phenolic and lactonic groups are formed on the CCs-SA₅₀ surface. As a result, it is understood that during the activation of the original CCs with sulfuric acid, the new adsorbents in which their surface groups are highly variable and rich are formed.

Another remarkable result in this study is that although the starting material (CCs) and activating agent (H₂SO₄) are the same, only by changing the percentage concentration of the activating agent, adsorbents with quite different surface characteristics can be produced. Therefore, it is possible to produce adsorbents with very different characteristics according to the purpose.

The results found by calculating the pH and pH_{pzc} values of the adsorbents are given in Table 2 and the relevant graphics in Fig. 2. From the table, an increase is observed in the pH values of the adsorbents obtained with increasing sulfuric acid concentration. This result supports the SAFG analysis results (Table 2). Since the adsorbent with richer surface acidic groups (CCs-SA₅₀) will release more protons in its extraction with water, the pH value of the relevant adsorbent will be lower. The opposite of this situation is generally observed at pH_{pzc} values. Since more base will be required to neutralize the surface of the adsorbent with richer surface acidic groups, the corresponding adsorbent will generally have a higher pH_{pzc} value.

Table 1. Quantitative levels of surface acidic functional groups of adsorbents determined by Boehm titration

Adsorbent	Surface acidic groups (mmol/g)			
	Total	Carboxylic	Phenolic	Lactonic
CCs	2.43	1.75	0.35	0.32
CCs-SA ₅₀	6.18	1.60	3.20	1.38
CCs-SA ₇₅	5.23	1.63	2.75	0.85
CCs-SA ₉₈	4.15	1.05	1.75	1.35

CCs: Original Corn Cobs
 CCs-SA50: The adsorbent obtained by activation of 50% H2SO4
 CCs-SA75: The adsorbent obtained by activation of 75% H2SO4
 CCs-SA98: The adsorbent obtained by activation of 98% H2SO4

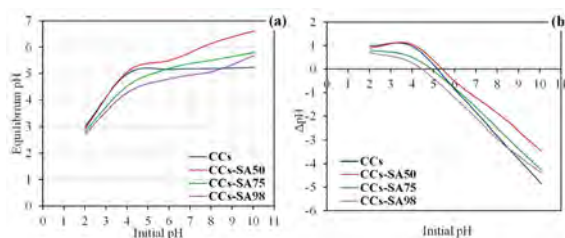


Figure 2. Determination of pH_{pzc} values: (a) Equilibrium pH vs initial pH graph, (b) Initial pH vs ΔpH graph

Comparing the differences between the initial and equilibrium pH values from the graph (Fig. 2(a)), positive differences were observed at low pH values, while negative differences were generally observed at high pH values. Since no buffer is used when adjusting the initial pH of NaCl solutions, the surface groups of the adsorbents can easily interact with the H⁺ and OH⁻ ions in the solution. While H⁺ ions pass from solution to adsorbent at low pH values, OH⁻ transitions occur at high pH values.

Table 3 shows the I₂ and MB numbers of the adsorbents. Looking at the table, it is seen that CCs-SA₅₀ has the highest number of I₂ and MB. Not only porosity but also rich functional groups contribute to the adsorption of large molecule structures. Also, the adsorption of large organic molecules on various adsorbents does not only occur with electrostatic interactions as with small metal ions, besides, but there are also relatively stronger bonds via π-π interactions. I₂ is a small molecule, and the high number of I₂ indicates the affinity of the adsorbent for small ion or molecules such as metal ions. As seen in this study, I₂ numbers are higher than MB numbers. That is, the surface and pore structures of the respective adsorbents may be more favorable for the adsorption of small molecules or ions. However, additional experiments are required to support this result.

The IR spectra taken to determine the types of surface functional groups of adsorbents are shown in Figs. 3 and 4. A comparison is made by taking spectra both before and after adsorption.

Fig. 3(a) shows the IR spectrum for CCs, the starting material used to produce the adsorbents. A slightly flat peak that appears at 3329 cm⁻¹ is caused by both moisture and hydroxyl (-OH) groups present in the sample. Hydroxyl

Table 2. pH and pH_{pzc} values of the adsorbents

Adsorbent	pH	pH _{pzc}
CCs	5.30	5.20
CCs-SA ₅₀	5.58	5.42
CCs-SA ₇₅	5.72	4.90
CCs-SA ₉₈	6.26	4.46

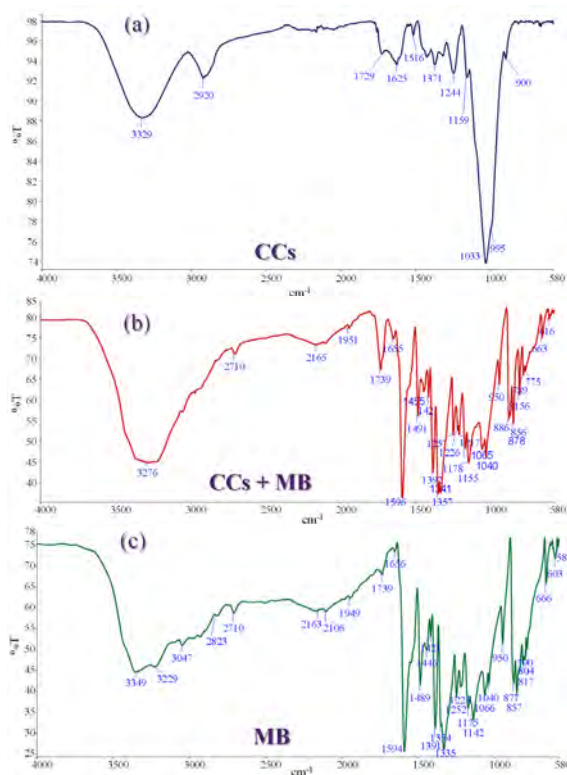
Table 3. I_2 and MB numbers of the adsorbents (mg/g)

Adsorbent	I_2 number	MB number
CCs	457.7	125.7
CCs-SA ₅₀	546.9	166.6
CCs-SA ₇₅	504.8	132.7
CCs-SA ₉₈	525.0	110.3

containing structures; phenols, alcohols, and carboxylic structures. The two peaks at 2920 and 1371 cm^{-1} are aliphatic C–H peaks. The peak appearing at 1729 cm^{-1} is the C=O stretching peak caused by carbonyl groups. The sharp peak at 1033 cm^{-1} indicates the C–C bond, while the peak at 1625 cm^{-1} is the C=C and C–O stretching peaks. The peak at 900 cm^{-1} indicates the C–O–H group.

Fig. 3(b) shows the IR spectrum taken after adsorption of MB on CCs. It is observed that there is a shift in the transmittance of CCs from 98% to 80% after adsorption of MB (Fig. 3(b)). In other words, a decrease in the transmittance occurred as expected. Also, it is observed that especially the peaks between 1729–900 cm^{-1} are completely closed and replaced by the peaks seen in the spectrum of pure MB in Fig. 3(c). This result proves that MB is adsorbed on CCs.

Fig. 4(a) shows the IR spectrum of the CCs-SA₅₀ coded adsorbent. The basic peaks to be interpreted here are the peaks at 3360, 1701, 1582, 1368, 1222 and 1039 cm^{-1} and

**Figure 3.** IR spectra for (a) original CCs, (b) MB loaded CCs, and (c) MB

belong to the –OH, C=O, C=C, C–H, S=O and C–O functional groups, respectively. Comparing with the starting material CCs, it is seen that the surface of the new product (CCs-SA₅₀) obtained by chemical activation has a different chemistry.

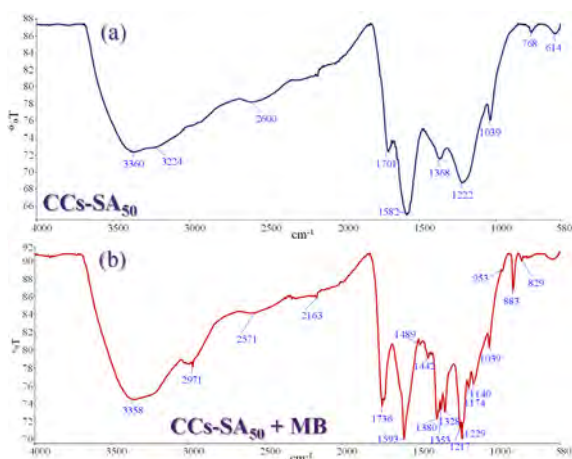
The spectrum in Fig. 4(b) was taken after the adsorption of MB on CCs-SA₅₀. Here, just as in Fig. 3(b), it is seen that the spectrum becomes complex and peaks originating from MB appear. In addition, the transmittance value has also changed somewhat here. So as a result, it has been proven that MB molecules are adsorbed on CCs-SA₅₀ (Fig. 4 (b)).

Adsorption Performance of the Adsorbents from Aqueous Solution

Effect of Initial pH

In this study, as the first parameter, the effect of the initial pH of the MB solutions on the adsorption efficiency was examined. For this, ten separate MB solutions, each with a concentration of 250 mg/L and adjusted to pH values between 1–12, were prepared. 10 mL of these solutions and 0.05 g of adsorbent (5.0 g/L suspension) were mixed and subjected to agitation on a mechanical shaker for 12 hours. At the end of the process, the adsorbent (CCs-SA) and adsorbate molecules (MB) were separated from each other by 0.45 μm cellulose nitrate membrane filter by a vacuum filtration device. Absorbance values of unadsorbed MB molecules (C_e , mg/L) remaining in the solution were read at 668 nm in a UV-Vis spectrophotometer and concentrations were calculated with the help of calibration graph plotted with the standard MB solutions. The results were converted to mg/g by Eq. 6.

The initial pH vs Q_e (mg/g) plots were drawn with the data obtained in this parameter (Fig. 5). Fig. 5 illustrated that MB adsorption efficiency is higher at increasing pH values. However, there is not a very sharp increase or decrease.

**Figure 4.** IR spectra for (a) CCs-SA₅₀ and (b) MB loaded CCs-SA₅₀

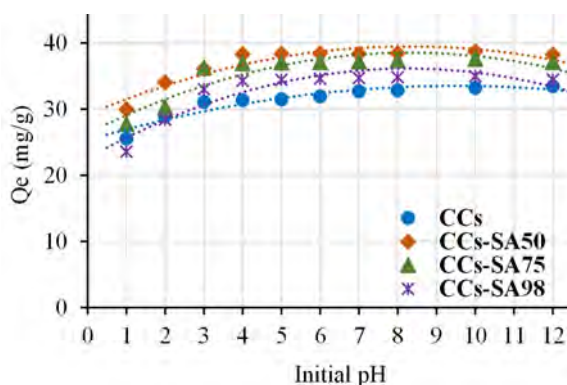


Figure 5. The effect of the initial pH on removal of MB from aqueous solution by CCs and CCs-SA (Co: 250 mg/L, adsorbent amount: 5.0 g/L, agitation time: 4.0 hours, temperature: 25 °C)

When the performances of the adsorbents are compared with each other, it is seen that the CCs-SA₅₀ coded adsorbent obtained with 50% sulfuric acid has a slightly higher performance. This difference will become more pronounced as the concentration of MB increases.

The MB adsorption performance of CCs used directly after being milled without activating with any agent is lower than the other adsorbents. The most important point to be evaluated here is that adsorbent produced with the lowest concentration of sulfuric acid has shown the highest performance. As it is known, strong acids such as sulfuric acid need an aqueous medium to bring out their acidity strength. If there is enough water (or any solvent in which acid can easily release its protons), acids can easily dissociate by donating protons. Since there is relatively more solvent in 50% sulfuric acid, sulfuric acid will certainly dissociate more easily. Concentrated acids are therefore considered to be difficult to dissociate.

In the light of the results obtained, it is seen that pH does not affect much the adsorption efficiency and the optimum pH range is approximately in the range of 4–10. pH is the main factor that controls the electrostatic interactions between the adsorbate and the adsorbent. When the solution pH reaches pH_{pzc} , the net surface charge of the adsorbent will be zero. The pH_{pzc} values of the adsorbents from Table 2 range from 4.46 to 5.42. Although the MB solution is acidic at these pH values, the surface of the adsorbents is neutral. The net charge of the adsorbent surface just above the pH_{pzc} value is negative, but the MB solution is still acidic. Therefore, at these pH values, strong electrostatic interactions will occur between MB, a cationic dye, and the adsorbent surface.

Not only electrostatic interactions occur between large organic molecules such as MB and the respective adsorbent surface, but also strong π - π interactions between the aromatic rings in the organic molecules and the C skeleton of the adsorbent. Besides, non-electrostatic partial H bonds

contribute the adsorption. These interactions are much stronger than electrostatic ones and are almost independent of pH.

Since the original pH values of MB solutions are between about 4.0–6.0, no pH adjustment was required in this study.

There are studies in the literature reporting that pH has little effect on MB adsorption on various adsorbents.

Effect of Contact Time on MB Adsorption Efficiency and Adsorption Kinetics

At this stage, the time to reach equilibrium for the adsorption of MB molecules on the adsorbents was investigated. For this, 5.0 g/L adsorbent suspension and 250 mg/L MB solutions were treated for 0–12 hours. After the solutions taken in different periods were determined by UV-Vis spectrophotometer, the adsorbed amounts (Q_t) per gram adsorbent were calculated. To examine how the adsorption performance has changed during a certain time interval, firstly the t - Q_e graph was plotted as seen in Fig. 6 (a). As can be seen from the graph, the adsorption process was completed after 120 minutes for all adsorbents, so equilibrium was almost reached. However, to be guaranteed, the equilibrium time was optimized as 4.0 hours at this stage, and the contact time was applied as 4.0 hours in further applications.

Various kinetic models have been derived to examine how adsorbate molecules/ions behave on adsorbents in terms of the time dependence of adsorption. The three most famous of these models are: (i) pseudo-first-order kinetic model, (ii) pseudo-second-order kinetic model, and (iii) intraparticle diffusion kinetic model [35–37].

The pseudo first-order kinetic model is a model proposed by Lagergren in 1898 [38]. This model is generally applicable for the first minutes of the adsorption event, not for the total adsorption time. That is, it can be applied from the beginning of the adsorption to the period when equilibrium has not yet been reached. This adsorption rate equation is expressed in Eq. (8) below [39]:

$$\frac{dQ}{dt} = k_1(Q_e - Q_t) \quad (8)$$

The linear shape of this equation is given in Eq. 9 below:

$$\ln(Q_e - Q_t) = \ln Q_e - k_1 t \quad (9)$$

where Q_e (mg/g) and Q_t (mg/g) indicate the amounts of adsorbate adsorbed on the adsorbent at equilibrium and at time t , respectively. k_1 (1/min) is the pseudo-first-order rate constant. If the data fit this model, the $\ln(Q_e - Q_t)$ versus t graph (Fig. 6 (b)) is expected to be linear and this

gives information about whether the kinetic model is suitable for the adsorption data. Q_e and k_1 can be found from the intercept and the slope of the graph, respectively. The pseudo-first order kinetic model can be applied more successfully in the case of a relatively high concentration of adsorbate in the solution [40].

Another model used in the analysis of adsorption kinetic data, the pseudo-second-order kinetic model, unlike the pseudo-first-order kinetic model, works in harmony with the rate control step mechanism throughout the entire adsorption period. Moreover, the kinetic results obtained from adsorption studies with relatively low concentrated adsorbate solutions are better fitted to this model. This model is given by the following Eq. (10) [40]:

$$\frac{dQ_t}{dt} = k_2(Q_e - Q_t)^2 \quad (10)$$

When this equation is transformed into its linear form, Eq. 11 below is obtained:

$$\frac{t}{Q_t} = \frac{1}{k_2 Q_e^2} - \frac{t}{Q_e} \quad (11)$$

where k_2 (g/mg.min) is the second-order rate constant. If a graph to be plotted between t/Q_t and t (Fig. 6(c)) is linear and the value of R^2 is greater than 0.95, it can be said that the second-order kinetic model is compatible with the experimental data. Q_e and k_2 can be determined from the slope of the linear graph and the intercept, respectively.

The kinetic data show that the adsorption rate is not compatible with the pseudo-first-order kinetic model but is quite compatible with the pseudo-second-order model. When the experimental Q_e values are compared with the theoretical Q_e values, it is seen that the experimental data are quite compatible with the second-order rate expression. Additionally, R^2 values support this result (Table 4).

The third kinetic model is different from the first two kinetic models. If the diffusion mechanism in porous structures cannot be clearly explained by pseudo-first- and second-order equations, the intraparticle diffusion kinetics can be used. This kinetic model is expressed by the following Eq. (12):

$$Q_t = k_{id}t^{1/2} + C \quad (12)$$

where Q_t is a constant that characterizes the adsorbed quantity (mg/g) at any time t , k_{id} (mg/g.min^{1/2}) intraparticle diffusion rate constant, and C (mg/g) the boundary layer thickness. k_{id} and C can be determined from the slope and intercept of the graph to be plotted between Q_t and $t^{1/2}$, respectively [41].

The intraparticle diffusion model assumes that the adsorption mechanism generally consists of three steps, and that the adsorption rate is controlled by at least one of these steps: (i) mass transfer from aqueous solution to the external boundary layer of the adsorbent particles as a thin film, (ii) adsorption at sites on the internal or external surface of the adsorbent. Energy at this stage depends on whether the adsorption mechanism is physical or chemical, and this stage is thought to occur quite rapidly, (iii) diffusion towards adsorption sites within the pores of the adsorbent particles [42].

More than one linear correlation can be observed in the graph to be plotted between Q_t and $t^{1/2}$. The first sharp line observed indicates film diffusion (or boundary layer diffusion) or film adsorption. The second straight line is the section in which the excess adsorbate molecules are adsorbed towards the interior of the pore due to the saturation of the boundary layer, in other words, where intraparticle diffusion is the rate control step. The third part represents the equilibrium state, and in this part, intraparticle diffusion begins to slow down due to the very little adsorbate concentration remaining in the solution. If the second line, the intercept (C) of the line representing intraparticle diffusion, passes through the origin, it is concluded that only intraparticle diffusion is the step controlling the adsorption rate. If it does not pass through the origin, it can be said that the adsorption rate is controlled by more than one mechanism [43].

When looking at the graph for the intraparticle diffusion model in Fig. 6(d), it is seen that two different linear lines are formed. Here, the first line represents intraparticle diffusion. As seen in Fig. 6(d), the first line almost passes through zero. Therefore, it can be said that the rate control step in the adsorption of MB on the adsorbents is generally controlled by the intraparticle diffusion mechanism. It is also seen from Table 4 that C values are very close to zero.

Concentration Effect on MB Adsorption and Adsorption Isotherms

In this section, the effect of increasing concentrations of MB solutions on the adsorption mechanism was investigated by using the fixed mass of four different adsorbents. The relationship between the increasing adsorbate molecule/ion in the solution and the amount of adsorbate adsorbed on per unit quantity of the relevant adsorbent is called "adsorption isotherm". Adsorption isotherms are useful for selecting the most suitable adsorbent in an adsorption process, and also they are very useful in assessing the performance of systems in which adsorption occurs [44].

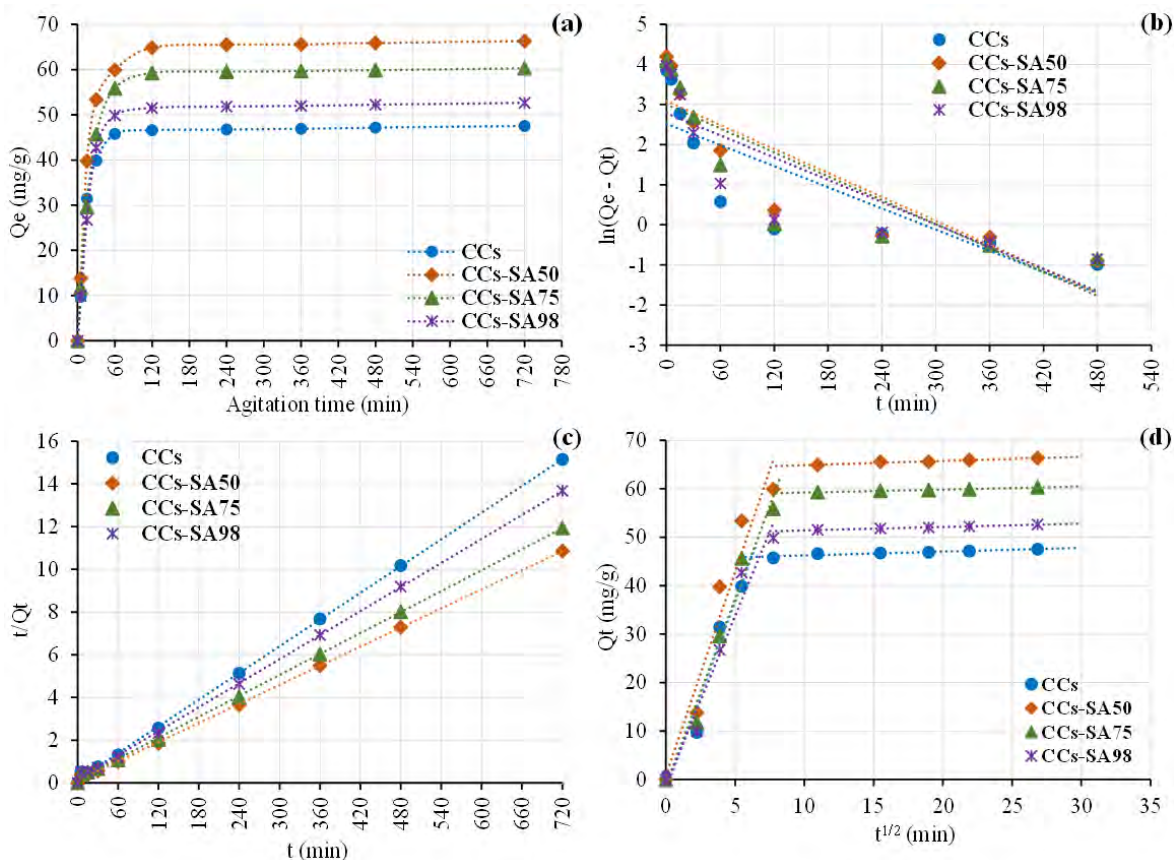


Figure 6. Effect of equilibrium time on the removal of MB from aqueous solution by CCs-SA, and the kinetic models: (a) Effect of time to reach equilibrium, (b) Linear plot of $\ln(Q_e - Q_t)$ vs t for pseudo-first-order kinetic model, (c) linear plot of t/Q_t vs t for pseudo-second-order kinetic model, (d) plot of $t^{1/2}$ vs Q_t for intraparticle diffusion kinetic model (pH: 6.0, C_0 : 500 mg/L, adsorbent amount: 5.0 g/L, agitation time: 0–12 hours, temperature: 25 °C)

5.0 g/L adsorbent suspensions and six different MB solutions with increasing concentrations between 50 and 1000 mg/L were treated for 4.0 hours. Adsorbent particles and adsorbate molecules were separated from each other by filtration, and unadsorbed MB molecules in the solution were determined by UV-Vis spectrophotometer. The quantities of MB adsorbed per gram of the adsorbent were calculated from the relevant equations.

As can be seen from the C_0 vs Q_e plot in Fig. 7 (a), the quantity of MB adsorbed against increasing MB concentration increases. However, this increase is not linear. The

presence of adsorbate molecules increasing against the fixed amount of adsorbent will cause the adsorbent to become saturated after a while and thus the adsorption rate to slow down. Even if the quantity of adsorbate increases after a while, the adsorbent will not be able to adsorb more adsorbate molecules.

It is very useful the adsorption equilibrium isotherms to determine the adsorption capacity of an adsorbent for an adsorbate. In the equilibrium state, there is no concentration change either on the surface of the adsorbent or in the solution. The adsorption capacity of an adsorbent for an ad-

Table 4. Kinetic model constants for MB adsorption from aqueous solution

Adsorbent	$Q_e(\text{exp.})$ (mg/g)	Pseudo-first-order kinetic			Pseudo-second-order kinetic			Intraparticle diffusion		
		$Q_e(\text{theo.})$ (mg/g)	k_1 (min^{-1})	R^2	$Q_e(\text{theo.})$ (mg/g)	k_2 (g/mg.min)	R^2	k_{id} (mg/g.min ^{1/2})	C (mg/g)	R^2
CCs	47.53	12.38	8.79×10^{-3}	0.6848	47.96	3.02×10^{-2}	0.9995	7.74	-2.15	0.9538
CCs-SA ₅₀	66.31	21.92	9.96×10^{-3}	0.7876	67.11	1.85×10^{-2}	0.9996	8.40	0.88	0.9420
CCs-SA ₇₅	60.31	20.07	9.95×10^{-3}	0.7508	61.20	1.75×10^{-2}	0.9994	7.70	-1.18	0.9770
CCs-SA ₉₈	52.65	16.26	9.26×10^{-3}	0.7277	53.33	2.12×10^{-2}	0.9994	6.98	-1.14	0.9644

$Q_e(\text{exp.})$: Experimental Q_e value

$Q_e(\text{theo.})$: Theoretical Q_e value

sorbate generally includes the relationship of three properties; (i) the concentration of the adsorbate in the fluid phase (C_e), (ii) the concentration of the adsorbate on the adsorbent (Q_e), and (iii) the temperature of the system (T). If the temperature of the system is kept constant, C_e and Q_e can be used to create a graph expressing the equilibrium state. This graph is the adsorption isotherm [45].

The graph plotted between the adsorbate concentration (C_e , mg/L) remaining in the solution after the adsorption process and the quantity of MB (Q_e , mg/g) adsorbed on 1 g of the adsorbent is shown in Fig. 7(b).

Two well-known isotherm models, which provide important information about the adsorption process and the surfaces of adsorbents by establishing a relationship between C_e and Q_e , stand out today: Langmuir and Freundlich isotherm models.

In the Langmuir adsorption isotherm developed by Irving Langmuir in 1932, the following assumptions were mainly proposed [46]:

- Adsorption of the adsorbate ion or molecules occurs at specific binding sites localized on the surface of the adsorbent.
- All adsorption sites on the surface of the adsorbent have very similar properties to each other.
- At the end of the adsorption process, the surface of the adsorbent is covered with the only monolayer of adsorbed molecules.
- There is no interaction between the adsorbate ion or molecules adsorbed on the adsorbent surface, that is, it is assumed that there is no adsorbate-adsorbate interaction.

The mathematical equation for the curvilinear form of the Langmuir isotherm is as in Eq. 13 below:

$$Q_e = \frac{bC_e}{1 + bC_e} \quad (13)$$

In Eq. 14, the linearized form of Eq. 13 is given:

$$\frac{C_e}{Q_e} = \frac{C_e}{Q_{\max}} + \frac{1}{bQ_{\max}} \quad (14)$$

where Q_e is the quantity of adsorbate adsorbed by 1 g adsorbent (mg/g), Q_{\max} is the maximum monolayer adsorption capacity (mg/g), C_e is the concentration of the adsorbate solution after reaching equilibrium (mg/L), and b represents the Langmuir constant associated with free energy or adsorption enthalpy (L/mg). The plot of C_e/Q_e vs C_e is a straight line indicating the suitability of

the adsorption to the Langmuir model. Q_{\max} and b can be determined from the slope and intercept, respectively.

Another model Freundlich isotherm model, which allows examining the adsorption equilibrium conditions on heterogeneous surfaces with a multi-layer adsorption mechanism, and which was first proposed by German Physical Chemist Herbert Max Finley Freundlich [47].

The curvilinear and linear forms for the Freundlich isotherm model are as Eq.s 15 and 16 below:

$$Q_e = K_f \times C_e^{1/n} \quad (15)$$

$$\ln Q_e = \ln K_f + \frac{1}{n} \ln C_e \quad (16)$$

where K_f (mg/g) is an empirical parameter associated with the adsorption capacity and n is the adsorption intensity and indicates the strength of the relationship between adsorbate and adsorbent. High values of K_f are an indication of how close the affinity of adsorbent and adsorbate to each other. The value of n varies with the heterogeneity of adsorption sites on the adsorbent surface. Also, the value of n is expected to be between 1 and 10 in terms of suitability of the adsorption process for an adsorbent-adsorbate couple to be selected. The value $1/n$ is the heterogeneity factor and generally takes values in the range 0–1. The more heterogeneous the adsorbent surface is, the closer the $1/n$ value becomes zero. The accuracy of this isotherm in heterogeneous adsorption systems is, of course, better than the Langmuir isotherm.

The plot of $\ln C_e$ versus $\ln Q_e$ is linear, and K_f and $1/n$ can be easily found from the intercept and slope of the line.

Figs 7(c) and 7(d) show linear Langmuir and Freundlich isotherm plots for adsorption of MB on four adsorbents. When the R^2 values of the lines are examined first (in Table 5), it is seen that the data fit both models with a high correlation. However, when looking at Table 5, R^2 values for the Langmuir isotherm of other adsorbents except CCs are greater than those for the Freundlich isotherm. In other words, while MB adsorption on CCs is more compatible with the Freundlich model, the Langmuir isotherm model for the other three adsorbents seems more compatible. This result arises from the R^2 values obtained from the linear graphs. From the Langmuir linear isotherm, the Q_{\max} values can be calculated. Q_{\max} and other constants are given in Table 5. However, an important point here is that these constants change as the quantity of adsorbent changes. As the quantity of adsorbent decreases, the Q_{\max} values will also increase. The reason for this is discussed in the next parameter (Table 5). Therefore, the quantity of adsorbent used should be considered when comparing the obtained Q_{\max} values with the literature.

Looking at the Q_{\max} values in Table 5, the adsorbent with the code CCs-SA₅₀ has the highest value as expected. The Q_{\max} value of 1.0 g/L adsorbent amount is 295.5 mg/g and this value is higher than many values obtained from other studies in the literature. A comparison with some studies in the literature on maximum adsorption capacities (Q_{\max}) is given in Table 7. (See Conclusion section)

It will be more useful to evaluate the curvilinear isotherm forms to determine which isotherm model is compatible with the adsorption data. New theoretical Q_e values are derived by replacing the constants obtained from linear graphs in curvilinear Eqs (Eq.s 13 and 15) and these values are compared with experimental Q_e values on a curvilinear graph. In this respect, when looking at the curvilinear graphs drawn in Fig. 8, it can be interpreted which curve better represents the experimental Q_e values (round symbols in black). The first curvilinear graph is for CCs and the experimental points here represent the Freundlich isotherm model best. Because the Freundlich curve follows the experimental points relatively better than the Langmuir curve. Anyway, the R^2 value of the related linear graph is slightly higher for the Freundlich isotherm. This height has been proven better here. However, for the other three adsorbents obtained by activation with sulfuric acid, the experimental points represent the best Langmuir isotherm. Both results are understandable. Because, since the original CCs is a natural structure, there are extremely heteroge-

neous formations on its surface. The structure has highly amorphous properties and on its surface, there are functional groups and chemical structures of quite different types and strengths.

Effect of Adsorbent Quantity on MB Adsorption

In the previous parameter, the changes in the adsorption with increasing MB concentrations in the fixed adsorbent mass were examined and discussed. Here, the adsorption behavior was observed by increasing the adsorbent mass while the MB concentration was constant, and the data obtained were interpreted. Here, two different MB concentrations and different adsorbent mass were treated separately, and the maximum capacities were calculated. 10 mL of 250 mg/L and 500 mg/L MB solutions were treated separately with three different adsorbent quantities of 10, 50 and 100 mg (1.0, 5.0 and 10.0 g/L adsorbent suspensions). At the end of the agitation process, after determining the concentrations of unadsorbed MB in the solution by UV-Vis spectrophotometer, the quantity of MB adsorbed on the adsorbents with the relevant equations were calculated as both % and mg/g, and the graphs were plotted (Fig. 9).

From the Fig. 9, while MB% adsorption increased with increasing the adsorbent mass, the quantity of adsorbed MB per gram adsorbent decreased. Because, as can be seen from

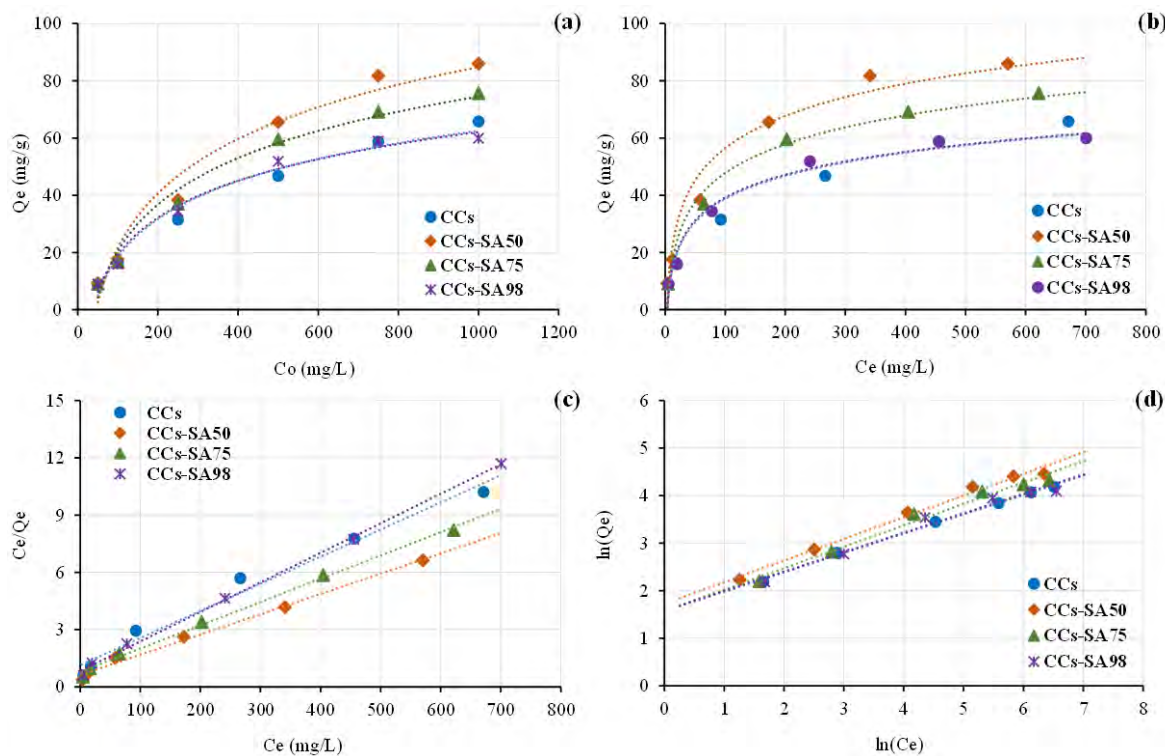


Figure 7. Concentration effect and adsorption isotherms on removal of MB from aqueous solution by CCs-SA: (a) C_o vs Q_e plot, (b) C_e vs Q_e plot, (c) Linear Langmuir isotherm plot (C_e vs C_e/Q_e plot), (d) Linear Freundlich isotherm plot ($\ln(C_e)$ vs $\ln(Q_e)$ graph) (pH: 6.0, C_o : 50–1000 mg/L, adsorbent quantity: 5.0 g/L, agitation time: 4.0 hours, temperature: 25 °C)

Table 5. Constants from Langmuir and Freundlich isotherms

Adsorbent quantity (g/L)	Adsorbent	LANGMUIR			FREUNDLICH		
		Q_{max} (mg/g)	b (L/mg)	R^2	K_f (mg/g)	n	R^2
1.0	CCs	202.5	6.46×10^{-3}	0.9698	9.63	2.291	0.9930
	CCs-SA50	295.5	8.31×10^{-3}	0.9953	11.25	2.028	0.9745
	CCs-SA75	215.9	1.10×10^{-2}	0.9980	12.78	2.339	0.9596
	CCs-SA98	175.7	1.39×10^{-2}	0.9995	14.09	2.605	0.9410
5.0	CCs	70.4	1.24×10^{-2}	0.9787	4.83	1.574	0.9973
	CCs-SA50	94.3	1.69×10^{-2}	0.9931	5.61	1.724	0.9882
	CCs-SA75	82.0	1.56×10^{-2}	0.9959	4.84	1.576	0.9811
	CCs-SA98	64.7	1.86×10^{-2}	0.9979	4.87	1.583	0.9736
10.0	CCs	55.2	1.14×10^{-2}	0.9714	2.37	0.863	0.9984
	CCs-SA50	61.5	2.00×10^{-2}	0.9955	3.19	1.159	0.9586
	CCs-SA75	56.2	1.96×10^{-2}	0.9963	2.96	1.086	0.9533
	CCs-SA98	51.4	2.07×10^{-2}	0.9971	2.83	1.039	0.9422

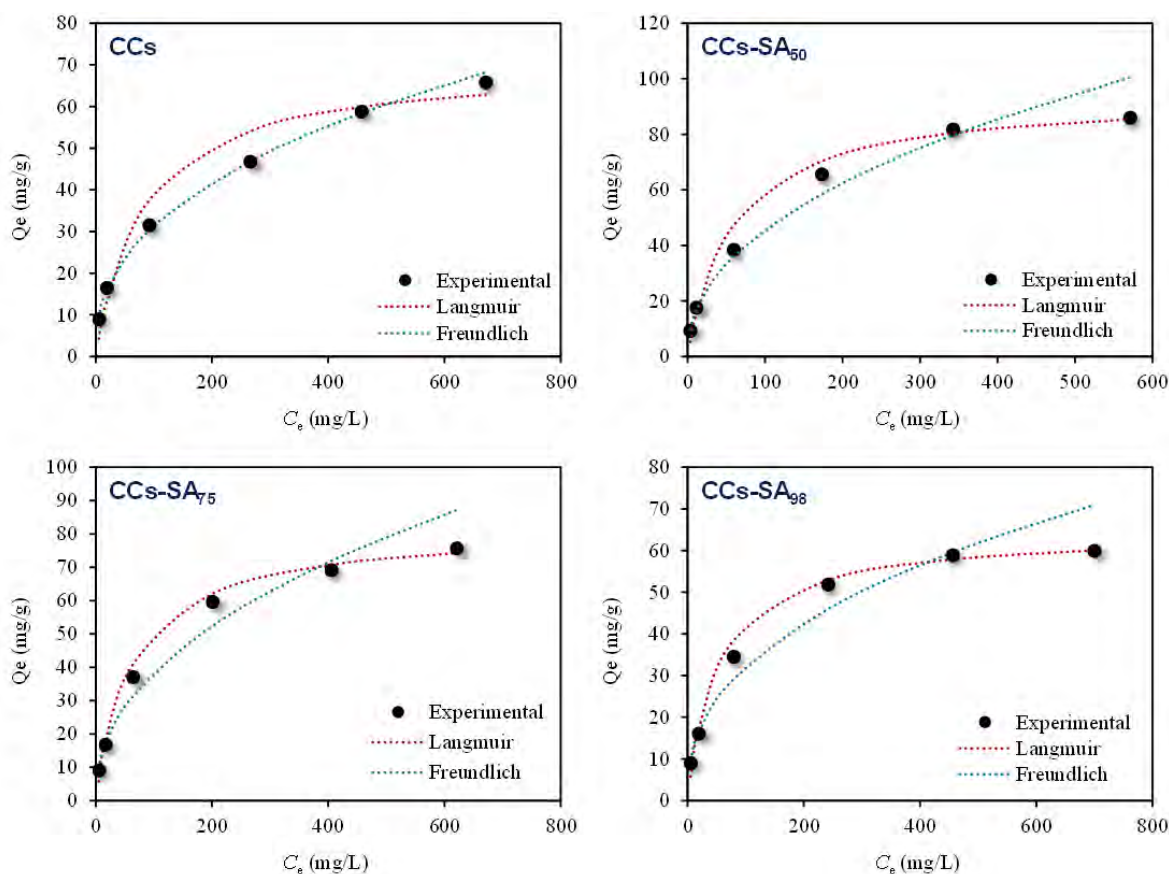


Figure 8. Curvilinear Langmuir and Freundlich isotherms derived for MB adsorption

the figure, the % increase quantity is not linear. Therefore, when all results obtained are converted into adsorbed quantities per unit adsorbent (mg/g), the adsorption efficiency will decrease as expected.

This result can be proved mathematically. If Eq.s (5) and (6) are combined, the following new Eq. (17) is derived. As seen in the equation, the adsorbent mass (m) and Ads.% are inversely proportional.

$$Q_e = \frac{Ads.\% \times C_o \times V}{100m} \quad (17)$$

This may be mainly due to two reasons: (i) Increasing the quantity of adsorbent at constant MB concentration leads to the formation of unsaturated sites on the adsorbent surface. (ii) The adsorption capacity of the adsorbent becomes smaller as the agglomeration of large quantities of adsorbent particles will lead to a decrease in the total surface area. Considering Table 5 given in the previous parameter, as can be seen, the highest capacity value is reached with the lowest adsorbent quantity.

Desorption of MB Molecules Adsorbed on CCs-SA

Re-use of adsorbents used to remove various types of contaminants from water and wastewater after regeneration is very important for the economics of the process. Therefore, in this parameter, various desorption solutions (1:1 diluted acetone and alcohol solutions, and 0.1 M HCl, NaCl and NaOH solutions) were prepared for the regeneration of loaded adsorbents and their performance was tested.

First, 10 mL of 100 mg/L MB solution was added into a serial tube containing 0.05 g of adsorbent. After 4.0 hours of agitation under optimum conditions, the adsorbent and adsorbate were separated by filtration. After the loaded adsorbents were thoroughly washed and dried in the air, the desorption solutions shown in Fig 10 were added to them. These desorption solutions were selected based on those used in similar studies in the literature. It can be considered that acetone and alcoholic solvents will perform higher. As can be seen from the column charts in Fig 10, the performance of organic solvents is higher. However, the loaded MB molecules could not be desorbed quantitatively with any desorption solution. There could be several reasons for this. First, MB molecules may be linked by chemical bonds on respective adsorbents. Second, adhesion can be through many mechanisms, not necessarily chemical bonds, but strong and weak. The adsorption mechanisms of dyestuffs can be not only through electrostatic interactions as in metal ions, but also through strong π - π dispersion interactions between the aromatic rings of the dye molecules and the graphene layers of the adsorbent, and non-electrostatic partial H-bonds [48].

Interactions between the adsorbent and the adsorbate basically occur in two ways; electrostatic and non-electrostatic. Electrostatic interactions occur where the adsorbate is an electrolyte, that is, it can ionize in the aqueous solution by accepting or donating electrons. These interactions can be attractive or repulsive depending on the solution pH. Non-electrostatic interactions are attractive in all conditions, and mainly include van der Waals forces,

hydrophobic interactions, and H-bonding. The factors affecting the adsorption process are the properties of the adsorbent and adsorbate, the solution chemistry, and the adsorption temperature. Compounds containing aromatic groups such as MB are adsorbed on carbon materials mostly with π -electrons in the aromatic ring [49].

In the next parameter, the physical and chemical mechanism of the adsorption process taking place on the relevant adsorbent is discussed from the thermodynamic data.

Temperature Effect on MB Adsorption and Adsorption Thermodynamics

The effect of temperature on the adsorption yield is important for the applicability of the process in all seasons. Also, the effect of temperature can give important information about the adsorption mechanism. Thermodynamic evaluations can be made with temperature change. In this regard, 250 mg/L MB solutions and 5.0 g/L of each adsorbent were treated for 4.0 hours. Then, the MB amount (mg/g) retained by 1 g adsorbent was calculated, and temperature change graphs were plotted.

As seen in Fig. 11(a), an increase in temperature reflected positively on the adsorption efficiency. When the temperature increased from 5 °C to 50 °C, MB adsorption increased from 26.4 mg/g to 39.0 mg/g (from 52.9% to 78.0%) on CCs, 30.1 mg/g to 41.5 mg/g (from 60.2% to 83.0%) on CCs-SA₅₀, 28.9 mg/g to 39.2 mg/g (57.7% to 78.3%) on CCs-SA₇₅ and 28.0 mg/g to 38.3 mg/g (55.9% to 76%) on CCs-SA₉₈.

The results show that the adsorption behavior of MB on the relevant adsorbents is endothermic, that is, a process that takes place with higher efficiency by accepting the temperature of the environment. The positive effect of temperature increase on the efficiency of adsorption can be attributed to reasons such as the increase in the interaction between the adsorbent and the adsorbate more, the passive sites becoming more active, and the expansion of the pore structures of the adsorbent, and the more effective role of intra-particle diffusion.

Adsorption thermodynamics were also examined from the temperature change data obtained at this stage. Thermodynamics determines the internal energy, enthalpy, entropy, and free energy values of the system during a physical or chemical transformation and examines their dependence on the reaction conditions [50]. The thermodynamic parameters ΔG , ΔS and ΔH can be found from the following equations:

$$\Delta G = \Delta H - T\Delta S \quad (18)$$

$$K_d = C_a / C_e \quad (19)$$

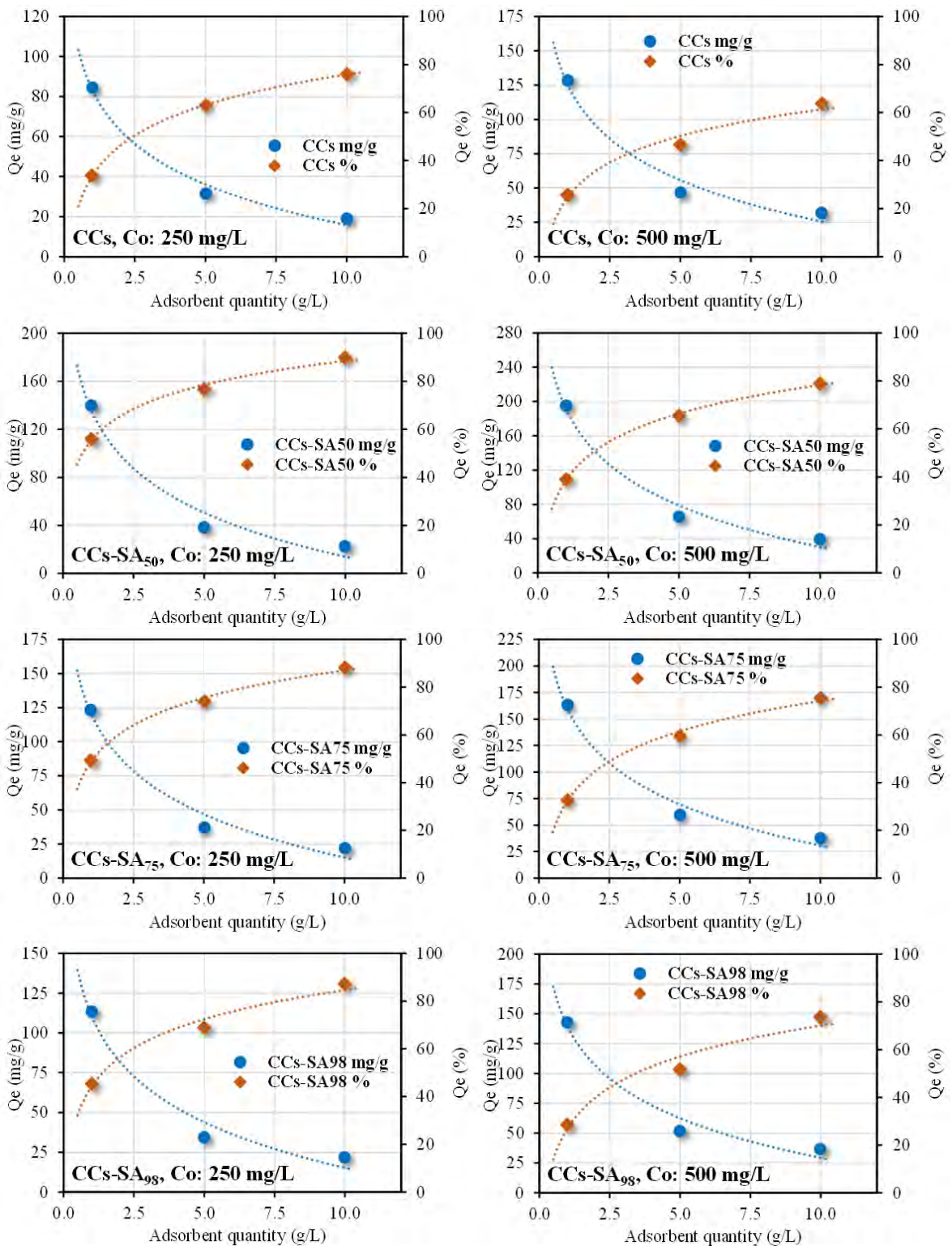


Figure 9. The effect of the adsorbent quantity on the removal of MB from the aqueous solution by CCs-SA (pH: 6.0, C_i: 250 and 500 mg/L, adsorbent quantity: 1.0, 5.0 and 10.0 g/L, agitation time: 4.0 hours, temperature: 25 °C)

$$\Delta G = -RT \ln K_d \quad (20)$$

$$\ln K_d = \frac{\Delta S}{R} - \frac{\Delta H}{R} \quad (21)$$

ΔG : Gibbs free energy change (kJ/mol)

ΔH : Enthalpy change (kJ/mol)

ΔS : Entropy change (kJ/mol.K)

T : Absolute temperature (K)

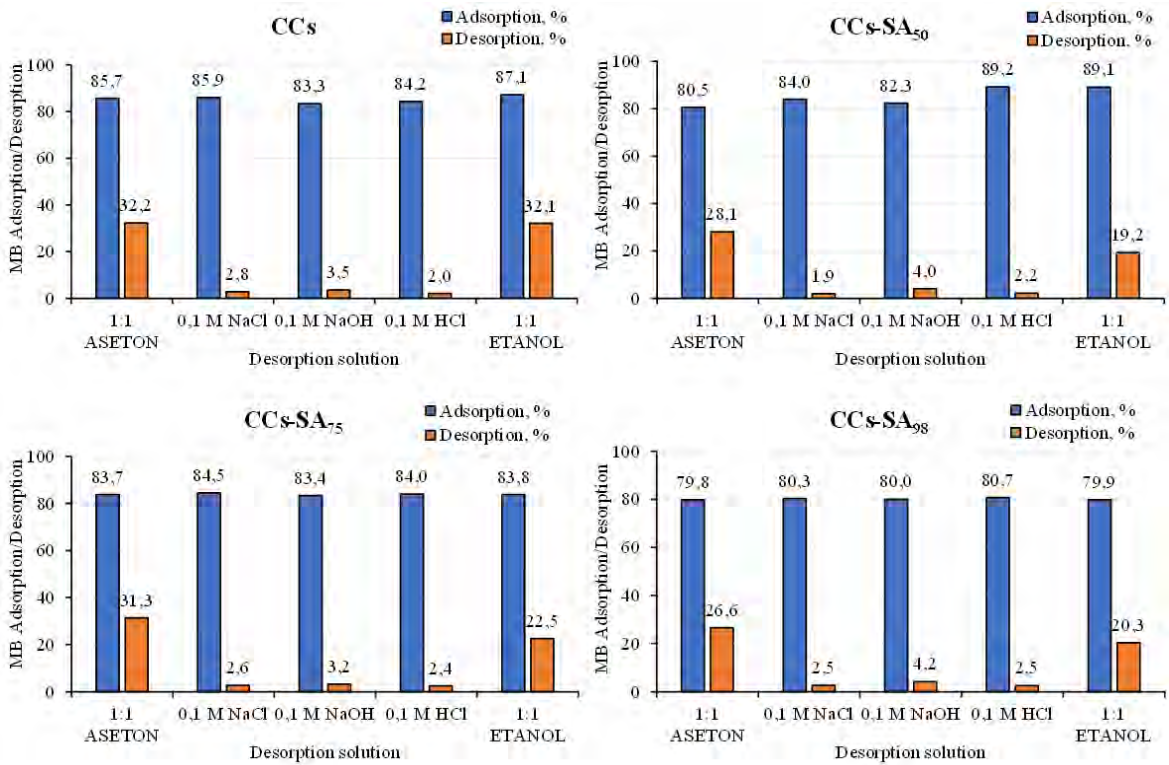


Figure 10. Desorption of MB molecules adsorbed on the adsorbents (C_e : 100 mg / L)

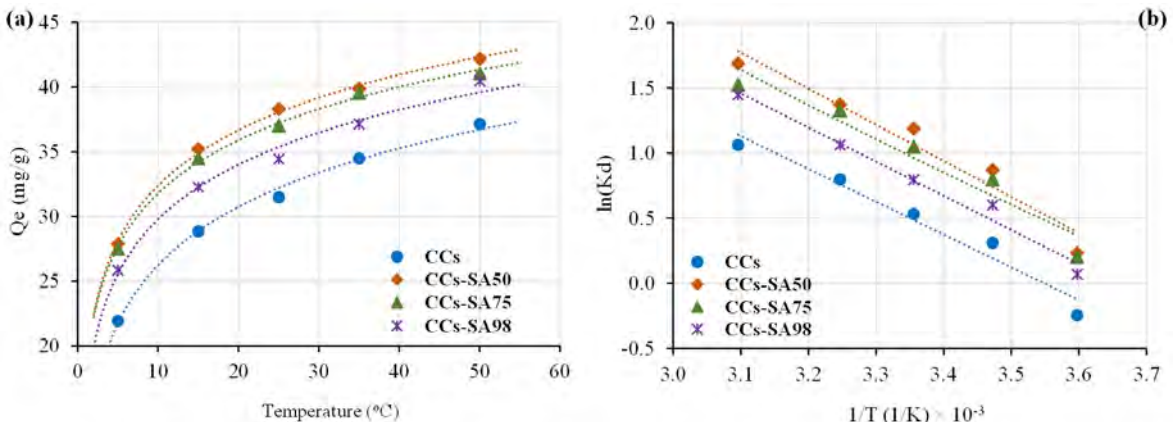


Figure 11. (a) Effect of medium temperature on removal of MB from aqueous solution by CCs-SA, (b) $1/T - \ln(K_d)$ graph for thermodynamic data (pH: 6.0, C_e : 250 mg/L, adsorbent quantity: 5.0 g/L, agitation time: 4.0 hours, temperature: 5 – 50 °C)

R: Universal gas constant (J/mol.K)
 K_d : Adsorption equilibrium constant
 C_a : The concentration of adsorbate retained in the unit mass of the adsorbent (mg/L)
 C_e : The concentration of adsorbate left in the solution after adsorption (mg/L)

First, the equilibrium constant K_d is calculated from Eq. 19. A graph to be plotted between $\ln(K_d)$ and $1/T$ in Eq. 21 is expected to be linear as in Fig. 11(b). While the slope of this graph gives ΔH , ΔS can be found from the intercept.

The data obtained from thermodynamic calculations are given in Table 6. With increasing temperature, ΔG values

become increasingly negative. A negative value of ΔG indicates that adsorption occurs spontaneously. The enthalpy value of physical adsorption is generally not greater than 4 kJ/mol, but not less than 20 kJ/mol for chemical adsorption [51]. Therefore, when looking at the ΔH values obtained from this study in Table 6, it is seen that all of them are slightly higher than 20 kJ/mol. In other words, it can be said that the adsorption process proceeds by chemical means. In the previous parameter, it was discussed that MB molecules retained on the adsorbents could not be quantitatively desorbed. The results obtained from the thermodynamic data also confirm this result due to the possibility of the process being chemical.

Table 6. The effect of ambient temperature on the removal of MB from aqueous solution by CCs-SA: Thermodynamic data

Adsorbent	T (°C)	K _a	ΔG (kJ/mol)	ΔS (J/mol.K)	ΔH (kJ/mol)
CCs	5	0.78	0.57		
	15	1.37	-0.75		
	25	1.70	-1.32	74.26	20.92
	35	2.22	-2.05		
	50	2.89	-2.85		
CCs-SA ₅₀	5	1.31	-0.62		
	15	2.36	-2.06		
	25	3.28	-2.94	82.64	22.00
	35	3.90	-3.49		
	50	5.20	-4.43		
CCs-SA ₇₅	5	1.23	-0.47		
	15	2.22	-1.91		
	25	2.85	-2.60	79.76	21.35
	35	3.78	-3.40		
	50	4.60	-4.10		
CCs-SA ₉₈	5	1.07	-0.16		
	15	1.82	-1.44		
	25	2.21	-1.97	79.64	21.78
	35	2.89	-2.72		
	50	4.24	-3.88		

Positive ΔS values increase the probability of random formation of the adsorption equilibrium occurring at the solid-liquid interface during adsorption. In other words, it indicates an increase in the amount of energy that cannot be used, that is, an increase in the disorder of the system.

CONCLUSION

In this study, three new adsorbents were produced by chemical activation using different concentrations of sul-

furic acid from corn cobs (CCs). Based on the results obtained from the characterization and adsorption studies, the following results were obtained:

- The adsorbent with the richest surface acidic functional groups is CCs-SA₅₀ (Table 1), which was obtained by activating with the lowest concentration of sulfuric acid (50%).
- When the I₂ and MB numbers of the adsorbents were evaluated, it was found that the adsorbent with the code CCs-SA₅₀ had the highest values.
- It has been observed that MB molecules are adsorbed on all adsorbents with high efficiency over a wide initial pH range, and it has been observed that a precise pH adjustment is not required before adsorption tests. Since the original pH values of the MB solutions are around 6, there is no need to make any pH adjustment before the operations.
- When Langmuir adsorption capacities of adsorbents are compared, the MB capacity of the adsorbent with the code CCs-SA₅₀ is the highest. This result proves that the adsorbent produced by dilute sulfuric acid activation has a higher capacity.
- Table 7 presents a comparison of the capacity value obtained from this study with the literature. As can be seen from the table, the capacity value obtained from this study is higher than many studies in the literature. Therefore, it has been proven that especially the adsorbent with the CCs-SA₅₀ code can be used effectively in removing dyes from contaminated water.
- It has been determined that the increase of the medium temperature has a positive effect on MB adsorption, ad-

Table 7. Comparison of the MB adsorption capacities with the literature

Q_{max} (mg/g)	Qmax (mg/g)	Adsorbent mass (g/L)	Solution pH	Ads. Temp. (oC)	Ref.
Sunflower oil cake	16.43	2.0	6.0	25	[52]
<i>Posidonia oceanica</i> (L.) dead leaves	270.3	5.0	6.5	30	[53]
CuO loaded coconut shell AC*	331.5	3.0	9.0	45	[54]
Surfactant-modified AC	232.5	0.15	5.0	25	[55]
Corn cob activated carbon	37.45	0.5	6.0	35	[56]
Jute fiber carbon	225.64	1.5	4.0	28	[57]
Graphene	153.85	0.5	3.0 – 10.0	20	[58]
Garlic peel	82.64	3.0	6.0 – 10.0	30	[59]
Cedar sawdust	111.97	5.0	7.0	20	[60]
Activated corn cobs	295.5	1.0	6.0	25	This study

*AC: Activated carbon

sorption is a spontaneous process, and since ΔH values are greater than 20 kJ/mol, MB adsorption on the adsorbents mainly proceeds chemically.

In conclusion, thanks to this study, both the waste materials have been regained an economic value and the possible damages of these wastes to the environment have been prevented. Besides, it will be possible to eliminate other pollution with the adsorbents produced from these wastes.

References

- Carneiro PA, Umbuzeiro GA, Oliveira DP, Zanoni MVB. Assessment of water contamination caused by a mutagenic textile effluent/dyehouse effluent bearing disperse dyes. *Journal of Hazardous Materials* 174 (2010) 694–699.
- Zollinger H. *Color Chemistry – Synthesis, properties and applications of organic dyes and pigments*. V.C.H. Publishers, New York, 1991.
- McKay G, Otterburn MS, Sweeney AG. The removal of colour from effluent using various adsorbents — III. Silica: Rate process. *Water Research* 14(1) (1980) 15–20.
- Garg VK, Amita M, Kumar R, Gupta R. Basic dye (methylene blue) removal from simulated wastewater by adsorption using Indian Rosewood sawdust: a timber industry waste. *Dyes Pigments* 63(3) (2004) 243–250.
- Ramakrishna KR, Viraraghavan T. Dye removal using low cost adsorbents. *Water Science & Technology* 36 (1997) 189–196.
- Waranusantigul P, Pokethitiyook P, Kruatrachue M, Upatham ES. Kinetics of basic dye (methylene blue) biosorption by giant duckweed (*Spirodela polyrrhiza*). *Environmental Pollution* 125 (2003) 385–392.
- Pilatin S, Kunduhoğlu B. Biyoadsorbsiyon ve katı-faz fermantasyonu ile boya gideriminde tarımsal atıkların kullanım potansiyeli. *Biyoloji Bilimleri Araştırma Dergisi* 11(2) (2018) 30–34.
- Korkut Z. Removal of some heavy metals from aqueous solutions by modified carrot peel. Istanbul Technical University, Graduate Institute of Natural and Applied Sciences, Master Thesis, Istanbul, 2014.
- Bayraktar AK. Removal of lead(II), nickel(II), methylene blue and Rhodamine B by natural and activated alder sawdust (In Turkish). Karadeniz Technical University, Graduate Institute of Natural and Applied Sciences, Chemistry MSc, Master Thesis, Trabzon, 2012.
- Pellera F-M, Giannis A, Kalderis D, Anastasiadou K, Stegmann R, Wang J-Y, Gidarakes E. Adsorption of Cu(II) ions from aqueous solutions on biochars prepared from agricultural by-products. *Journal of Environmental Management* 96 (2012) 35–42.
- Mahmoodi NM, Taghizadeh M, Taghizadeh A. Mesoporous activated carbons of low-cost agricultural bio-wastes with high adsorption capacity: Preparation and artificial neural network modeling of dye removal from single and multicomponent (binary and ternary) systems. *Journal of Molecular Liquids* 269 (2018) 217–228.
- Karthika M, Vasuki M. Adsorption of alizarine red-s dye from aqueous solution by sago waste: Resolution of isotherm, kinetics and thermodynamics. *Materials Today: Proceedings* 14 (2019) 358–367.
- Tran TH, Le AH, Pham TH, Nguyen DT, Chang SW, Chung WJ, Nguyen DD. Adsorption isotherms and kinetic modeling of methylene blue dye onto carbonaceous hydrochar adsorbent derived from coffee husk waste. *Science of the Total Environment* 725 (2020) 138325.
- Garg D, Kumar S, Sharma K, Majumder CB. Application of waste peanut shells to form activated carbon and its utilization for the removal of Acid Yellow 36 from wastewater. *Groundwater for Sustainable Development* 8 (2019) 512–519.
- Yusmaniar Y, Erdawati E, Ghifari YF, Ubit DP. Synthesis of mesopore silica composite from rice husk with activated carbon from coconut shell as absorbent methyl orange color adsorbent. *IOP Conference Series: Materials Science and Engineering* 830 (2020) 032078.
- Imamoglu M, Ozturk A, Aydın Ş, Manzak A, Gündoğdu A, Duran C. Adsorption of Cu(II) ions from aqueous solution by hazelnut husk activated carbon prepared with potassium acetate. *Journal of Dispersion Science and Technology* 39(8) 2018 1144–1148.
- Gundogdu A, Duran C, Senturk HB, Soylak M, Imamoglu M, Onal Y. Physicochemical characteristics of a novel activated carbon produced from tea industry waste. *Journal of Analytical Applied. Pyrolysis* 104 (2013) 249–259.
- URL-1. Bitkisel Üretim Genel Müdürlüğü Tarım Havzaları Daire Başkanlığı, Mısır Bülteni (Kasım 2019), <https://www.tarimorman.gov.tr/BUGEM/Belgeler/M%C4%B0LL%C4%B0%20TARIM/MISIR%20KASIM%20B%C3%9CLTEN%C4%B0.pdf>. Retrieved August 15, 2020.
- Vadivelan V, Kumar KV. Equilibrium, kinetics, mechanism, and process design for the sorption of methylene blue onto rice husk. *Journal of Colloid and Interface Science* 286 (2005) 90–100.
- Vargas AMM, Cazetta AL, Kunita MH, Silva TL, Almeida VC. Adsorption of methylene blue on activated carbon produced from flamboyant pods (*Delonix regia*): Study of adsorption isotherms and kinetic models. *Chemical Engineering Journal* 168(2) (2011) 722–730.
- Theydan SK, Ahmed MJ. Adsorption of methylene blue onto biomass-based activated carbon by FeCl₃ activation: Equilibrium, kinetics, and thermodynamic studies. *Journal of Analytical and Applied Pyrolysis* 97 (2012) 116–122.
- Raposo F, De La Rubia MA, Borja R. Methylene blue number as useful indicator to evaluate the adsorptive capacity of granular activated carbon in batch mode: Influence of adsorbate/adsorbent mass ratio and particle size. *Journal of Hazardous Materials* 165 (2009) 291–299.
- Söyleyici Cergel M, Demir E, Atay F. The effect of the structural, optical, and surface properties of anatase-TiO₂ film on photocatalytic degradation of methylene blue organic contaminant. *Ionics* 25 (2019) 4481–4492.
- Pathania D, Sharma S, Singh P. Removal of methylene blue by adsorption onto activated carbon developed from *Ficus carica* bast. *Arabian Journal of Chemistry* 10(1) (2017) 1445–1451.
- Jawad AH, Mohammed SA, Mastuli MS, Abdullah MF. Carbonization of corn (*Zea mays*) cob agricultural residue by one-step activation with sulfuric acid for methylene blue adsorption. *Desalination and Water Treatment* 118 (2018) 342–351.
- URL-2. Methylene blue, https://en.wikipedia.org/wiki/Methylene_blue. Retrieved August 15, 2020.
- Duran C, Ozdes D, Gundogdu A, Imamoglu M, Senturk HB. Tea industry waste activated carbon, as a novel adsorbent, for separation, preconcentration and speciation of chromium. *Analytica Chimica Acta* 688(1) (2011) 75–83.
- Boehm HP. Chemical identification of surface groups. *Advances in Catalysis* 16 (1966) 179–274.
- Muthmann J, Blaker C, Pase C, Luckas M, Schledorn C, Bathen D. Characterization of structural and chemical modifications

- during the steam activation of activated carbons. Microporous and Mesoporous Materials 309 (2020) 110549.
30. Girods P, Dufour A, Fierro V, Rogaume Y, Rogaume C, Zoulalian A, Celzard A. Activated carbons prepared from wood particleboard wastes: Characterisation and phenol adsorption capacities. *Journal of Hazardous Materials* 166 (2009) 491–501.
 31. Cimirro NFGM, Lima EC, Cunha MR, Dias SLP, Thue PS, Mazzocato AC, Dotto GL, Gelesky MA, Pavan FA. Removal of pharmaceutical compounds from aqueous solution by novel activated carbon synthesized from lovegrass (Poaceae). *Environmental Science and Pollution Research* 27 (2020) 21442–21454.
 32. Saha A, Basak BB, Ponnuchamy M. Performance of activated carbon derived from Cymbopogon winterianus distillation waste for scavenging of aqueous toxic anionic dye Congo red: Comparison with commercial activated carbon. *Separation Science and Technology* 55(11) (2020) 1970–1983.
 33. Sun K, Jiang JC. Preparation and characterization of activated carbon from rubber-seed shell by physical activation with steam. *Biomass & Bioenergy* 34 (2010) 539–544.
 34. ASTM D4607-94(1999). Standard test method for determination of iodine number of activated carbon, annual book of ASTM standards, 2006, vol.15.01.
 35. Moussout H, Ahlafi H, Aazza M, Maghat H. Critical of linear and nonlinear equations of pseudo-first order and pseudo-second order kinetic models. *Karbala International Journal of Modern Science* 4(2) 2018, 244–254.
 36. Simonin J-P. On the comparison of pseudo-first order and pseudo-second order rate laws in the modeling of adsorption kinetics. *Chemical Engineering Journal* 300(15) (2016) 254–263.
 37. Wu F-C, Tseng R-L, Juang R-S. Initial behavior of intraparticle diffusion model used in the description of adsorption kinetics. *Chemical Engineering Journal* 153(1–3) (2009) 1–8.
 38. Lagergren S. About the theory of so-called adsorption of soluble substance. *Kungliga Svenska Vetenskapsakademiens Handlinga* 24 (1898) 1–39.
 39. Kumar KV. Linear and non-linear regression analysis for the sorption kinetics of methylene blue onto activated carbon. *Journal of Hazardous Materials* 137(3) (2006) 1538–1544.
 40. Ray SS, Gusain R, Kumar N. Carbon nanomaterial-based adsorbents for water purification, fundamentals and applications micro and nano technologies: Chapter five – Adsorption equilibrium isotherms, kinetics and thermodynamics. 2020, Pages 101–118, Elsevier Inc.
 41. Weber Jr WJ, Morris JC. Kinetics of adsorption on carbon from solution. *Journal of the Sanitary Engineering Division* 89 (1963) 31–59.
 42. Cheung WH, Szeto YS, McKay G. Intraparticle diffusion processes during acid dye adsorption onto chitosan. *Bioresource Technology* 98(15) (2007) 2897–2904.
 43. Kavitha D, Namasivayam C. Capacity of activated carbon in the removal of acid brilliant blue: determination of equilibrium and kinetic model parameters. *Chemical Engineering Journal* 139 (2008) 453–461.
 44. Doran PM. *Bioprocess engineering principles* (Second Edition), Chapter 11 – Unit operations. 2013, Pages 445–595, Elsevier Inc.
 45. Qada ENE, Allen SJ, Walker GM. Adsorption of methylene blue onto activated carbon produced from steam activated bituminous coal: A study of equilibrium adsorption isotherm. *Chemical Engineering Journal* 124 (2006) 103–110.
 46. Langmuir I. The adsorption of gases on plane surfaces of glass, mica and platinum. *Journal of American Chemical Society* 40 (1918) 1361–1403.
 47. Freundlich HMF. Über die Adsorption in lösungen, zeitschrift für physikalische chemie. 57 (1906) 385–470.
 48. Bhomick PC, Supong A, Baruah M, Pongener C, Gogoi C, Sinha D. Alizarin red S adsorption onto biomass based activated carbon: Optimization of adsorption process parameters using Taguchi experimental design. *International Journal of Environmental Science and Technology* 17 (2020) 1137–1148.
 49. Moreno-Castilla C. Adsorption of organic molecules from aqueous solutions on carbon materials. *Carbon* 42 (2004) 83–94.
 50. Gundogdu A, Duran C, Senturk HB, Soylak M, Ozdes D, Serencam H, Imamoglu M. Adsorption of phenol from aqueous solution on a low-cost activated carbon produced from tea industry waste: Equilibrium, kinetic, and thermodynamic study. *Journal of Chemical and Engineering Data* 57(10) (2012) 733–743.
 51. Khormaei M, Nasernejad B, Edrisi M, Eslamzadeh T. Copper biosorption from aqueous solutions by sour orange residue. *Journal of Hazardous Materials* 149 (2007) 269–274.
 52. Karagoz S, Tay T, Ucar S, Erdem M. Activated carbons from waste biomass by sulfuric acid activation and their use on methylene blue adsorption. *Bioresource Technology* 99 (2008) 6214–6222.
 53. Dural MU, Cavas L, Papageorgiou SK, Katsaros FK. Methylene blue adsorption on activated carbon prepared from Posidonia oceanica (L.) dead leaves: Kinetics and equilibrium studies. *Chemical and Engineering Journal* 168 (2011) 77–85.
 54. Prajapati AK, Mondal MK. Comprehensive kinetic and mass transfer modeling for methylene blue dye adsorption onto CuO nanoparticles loaded on nanoporous activated carbon prepared from waste coconut shell. *Journal of Molecular Liquids* 307 (2020) 112949.
 55. Kuang Y, Zhang X, Zhou S. Adsorption of methylene blue in water onto activated carbon by surfactant modification. *Water* 12(2) (2020) 587.
 56. Aljeboree AM, Hussein FH, Alkaim AF. Removal of textile dye (methylene blue mb) from aqueous solution by activated carbon as a model (corn-cob source waste of plant): As a model of environmental enhancement. *Plant Archives* 19(2) (2019) 906–909.
 57. Senthilkumaar S, Varadarajan PR, Porkodi K, Subbhuraam CV. Adsorption of methylene blue onto jute fiber carbon: kinetics and equilibrium studies. *Journal of Colloid and Interface Science* 284(1) (2005) 78–82.
 58. Liu T, Li Y, Du Q, Sun J, Jiao Y, Yang G, Wang Z, Xia Y, Zhang W, Wang K, Zhu H, Wu D. Adsorption of methylene blue from aqueous solution by graphene. *Colloids and Surfaces B: Biointerfaces* 90 (2012) 197–203.
 59. Hameed BH, Ahmad AA. Batch adsorption of methylene blue from aqueous solution by garlic peel, an agricultural waste biomass. *Journal of Hazardous Materials* 164 (2009) 870–875.
 60. Hamdaoui O. Batch study of liquid-phase adsorption of methylene blue using cedar sawdust and crushed brick. *Journal of Hazardous Materials* 135(1-3) (2006) 264–273.

